COLLEGE DOCTORAL BRETAGNE SCIENCES POUR L'INGENIEUR

INSA INSTITUT NATIONAL DES SCIENCES APPLIQUÉES RENNES

THESE DE DOCTORAT DE

L'INSTITUT NATIONAL DES SCIENCES APPLIQUEES DE RENNES

ECOLE DOCTORALE N° 647
Sciences pour l'Ingénieur
Spécialité : *Génie civil*

Par

Runqi HAO

Effect of internal curing on shrinkage and self-healing of cementitious materials

Thèse présentée et soutenue à Rennes, le 24.09.2025
Unité de recherche : Le laboratoire de Génie Civil et Génie Mécanique (LGCGM)
Thèse N° : 251SAR 18 / D25 - 18

Rapporteurs avant soutenance :

Amor BEN FRAJ Directeur de Recherche, UMR MCD – Cerema, Université Gustave Eiffel, France
Farid BENBOUDJEMA Professeur des universités, ENS Paris-Saclay, Université Paris-Saclay, France

Composition du Jury :

Examinateurs : Amor BEN FRAJ Directeur de Recherche, UMR MCD – Cerema, Université Gustave Eiffel, France
Farid BENBOUDJEMA Professeur des universités, ENS Paris-Saclay, Université Paris-Saclay, France
Ouali AMIRI Professeur des universités, Université de Nantes, France
Jacques JABBOUR Docteur, Responsable Technique & Développement Ciment & Construction, Timab Magnesium, France

Dir. de thèse : Aveline DARQUENNES Professeur des Universités INSA Rennes, France
Co-enc. de thèse : Kinda HANNAWI Maître de conférences INSA Rennes, France

Résumé

Cette recherche traite du problème de la fissuration prématurée du béton en étudiant le rôle des matériaux de cure interne dans la réduction du retrait endogène et du retrait de dessiccation, ainsi que dans l'amélioration des capacités d'auto-cicatrisation des matériaux à base de ciment. Plus précisément, les granulats légers (LWA), les granulats de béton recyclé (RCA) et le biochar ont été systématiquement étudiés afin d'évaluer leur comportement d'absorption et de libération d'eau, ainsi que leurs effets sur l'hydratation du ciment, la structure poreuse, les propriétés mécaniques et l'auto-cicatrisation.

Premièrement, des expériences ont été menées pour déterminer l'influence de différentes tailles et teneurs en LWA et RCA sur l'efficacité de la cure interne dans les mortiers. Les résultats ont montré que les granulats de petite taille réduisent plus efficacement le retrait endogène, améliorent la distribution de l'humidité relative interne et renforcent les performances mécaniques. En outre, les RCA présentent une excellente capacité de libération d'eau en raison de la pâte de ciment résiduelle à leur surface, ce qui améliore considérablement l'auto-cicatrisation du matériau.

Deuxièmement, l'incorporation de biochar dans les mortiers a été étudiée en ce qui concerne son influence sur le processus d'hydratation et la structure des pores. Il a été démontré que le biochar réduit efficacement le retrait à jeune âge grâce à sa porosité élevée et à sa libération d'eau. De plus, les effets de la combinaison du biochar avec l'oxyde de magnésium (MgO) ont été examinés, montrant des améliorations notables des propriétés mécaniques et de la réduction du retrait.

Enfin, des méthodes 2D et 3D ont été mises en œuvre pour évaluer la capacité d'auto-cicatrisation apportée par les matériaux de cure interne. La combinaison du LWA et du RCA a considérablement accéléré la fermeture des fissures et amélioré la durabilité à long terme des matériaux à base de ciment.

Abstract

This research addresses the issue of early-age cracking in concrete by investigating the role of internal curing materials in mitigating autogenous and drying shrinkage, as well as enhancing self-healing capabilities of cement-based materials. Specifically, lightweight aggregates (LWA), recycled concrete aggregates (RCA), and biochar were systematically studied to assess their water absorption and release behaviors, and their effects on cement hydration, pore structure, mechanical properties, and self-healing abilities.

Firstly, experiments were conducted to determine the influence of different particle sizes and contents of LWA and RCA on internal curing efficiency in mortar. Results indicated that smaller-sized aggregates more effectively reduced autogenous shrinkage, improved internal humidity distribution, and enhanced mechanical performance. Furthermore, RCA exhibited excellent water-release capabilities due to residual cement paste on their surfaces, significantly improving the self-healing capacity of the material.

Secondly, the incorporation of biochar into mortar was studied regarding its influence on hydration processes and pore structure. It was found that biochar effectively reduced early-age shrinkage due to its high porosity and effective water release. Additionally, the synergistic effects of combining biochar with magnesium oxide (MgO) were investigated, showing substantial improvements in mechanical properties and shrinkage reduction.

Lastly, two-dimensional and three-dimensional monitoring techniques were utilized to systematically evaluate the enhancements in self-healing performance provided by internal curing materials. The combination of LWA and RCA notably accelerated crack closure rates and significantly improved the long-term durability of cement-based materials.

Contents

General introduction 1
Objectives of the present research project 3
Chapter 1 Literature review 7
1.1 Delayed deformations of cementitious materials 7
1.1.1 Autogenous shrinkage 10
1.1.2 Drying shrinkage 13
1.1.3 Restraint of shrinkage 16
1.2 Internal curing 17
1.2.1. Internal curing materials 18
1.2.2 Mechanisms of internal curing 28
1.3 Factors affecting the effect of internal curing 33
1.3.1 Key factors of ICAs 34
1.3.2 The migration of internal curing water 37
1.4 The influence of internal curing on the properties of cement-based materials 40
1.4.1 Effects on the interface transition zone (ITZ) 41
1.4.2 Effects on Mechanical Properties of Cement-based Materials 42
1.4.3 Influence on durability of Cement-based Materials 44
1.5 Self-healing of cementitious material 45
1.5.1 The healing of cementitious material 46
1.5.2 Encapsulated ICA systems for self-healing 48
1.6 Conclusion 50
Chapter 2. Characterization of internal curing agents 52
2.1 Materials 52
2.2 Experimental methods 54
2.2.1 Water absorption and density 54
2.2.2 Water release 61
2.2.3 Pore size distribution and specific surface area 62
2.2.4 Thermogravimetric analysis of ICAs 63
2.3 Properties of the ICAs 64
2.3.1 LWA and RCA 64
2.3.2 Biochar 75
2.4 Summary 81
Chapter 3 Mortar Design, Preparation, and Characterization Methods 83
3.1 Mortars designed with LWA and RCA 83
3.2 Mortars with biochar 87
3.3 Mortars mixing process 89
3.4 Techniques for Mortar Characterization 90
3.4.1 Microstructure 91
3.4.2 Mechanical performances 99
3.4.3 Shrinkages from early age to long term 101

3.4.4 Healing process 107
3.5 Summary 110
Chapter 4. Size and content effect of LWA and RCA as internal curing agent 111
4.1 Protected paste volume ratio 112
4.2 Hydration and microstructure of mortars with LWA and RCA 118
4.2.1 Hydration products 118
4.2.2 Porosity 122
4.3 Mechanical properties of mortars with LWA and RCA 127
4.3.1 Compressive strength 128
4.3.2 Flexural strength 130
4.3.3 Dynamic modulus 132
4.3.4 Summary 133
4.4 Autogenous Shrinkage of mortars with LWA and RCA 134
4.4.1 Autogenous deformation before 1 day 134
4.4.2 Effect of LWA from 1 day to long term 138
4.4.3 Effect of RCA from 1 day to long term 143
4.5 Total and Drying Shrinkages of mortars with LWA and RCA 151
4.5.1 The effect of LWA 151
4.5.2 The effect of RCA 155
4.5.3 Effect of broader particles size ranges for RCA 157
4.6 Summary 159
Chapter 5 Effect of biochar on internal curing of cement-based materials 161
5.1 Hydration and pore structure of mortars with biochar 161
5.1.1 Hydration products 162
5.1.2 Total water porosity and real density 170
5.2 Mechanical properties of mortars with biochar 172
5.2.1 Compressive strength 172
5.2.2 Flexural strength 173
5.2.3 Dynamic modulus 174
5.2.4 Summary 175
5.3 Autogenous Shrinkages of mortars with biochar 176
5.3.1 Deformation at early age 176
5.3.2 Autogenous deformation beyond 1 days 179
5.3.3 Autogenous deformation from setting time 187
5.4 Total and drying shrinkages of mortars with biochar 188
5.4.1 Total shrinkage 188
5.4.2 Drying shrinkage 189
5.4.3 Comparison with SAP and SIL 193
5.4.4 Effect of the curing 195
5.5 Summary 197
Chapter 6. The effect of LWA and RCA on self-healing capacity 199
6.1 Healing process under water curing 200
6.1.1 Crack width evolution : 2D approach 200

6.1.2 Water Flow : 3D approach 204
6.2 Healing process under sealed condition 208
6.2.1 Crack width evolution: 2D approach 208
6.2.2 Water flow: 3D approach 210
6.3 Summary 212
Chapter 7 General Conclusion 214
Reference 217
Appendix A 228
Appendix B 229
Appendix C 231

General introduction

The problem of concrete cracking is a problem that has not been fundamentally solved but cannot be avoided. Modern concrete requires concrete with high durability, but the occurrence of cracks is bound to be detrimental to the durability of concrete [1]. Cracks provide a way for external aggressive substances (such as various ions, water, air, etc.) making easier the corrosion of the reinforced concrete [2]. Existence of cracks greatly reduces the service life of the structure and reduces the durability [3]. To enhance the performance and durability of modern concrete, it is essential to minimize cracking and its subsequent impact on the long-term integrity of the structure. Many factors can cause tensile stresses into concrete leading to a cracking risk, such as a mechanical loading and restrained deformations, e.g.. However, many cracks arise in the absence of external loading factors [1]. These cracks are often caused by the restriction of delayed deformations, whether by internal or external elements [2]. As a result, controlling these deformations has become a primary focus of research aimed at mitigating concrete cracking.

Among the main problems of early cracking in concrete, autogenous and drying shrinkage are two key points. Autogenous shrinkage refers to the reduction in the macroscopic volume of concrete caused by chemical shrinkage and self-desiccation resulting from the ongoing hydration of cement paste under conditions of constant temperature and external relative humidity [3]. Autogenous shrinkage is problematic because it begins at a very early age and may continue for several weeks. Even after 28 days, in particular for low-carbon concretes within a high content of mineral additions [4], the material may still be vulnerable to cracking due to ongoing internal volume reduction. Such delayed cracking increases permeability and makes the structure more susceptible to water penetration and chemical attack [2]. Conversely, drying shrinkage arises due to hydric exchanges between the material and its environment. This process is characterized by volume changes due to the variations in water content into the

porous network and the capillary pressure [3].

To mitigate the adverse effects of autogenous and drying shrinkage, several strategies have been developed. These include external curing methods [5], the use of shrinkage-reducing admixtures, incorporation of expansive agents [6], and the application of internal curing (IC) techniques. Among these, internal curing has emerged as one of the most promising approaches due to its ability to maintain internal relative humidity (IRH) and support continued hydration, especially in mixtures with low water-to-binder ratios [2-4]. The effectiveness of internal curing relies on the use of pre-saturated porous materials such as lightweight aggregate (LWA) [1-4], recycled concrete aggregate (RCA) [8], and biochar [9], which serve as internal water reservoirs. These materials can gradually release water during the hydration process, thereby reducing capillary tension and limiting shrinkage-induced stresses [8].

The primary objective of this study is to assess the ability of lightweight aggregate (LWA), recycled concrete aggregate (RCA) and biochar to mitigate autogenous and drying shrinkage in cement-based materials through internal curing. These two types of shrinkage are key contributors to early-age cracking, which compromises durability. By evaluating the internal curing potential of these alternative materials, the study aims to determine their effectiveness in reducing shrinkage-related stresses. A secondary objective is to explore how such internal curing may contribute to self-healing processes. Since cracking in concrete is inevitable, enabling early-stage autonomous crack closure can significantly improve long-term durability and reduce the need for costly maintenance and repairs. In this context, the potential of RCA and LWA to act as internal curing agents for both shrinkage reduction and enhanced self-healing is thoroughly investigated.

Objectives of the present research project

This research is based on the fundamental requirement that internal curing agents (ICAs) must effectively retain and release water to mitigate shrinkage. Our study builds on the proven internal curing capacity of lightweight aggregate (LWA), while exploring two alternative and less-studied materials: recycled concrete aggregate (RCA) and biochar. Despite their promising characteristics, RCA and biochar have received limited attention in the context of internal curing. Here, RCA is directly compared to LWA to evaluate its performance against a conventional benchmark, whereas biochar is examined for its distinctive porous structure. The main objective of this research work is to use these materials to reduce shrinkage and promote self-healing in mortar, without significantly compromising mechanical strength. Figure 1 presents a schematic overview of the framework that underpins this investigation.

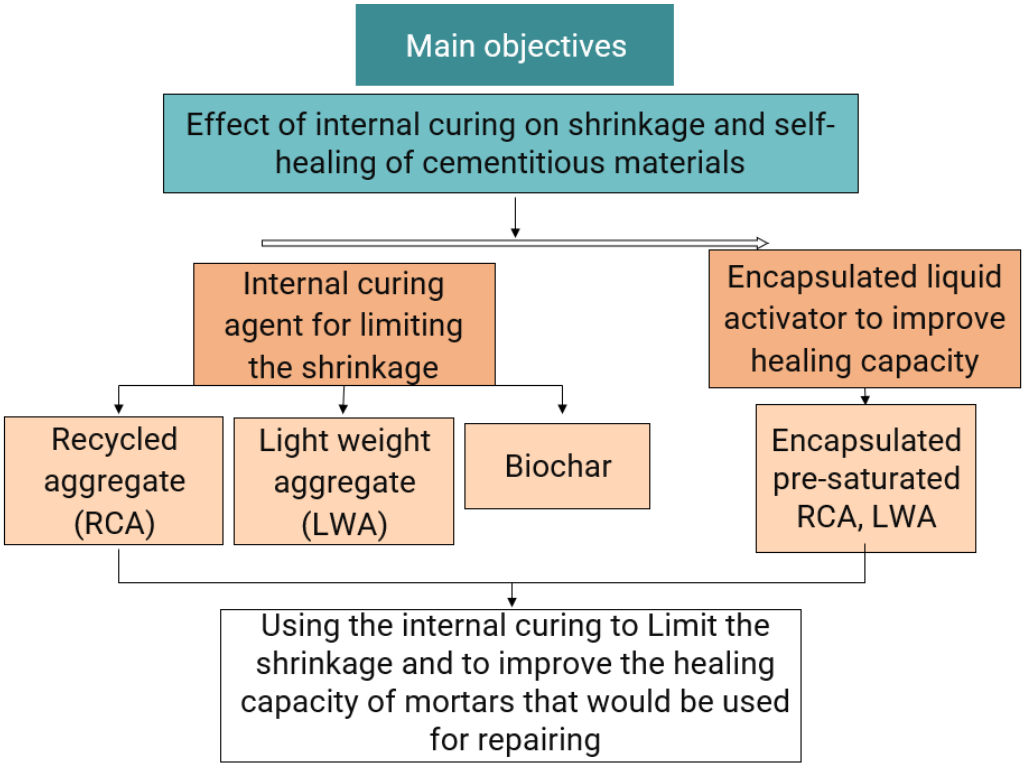


Figure.1 Schematic overview of the framework of the PhD thesis

This research is guided by a series of critical questions aimed at addressing fundamental challenges in the field of the internal curing of cementitious materials. The core problems and areas of investigation include:

1. ***How do the water absorption and release characteristics of LWA, RCA and biochar affect the internal hydration mechanisms and relative humidity within cementitious systems?*** Understanding the role of these ICAs in the hydration process is essential for limiting the shrinkage development and for optimizing the durability and strength of concrete structures.

2. ***What is the impact of varying particle sizes and quantities of LWA and RCA on the physical and mechanical properties of cementitious materials?*** This question seeks to unravel the relationship between the incorporation of these aggregates and the observed changes in contraction, pore structure, and hydration at different stages of material development. The objective is to identify the formulations that achieve the best compromise between mechanical strength and shrinkage mitigating.

3. ***In what ways do biochar, particularly when combined with magnesium oxide (MgO), influence the fundamental properties of cement-based materials?*** The study focuses on assessing the modifications in mechanical and shrinkage properties introduced by different proportions of biochar and the synergistic effects of biochar and MgO on hydration dynamics across various water-cement ratios. The objective is to identify the formulations that achieve the best compromise between mechanical strength and shrinkage mitigating.

4. ***How do LWA and RCA contribute to the self-healing capabilities of cementitious materials?*** Identifying formulations that balance mechanical integrity with the ability to self-repair could revolutionize the sustainability and longevity of concrete infrastructure.

By tackling these questions—how ICAs such as LWA, RCA, and biochar influence hydration, shrinkage, and self-healing behavior in cement-based materials—this

research aims to contribute to the development of more durable and efficient mortars. The adopted methodology and results are organized as follows in the present manuscript :

- **Chapter 1** provides a literature review on internal curing strategies, examining the underlying mechanisms, typical materials (LWA, RCA, superabsorbent polymers, biochar), and key challenges in mitigating autogenous and drying shrinkages and promoting long-term durability. In addition, the healing process of cementitious materials is introduced, with a focus on how ICAs such as LWA and RCA contribute to autogenous self-healing.

- **Chapter 2** presents the characterization of the ICAs used in this study, including their physical properties such as water absorption and water release behavior, and microstructure, such as porosity. The effect of the particles size on some of these properties is also investigated for selecting the more interesting curing agents.

- **Chapter 3** outlines the mortar mix design, sample preparation, and experimental methods used to evaluate hydration process, mechanical properties, autogenous and drying shrinkage from early age to long term, and healing performances.

- **Chapter 4** investigates the effect of LWA and RCA particles size and content on hydration kinetics, mechanical performances and shrinkage mitigation. It identifies optimal mixture proportions that balance internal curing efficiency with strength performances.

- **Chapter 5** explores the potential of biochar as an ICA, analyzing its impact on autogenous and drying shrinkage and compatibility with cementitious matrices as well as its combination with another shrinkage-reducing agent, magnesium oxide.

- **Chapter 6** examines the self-healing capacity of mortars incorporating LWA and RCA, with and without magnesium oxide (MgO) encapsulation, under two types of curing. Crack width (CW) evolution and healing rate (HR) are tracked to assess long-term healing potential.

The manuscript concludes by summarizing the key findings and identifying the most effective combinations of internal curing agents and mix proportions. It underscores the significance of internal curing not only in enhancing the sustainability of cement-based materials, but also in reducing maintenance requirements and enabling the design of mixtures with autonomous self-healing capabilities.

Chapter 1 Literature review

The chapter begins by exploring the delayed deformations of cementitious materials, which are essential in understanding the durability of concrete. Autogenous and drying shrinkages are significant contributors to the early cracking of concrete, compromising its long-term performance. The chapter highlights the various types of shrinkage and their impact on the integrity of cement-based materials.

Following this, the chapter introduces the concept of internal curing as a method to mitigate shrinkage. Materials such as lightweight aggregate (LWA), recycled concrete aggregate (RCA), and other porous materials are discussed for their role in promoting internal curing by retaining water and gradually releasing it to sustain hydration. The importance of selecting proper internal curing agents (ICAs) based on their water absorption and release capacities is emphasized. The chapter then transitions to the topic of internal curing materials, examining their properties and the mechanisms by which they reduce shrinkage. Various agents, such as biochar, SAP (superabsorbent polymers), and silica, are compared for their effectiveness.

Finally, the introduction addresses the self-healing potential of cementitious materials, particularly in relation to encapsulated ICAs. The autonomous healing capability and the mechanisms by which cracks can heal are explored, with a focus on the role of ICAs in facilitating this process.

1.1 Delayed deformations of cementitious materials

Concrete cracking can be the result of the combined effects of different types of delayed deformations when they are restrained. Cement-based materials, essential in construction, undergo volumetric variations due to chemical, thermal, and microstructural changes, and hydric exchanges with their environment. These deformations, when restrained (e.g., by the concrete substrate in the case of repair

mortars), can generate tensile stresses that lead to cracking within the concrete structure [7, 10, 11] (Figure 1.1). Cracks allow an easier penetration of water and aggressive agents like chloride ions and carbon dioxide [6], damaging the cement matrix and steel reinforcements in accelerating corrosion of the reinforcement, undermining the structure's durability. Understanding and addressing these deformations are crucial for the longevity and reliability of concrete structures.

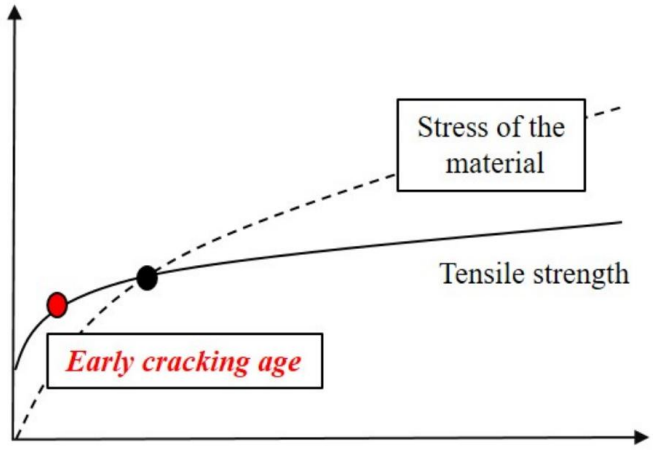


Figure. 1.1 Cracking risk as a function of time [7]

The common types of deformation in concrete are as follows [1, 10, 12]: autogenous shrinkage, drying shrinkage, thermal deformation, carbonization shrinkage, plastic shrinkage, crystal expansion, Phase transformation shrinkage, etc.

Here are a short explanation of different deformations:

- **Chemical shrinkage:** This is the reduction in absolute volume of cement-based materials due to the hydration reactions, as the volume of hydration products is smaller than that of the reactants [12,13].

- **Autogenous shrinkage:** Autogenous shrinkage in concrete comprises chemical shrinkage and self-drying shrinkage – generally named autogenous shrinkage. Initially, autogenous shrinkage aligns with chemical shrinkage, where internal and external volume changes are equivalent. After the initial setting, as the concrete forms a solid skeleton, observed deformation is less than the concrete's total volume

change due to capillary pores formed by chemical shrinkage, which then lead to autogenous shrinkage. Thus, shrinkage deformation measured under sealed conditions reflects chemical shrinkage before initial setting and combines chemical and self-drying shrinkage after. Self-drying shrinkage refers to the volumetric decrease of cement-based materials under sealed and isothermal conditions, resulting from the hydration process which reduces free water in capillary pores [12].

- **Drying shrinkage:** This is the decrease in volume of cement-based materials due to water loss under drying conditions, leading to the formation of meniscus in the capillary pores [15].
- **Thermal deformations:** This occurs when the exothermic hydration reaction of cement causes initial thermal expansion in fresh concrete, followed by shrinkage as the reaction rate decreases and the temperature drops. Thermal deformations can also be influenced by changes in the external environment, where fluctuations in ambient temperature can further contribute to the expansion and contraction of the concrete [14].
- **Carbonization shrinkage:** This is the reduction in volume resulting from the reaction of calcium hydroxide and C-S-H type gels, produced during cement hydration, with carbon dioxide in the air [15, 17].
- **Plastic shrinkage:** This refers to the shrinkage occurring before concrete sets, starting with settlement due to gravity and continuing with water evaporation and hydration process [2, 16].
- **Crystal expansion:** During cement hydration, the formation of crystalline materials can cause slight expansion due to crystallization pressure, which occurs when crystal growth is restricted by the solid skeleton of the concrete [18].
- **Shrinkage caused by morphological transformation:** Volume changes occur as certain cement components (e.g., aluminate) hydrate and transform into a more

stable form, more pronounced in cement with higher alumina content [16].

- **Synergism:** This refers to the volume changes in concrete when well-crystallized components lose chemically bound water under specific humidity conditions. For example, when calcium silicate hydrate (C-S-H) in concrete loses chemically bound water in low humidity, the material shrinks due to the collapse of its crystalline structure. If humidity rises again, some water can be reabsorbed, partially reversing the shrinkage. [26].

This study focuses on two primary types of deformation in concrete: autogenous shrinkage, which occurs due to the hydration of cementitious materials, and drying shrinkage, caused by hydric exchanges with the environment. These two forms of shrinkage are critical to the long-term durability of concrete and are the main focus of the research, as they play a significant role in structural integrity.

In response to the complexity of concrete shrinkage and the persistent issue of early shrinkage cracks, this thesis reviews existing control strategies and mechanisms for mitigating shrinkage. It then outlines the research aims of this study, contributing to efforts in tackling early shrinkage challenges in concrete structures.

1.1.1 Autogenous shrinkage

Autogenous shrinkage occurs in concrete due to internal volume changes during hydration, primarily driven by the chemical reactions between water and cement [3, 10, 12]. Unlike drying shrinkage, which is caused by external moisture loss, autogenous shrinkage happens in sealed conditions, and it is more pronounced in high-performance concrete with low water-binder ratios. This type of shrinkage results from self-desiccation, where the internal capillary pores formed during hydration cause internal drying and subsequent deformation, which can lead to early-age cracking and affect the durability of concrete [10]. Understanding and mitigating autogenous shrinkage is essential for improving the long-term performance of modern cementitious materials.

1.1.1.1. Mechanism [12, 13]

Autogenous shrinkage is driven by two coupled mechanisms: capillary pressure development as capillary pore water is consumed and menisci form, and C-S-H gel network densification and collapse as internal humidity drops during hydration. These processes, rigorously quantified by Lura [12] following the Jensen & Hansen [13] theoretical framework. Internal curing, particularly using pre-saturated LWA, serves to maintain internal RH and delay or mitigate both mechanisms: higher LWA replacement ratios correspond to larger reductions in autogenous shrinkage, effectively maintaining internal humidity over the critical early ages [10].

1.1.1.2.Parameters affecting autogenous shrinkage

Many researchers [3, 4, 10, 16, 19-23, 27] have investigated the influence of chemical admixtures, mineral additions, water-cement ratio and other factors on autogenous shrinkage. The main information is summarized hereafter:

1. Water-cement ratio: The water-cement ratio is one of the most influential parameters governing autogenous shrinkage. Several studies have demonstrated that lower water-cement ratios tend to intensify self-desiccation, leading to more pronounced autogenous shrinkage in cementitious systems [3, 11, 16, 21,22]. As the water content decreases, the internal relative humidity (IRH) drops rapidly due to insufficient free water to sustain continued hydration, thereby accelerating capillary pressure development [3, 13]. In low w/c systems, the absence of internal water reserves results in greater tensile stress accumulation under restrained conditions, making the material more prone to early-age cracking [1, 12]. Therefore, reducing the water-cement ratio, although beneficial for strength development, significantly increases the autogenous shrinkage .

2. Cement nature and mineral additions : The development of autogenous shrinkage in cementitious systems is strongly influenced by both the mineralogical composition of the cement and the incorporation of supplementary cementitious materials (SCMs). High-alumina cements and early-strength formulations typically promote greater early-

age shrinkage due to their rapid hydration kinetics and heat evolution. In particular, the hydration of tricalcium aluminate (C_3A) and tetracalcium aluminoferrite (C_4AF) contributes to accelerated internal water consumption, which intensifies self-desiccation and internal stress development [27].

The incorporation of supplementary cementitious materials (SCMs) notably modifies autogenous deformation behavior. In particular, partial replacement of Portland cement with ground granulated blast furnace slag (GGBFS) often mitigates early-age shrinkage due to its slower hydration kinetics and refinement of the pore structure [16]. However, as the slag content increases beyond a certain threshold (e.g., above 70%), autogenous shrinkage may be exacerbated owing to prolonged self-desiccation under sealed conditions [11,16].

Silica fume, due to its high pozzolanic reactivity and ultra-fine particle size, increases autogenous shrinkage significantly by accelerating self-desiccation during early hydration [23]. In contrast, fly ash is known to reduce autogenous shrinkage, especially at early ages. Its slower hydration rate delays water consumption and maintains IRH for longer periods. Additionally, the incorporation of fly ash tends to refine the pore structure and reduce the connectivity of capillary pores. While smaller pores can generate higher capillary pressures according to the Kelvin–Laplace relationship, the reduced connectivity and slower moisture transport delay self-desiccation, thereby lowering the rate and extent of shrinkage development [13, 23].

Metakaolin (MK), due to its high pozzolanic activity and fine particle size, significantly increases autogenous shrinkage. It promotes rapid water consumption during the early hydration stage and contributes to matrix densification, thereby accelerating internal RH reduction and capillary pressure development [13].

Therefore, the selection and content of SCMs must be carefully optimized to balance strength development, durability enhancement, and shrinkage control. When used improperly—especially in low w/b systems—SCMs may exacerbate autogenous shrinkage and induce early-age cracking if no preventive measures are implemented [4,

11, 13, 16, 23, 27].

3. Chemical admixtures: Chemical admixtures can influence autogenous shrinkage to varying degrees, depending on their type and dosage. Superplasticizers (SP), widely used to improve workability at low water-to-binder ratios, have been found to slightly reduce autogenous shrinkage [27]. This effect is generally attributed to their ability to slow down the hydration rate during the early age, which delays self-desiccation and capillary pressure build-up. However, the influence of SP on autogenous shrinkage is relatively limited, and variations between different types and dosages are not substantial [35-37].

In contrast, shrinkage-reducing admixtures (SRA) are specifically designed to lower the surface tension of pore solution, thereby reducing capillary stresses that drive autogenous shrinkage. Experimental studies have demonstrated that the percentage reduction in autogenous shrinkage closely corresponds to the reduction in surface tension achieved by SRA incorporation [27]. This correlation highlights the mechanism by which SRA acts: by decreasing the meniscus curvature and associated capillary pressure within the pore network, SRAs help mitigate internal tensile stress and thus reduce volumetric contraction. Their effectiveness makes SRAs a promising strategy in systems vulnerable to early-age cracking, especially when combined with other mitigation methods such as internal curing.

4. Cement fineness: finer cement particles accelerate the hydration process due to their larger surface area, leading to quicker water consumption and higher internal drying (self-desiccation). This generates greater capillary pressure, causing more pronounced autogenous shrinkage at early age period [29].

1.1.2 Drying shrinkage

Drying shrinkage refers to the volume reduction in concrete caused by moisture loss when exposed to a dry environment [32]. The magnitude of drying shrinkage is not

directly proportional to the total amount of water evaporated from the material. In the early stages of drying, evaporation mainly occurs from larger pores (macropores), which has little effect on shrinkage because the meniscus curvature is small and capillary tension is negligible [13,40]. As drying progresses, moisture is gradually removed from finer capillary pores, where the smaller pore radius generates higher capillary tension according to the Kelvin–Laplace relationship [3]. This capillary tension induces internal tensile stresses within the pore walls, drawing the solid matrix closer together and resulting in volumetric contraction. Additionally, the loss of adsorbed water from gel pores at later stages can further contribute to shrinkage through changes in surface free energy at the solid–water interface [3]. Thus, capillary tension in fine pores, rather than total moisture loss, is the principal driving force behind drying shrinkage.

1.1.2.1 Driving mechanisms

In the literature, several mechanisms drive the drying shrinkage in cement-based materials as function of the IRH, as described hereafter:

When IRH > ~40%, shrinkage is primarily driven by capillary tension. As drying progresses, water menisci form in partially saturated capillary pores, generating negative capillary pressure that pulls the solid skeleton together and induces contraction. In this range, water is still present in capillary pores, and shrinkage magnitude correlates with the rate of IRH decrease due to water loss from these pores [23, 26, 32, 40].

As IRH decreases below ~40%, capillary theory alone becomes insufficient because the pore size becomes too small to sustain stable menisci. Instead, shrinkage continues due to disjoining pressure between adjacent C–S–H layers. In this regime, attractive van der Waals forces increasingly dominate over repulsive hydration forces, leading to densification of the solid network. The loss of physically adsorbed water from gel pores increases surface energy and draws the layers closer, contributing to irreversible deformation even when mass loss is minimal [26, 32, 40].

At very low IRH (<~20%), interlayer water within the C–S–H structure is released. This process alters the basal spacing of C–S–H sheets, producing significant and partially irreversible volume change due to structural rearrangement and collapse of the smallest pores. In this final stage, water removal is strongly associated with changes in C–S–H crystallographic order rather than bulk water transport, making recovery upon rewetting limited [26, 32, 40].

1.1.2.2 Parameters affecting the deformation

(1) Effect of w/b ratio

1. Water-cement ratio: The w/b ratio directly influences the pore structure and moisture transport properties of concrete, thereby affecting its drying shrinkage. A lower w/b ratio produces finer capillary pores, leading to faster R.H. reduction near the surface during drying, which increases shrinkage gradients. Conversely, a higher w/b ratio may reduce early-age drying shrinkage but can increase total shrinkage over long-term exposure due to higher total water content [32].

(2) Effect of mineral additions

Mineral additions, such as fly ash, silica fume, or bottom ash, modify pore size distribution and water retention capacity, influencing both drying shrinkage and autogenous shrinkage. Wyrzykowski et al. [49] reported that bottom ash improved internal RH distribution and delayed surface moisture loss in high-performance mortars, reducing early-age shrinkage and mitigating later-age drying shrinkage. Pozzolanic additions can also refine pores, slowing moisture loss, though in some cases this refinement can intensify autogenous shrinkage if not balanced with internal curing [46,49].

(3) Size effect

Drying shrinkage is strongly size-dependent. Smaller cross-section elements lose moisture faster, developing steeper RH gradients and higher surface shrinkage

compared to larger members [40,41]. This effect is especially critical for thin slabs or repair overlays, where drying from multiple surfaces accelerates moisture loss and increases cracking risk.

1.1.2.3 Other influencing parameters

Apart from w/b and mineral additions discussed earlier, several other material- and process-related parameters significantly affect internal RH evolution and drying shrinkage. The cement type and mineral composition influence hydration kinetics, pore structure development, and capillary tension formation. Cements with higher fineness or higher C_3S content typically generate finer capillary pores, leading to higher capillary stresses during drying [41].

Curing conditions and drying history are also critical. Adequate moist curing delays surface drying, moderates RH gradients, and reduces shrinkage potential, whereas insufficient curing accelerates moisture loss and sharpens RH gradients, particularly in large or exposed members [42]. Poor curing may lead to severe drying shrinkage concentrated near the surface, creating tensile stresses that drive crack formation.

Finally, environmental conditions such as ambient temperature, relative humidity, and wind speed directly control the drying rate. Low ambient RH and high temperature increase evaporation flux, accelerating internal RH reduction and shrinkage development [15, 42]. In practice, many shrinkage mitigation measures—such as internal curing, surface coatings, or the use of shrinkage-reducing admixtures—are essentially aimed at controlling these moisture gradients and reducing capillary stress formation during drying [46, 49].

1.1.3 Restraint of shrinkage

When the shrinkage is restrained leading sometimes to the tensile stresses equal to the tensile strength of the concrete, the concrete can present a cracking risk. The restraint

can be related to internal or external elements.

The internal restraint causes can be the humidity gradient [10, 20, 40], the aggregates [41], e.g.. The humidity gradient results in differential shrinkage within the material as describing in section 1.1.2. This differential shrinkage generates tensile stresses near the drying surface [31]. These stresses are balanced by compressive stresses in the core of the specimen. Cracks appear on the surfaces when these tensile stresses reach the material's tensile strength. A second type of internal restraint in cement-based composites arises from the stiff aggregate particles [41]. The interaction between these non-shrinking aggregates and the shrinking cement paste matrix creates localized stress concentrations [31]. Cracking occurs when the restraint exerted by an aggregate particle is sufficiently strong, leading to the development of radial and circumferential (or bond) cracks around the aggregate. Hiller [26] pointed out that in the concrete with low water-cement ratio and silica fume, the confinement effect of aggregate is one of the reasons for the tensile stress caused by shrinkage. Lura et al. [19] found that the shrinkage value of concrete is always smaller than that of cement paste with the same water-binder ratio, and increasing the volume of coarse aggregate can reduce the shrinkage. Similarly, Aitcin [15] proposed that when the shrinkage caused by cement paste remains unchanged, increasing the volume of coarse aggregate represents more constraints on shrinkage.

1.2 Internal curing

After the concrete is poured, the surrounding environment has a great influence on its strength and durability [26, 28], thus proper curing is essential. The purposes of curing are threefold: to prevent water loss that causes plastic shrinkage and early-age cracking; to accelerate hydration and enhance early strength (e.g., through high-temperature steam curing); and to protect the low-strength concrete at early ages from mechanical or environmental damage. In practice, the primary goal of curing is to avoid early cracking.

To mitigate early-age cracking, particularly in concrete with a low water-to-binder ratio, various shrinkage control strategies have been developed based on the underlying mechanisms [7, 24–26]. These approaches can be broadly classified into external curing, internal curing, shrinkage-reducing admixtures, expansion compensation, and permanent formwork. External curing maintains surface moisture through methods such as water spraying, wet coverings, or curing compounds, but its effectiveness is limited in low-permeability concrete where moisture cannot easily penetrate to the interior. Permanent formwork can reduce surface drying but has little influence on internal moisture distribution. Among these strategies, internal curing—achieved by incorporating water-retaining materials (ICAs) uniformly within the concrete—has proven to be the most effective and reliable for improving volume stability and minimizing early-age cracking, especially in high-performance and mass concrete [32, 35, 39]. ICAs gradually release stored water into the cementitious matrix, sustaining IRH, promoting continued hydration, refining the microstructure, and thereby enhancing both strength and durability [28, 30–32].

The main steps of the internal curing process are described hereafter. During the hardening of concrete, the internal water content of the concrete decreases with the hydration of the cementitious material and diffuses through the environment. The IRH inside the concrete begins to decrease from the initial saturated state. The ICA starts to add water to the interior porous network of the concrete to maintain the IRH at a high level. Thus, on the one hand, the early shrinkage of concrete is reduced, and on the other hand, a higher relative humidity promotes the continuous hydration of the cementitious materials, which makes the interior of the concrete denser and improves the strength of the concrete [, 30-32].

1.2.1. Internal curing materials

The basic requirements of internal curing for materials include "thermodynamic availability" and "dynamic availability" [19]. The former represents that the material

for the internal curing needs to have excellent water absorption performance, and the latter represents that it needs to have excellent water release performance [32]. These two performances will be determined for the internal curing materials studied in the present research.

The nature of materials used for the internal curing is various. Here are some examples [32]: lightweight expanded clay aggregate (LECA), pumice, expanded shale, zeolite, perlite, cenospheres, superabsorbent polymer (SAP), recycled aggregate (RCA), wood-derived powders and fibers, rice husk ashes (RHA), coal bottom ashes, biological lightweight aggregate (LWA), bentonite clay, etc. Although there are many types of materials that can be used for internal curing, the commonly used internal curing materials can be summarized into two categories: (1) substances containing physically absorbed water and (2) porous materials as shown in Table 1.1. Their detailed description is provided in the following paragraphs. The three main key factors [32] affecting the internal curing performances are : (1) volume of water needed to saturate the ICAs,(2) desorption properties of the ICAs and (3) distribution of the ICAs into the mixture. They are also discussed in these sections.

Table 1.1 Summary of internal curing materials based on water absorbing mechanism [32].

Type		Water-absorbing mechanism	Examples
Substances containing physically absorbed water		Absorption of water by the physical bonds or van der Waals force	Bentonite clay [32] SAP [25]
Porous materials	LWA and biochar	Porous aggregates generally absorb significant amounts of water (about 10%–30% by mass), mainly by physical capillary force	LECA [35-37] pumice [38,39] RCA [42] expanded shale [43] zeolite [36,44] perlite [45] bio-LWA [46] biochar [9]
	Porous superfine powders	Low water absorption capacity mainly by physical capillary force, and it has nm-size pores	RHA [46,47] acid leaching residue of boron [47] mud [48] bottom ash [49]

1.2.1.1 Superabsorbent polymers

Superabsorbent polymers (SAPs) have superior desorption capacity compared to other internal curing materials [50-54]. These polymers are typically used as a dry concrete admixture, absorbing water during the mixing process. Furthermore, SAP allows for flexible design of the shape and size of the voids formed [54].

The underlying mechanism of SAP involves polymer hydrogels with polyelectrolyte chains that form a three-dimensional network [55]. These particles swell when in contact with water due to osmotic pressure and water affinity [56]. The high ion concentration within the SAP, compared to the external environment, generates this osmotic pressure [57].

Notably, the most common SAPs used in concrete are cross-linked copolymers of acrylic acid and acrylamide. These materials are stable and can swell in the alkaline

cement pore solution [58]. At pH levels above 5, the carboxylic acid groups of acrylic acid deprotonate, while the amide groups of acrylamide partially hydrolyze at pH levels above 12 [57,59].

The amount of SAP used significantly affects internal curing. For exemple, Watanabe [59] reported that adding 0.35% SAP (by mass of cement) in a mixture with w/b = 0.25 reduced autogenous shrinkage to approximately one-third of the reference. Doubling the SAP dosage to ~0.70% essentially eliminated autogenous shrinkage.

Moreover, the size of SAP particles also impacts curing efficiency. Reported SAP particle sizes typically span 80 μm to 1000 μm, with the most effective hydration enhancement zones observed around 400 μm particles [54,62–65]. While larger particles absorb more water [62], smaller particles can be more effective for internal curing due to their ability to create larger protected zones in denser matrices. Mihaljevic et al. [54] found that the effective diffusion distance for SAP-entrained water is limited to 200 μm. Larger particles have longer water migration distances [63, 64]. However, it is crucial to note that large particles can negatively impact mechanical properties [65].

For pre-treatment, SAP particles that are partially swollen by water can adhere together. To prevent 'gel blocking', smaller particles that absorb water faster can be blended with cement and supplementary cementitious materials (SCMs) before adding water.

In summary, SAPs offer significant benefits for internal curing in concrete through their superior desorption capacity and ability to form customizable voids. Their functionality, dependent on pH levels and particle size, plays a critical role in mitigating autogenous shrinkage and optimizing curing efficiency.

Despite their promising performance, SAPs also present several limitations that restrict their universal application. First, the formation of voids after water desorption can negatively affect mechanical properties, particularly compressive strength, if not properly accounted for in the mix design [65]. Second, SAPs are highly sensitive to environmental conditions, such as pH and ionic concentration in the cement pore

solution, which can significantly alter their swelling capacity and kinetics [57,58]. Third, the effective diffusion distance of SAP-entrained water is limited, typically within a few hundred microns [62], meaning that homogeneous distribution is critical yet difficult to achieve in large-scale or dense matrices. Moreover, overdosing SAP may cause bleeding, segregation, or excessive void content, while underdosing fails to achieve the desired curing effect [61]. Lastly, cost and material compatibility issues can limit their use in conventional concretes, making SAPs more suitable for specialized applications such as high-performance or self-healing concretes rather than general-purpose mixtures [65].

1.2.1.2 Porous materials

Porous materials are characterized by their high porosity, a feature that enables them to store water efficiently within their pores. This distinctive capability renders them highly suitable for use as ICAs in various applications. In this context, understanding the role of porous materials extends beyond recognizing their water retention properties; it involves a comprehensive evaluation of their performance in internal curing processes. Therefore, this section is dedicated to exploring the advantages and disadvantages of different types of porous materials when employed as ICAs.

- ***Lightweight aggregates***

LWA are defined as construction materials that have a bulk density lower than that of common construction aggregates [22]. LWA used in cement-based materials is often used to replace aggregate or sand. LWA can be light expanded clay aggregate [35], zeolite [36], pumice [38], etc. (Table 1.2).

LWA is a porous material, and its water absorption ability is related to inner continuous porosity and particle size. The porosity and pore size of LWA must fall within an optimal range to ensure effective internal curing. In general, a total porosity of 20%–40% is considered suitable for water absorption without compromising mechanical

strength, while the pore diameter should predominantly fall within the 0.1–10 μm range to balance sufficient water storage with timely desorption during cement hydration [1, 22, 35, 39]. If the pores are too small (< 0.05 μm), water may be retained too tightly and not released efficiently. Conversely, excessively large pores (> 50 μm) may lead to premature water release and reduced curing efficiency [32]. Jensen [66] thought that an improved spatial distribution can be achieved by reducing the size of the single water containers and increasing their number. If the pores in LWA were too large, the water retention capacity of LWA would be poor. Light Expanded Clay Aggregate (LECA) showed high absorption rate and can release the water at high R.H. [32] (Table 1.2). LWA have been successfully employed as partial replacement of conventional coarse aggregate and sand [67,68] to reduce shrinkage (Table 1.2). In addition, the content of LWA must be sufficient to ensure uniform distribution throughout the cementitious matrix and to provide adequate internal curing water. Typically, a volume replacement ratio of 15%–25% of fine aggregate or a mass content equivalent to 8%–12% of cement weight is recommended, depending on the water absorption capacity of the LWA and the target water demand for internal curing [22, 28]. Insufficient content may result in localized self-desiccation, while excessive replacement can affect the workability and strength of the mixture.

Table 1.2 The effect of different LWA on shrinkage.

Type of LWA	Water absorption (%)	LWA content (%)	Shrinkage reduction at 28-day (%)
LECA [35]	11.0	20	Total shrinkage : 20
Zeolite [36]	15.6	20	Total shrinkage : 15
Pumice [38]	19	4	Autogenous shrinkage : 25
Expanded shale [43]	15	6	Autogenous shrinkage : 30
Perlite [45]	30	25	Autogenous shrinkage : 80

- ***Recycled aggregates***

RCA is a sustainable construction material prepared from waste concrete. RCA is also a kind of porous aggregate, and using it as an ICA could have similar effects to LWA.

The difference is that the water absorption capacity of RCA is less than most LWA [69, 74], which means that compared to LWA, more RCA is needed to introduce the same amount of water. But compared with natural aggregates, RCA has higher water absorption and porosity, RCA has a relatively high porosity (5%-20%) and a water absorption capacity ranging from 3% to 12%, compared to approximately 0.5–1% for natural aggregates [73, 74]. At the same time, one notable feature is the significant presence of hydrated cement paste on the surface of RCA particles. This layer of hydrated cement paste not only enhances the bonding properties of RCA with the new cement paste but also plays a crucial role in RCA's ability to release water during the curing process [42, 75-78].

Table 1.3 The efficiency of different size of RCA on shrinkage.

Size of RCA (mm)	Water absorption (%)	content (%)	Shrinkage reduction at 28-day (%)
0.6-1.18 [39]	11.8	50	Autogenous shrinkage : 155
1.18-2.36 [39]	10.76	50	Autogenous shrinkage : 120
2.36-4.75 [39]	8.52	50	Autogenous shrinkage : 78
0.25-4 [47]	7.39	50	Drying shrinkage : 10
4-5.6 [54]	6.9	25	Autogenous shrinkage : 35

- ***Biochar***

Biochar is a by-product obtained from the thermal decomposition of biomass materials (livestock manure, crop residues, and sewage sludge) without or with little oxygen (usually at 300 – 700 °C) [79]. The release of volatiles and organic matter during pyrolysis forms a hierarchical porous structure, often described as honeycomb-like, with micro-, meso-, and macropores. This porous network endows biochar with a high water absorption capacity, with reported values ranging from 100% to over 500% of its own weight, depending on pyrolysis temperature and raw material [80].

Furthermore, the low thermal conductivity and abundant pores (particle size < 600 μm) of the biochar material improve the thermal insulation of concrete by disrupting thermal bridges [79]. Additionally, biochar generates numerous interconnected pore networks

within concrete [82, 83], causing sound waves to refract and dissipate into heat upon entering the material, thereby enhancing its sound absorption properties [83].

In addition to these functional benefits, recent studies have reported that incorporating biochar can reduce shrinkage: 100% replacement level of sand with biochar achieved 65 % reductions in total shrinkage [81]; incorporating waste-derived biochar into UHPC reduced autogenous shrinkage by approximately 15–30%, depending on the pretreatment method, due to its ability to store and gradually release water during hydration [82]. These findings highlight biochar's potential as an internal curing agent and shrinkage mitigator.

1.2.1.3 Porous superfine powders

Small particle size materials with large specific surface area, mesoporous structure and absorbing ability of the aqueous phase mainly characterize porous superfine powders, and absorbed water of porous superfine powders supplies for further hydration of cementitious materials [32]. It includes RHA [46], acid leaching residue of boron mud [48], and bottom ash [49], and the main properties of porous superfine powers is shown in Table 1.4. The use of porous superfine powders can delay and slow down the decrease of the internal R.H. (self-desiccation) of UHPC, hence strongly mitigating its autogenous shrinkage [46]. For instance, the incorporation of 10%–15% porous silica fume or nano-metakaolin has been shown to reduce autogenous shrinkage by approximately 30%–50% at 7 days, particularly in mixtures with low water-to-binder ratios (< 0.25), where internal RH depletion is severe [45]. RHA is a by-product of agricultural waste that has a mesoporous structure that has internal curing capability [84], as shown in Figure 1.2. In HPC, water absorbing capacity of RHA is 17.15 L/m^3 according to [46]. In addition, the size of pores in RHA particles, i.e. from 2 to 50 nm in diameter (see Figure 1.2), is much smaller than that of SAP particles (whose size ranges from about 100 to 300 μm, with a maximum of approximately 450 μm [85]) and that of LWAs (about 10-20 μm [71]). According to Kelvin equation [86],

the pores responsible for internal curing exhibit capillary activity primarily within a R.H. range of 75% to 98%, meaning that their size distribution enables them to absorb or release water in response to environmental humidity fluctuations within this interval:

$$r = -\frac{2\gamma V_m}{RTln(RH)} \tag{1.1}$$

where r is the pore radius (m), γ is the surface tension of water (N/m), V_m is the molar volume of water (m^3/mol), R is the universal gas constant (8.314 J/mol·K), T is the absolute temperature (K), and RH is the relative humidity in decimal form.

This means that when the internal R.H. in UHPC drops below 98%, the absorbed water in these mesopores will release to compensate the self-desiccation during hydration. It postpones and slows the internal R.H. reduction in the RHA-blended matrices. Thus, RHA also plays as an ICA to reduce the self-desiccation, and hence to mitigate autogenous shrinkage of UHPCs. In addition, the dosage and particle size of RHA have great influence in autogenous shrinkage of high-performance cement-based materials.

Table 1.4 Main properties of porous superfine powders [32].

Type	RHA	Acid leaching residue of boron mud	Bottom ash
Density (g/cm^3)	2.19	--	1.4-2.2
Blaine (BET) SSA (m^2/g)	50-150	50.2	--
Mean particle size (μm)	3-10	3.89	100-600
Pore size	2-50 nm	--	3 nm-1 μm
Absorption (ml/g)	0.180	0.1-0.2	--
Content of silica	90%-96%	58.3%	--
Reference	[39-41, 87-89]	[47]	[48]

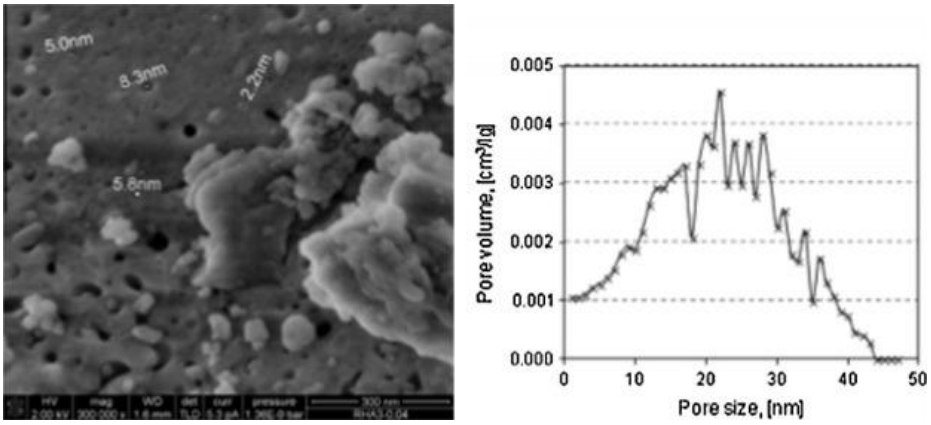


Figure. 1.2 Porous surface structure and pore size distribution of ground RHA [46].

1.2.1.4 Other materials influence internal curing

Other materials can be added to the cement matrix to mitigate the shrinkage as the expansive agents, which react chemically with water to form crystalline hydration products generating volume expansion at the macroscale. This expansion can offset early shrinkage, particularly autogenous shrinkage in low water-to-cement ratio concretes [6, 18, 90-93].

Currently, the commonly used expansive agents include sulfoaluminate cement (CSA)-based, calcium oxide (CaO)-based, and magnesium oxide (MgO)-based systems. CSA expansive agent requires a large amount of water for hydration, and its hydration products exhibit poor thermal stability, undergoing dehydration decomposition at

temperatures above 70 °C [94, 95]. Conversely, the hydration rate of the calcium oxide expansive agent is very rapid, making it difficult to control [96]. Compared to calcium oxide and sulfur aluminate expansive agents, the magnesium oxide (MgO) expansive agent requires less water for hydration, and its hydration products possess more stable physical and chemical properties. Moreover, the expansion rate of magnesium oxide can be regulated and designed, which enhances its application in engineering practices [97,98].

The individual use of expansive agents can effectively compensate for shrinkage [6]. Furthermore, their combined use with ICAs can amplify this effect [91-93]. For example, Li et al. [98] reported that combining 8% CaO-based expansive agent with 10% pre-saturated LWA in a concrete mix (w/c = 0.4) increased early expansion and reduced total shrinkage by approximately 25% compared to the use of the expansive agent alone. The coupled system also limited the reduction in mechanical properties typically caused by the use of a single expansive agent to just 8%.

In summary, the integration of expansive agents, either individually or in combination with ICAs, presents a viable solution for mitigating shrinkage-induced issues in concrete.

1.2.2 Mechanisms of internal curing

The Powers model and some of its developments can illustrate how LWA plays a key role by maintaining moisture for improved hydration. This section examines LWA's mechanisms in promoting uniform hydration, directly contributing to shrinkage reduction and enhancing the durability of cement-based materials.

1.2.2.1 Powers model

The Powers model [99] provides a theoretical framework for understanding the influence of ICAs on hydration and shrinkage control in cement-based materials. With

a known w/c ratio, the model predicts the volumetric distribution of gel (mainly C–S–H), capillary pores, gel water, and unhydrated cement during hydration [100,101]. For mixes with w/c < 0.36, hydration may be limited by either the available space to accommodate hydration products or the amount of water available. When the system lacks sufficient water, self-desiccation leads to a reduction in capillary water, causing a drop in IRH and the development of capillary tension. Gel water, being strongly adsorbed within the C–S–H structure, does not affect IRH changes above about 75% [102].

Capillary tension is the main driving force behind early-age autogenous shrinkage. As hydration progresses, smaller pores empty, increasing capillary pressure, while the degree of saturation decreases. At early ages, the stiffness of the paste is low, and its viscous response is high, so even small stresses can cause large shrinkage strains. The inclusion of saturated LWA—whose pores (about 10–20 μm [71]) are significantly larger than those in the cement paste—can alleviate this effect. During self-desiccation, water moves from larger pores to smaller ones, and the largest pores in LWA empty first [81], effectively increasing the radius of the liquid–vapor menisci and reducing capillary tension.

In the volumetric phase diagram of the Powers model, adding LWA is equivalent to increasing the available water reservoir and modifying the pore size distribution, thereby slowing the IRH drop and sustaining hydration over a longer period. This not only mitigates autogenous shrinkage but also increases the ultimate degree of hydration. Figure 1.3 compares the phase distribution of cement-based materials without ICAs and with saturated LWA, illustrating that timely replenishment of pore water is crucial for effective internal curing. As will be shown later in this study, the particle size and content of LWA influence the efficiency of water release and, consequently, its shrinkage mitigation performance.

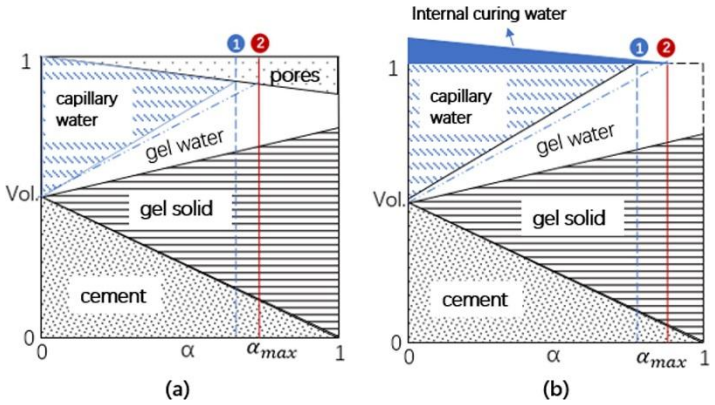


Figure. 1.3 Volumetric phase distribution of cement paste as a function of the degree of hydration without (a) and with (b) internal curing (sealed system) [102].

1.2.2.2 Effect of LWA on hydration

To illustrate the internal curing mechanism of LWA and its effect on cement hydration, this section analyzes the water transfer behavior between LWA and the surrounding cement paste, as well as its impact on the hydration degree and pore saturation.

As hydration progresses, the IRH of cement paste decreases, generating a difference in pore pressure between the paste and the water-filled pores of the LWA. Henkensiefken et al. [2] reported that this pore pressure difference enables the cement paste to extract water from nearby LWA particles. Bentur et al. [35] further confirmed that water tends to migrate from larger to smaller pores, driven by capillary forces. Since LWA typically releases water from its largest pores first [28], its effectiveness depends on having pores larger than those in the cement paste [32].

The concept of critical pore size refers to the smallest pore size that can remain saturated under a given capillary pressure. When the internal curing water from LWA is released into the surrounding paste, it helps maintain saturation in smaller capillary pores by increasing the critical pore radius. As shown in Figure. 1.4, without LWA, pores smaller than r_1 remain saturated, while larger ones dry out. With LWA, additional water raises the critical radius, keeping more pores saturated and mitigating autogenous shrinkage.

Building on this mechanism, Castro et al. [22] observed that LWA continues to release water until moisture equilibrium is reached with the surrounding paste, thereby delaying self-desiccation. Moreover, Cusson et al. [43] demonstrated that sufficient LWA content helps the material develop internal compressive stress during the early stages of hydration, giving the matrix time to build tensile resistance and thus reducing early-age cracking risk.

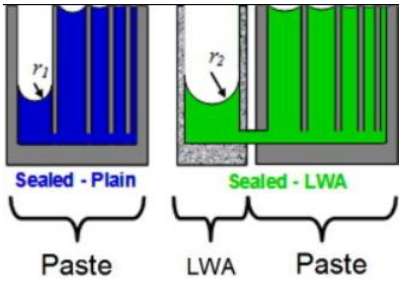


Figure.1.4 Concept drawing of internal curing in closed condition [12].

To illustrate the quantitative influence of LWA on sustaining hydration under low w/c conditions, Figure 1.5 presents the internal curing effect of varying LWA contents. Figure 1.5 illustrates how increasing LWA content enhances the degree of hydration. In sealed conditions without LWA (Figure 1.5(a)), hydration ceases once the initial mixing water is consumed, reaching a limit of 0.73. With 11% LWA providing 3.2% additional water (Figure 1.5(b)), hydration continues until 0.77. At 23.7% LWA (Figure 1.5(c)), the hydration limit reaches 0.83. This hydration limit refers to the maximum attainable degree of hydration under the available water supply, which increases with the amount of internal curing water. As water migrates from LWA to the cement paste, pore saturation is sustained, and hydration continues, effectively “transferring” the pore volume from the paste into the LWA.

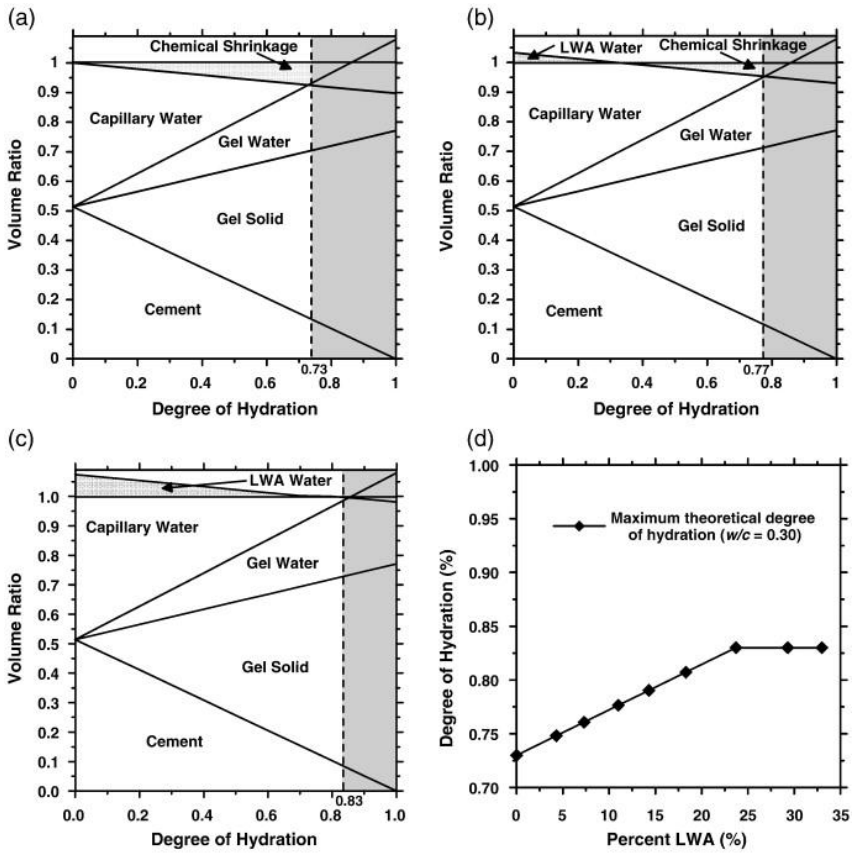


Figure. 1.5 Internal curing effect of different amounts of extra water in mortar with w/c = 0.30 [103]: no LWA (a) 11% LWA (b) 23.7% LWA (c) relationship between degree of hydration and LWA content (d).

1.2.2.3 The effect of internal curing on drying shrinkage

This section discusses how IC, especially via saturated LWA, can mitigate drying shrinkage by regulating internal moisture transport and reducing capillary stress development during the drying process.

While drying shrinkage and autogenous shrinkage are often distinguished by their triggers—external water loss versus internal self-desiccation—they share the same underlying mechanism: capillary tension generated by pore water depletion. Studies by Bentz et al. [3] and Tazawa et al. [27] confirmed this equivalence, as drying shrinkage-reducing admixtures were also found to reduce autogenous shrinkage. Liu [32] further explained that the magnitude of shrinkage is governed by the critical capillary tension,

which refers to the maximum capillary pressure that develops when pores of a certain size begin to desaturate. This parameter is closely related to pore size distribution (smaller pores induce higher tension), degree of saturation (lower saturation increases the tension in remaining pore water), and the internal–external humidity gradient, which together influence moisture migration and stress development in the cement paste.

Figure 1.6 conceptually shows how IC can counter this effect. In unsealed plain concrete, the drying front progresses inward until equilibrium is reached, and the critical pore radius (r_3) shifts to smaller values—meaning only very small pores remain saturated. However, in mixtures with LWA, moisture stored in the aggregate is gradually released into the surrounding cement paste. This slows the advancement of the drying front, delays the drop in internal RH, and maintains pore saturation in a broader range of pores. As a result, the development of capillary tension is moderated, thus reducing drying shrinkage.

In summary, by sustaining internal saturation and smoothing humidity gradients, internal curing with LWA effectively reduces drying-induced shrinkage and delays early-age cracking, particularly under unsealed or drying conditions.

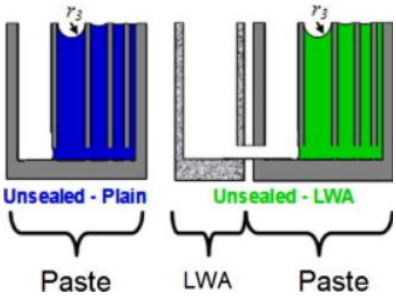


Figure.1.6 Conceptual illustration of internal curing under dry conditions [12].

1.3 Factors affecting the effect of internal curing

The curing effect of LWA is affected by three factors [12, 32]: LWA water storage capacity, water release properties, and LWA distribution. Suzuki et al. [1] believed that the internal curing effect basically depends on the contents and some properties of LWA, such as water absorption, pore structure, particle size distribution, ratio of open pores

to closed pores, and mechanical properties.

1.3.1 Key factors of ICAs

1.3.1.1 Water absorption

Due to the differences in pore structure, such as internal pore size and connectivity, ICAs with different particle sizes exhibit distinct porosity, water absorption, and pore size distribution [12]. Larger LWA particles generally have larger pores, and when they are crushed, the fracture surfaces often intersect these large pores, making them accessible for water penetration and thus increasing the water absorption rate [30]. As shown in Figure 1.7, LWA particles with a size of 2.36 mm reach over 20% absorption after 7 days, while 1.18 mm and 0.60 mm particles show significantly lower absorption, confirming the positive correlation between particle size and absorption capacity [104, 106]. However, pore size and structure also govern the water release rate: small pumice particles, despite their lower water absorption coefficient, can release up to 90% of absorbed water during the early stages of hydration [13, 106], whereas larger particles often release water more slowly due to “ink-bottle” pores. When the RH decreases to a level where the critical radius of curvature matches the narrow inlet of such pores, large pores empty first.

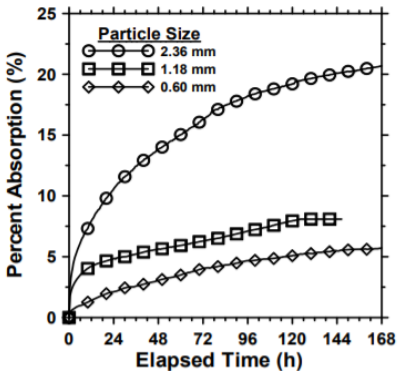


Figure.1.7 The water absorption of light aggregate particles with different sizes varied with time [104].

The particle size and pore structure of ICAs play a critical role in determining their water absorption behavior and, consequently, their effectiveness in mitigating shrinkage and enhancing hydration. However, the optimal characteristics vary with ICA type. For SAP, larger particle sizes tend to provide greater water storage capacity due to their lower surface-area-to-volume ratio and greater internal pore volume, enabling a more prolonged water supply. Yet, excessively large SAP particles can lead to non-uniform spatial distribution in the matrix [85, 101, 105]. In the case of RCA, its internal curing capacity is mainly derived from the adhered old mortar, which contains numerous pores. Finer RCA particles (<1.25 mm) typically have higher paste content and water absorption, with absorption decreasing linearly with particle size [109]. Biochar exhibits high variability in absorption (50%–500% by mass) depending on feedstock and pyrolysis conditions [79–81], due to its hierarchical micro- and mesoporous structure. However, excessive microporosity may lead to premature desorption, reducing long-term curing effectiveness [61].

Overall, neither larger particle size nor higher porosity inherently guarantees better performance. Extremely fine pores or overly large porosity may cause early water loss, effectively raising the initial w/c and diminishing the intended curing effect. For optimal performance, pores should predominantly be in the mesopore range (2–50 nm) and total porosity should generally not exceed ~50% to retain moisture without compromising mechanical integrity [22].

1.3.1.2 Water release

Water release refers to the capacity of ICAs to gradually supply stored water to the surrounding cement paste during hydration. This process is controlled by the ICA's pore structure—specifically, pore size, connectivity, and distribution—which together determine the timing and effectiveness of water delivery.

For LWA and RCA, efficient water release is associated with high porosity and open, interconnected pore networks that allow stored water to migrate under the high IRH

conditions typical during early hydration [102, 106]. Biochar also features a complex micro- and mesoporous structure. While it can store significant water, its release efficiency depends on the accessibility of these pores. Closed or ultrafine pores may inhibit water release, especially at early ages when IRH remains high [84, 85].

Experimental observations have shown that the ability of a pore to release water depends strongly on its size and the surrounding IRH. When the meniscus radius within a saturated pore is around 100 nm, the IRH is approximately 99% [103]. This implies that only pores larger than about 100 nm are capable of releasing water under such conditions [12]. Therefore, if the majority of pores in LWA, RCA, or biochar are smaller than this threshold, water remains trapped and unavailable for hydration. In such cases, a much greater quantity of ICA is required to compensate for autogenous shrinkage, which may compromise mix proportions. Zhutovsky et al. [106] also reported that below a certain particle size, further reducing the LWA size does not improve internal curing efficiency, because both porosity and pore size tend to decrease, limiting water release.

1.3.1.3 Spatial distribution

The spatial distribution of ICAs plays a critical role in determining their efficiency in mitigating autogenous shrinkage. In cement-based materials with a low water-to-cement ratio, the permeability of the capillary pore network is significantly reduced, limiting long-range water migration. When ICAs are poorly distributed, the average distance between cement paste and the nearest ICA increases. Even with sufficient internal curing water, ineffective spatial coverage leads to localized self-desiccation and high shrinkage values [16,19]. In contrast, a homogeneous ICA distribution reduces water transport distance and enhances curing efficiency by sustaining local IRH [12].

Bentz et al. [107] proposed using the “protected paste volume” concept to evaluate ICA effectiveness. This volume refers to the zone of paste whose IRH is maintained by nearby ICAs. Smaller ICA particles provide a greater number of curing points per unit

volume, resulting in denser coverage and improved hydration support. Akcay et al. [108] confirmed this in experiments, showing that fine LWA reduced autogenous shrinkage and improved mechanical performance more effectively than coarse LWA, due to better spatial distribution.

SAP shows similar behavior: larger SAP particles offer greater water storage, but smaller particles distribute more uniformly and extend protected zones in dense matrices like UHPC [101]. Jensen et al. [102] introduced the concept of an "optimal particle size" for internal curing. Deviations from this optimal size—either too small or too large—can reduce curing efficiency, not only due to altered absorption behavior, but also diminished spatial coverage. Optimizing both particle size and spatial dispersion enables effective internal curing with minimal ICA content [69].

For RCA, the effectiveness of internal curing depends on the amount of adhered mortar and its particle size. Finer RCA tends to distribute more evenly in the matrix and contains more residual paste, offering greater water absorption and a more favorable spatial profile for internal curing [109]. Similarly, biochar—with its fine particle size, low density, and high porosity—can be well dispersed throughout the cement matrix, forming an interconnected network of internal reservoirs. However, excessive fineness or poor dispersion may lead to particle clustering, limiting the spatial reach of curing water [80–84].

In conclusion, the spatial distribution of ICAs—governed by their size, density, and dispersion uniformity—is as important as their water retention capacity. A uniformly distributed ICA system ensures localized IRH support, promotes continuous hydration, and effectively suppresses autogenous shrinkage in high-performance cementitious materials.

1.3.2 The migration of internal curing water

The efficiency of IC is not only determined by the total amount of water absorbed by ICAs, but also by the ability of this water to migrate through the cementitious matrix

and reach the unhydrated cement. This section focuses on three critical aspects that govern this process: water migration distance, the factors influencing this distance, and the timing of water release. Although most studies have focused on LWA, similar migration mechanisms are applicable to other ICAs, such as RCA, biochar, and SAP, each showing different behavior due to their intrinsic material properties.

1.3.2.1 Water migration distance

The water migration distance refers to the maximum radius around an ICA particle within which its absorbed water can effectively influence cement hydration. Lura et al. [12] proposed that a longer migration distance results in a larger "protected zone," i.e., the volume of cement paste that remains hydrated with a limited self-desiccation. As shown in Figure 1.8, increasing the water migration distance can enhance IC efficiency even when the ICA content remains constant, by enlarging the volume of protected paste. Conversely, if the migration distance is short, the ICAs must be more densely distributed to maintain uniform hydration as presented in section 1.3.1.3.

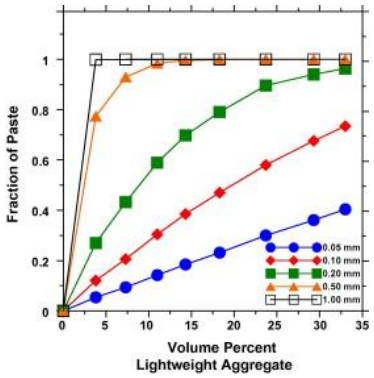


Figure.1.8 Effects of different water migration distances and volume percent of LWA on the volume of the protected paste [102].

This mechanism is relevant to all ICAs. For instance, SAP particles, which are immobilized within the hardened matrix, the migration radius of released water [55, 56] is inherently limited, and their elastic nature means that internal water may remain trapped under mechanical or capillary pressure [25,64]. In contrast, stiffer ICAs such as LWA, RCA, and biochar are less susceptible to compression-induced pore closure,

allowing more consistent water release through connected pore networks [62]. However, when RCA or biochar are ground to very fine sizes, poor connectivity between internal pores and the surrounding matrix can still restrict migration [62], leading to localized desiccation and microcracking even when the total absorbed water is sufficient.

1.3.2.2 Factors affecting water migration distance

Water migration is primarily governed by two interrelated parameters: the pore structure of the ICA and the permeability of the cement paste. Zhutovsky et al. [106] and Lura et al. [12] emphasized that it is not merely the ICA content that determines IC performance, but rather how effectively water can travel through the pore network. A more open and connected ICA pore structure—such as that found in highly porous LWA or RCA—enhances the ability to release water. Likewise, the permeability of the paste controls the movement of water toward desiccated zones. However, this permeability decreases over time due to the hydration process. The new products (primarily C-S-H and CH) fill capillary pores and reduce connectivity, thereby shortening the effective migration distance. This progressive densification underscores the importance of initiating internal curing before significant pore blockage occurs [106].

1.3.2.3 Water release time

The timing of internal water release is crucial for mitigating early-age shrinkage. Lura et al. [12] described water release as a balance between the "driving force"—chemical shrinkage during hydration—and the "resistance"—developing impermeability of the paste. Water release is most effective in the first 4–5 days after mixing, before capillary pores become significantly blocked. During this window, ICAs such as LWA or RCA can readily discharge water to mitigate the drop in IRH.

Biochar exhibits distinct water release profiles depending on pyrolysis conditions [80-84]. While its high surface area promotes rapid water absorption, closed or tortuous

pores may delay water desorption, potentially aligning its release with ongoing hydration demands. In contrast, SAPs may experience premature release due to osmotic pressure gradients, making their effectiveness more sensitive to the environmental conditions and matrix permeability [85, 101].

Therefore, optimizing water release time requires matching ICA properties—such as pore size distribution and connectivity—with the evolving microstructure of the cement paste.

1.4 The influence of internal curing on the properties of cement-based materials

The utilization of internal curing materials, such as LWA, RCA and biochar, in the context of cement-based materials introduces a dual-pronged influence. On one hand, these materials, despite their efficacy in promoting internal curing, present challenges. Their inherent characteristics, including low strength, high porosity, and a reduced elastic modulus, can potentially weaken the mechanical properties of the cementitious materials [43, 45, 78, 79]. Furthermore, the high porosity can compromise the durability of the final product [43, 75, 76], while the lower elastic modulus may lead to an increase in shrinkage [72, 74].

Conversely, the process of internal curing exerts a beneficial impact on cement hydration, thereby enhancing the mechanical properties [19, 47, 81] and durability [47, 79] of the cementitious materials. Additionally, it has a counteracting effect on shrinkage, as the internal curing water effectively fills the pores within the paste, mitigating the propensity for shrinkage to occur [12, 19, 102].

In summation, the incorporation of internal curing materials entails a careful balance of advantages and potential drawbacks. The efficacy of this approach lies in the strategic management of these dual effects to optimize the mechanical properties, durability, and shrinkage characteristics of cement-based materials. This section has therefore

discussed the fundamental mechanisms, influencing factors, and performance implications of ICAs, covering their effects on the ITZ, mechanical properties, and durability.

1.4.1 Effects on the interface transition zone (ITZ)

The interfacial transition zone (ITZ) refers to the thin layer between aggregate particles and the surrounding cement paste. Due to its relatively high porosity, low strength, and poor microstructural integrity, the ITZ is often considered the weakest region in cementitious composites and plays a critical role in determining the durability and mechanical properties of the material [45, 110]. The structure and performance of the ITZ are significantly influenced by the type, surface texture, porosity, and moisture condition of ICAs, such as LWA, RCA, and biochar [13, 83].

The porosity and permeability of the ITZ are typically higher than those of the surrounding paste, contributing to greater water sorptivity in mortar [15, 28]. For example, comparisons between mortars and pastes with the same water-to-cement ratio have shown higher absorption in mortars due to the presence of a porous ITZ. Moreover, scanning observations have confirmed that the ITZ exhibits more pores than the bulk paste matrix [17]. These characteristics can compromise durability but also offer potential for improvement through ICA design.

Porous ICAs such as LWA and RCA can enhance ITZ performance by locally releasing moisture, thereby improving the degree of hydration at the aggregate–paste interface [15, 17, 75]. This localized hydration densifies the microstructure and reduces ITZ porosity. For LWA, its rough surface and continuous water supply improve both the chemical bonding and mechanical interlocking with the surrounding paste [111]. RCA, due to its adhered old mortar and high porosity, also participates in moisture release; however, it introduces greater variability and microcracking potential in the ITZ, depending on its paste content and saturation state [109].

Biochar, as a novel ICA, also affects the ITZ. Its high specific surface area and porous structure serve as nucleation sites for hydration products. When well dispersed, biochar enhances local hydration and reduces ITZ porosity; however, clustering or poor distribution may weaken this benefit [81–83].

ICAs affect the ITZ through three key mechanisms:

(1) Physical and mechanical interaction: porous ICAs like LWA and RCA form stronger interfacial bonds than dense ordinary aggregates due to better surface compatibility and mechanical interlocking [111];

(2) Chemical effects: Depending on their chemical composition and mineralogical characteristics, ICAs may exhibit pozzolanic activity or act as inert fillers. For example, LWA containing amorphous aluminosilicates can participate in secondary hydration through volcanic ash reactions with calcium hydroxide, thereby refining the pore structure and enhancing matrix strength [12, 112];

(3) Moisture supply: ICAs act as localized water reservoirs, improving the hydration degree near the interface and increasing the content of hydration products in the ITZ compared with the surrounding paste [12, 15, 59, 69].

1.4.2 Effects on Mechanical Properties of Cement-based Materials

ICAs can influence the mechanical performance of cement-based materials . While these materials are introduced to improve hydration and mitigate shrinkage, their intrinsic properties—such as high porosity and low strength—may counteract these benefits if not properly optimized.

For LWA, the inclusion of saturated particles often enhances hydration in low water-to-binder ratio systems, leading to strength gains that compensate for the porous nature of the aggregate. For instance, in mortars with a water-to-binder ratio of 0.35, internal

curing was shown to increase 28-day compressive strength by approximately 10% compared to non-internally cured counterparts, demonstrating that enhanced hydration can offset strength loss due to LWA porosity [111]. Furthermore, increasing the content of LWA has been found to correlate positively with compressive strength when sufficient curing water is available [35, 43]. Importantly, ICAs such as LWA do not appear to negatively affect early-age mechanical properties or modulus of elasticity when content appropriately [38].

In contrast, RCA tends to reduce compressive and flexural strengths compared to natural aggregate concrete, largely due to its heterogeneous composition and higher porosity. However, this negative effect can be partially offset through mix design modifications. The use of SCMs, such as silica fume or fly ash, can enhance the packing density of the matrix and reduce porosity, thus improving strength [70]. Additionally, pre-treatment methods like carbonation can improve RCA particle integrity by reducing water absorption and microcracking potential, leading to notable gains in compressive strength [109].

Biochar, as a novel ICA, exerts a complex influence on the mechanical performance of cement-based materials, with outcomes highly dependent on its dosage, particle size, and pore structure. Its high porosity and substantial water absorption capacity—often reaching several hundred percent—facilitate internal curing by sustaining hydration, promoting C–S–H gel formation, and contributing to strength gain at later ages [80–82]. Additionally, finely ground biochar can act as a micro-filler, refining the pore structure and improving the ITZ through physical filling and potential pozzolanic reactivity, thereby enhancing both compressive and flexural strength [81, 83]. For example, Wang et al. [81] reported that replacing 5–10% of sand with biochar increased 28-day compressive strength by 5–8% and flexural strength by up to 12%, mainly due to improved hydration and microstructure densification. Sirico et al. [83] similarly observed a modulus of elasticity improvement of approximately 6% at moderate replacement levels.

However, excessive biochar content or poor dispersion can reduce density, weaken the load-transfer capability of the matrix, and introduce stress concentrators. Cuthbertson et al. [80] found that high-volume biochar (>15% by mass of sand) led to a reduction in compressive strength exceeding 10%, attributed to increased porosity and weak interfacial bonding. Moreover, large biochar particles with irregular morphology may disrupt the homogeneity of the cementitious matrix, while extremely fine particles with closed or tortuous pores can prematurely release stored water under rapid IRH decline, limiting sustained hydration benefits [82].

Overall, while LWA, RCA, and biochar differ in composition and morphology, their impact on mechanical properties depends on a balance between internal curing efficiency and the microstructural integrity of the composite. Optimizing ICA dosage, particle size, and surface treatment is crucial to maximizing strength benefits while minimizing structural drawbacks.

1.4.3 Influence on durability of Cement-based Materials

The durability of cement-based materials is primarily influenced by resistance to chloride ingress, permeability, water absorption, shrinkage, and freeze–thaw degradation. The use of ICAs—including LWA, RCA, and biochar—has shown significant potential to enhance durability by refining pore structures, regulating moisture transport, and prolonging hydration.

LWA contributes to improved durability through gradual water release, which increases long-term hydration and reduces capillary porosity and connectivity. Studies have reported over 25% reductions in chloride penetration when 31% saturated LWA is incorporated, with chloride diffusion coefficients falling to 55–75% of control mixes [15, 90, 113]. Additionally, pores vacated after water release enhance freeze–thaw resistance. However, when LWA is highly porous or poorly integrated, the benefit can be diminished, with permeability dominated by the matrix rather than the ICA itself [48, 49, 113].

RCA generally increases permeability due to its residual porosity and weak interface bonding, but treatments such as carbonation or incorporation of supplementary binders (e.g., silica fume) can densify the matrix and reduce void connectivity, leading to improved durability and reduced dimensional instability [75, 109].

Biochar demonstrates similar mechanisms. Its high water absorption capacity and microporosity contribute to improved IRH maintenance and reduced drying shrinkage [81]. At moderate dosages (approximately 5–10% by volume replacement of fine aggregate), biochar decreases permeability and enhances chloride resistance [80–83]. Freeze–thaw resistance is also enhanced when biochar is properly dispersed within the matrix, functioning as a hybrid ICA and pore moderator [80,81,83].

In summary, LWA, RCA, and biochar can all enhance durability when properly selected and proportioned. Common mechanisms include improved IRH stability, densification of the pore network, and reduction of shrinkage-induced cracking. Optimization of ICA type, content, and particle size remains critical to balancing durability and mechanical performance.

1.5 Self-healing of cementitious material

The challenge of repairing concrete cracks effectively and promptly has long perplexed the construction industry. Various traditional methods for concrete crack repair, including surface repair, grouting, penetration crystallization, and epoxy injection sealing [115], have been employed to enhance the strength and durability of concrete. However, these conventional approaches are primarily reactive, often requiring periodic maintenance or subsequent repairs. They tend to be less cost-effective and, in many cases, less efficient in meeting the evolving demands of modern construction projects, which emphasize long-term usability and reduced maintenance [116].

An additional issue lies in the limited ability of traditional methods to detect concrete cracks in a timely manner, resulting in a certain delay in addressing structural

deficiencies. In practical applications, if microscopic defects could be automatically rectified before they develop into more significant, visible cracks, it would have a substantial impact on the durability, stability, and safety of concrete structures. This proactive approach could not only reduce maintenance expenses but also enhance the overall economic viability of such structures.

Consequently, self-healing concrete technology has garnered significant attention over the past two decades [117]. This innovative approach represents a paradigm shift in concrete construction, with the potential to address the shortcomings of traditional repair methods, promote sustainability, and advance the industry towards a more economically viable and long-lasting future.

1.5.1 The healing of cementitious material

Cementitious materials possess a remarkable intrinsic ability for self-healing, a phenomenon known as autogenous healing. This fascinating capability was initially documented as early as 1836 by the French Academy of Sciences. Autogenous healing is primarily attributed to two key processes: the further hydration of unhydrated cement particles and the dissolution of calcium hydroxide ($Ca(OH)_2$) to form calcium carbonate ($CaCO_3$) through carbonization [97].

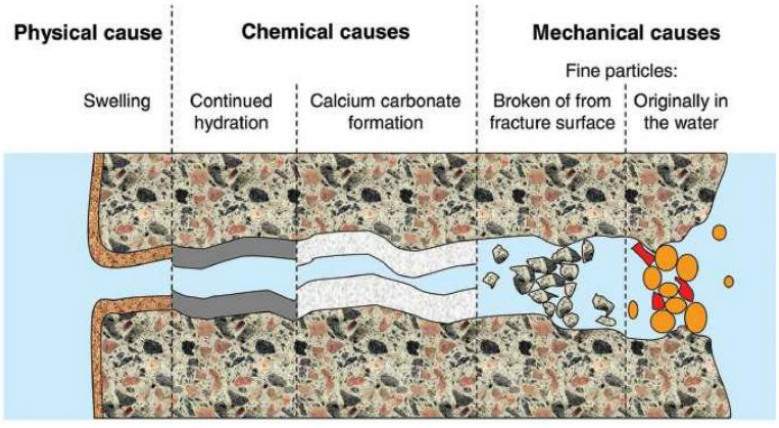


Figure.1.9 The mechanisms of autogenous healing cementitious material [118].

The self-healing effect in cementitious materials can be related to four distinct

mechanisms [117, 118], as illustrated in Figure 1.9. Notably, the continuous hydration of unhydrated cement particles plays a pivotal role in enhancing the self-healing phenomenon [124, 125]. Additionally, the presence of carbonates resulting from the dissolution of calcium and magnesium ions from the cement matrix contributes to this effect [126-128]. Moreover, as water flow (WF), fine particles are transported, effectively filling the cracks in the material [127, 129, 130]. Furthermore, the micro-expansion of the cement-based material upon water absorption aids in sealing minor cracks [120-123].

This multifaceted self-healing process underscores the robustness of cement-based materials in maintaining structural integrity and durability, particularly in aqueous environments. The synergy of these mechanisms exemplifies the impressive potential for self-healing, offering promising prospects for enhancing the resilience and longevity of such materials in construction and various applications. However, it is imperative to acknowledge that the autogenous healing capacity is inherently limited, primarily effective for cracks with openings measuring less than 200 μm [124, 125].

To enhance the autogenous healing capability of cementitious material, various functional components are incorporated into the cementitious material to obtain an autonomous healing. These components primarily fall into three distinct categories, as outlined in Table 1.5 [119].

Table 1.5 The method to improve autogenous healing capacity for cementitous materials

Excitation methods	**Healing materials**
Incorporating mineral admixtures/additions	Fly ash (FA) / Hydrated lime / Blast furnace slag / Limestone powder / Geomaterials / Chemical expansive agent / Swelling and Crystalline additives / Reactive magnesium oxide (MgO)
Incorporating nano-fillers	Nano-SiO2 / Nano-TiO2 / Nano-ZrO2 / Carbon nanotubes
ICAs	LWA/RCA

Among these, mineral admixtures stand out, encompassing high-calcium, aluminum, and magnesium minerals [6]. These substances serve as valuable sources of cations for crystallization nucleation. In some instances, mineral additives are combined with crystallization accelerators to expedite crystal formation. Furthermore, the integration of nanomaterials, such as nanosilica, titanium dioxide, and carbon nanotubes, has proven instrumental in stimulating healing mechanisms within cementitious material [119, 120]. Another key approach involves the utilization of ICAs, which serve to maintain adequate moisture levels and facilitate the continuous hydration of unhydrated cement particles, effectively sealing cracks in the process [117-121].

In the realm of ICAs, a critical challenge arises in the strategic placement of these agents within concrete and the preservation of internal water or a healing solution throughout the concrete mixing and pouring procedures. This challenge is undeniably the most formidable obstacle in the practical application of these agents. Nevertheless, experimental evidence demonstrates that appropriately dosed ICAs, such as LWA, RCA, and biochar, can achieve crack width (CW) reductions of 40–80% and healing rates (HRs) exceeding 60% under moist curing conditions [124–126]. These improvements are primarily attributed to sustained internal curing, secondary hydration, and precipitation of calcium carbonate within the crack plane.

1.5.2 Encapsulated ICA systems for self-healing

Encapsulated ICAs such as LWA and RCA have been investigated as water reservoirs for promoting self-healing in cementitious materials due to their porous structure and ability to retain and release moisture. To enhance their healing efficiency and ensure survival during mixing, various encapsulation strategies have been explored. Coating technologies using polymers, mineral-based layers, or hybrid systems allow controlled release of water or healing agents upon crack formation. For instance, styrene–acrylate emulsions, polyvinyl alcohol (PVA), and MgO-based coatings have been shown to

improve the mechanical robustness of ICA particles and regulate the release timing during damage events [126–134]. These coatings rupture under stress or cracking, enabling internal water migration or the release of embedded agents to support continued hydration or seal microcracks. Representative examples of such coated particles, including MgO-coated and styrene–acrylate/MgO-coated LWA, are shown in Figure 1.10 [133].

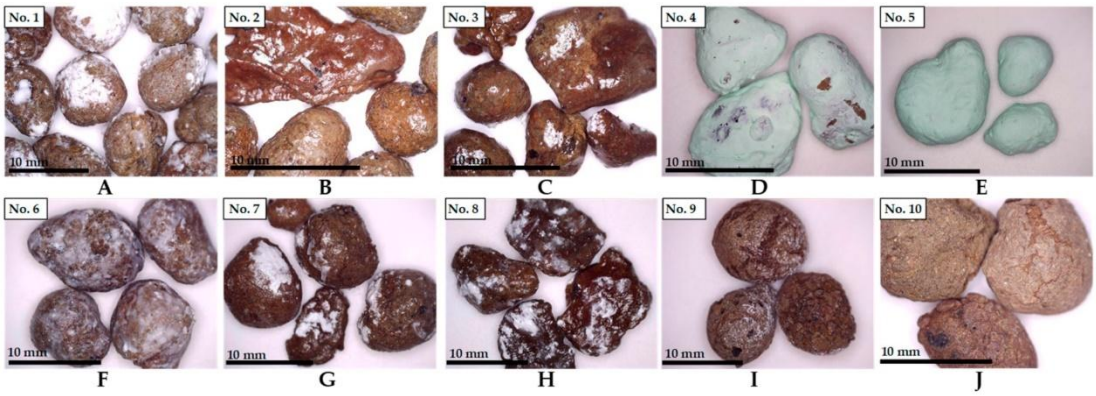


Figure.1.10 Expanded clay particles used in this study. (A–H) Particles coated with: (A) potassium magnesium phosphate cement; (B,C) one and two layers of styrene–acrylate emulsion, respectively; (D,E) one and two layers of waterborne, latex and acrylic-composite paint, respectively; (F) magnesium oxide and magnesium hydroxide; (G,H) styrene–acrylate and magnesium oxide solution, prepared with ratios 10:1 or 30:1, respectively; (I) uncoated control; (J) double-negative control. [133].

Comparative studies indicate that MgO-coated LWA (Figure 1.10(F, G, H)) demonstrates higher crushing strength, improved mechanical integrity during mixing, and a prolonged self-healing period compared to uncoated variants (Figure 1.10(I)). In particular, concrete containing MgO-coated LWA showed almost complete crack closure within 28 days, whereas uncoated LWA mixtures retained visible cracks at the same age [131, 134]. Similar improvements were observed for MgO-coated RCA, where the coating enhanced particle strength, reduced premature water loss, and enabled sustained crack sealing. Under moist curing, MgO-coated RCA mixtures

exhibited significantly narrower residual CWs and more extensive calcite deposition than their uncoated counterparts after 28 days [131, 134].

In summary, MgO coatings offer a dual benefit for both LWA and RCA by improving mechanical durability during mixing and enabling controlled water and chemical release upon cracking. This combined physical and chemical healing mechanism extends the effective healing window and enhances crack closure efficiency, making MgO-coated ICAs a promising approach for next-generation self-healing cementitious materials.

1.6 Conclusion

This chapter reviewed the fundamental mechanisms and implications of delayed deformations in cementitious materials, with a specific focus on shrinkage behavior and internal curing strategies. Delayed deformations—including autogenous, drying, chemical, and thermal shrinkage—were systematically discussed to establish a conceptual framework for understanding how moisture loss compromises dimensional stability and durability. Among these, autogenous shrinkage has emerged as a critical concern in low water-to-cement ratio systems, such as high-performance concretes (HPC), where self-desiccation is intensified due to limited free water.

This review highlighted the potential of porous ICAs—including LWA, RCA, and biochar—to serve as moisture buffers. However, while prior studies confirm their ability to absorb and release water, most research has emphasized absorption capacity alone, with less attention paid to release kinetics, spatial distribution, and interaction with cement hydration dynamics. Moreover, few studies have quantitatively assessed the contribution of pore structure characteristics to effective water delivery or the implications of particle size and ICA positioning on hydration uniformity and crack mitigation.

Although LWA has been extensively validated as an ICA, important knowledge gaps

remain for alternative ICAs such as RCA and biochar—especially their comparative performance in maintaining IRH, mitigating autogenous and drying shrinkage, and promoting self-healing under different curing regimes. Future work should prioritize side-by-side studies using harmonized mix designs, particle size/porosity classes, and saturation protocols to establish robust dose–response relationships and long-term durability outcomes.

Therefore, this research builds upon prior knowledge by systematically evaluating the pore characteristics, water absorption–release behavior, and shrinkage control efficiency of multiple ICA types. Special attention is paid to comparing the performance of different size fractions and material types (LWA, RCA, and biochar), in both sealed and drying environments, with an aim to quantify their water delivery capacity and evaluate their role in mitigating delayed deformations. Ultimately, this investigation establishes explicit correlations between ICA material parameters—such as water absorption capacity, desorption rate, pore size distribution, and mechanical integrity—and key functional outcomes in cement-based systems, including long-term IRH stability, reduction in autogenous and drying shrinkage, and enhancement of crack self-healing efficiency under both water and sealed curing regimes.

Chapter 2. Characterization of internal curing agents

This chapter focuses on the ICAs employed in this study, specifically LWA, RCA and biochar. These materials were selected for their porous structures and inherent ability to store and release water during the hydration process, making them effective candidates for mitigating autogenous shrinkage in cement-based materials.

The chapter begins with a description of the experimental methods used to characterize these materials, including procedures for evaluating water absorption, water desorption behavior, and pore structure.

This is followed by a detailed presentation and discussion of the key physical properties of each material, such as particle size distribution, porosity, saturation level, and internal water release capacity.

By establishing a comprehensive understanding of the ICAs, this chapter provides the basic data for analyzing their effects on cement hydration and shrinkage behavior in the subsequent experimental chapters..

2.1 Materials

The studied LWA (Figure 2.1 (a)) are expanded clay sourced from the Laterlite factory. The RCA (Figure 2.1 (b)) utilized in this research were obtained from uniform batches of laboratory-produced concretes. The concrete specimens were cured in a humidity chamber (T = 20 ± 1°C and RH ⩾ 98%) and crushed after curing periods of 90 days (batch n°1) and 2 years (batch n°2). The water-to-cement ratio for both concrete types was 0.45, and their compressive strengths ? at 28 days ?were 47 MPa and 47.9 MPa, respectively. To maintain the original particle size distribution of the mortar, LWA and RCA are pre-screened to match the particle size of the replaced sand.



Figure.2.1 LWA (a) RCA (b) of the present research work

Biochar is a porous material produced from biomass pyrolysis under limited oxygen conditions. In the present study, it is a vegetal charcoal derived from wood pyrolysis. It has high porosity and water retention capacity, making it useful for internal curing in cementitious materials. This study uses original biochar (Figure 2.2 (a)) and ground biochar with particle sizes smaller than 20 µm (Figure 2.2 (b)). The original biochar maintains its natural pore structure for maximum water absorption, while ground biochar has a modified porosity due to particle size reduction as shown hereafter.

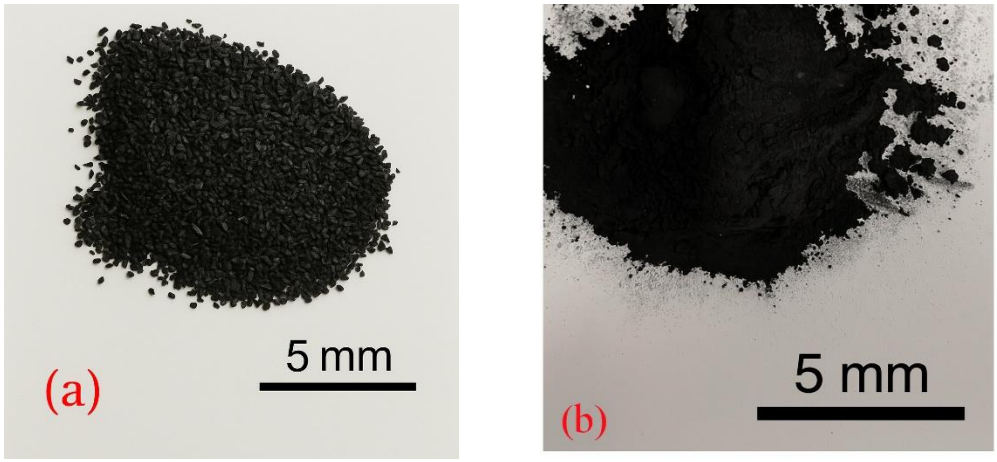


Figure. 2.2 Biochar before (a) and after (b) grinding

In addition to biochar, three other ICAs were employed in this study:

- Superabsorbent polymer named SAP (Figure 2.3(a)), a powder based on a high molecular weight synthetic polymer;

- Silica named SiL (Figure 2.3(b)), a synthetic, white, amorphous, precipitated silicon dioxide powder.
- MgO, a reactive expansive agent that undergoes hydration to form brucite ($Mg(OH)_2$), a process accompanied by volumetric expansion [6].

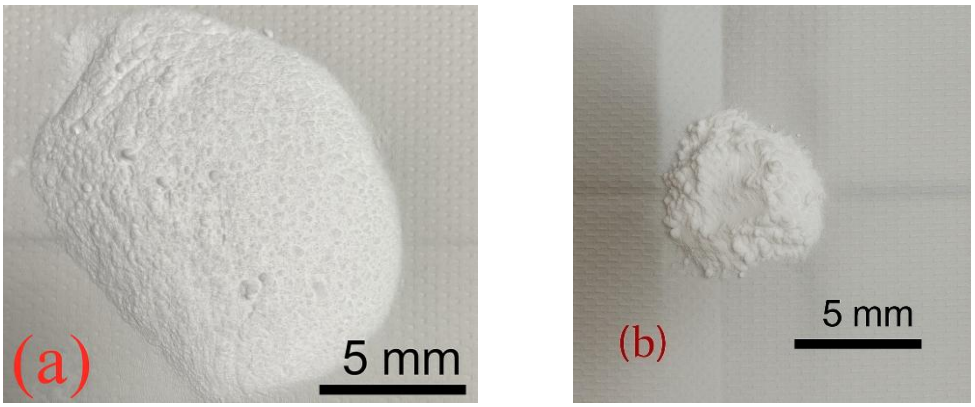


Figure. 2.3 SAP (a) Silica (b)

2.2 Experimental methods

This section outlines the testing methods used to study the properties of ICAs, focusing on their water absorption, density and release characteristics. LWA and RCA are tested for water absorption using a similar approach, as both can be separated from water and dried to a saturated surface-dry state. In contrast, biochar requires a distinct method involving filtration after water absorption. Its properties are compared to other more traditional ICAs such as SAP and silica particles. The water release capacity of all the studied materials is also assessed under varying relative humidity conditions in a controlled humidity chamber to better determine their benefit to limit shrinkage.

2.2.1 Water absorption and density

A. Natural sand, LWA and RCA

In this study, the water absorption coefficients of all used aggregates — including the RCA, LWA, and natural sand — were determined in accordance with the European standard EN 1097-6 [136]. This method is specifically applicable to aggregates with

particle sizes ⩾0.063 mm, making it suitable for the full range of coarse and fine aggregates employed in this research. The use of a standardized procedure ensures the reliability, consistency, and comparability of the measured water absorption characteristics across different aggregate types.

To better understand the advantages and limitations of the chosen method, it is necessary to compare it with alternative techniques used in aggregate water absorption testing. This comparison helps to justify the selection of EN 1097-6 [136] as the primary method while acknowledging the potential benefits of other approaches under different experimental conditions. The next paragraphs present a comparative overview of several commonly used techniques for quantifying the absorption characteristics of LWA, RCA, and natural aggregates in the context of this study.

The standard and IFSTTAR methods [138], while differing in procedure, are based on the same fundamental principle: determining the water absorption coefficient after a 24-hour saturation period, with reference to the saturated surface dry (SSD) condition. In the EN 1097-6 standard method [136], SSD is achieved by exposing saturated samples to a controlled warm air flow, followed by a slump cone test to assess surface cohesion. This test allows for the visual detection of the SSD state based on the shape stability of the aggregate pile (Figure 2.4(a)).

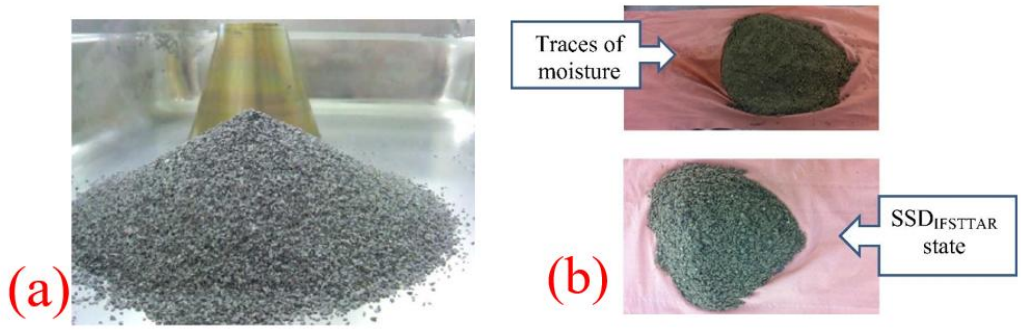


Figure. 2.4 Shape of cone correspoding to the SSD state [136] (a) Dry with absorbent paper (IFSTTAR method) [138] (b)

In contrast, the IFSTTAR method [138] uses absorbent paper to identify the SSD state. Aggregates are progressively dried using several layers of colored paper, and the SSD

condition is judged by the absence of visible water traces. The paper is regularly brushed to remove adhering fines, ensuring accuracy in detection (Figure 2.4(b)). While both methods are widely accepted, variations in the SSD determination procedure may result in discrepancies when comparing results across materials with different porosities. Beyond these standard approaches, two additional methods—the Real-time Assessment of Water Absorption (RAWA) and the Hydrostatic Weighing Method [104]—are increasingly used for continuous monitoring of absorption behavior. The RAWA method involves placing dry aggregate in a volumetric flask and recording the drop in water level as absorption progresses (Figure 2.5). The Hydrostatic method relies on mass change, where the sample is suspended in water and the increase in weight is used to calculate absorption (Figure 2.6).

Despite their advantages in monitoring time-dependent absorption, both the RAWA and hydrostatic weighing methods have limitations for aggregates with low water absorption. In this study, LWA absorbs over 20%, whereas RCA is below 10% and natural sand is around 1%. For low-absorption materials, the recorded weight increase or water-level drop is close to the detection limit of the instruments, making it difficult to separate true uptake from random measurement fluctuation. RAWA enables direct observation of absorption rate, but its accuracy declines when the water-level change is minimal; the hydrostatic method is simple and continuous, yet similarly affected when mass changes are very small. These constraints should be considered when interpreting results for such aggregates.

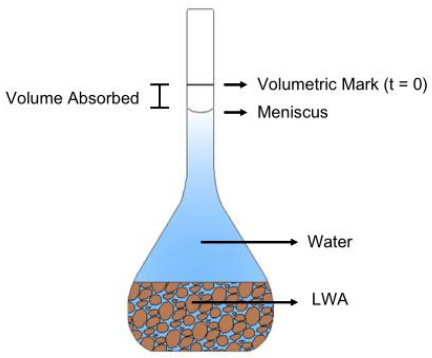


Figure. 2.5 RAWA method [139]

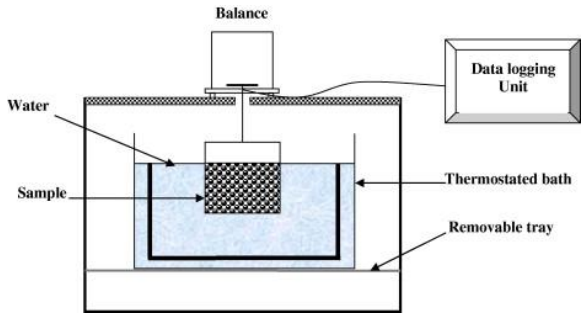


Figure. 2.6 Hydrostatic weighing method [140]

To ensure consistency and comparability across different aggregate types (NS, RCA, LWA), this study adopted the European standard EN 1097-6 [136] to determine water absorption and density. This method was selected because it provides higher accuracy for low-absorption aggregates, enabling more reliable detection of small changes in water uptake. Although alternative methods exist, EN 1097-6 was deemed more suitable for this study due to its broader recognition in European practice and its established use in characterizing both coarse and fine porous aggregates. The measurement process is detailed below to clarify the methodology employed:

- **Step 1:** Dry aggregates in an oven at (105 ± 5) °C for 24 hours, then remove it and allow it to cool to room temperature. Weigh the sample and transfer it into the pycnometer, using 300 g of RCA and of natural sand for each respective test, and 100 g for LWA.
- **Step 2:** Immerse the sample in water at (22 ± 1) °C within the pycnometer. Remove any entrapped air by gently rolling and jolting the pycnometer while holding it in a tipped position (Figure 2.7(a)).
- **Step 3:** Place the pycnometer in a water bath and maintain the test portion at (22 ± 1) °C for (24 ± 0.5) hours (Figure 2.7(b)).
- **Step 4:** At the end of the soaking period, remove the pycnometer from the water bath and remove any remaining entrapped air by gently rolling and jolting the pycnometer. Overfill the pycnometer with water and secure the cover without trapping air. Dry the outside of the pycnometer and weigh it (*M2*).
- **Step 5:** Decant most of the water from the pycnometer into a tray, refill it with water,

and place the cover back on. Dry the outside and weigh the pycnometer again (*M3*).

- **Step 6:** Spread the soaked aggregate evenly in a tray. Expose the aggregate to a gentle stream of warm air to evaporate surface moisture for 5 minutes, stirring frequently to ensure uniform drying. Continue drying for approximately 5 minutes until no free surface moisture is visible, and the particles no longer adhere to one another. Allow the sample to cool to room temperature while stirring for another 5 minutes.
  - **Step 7:** To confirm the surface-dry state:

Fill all the metal cone mold loosely with part of the drying sample.

Tamp the aggregate 25 times with the metal tamper falling under its own weight.

Do not refill the mold after tamping. Carefully lift the mold from the aggregates' cone. If the aggregates' cone does not collapse, continue drying and repeat the cone test until collapse occurs upon mold removal. Once the surface-dry state is achieved, weigh the test portion (*M1*, Figure 2.7(e)).

- **Step 8:** Dry the aggregate in a ventilated oven at (105 ± 5) °C until a constant mass is reached. Allow it to cool to ambient temperature and weigh the sample (*M4*).

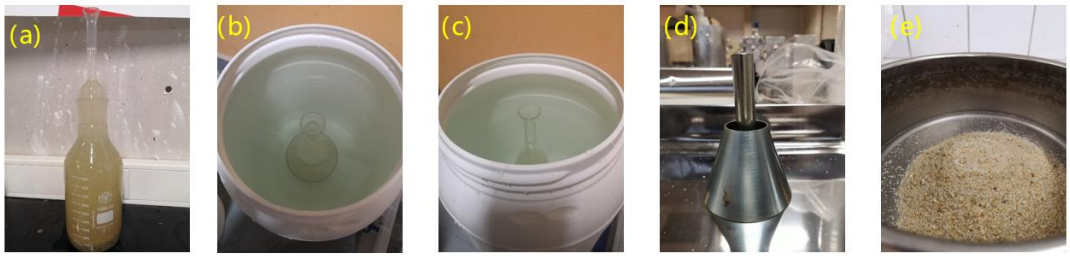


Figure. 2.7 Test Process: aggregates immersed in the pycnometer (a), pycnometer placed in the water bath (b)(c), detection method (d), natural sand in SSD state (e)

Based on these measurements, the water absorption after 24 hours of immersion (Equation 2.1), the apparent particle density (Equation 2.2), the oven-dried particle density (Equation 2.3), and the saturated and surface-dried particle density (Equation 2.4) are determined.

$$WA_{24} = \frac{100\times(M_1-M_4)}{M_4} \tag{2.1}$$

$$\rho_a = \rho_w \frac{M_4}{M_4-(M_2-M_3)} \tag{2.2}$$

$$\rho_{rd} = \rho_w \frac{M_4}{M_1-(M_2-M_3)} \quad (2.3)$$

$$\rho_{ssd} = \rho_w \frac{M_1}{M_1-(M_2-M_3)} \quad (2.4)$$

Where ρ_w is the density of water at the test temperature (g/cm^3), M_1 the mass of the saturated and surface-dried aggregate in the air (g), M_2 the mass of the pycnometer containing the sample of saturated aggregate and water (g), M_3 the mass of the pycnometer filled with water only (g), M_4 the mass of the oven-dried test portion in air (g).

Moreover, it is important to note that previous studies [22, 84] have shown that the 24-hour water absorption coefficient of LWA reaches only 70% of its long-term value under a water immersion (step 2). Interestingly, for a saturation under vacuum conditions, this value increases to 100%. In light of this, our study also evaluates the water absorption coefficient of both LWA and RCA under varying vacuum conditions for the saturation process, as shown in the setup in Figure 2.8. Thus, the effect of several parameters on the water absorption coefficient of LWA are investigated to optimize the saturation process: saturation under vacuum and duration of vacuum pump action.



Figure. 2.8 Device for vacuum saturation

B. Biochar

Biochar is also saturated with a similar method, but the difference is that in determining the SSD state, they need to be filtered to reach the SSD state. The test process is as follows:

1. Two samples (5g) are collected and placed in a beaker, which is then placed in a ventilated oven at 70°C for 24 hours (Figure 2.9(a)). This step eliminates both natural and acquired moisture from the samples prior to testing.
2. Each sample is combined with 100 g of distilled water, then left to stand and sealed in separate containers for 48 hours (Figure 2.9(b)), then weigh to get the saturated mass M_5.
3. A vacuum filtration test is then prepared, using a funnel with a cellulose filter (Whatman 0.7 mm Ø) to extract all the surface liquid from the samples (Figure 2.9(c)).
4. The wet sample is weighed (Figure 2.9(d)), then placed in the oven to dry at 105 °C. After drying, the dry sample's weight is recorded as M_6. The difference between the wet and dry weights provides the fluid retention capacity of the compound.

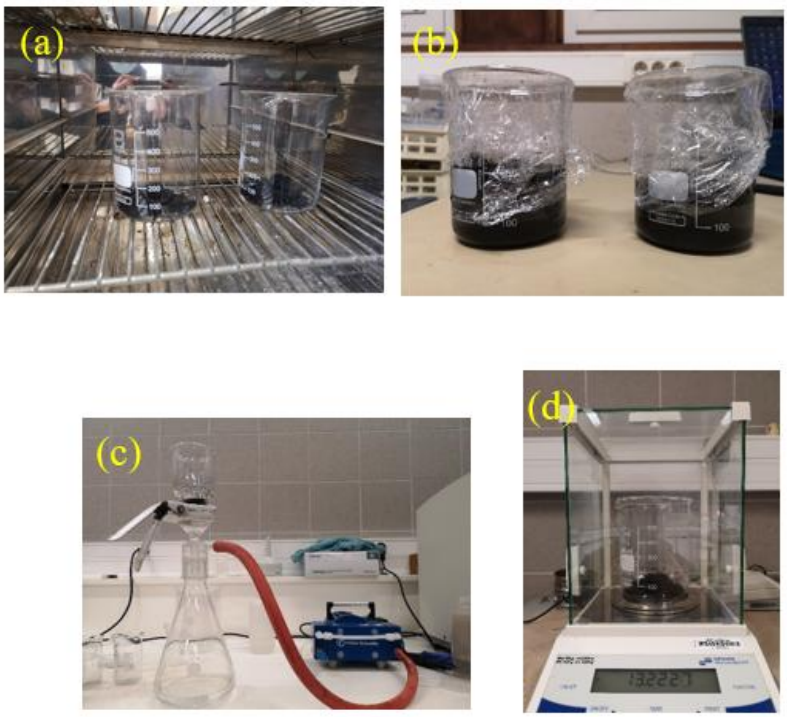


Figure. 2.9 Water absorption test process of sample: samples in the oven (a), samples sealed after adding water (b), vacuum filtering process (c), wet sample (d)

The water absorption after 24 hours of immersion is determined using Equation 2.5:

$$WA_{24} = \frac{100\times(M_5 - M_6)}{M_6} \quad (2.5)$$

Where M_5 is the mass of biochar saturated with water (g), and M_6 the mass of the biochar in dry state (g).

2.2.2 Water release

Water release testing is a critical evaluation for assessing the performance of ICAs as function of the IRH, and it is conducted within a relative humidity chamber (Figure 2.10) where the relative humidity is regulated thanks to salts (Table 2.1). The relative humidity range from 97% to 75% is explored. Three saturated samples for each studied particles' range of curing agents are tested. Their average initial mass is equal to 25 g, 45 g and 25 g for LWA, RCA and biochar respectively.

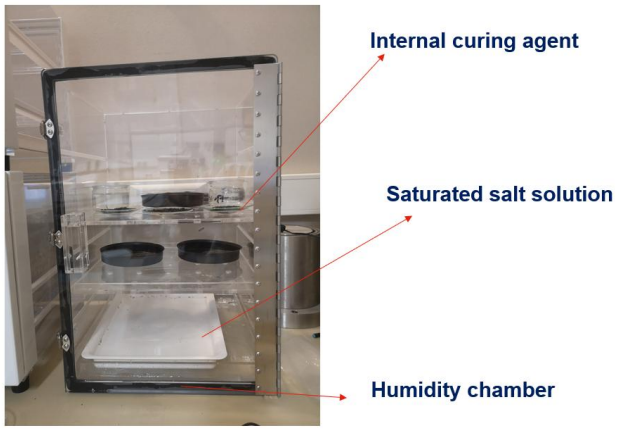


Figure 2.10 Water release test

Table 2.1. Types of salts used to regulate relative humidity.

R.H. (%)	Salt's nature
97%	potassium sulfate (K_2SO_4)
93%	potassium nitrate (KNO_3)
85%	potassium chloride (KCl)
75%	sodium chloride (NaCl)

Their mass changes are meticulously monitored to assess water release capabilities. During the first day, the mass of each sample is recorded every 4 hours. Subsequently, recordings are made daily, continuing until the mass of the sample stabilizes—indicated by a mass change of less than 0.05% within a 24-hour period. The test begins with the highest relative humidity (97% R.H. – Table 2.1). Based on these measurements, the saturation degree S_w is calculated as:

$$S_w = \frac{m_t - m_{dry}}{m_{initial} - m_{dry}} \times 100\% \quad (2.6)$$

Where m_t is the mass of aggregate test at different time during the test (g), m_{dry} is the mass of aggregate at drying condition (g), $m_{initial}$ is the mass of aggregate in the saturated condition at the initial time (g).

2.2.3 Pore size distribution and specific surface area

The nitrogen adsorption-desorption test was conducted to analyze the specific surface area (SSA) and pore size distribution of the studied materials. This technique is based on the Brunauer-Emmett-Teller (BET) theory for SSA determination and the Barrett-Joyner-Halenda (BJH) method for pore size distribution analysis. The procedure follows these steps:

1. Sample Preparation: The samples were dried at 105°C for 24 hours, then ground into a fine powder and sieved to obtain particles smaller than 80 μm.
2. Degassing Process: The powdered samples were placed in sealed tubes and subjected to a vacuum degassing process to remove adsorbed moisture and gases.
3. Adsorption-Desorption Measurement: The analysis was performed using Gemini VII 2390 equipment, with nitrogen as the adsorbate gas. The adsorption-desorption isotherms were recorded over a relative pressure range (P/P_0) from 0.01 to 0.95.
4. Data Analysis: The BET method was used to calculate the specific surface area, while the BJH method determined the pore size distribution and cumulative pore volume.

Each material and sample was tested once. The results provide insights into the porous structure of the materials, indicating their ability to retain and release water, which is crucial for their role as ICAs.

2.2.4 Thermogravimetric analysis of ICAs

To evaluate the hydration products and rates of the ICAs, ThermoGravimetric Analysis (TGA) is performed once for each ICA. Prior to TGA, the specimens are dried at 105°C for 24 hours to remove free water. The collected material is then ground into a fine powder (passing through a 80 μm sieve) for analysis. Around 70 to 90 mg of the sample is placed in a controlled nitrogen environment, where the temperature is gradually increased from 20 to 1000°C at a rate of 10°C per minute. TGA analysis identifies key crystalline phases which decompose within specific temperature ranges, including brucite [320-400°C] [92, 97], hydrotalcite [250-500°C] [103], portlandite [400-600°C] [103], and carbonates such as $CaCO_3$ and $MgCO_3$ [600-800°C] [79].

Since RCA includes hydration products from the adhered mortar, the portlandite content must be quantified; it is determined according to Equation (2.7):

$$m_{Ca(OH)2} = \frac{\left[|\Delta m_{400℃\to550℃}(t)| + m_{d,400℃\to600℃}(t)\right] - m_c \times PaF - m_B \times PaF(B) - m_{MgO} \times PaF(M)}{m_s} \cdot \frac{M_{Ca(OH)2}}{M_{H2O}} \quad (2.7)$$

Where, $\Delta m_{400℃\to550℃}(t)$ is the mass loss between 400 and 550 °C, $m_{d,400℃\to550℃}(t)$ is the drift of the device between 400 and 550°C, $m_c = \frac{m_{initial}}{(1+\frac{W}{C})\cdot(1+PaF)}$, m_c is the mass of anhydrous cement, $m_{initial}$ is the initial mass of the mortar, *PaF* is loss on ignition of anhydrous cement, obtained by TGA of CEM I, the value is 3.796% in this study, *PaF(B)* is the loss on ignition of biochar, the value is 25.67% in this study, *PaF(M)* is the loss on ignition of MgO, the value is 5.43% in this study, m_B is the mass of the biochar in the sample, m_{MgO} is the mass of MgO in the sample, m_s is the mass of mortar, $M_{Ca(OH)2}$ is the molar mass of portlandite, M_{H2O} is the molar mass of water.

To further evaluate the reactivity of MgO, special attention is given to its partial hydration behavior. Since MgO may convert into brucite during storage or mixing, TGA

is employed to quantify the extent of this hydration. The mass of brucite is then calculated according to Equation (2.8):

$$m_{Mg(OH)_2} = [|\Delta m(t)| + m_d(t)] \cdot \frac{M_{Mg(OH)_2}}{M_{H_2O}} \quad (2.8)$$

Where $\Delta m(t)$ is the mass loss associated with the temperature range of brucite dehydration, $m_d(t)$ is is the drift of the device in the same temperature range, $M_{Mg(OH)_2}$ is the molar mass of brucite, M_{H2O} is the molar mass of water.

The brucite content in MgO is calculated according to Equation (2.9):

$$\alpha_{Mg(OH)_2} = \frac{m_{Mg(OH)_2}}{m_{MgO,initial}} \times 100\% \quad (2.9)$$

Where $m_{MgO,initial}$ is defined as the initial mass of MgO contained in the specimen before TGA, accounting for both free periclase and the part that has transformed into brucite.

2.3 Properties of the ICAs

The main characteristics of the three studied ICAs (LWA, RCA and biochar) are presented in this section. The performances of LWA and RCA are compared, while biochar is evaluated against more conventional ICAs, such as SAP and silica particles. This choice is based on the particle size of curing agents.

2.3.1 LWA and RCA

To comprehensively evaluate the internal curing behavior of LWA and RCA, it is essential to consider the influence of particle size. Particle size affects water absorption, release dynamics, and interaction with the surrounding cement matrix, thereby impacting both early-age hydration and long-term shrinkage performance [39]. For this reason, different particle size ranges of LWA and RCA were specifically selected to reflect their size-dependent behaviors.

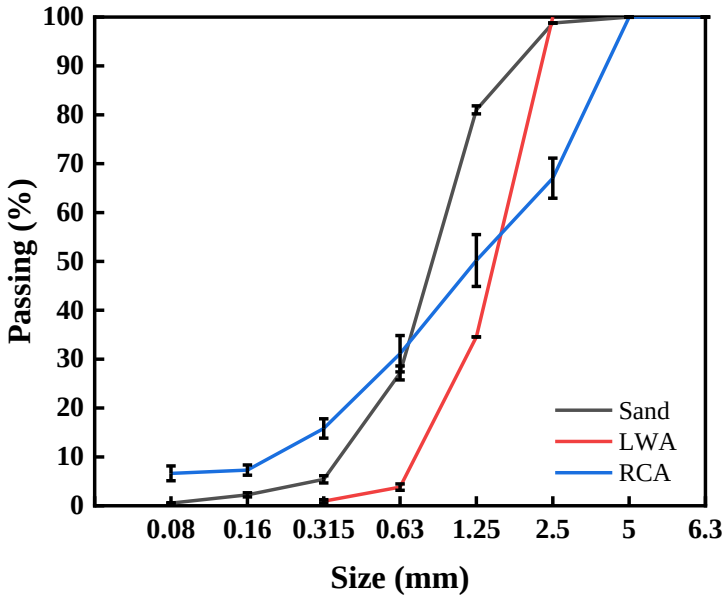


Figure. 2.11 Particle size distributions of three types of aggregates



Figure. 2.12 Crushing process with a consistent opening size of 1 mm

Since LWA and RCA were used to partially replace natural sand in mortars, their particle size distributions were aligned with that of sand to ensure comparable packing density and workability. The specific subranges used in this study (e.g., 0–0.63 mm, 0.63–1.25 mm, 1.25–2.5 mm) were determined based on the standard sieve series [137], allowing each fraction to represent a distinct shift in grading and pore structure characteristics. LWA was selected in the 0–2 mm range, while RCA was prepared with particles smaller than 2.5 mm. The RCA was obtained by crushing laboratory concrete using a jaw crusher (Figure 2.12). Particles larger than 2.5 mm were sieved out and re-crushed—up to three times—until the required size specification was achieved. This ensured a consistent and representative particle size distribution, as illustrated in Figure

2.11, facilitating meaningful comparison of internal curing effects across aggregate types and size ranges.

2.3.1.1 Impact of the saturation conditions on the water absorption coefficient

The primary objective of these tests is to investigate the water absorption behavior of both LWA and RCA under varying saturation conditions, with a particular focus on the influence of vacuum saturation compared to standard conditions. For LWA, the tests revealed that under normal conditions (pump duration = 0), the 24-hour water absorption coefficient is 20.7%. When the pump duration is extended to 1 hour, this value increases to 28.7%. However, further extending the pump duration beyond 1 hour resulted in a change in water absorption of less than 1%, indicating a negligible impact on the absorption rate. Based on these findings, all LWA in this study were pre-saturated under vacuum for 1 hour, after which the vacuum state was maintained for an additional 23 hours without further pumping.

For RCA, the water absorption tests were designed to assess its water retention capacity, particularly in relation to particle size, to evaluate its suitability as an ICA and its potential effect on the hydration process in concrete mixtures. RCA particles smaller than 2.5 mm were analyzed, with specific measurements taken for particles between 1.25-2.5 mm. The results show that under normal conditions, the 24-hour water absorption coefficient is 6.4%, while under vacuum, it is only marginally higher at 6.5%. This negligible difference indicates that vacuum conditions do not significantly enhance the water absorption capacity of RCA. Consequently, to avoid introducing unnecessary variables, RCA was pre-saturated under normal conditions for this study.

2.3.1.2 Water absorption coefficient

Table 2.2 and 2.3 presents the water absorption coefficients of natural sand (NS), LWA

and RCA across various particle size ranges.

Table 2.2 shows that the 24-hour water absorption coefficient of LWA is affected by the breadth of its particle size range rather than a simple correlation with particle size. When the particle size range is expanded, as in LT compared to LM, the proportion of both finer and larger particles increases. This change in grading alters the packing density and connectivity of the pore network, leading to higher accessible pore volume. As illustrated in Figure 2.13, the internal pore volume of LT is approximately 3.6 times greater than that of LM, which largely explains its higher water absorption coefficient.

Table 2.2 Water absorption test results of LWA and the natural sand (NS)

Name	Particle size (mm)	Water absorption coefficient (%)	Standard deviation (%)	Specific surface area (m^2/g)
NS	0-4	0.05	0	-
LM	0.63-1.25	24.5	0.25	0.56
LC	1.25-2.5	31.6	0.70	1.66
LT	0-2	28.7	0.06	-
LL	2-5	39	0.90	-

Table 2.3 Water absorption test results of RCA

Name	Particle size (mm)	Specific surface area of batch n°1 (m^2/g)	Water absorption coefficient of batch n°1 (%)	Standard deviation (%)	Water absorption coefficient of batch n°2 (%)	Standard deviation (%)
RF	0.315-2.5	2.76	7.2	0.15	6.9	0.25
RM	0.63-1.25	3.94	5.8	0.24	6.1	0.20
RC	1.25-2.5	0.64	6.4	0.15	5.9	0.15
RB	2.5-5	-	5.8	0.24	5.4	0.10

Additionally, Figure 2.13(b) indicates that the difference in pore volume between LT and LM is primarily concentrated in larger pores (pore radius > 5 nm), while the

variation in smaller pore volumes is relatively minimal. This further highlights the influence of larger pores on the water absorption properties of LWA.

In opposite, the water absorption coefficient decreases as the particle size of RCA increases (Table 2.3). This trend is attributed to the content of hydrated cement paste in the aggregate. It is well known that concrete consists of cement paste, coarse, and fine aggregates. Compared to coarse aggregates, cement paste is more prone to breaking into fine particles during crushing. Therefore, RCAs with smaller particle sizes contain more hydrated cement paste as shown by Figure 2.14 giving the portlandite content in RCA. This hydration product decreases with increasing particle size. The larger content of paste leads to a higher water absorption coefficient.

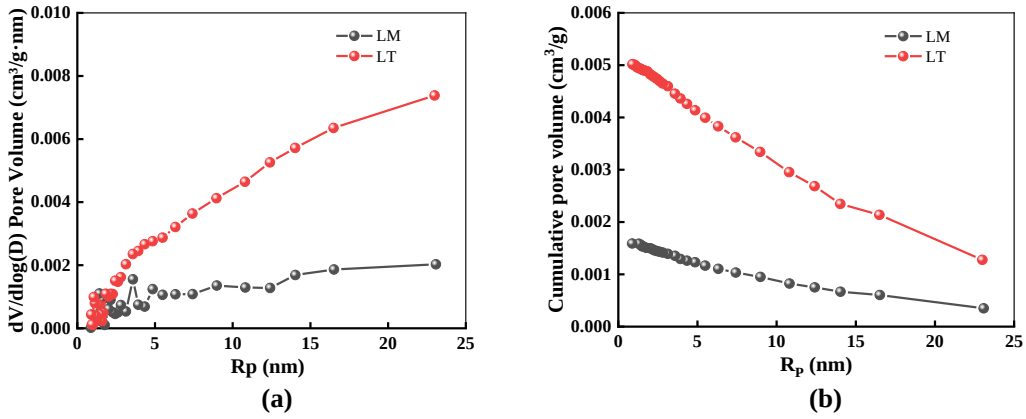


Figure. 2.13 Pore distribution of LWA: Differential distribution curve (a), Cumulative distribution curve (b)

The effect of the concrete age used to produce RCA on water absorption coefficient is presented in Table 2.3 for two different ages: 90 days (batch n°1) and 2 years (batch n°2) old. The second batch of RCA presents a lower water absorption coefficient for each particle size. This suggests that the water absorption coefficient of RCA is sligthly influenced by the age of the original concrete when RCA is produced.

This decrease in absorption with longer concrete age can be attributed to the continued hydration and densification of the cement matrix over time. As hydration progresses, capillary pores are gradually filled with reaction products, leading to a more refined microstructure and reduced porosity. Consequently, when older concrete is crushed, the

resulting RCA contains a lower volume of accessible pores, thereby exhibiting lower water absorption.

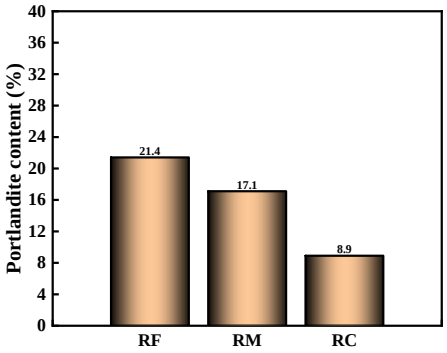


Figure. 2.14 Portlandite content of RCA

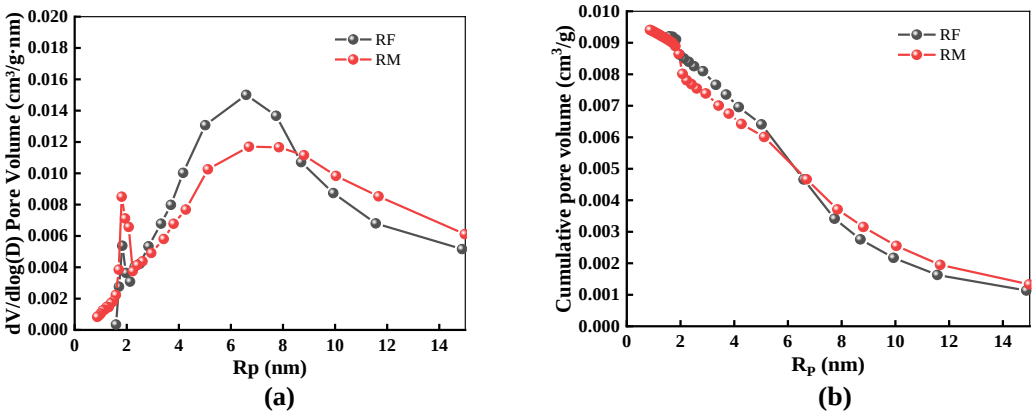


Figure. 2.15 Pore distribution of RCA (batch n°1): Differential distribution curve (a), Cumulative distribution curve (b)

Figure 2.15 illustrates the results of the pore structure test conducted on RCAs with particle sizes of 0.315-2.5 mm (RF) and 0.63-1.25 mm (RM). The key findings are as follows: RF and RM exhibit similar total pore volumes within the investigated pore range; RF contains a slightly higher proportion of pores with a radius of 4–8 nm, while RM has a greater number of pores with a radius of 8–14 nm (Figure 2.15(a)). Since water absorption is governed by capillary suction and the connectivity of the pore network, particle size distribution can influence the absorption coefficient [104]. Larger pores reduce the flow resistance and allow water to penetrate more rapidly, while finer pores can slow the movement of water despite increasing total absorbed volume [140].

Therefore, differences in the proportion of fine and coarse pores between RF and RM contribute to the observed variations in absorption coefficient.

2.3.1.3 Density

Table 2.4 presents data on the density of LWA with different particle sizes at saturated state (ρ_a), dry state (ρ_{rd}) and saturated surface dry state (ρ_{ssd}). LL has a significantly lower density than the other LWAs because LWA with a larger particle size has more macropores, which is also the reason for its high water absorption rate (Table 2.2).

Table 2.4 Density of LWA and RCA

Name	ρ_a (g/cm^3)	Standard deviation	ρ_{rd} (g/cm^3)	Standard deviation	ρ_{ssd} (g/cm^3)	Standard deviation
Sand	2.452	0.005	2.001	0.004	2.198	0.007
LM	1.204	0.006	0.930	0.005	1.157	0.003
LC	1.301	0.005	0.921	0.002	1.212	0.004
LT	1.206	0.004	0.873	0.001	1.149	0.005
LL	0.963	0.005	0.700	0.003	0.972	0.004
RF	2.452	0.003	2.001	0.005	2.198	0.004
RM	2.456	0.005	2.048	0.002	2.217	0.003
RC	2.460	0.002	2.113	0.001	2.253	0.003
RB	2.467	0.005	2.198	0.003	2.321	0.002

An opposite behavior characterizes the density of RCA, which increases with particle size in both dry and SSD states. This can be attributed to the reduction in residual cement paste content in larger RCA particles—since paste has a lower density than natural aggregates, a lower paste proportion leads to higher overall density. In parallel, the water absorption coefficient of RCA decreases with increasing particle size, indicating that larger RCA retains less absorbed water in the SSD state. As a result, the higher bulk density observed in larger particles under SSD conditions stems from a combination of reduced internal porosity and a higher proportion of solid aggregate relative to absorbed water.

2.3.1.4 Water release

Figures 2.16 and 2.17 present the water release behavior of LWA and RCA under various relative humidity (R.H.) conditions, while Tables 2.5–2.7 summarize the corresponding desorption rates.

At 97% RH, both LWA and RCA show clear particle-size-dependent water release behaviors. For LWA (Figure 2.16(a)), LT (–9.84%/day) and LL (–9.04%/day)—characterized by coarser average sizes and broader size distributions—exhibit faster initial desorption than LC (–6.68%/day) and LM (–7.86%/day). Although LC has larger nominal particles than LT, its narrower size range reduces the proportion of fine particles, thereby limiting pore connectivity and surface area available for evaporation, resulting in slower early-stage release. In the subsequent period (2–19 days), all LWA types show reduced release rates, with LC maintaining the slowest desorption, indicating stronger long-term water retention.

A similar size-related trend is observed for RCA (Figure 2.17(a)): larger particles desorb faster, reflecting their coarser internal pore structure. However, RCA's overall water release efficiency is substantially lower than that of LWA (typically 40–70% under high RH), which can be attributed to its lower pore connectivity, smaller proportion of fully saturated pores, and the dominance of finer pores that hold water tightly but release it slowly. These differences highlight that while particle size governs early-stage desorption in both materials, the absolute release efficiency is strongly influenced by intrinsic pore structure and connectivity, making LWA generally more effective as an internal curing agent under high-RH conditions.

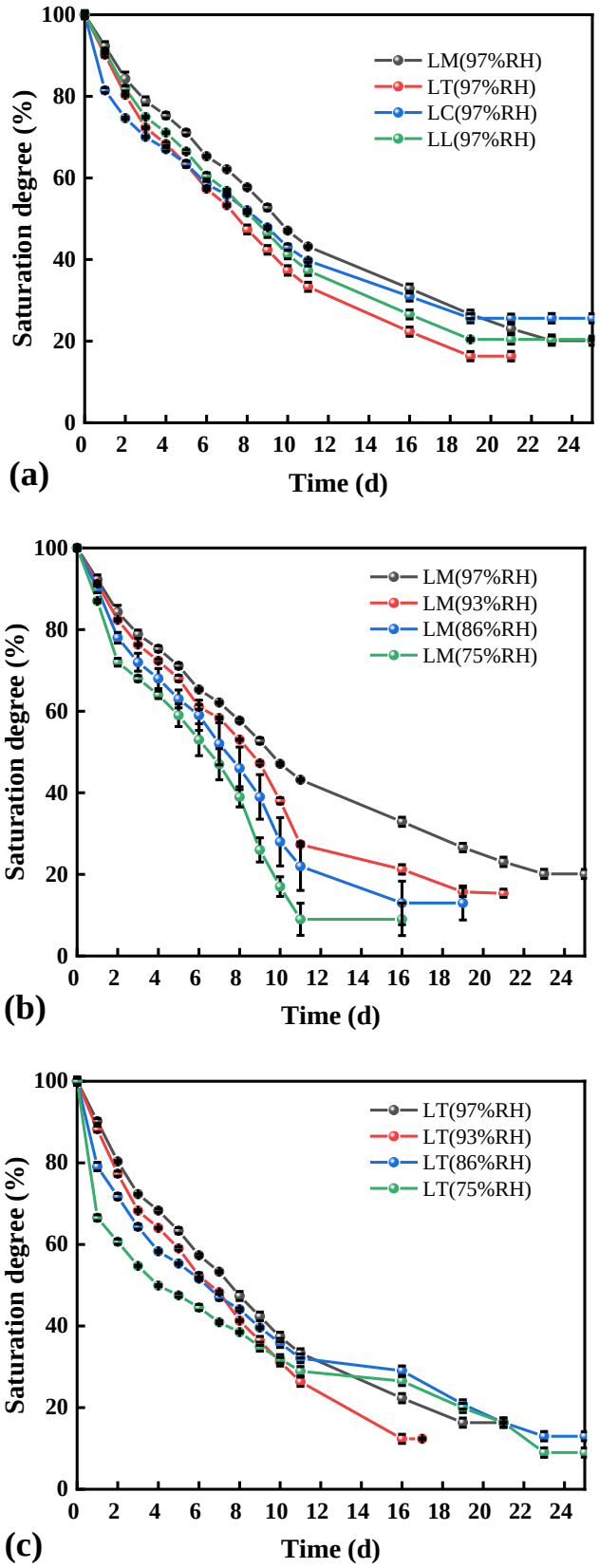


Figure 2.16 Water release curves at 97% R.H. (a) for LM at different R.H. (b) for LT at different R.H. (c)

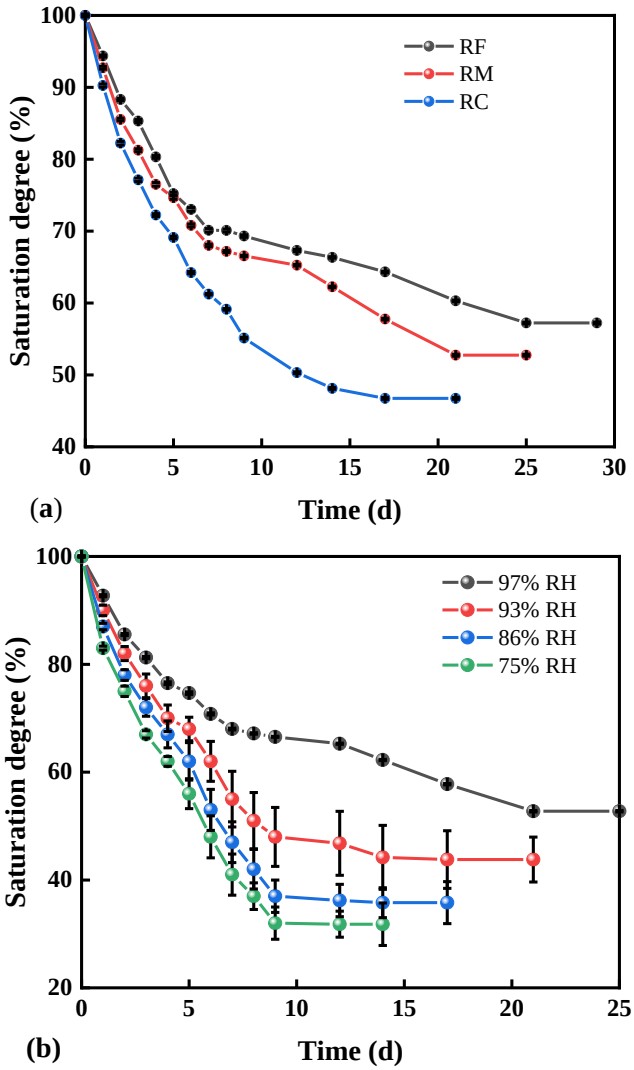


Figure 2.17 Water release curves of RCA for RF, RM and RC in 97% R.H. (a), for RM at different R.H. (b)

The influence of environmental RH on water release is further examined in Figure 2.16(b) and Figure 2.17(b). For both LWA and RCA, a clear trend emerges: as RH decreases, the early-stage desorption rate increases. For instance, the 0–2 day slope of LM increases from –7.86%/day at 97% RH to –14.00%/day at 75% RH; LT shows a similar increase from –9.84%/day to –11.34%/day. RCA responds similarly, with accelerated desorption under lower RH conditions (Table 2.7), although its release rates remain lower than those of LWA under all RH levels.

Table 2.5 The slope of the water release curve of LM, LT, LC and LL at 97% R.H.

Name	2 first days	2 d to 11 d	11 d to19 d
LM	-7.86	-4.54	-2.07
LT	-9.84	-5.15	-2.13
LC	-6.68	-3.86	-1.76
LL	-9.04	-4.91	-2.11

Table 2.6 The slope of the water release curve of LM and LT at different R.H.

RH	2 first days		2 d to 11 d		11 d to 19 d	
(%)	LM	LT	LM	LT	LM	LT
97	-7.86	-9.84	-4.54	-5.15	-2.07	-2.13
93	-8.82	-11.33	-5.68	-5.54	-1.43	-1.86
86	-11.00	-7.37	-6.15	-3.86	-1.19	-1.60
75	-14.00	-5.90	-7.15	-3.09	-1.53	-1.28

Table 2.7 The slope of the water release curve of RM at different R.H.

RH (%)	2 first days	2nd day to 9 day	After 9 day
97	-7.23	-2.71	-0.86
93	-9	-4.86	-0.35
86	-11	-5.86	-0.15
75	-12.5	-6.14	-0.04

These results on RCA and LWA lead to three key conclusions:

1. Water release from both LWA and RCA is strongly dependent on environmental R.H,. particularly in the early curing period (first 10 days);
2. Particle size and grading range govern the release pattern: coarser fractions with larger, well-connected pores discharge water more rapidly and reach lower final saturation, whereas finer fractions with smaller pores retain water for longer and release it more gradually;

3. While LWA shows superior overall release efficiency, RCA can be effectively optimized through particle size selection, making both materials viable for internal curing in cementitious systems when properly tailored to environmental conditions.

2.3.2 Biochar

In this part, the effect of the biochar grinding on some of these properties are analyzed. Firstly, it appears that grinding has minimal impact on the pores structure of biochar from 5 to 25 nm. Indeed, both types of biochar exhibit nearly pore size distributions (Figure 2.18) and similar specific surface areas (Table 2.8), which is beneficial for subsequent research.

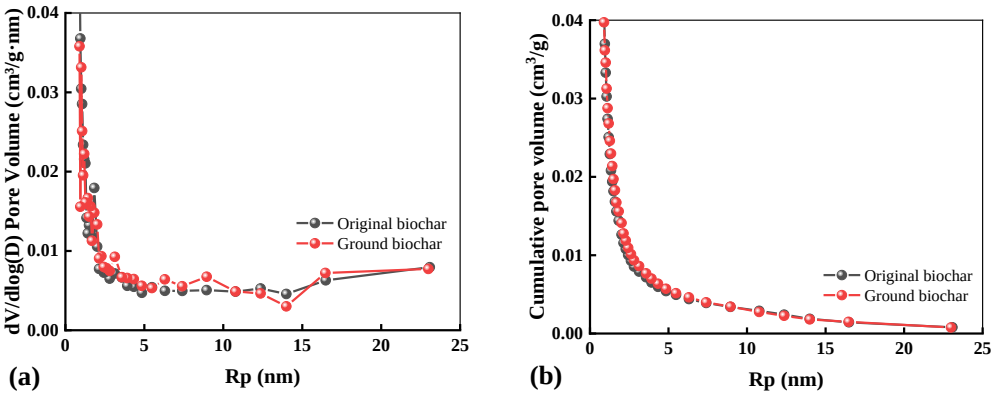


Figure. 2.18 Pore distribution of original biochar (O.B.) and ground biochar (G.B.): Differential distribution curve (a), Cumulative distribution curve (b)

Table 2.8 The specific surface area of biochar

Type	Specific surface area (m^2/g)	Standard deviation
Original biochar	385.49	10.35
Ground biochar	363.14	11.67

2.3.2.1. Absorption coefficient

The 24-hour water absorption capacity of biochar is equal to 324.3% (Table 2.9). This exceptional value is attributed to its unique honeycomb pore structure. Extending the

saturation period to 72 hours did not further increase water absorption, indicating that 24 hours is sufficient for full saturation (Table 2.9).

However, despite its high water absorption capability, the original biochar exhibits structural weaknesses, its fragile and loose nature makes it highly unstable when directly incorporated into mortar. It can also have a negative effect on the mechanical properties [81,82]. So, this study adopted a modified approach by grinding the original biochar into a powder form (Figure 2.2 (b)). While this mechanical process improved its stability, it also disrupted the honeycomb pore structure, reducing the 24-hour water absorption coefficient to 103.1%. This reduction is not only attributed to the loss of larger particles, as observed in LWA, but also to a decline in pore connectivity caused by particle grinding. As shown in the SEM micrograph of G.B. (Figure 2.19), the biochar cell walls exhibit noticeable fracture and collapse, with vessel pores being partially blocked or truncated. Such structural damage limits the continuity of water transport pathways within the biochar matrix, thereby reducing its water release efficiency. The skeletal density of biochar tested from pycnometer method is 1.141g/cm^3.

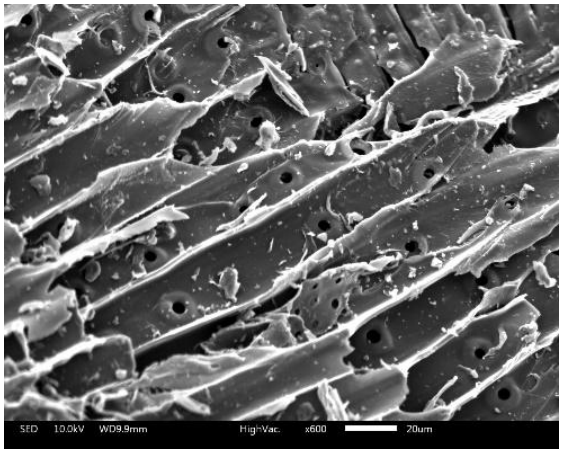


Figure. 2.19 SEM micrograph of G.B.

Table 2.9 Water absorption of biochar

Type	Saturation time (h)	Water absorption coefficient (%)	Standard deviation
O.B.	24	324.3	0.029
	72	320.3	0.019
G.B.	24	103.1	0.014

2.3.2.2. Water release

The water release characteristics of both raw and ground biochar are presented in the Figure 2.20 and the Table 2.10 for some external R.H. of 97%, 93%, 86%, and 75%. The both types of biochar exhibit an impressive water release capability – superior to 90% (Figure 2.20). In comparison, under the same R.H. of 97%, it is equal to about 80% and 50% for LWA and RCA respectively. These results underscore the suitability of both original and ground biochar as effective ICAs, given their robust water absorption and release properties.

From Figure 2.20(c), under high RH (97%–93%) both original (O.B.) and ground biochar (G.B.) display broadly similar desorption histories, with most water released within ~25 days. At 97% RH their linear release rates are essentially identical. At 93% RH, however, G.B. exhibits a faster linear release than O.B. (see Table 2.10).

As shown in Table 2.10, at lower relative humidity levels (86% and 75%), the original biochar exhibits slightly faster water release rates compared to the ground biochar, with slope differences of 0.2–0.4%/day. This trend is likely attributed to the larger macropore content retained in the unground structure. Nevertheless, considering the

standard deviation values, the differences remain minor, indicating that the grinding process has only a limited influence on the overall water release kinetics of biochar.

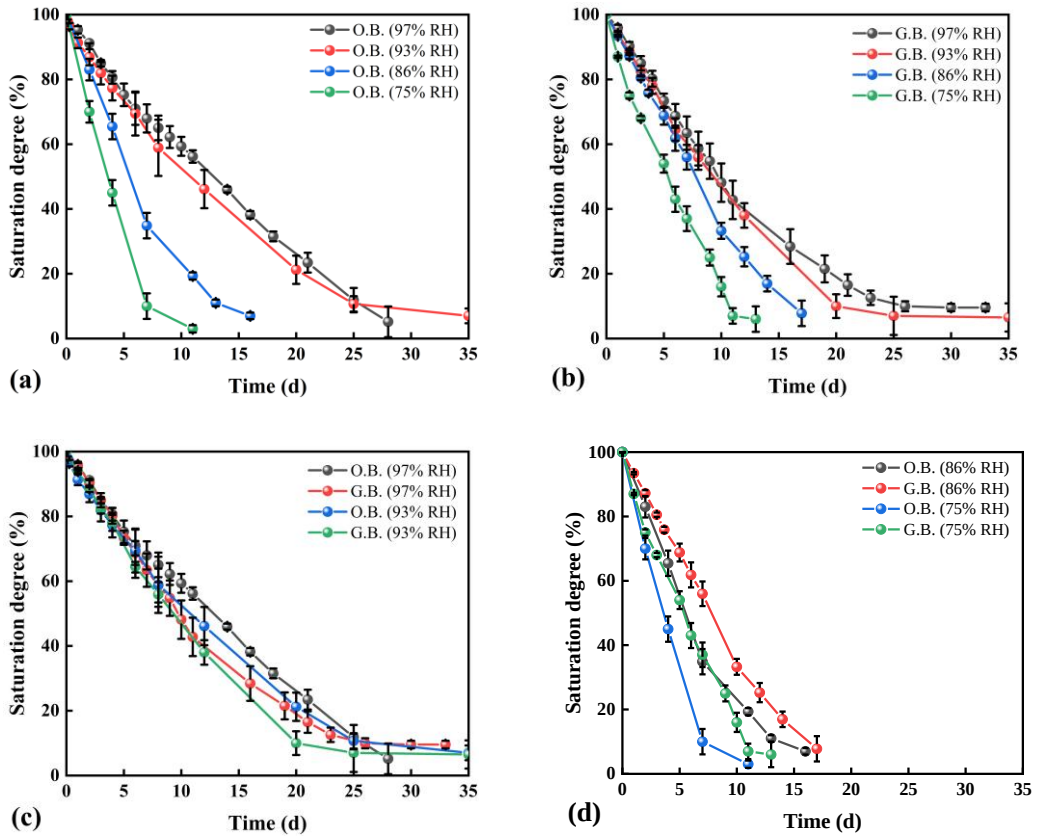


Figure. 2.20 Water release of original biochar (a) and ground biochar (b), as well as their comparison at different external R.H: 97% R.H. and 93% R.H. (c), 86% R.H. and 75%R.H.

Table 2.10 The slope of the linear part of the water release curve for original biochar (O.B.) and ground biochar (G.B.)

RH (%)	Slope for O.B.	Standard deviation	Slope for G.B.	Standard deviation
97	-4.4	0.21	-4.4	0.36
93	-5.6	0.33	-4.6	0.41
86	-6.2	0.25	-6.4	0.31
75	-9.0	0.42	-9.6	0.35

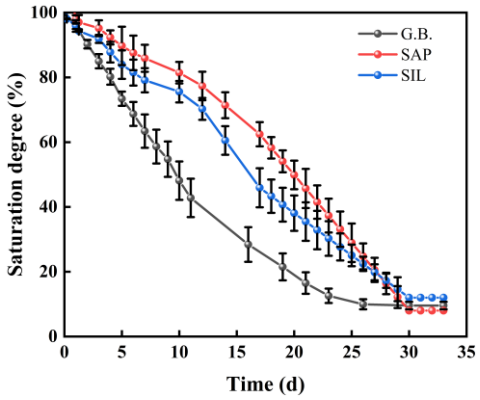


Figure. 2.21 Water release comparison of SAP, silica and biochar at 97% R.H.

Finally, the water release behavior of G.B. was compared with that of conventional ICAs - SAP and SIL, as illustrated in Figure 2.21. A key indicator of release efficiency is the average slope of the water retention curve during the first five days, which was calculated as −1.98%/day for SAP, −3.03%/day for SIL, and −5.29%/day for G.B. These values clearly demonstrate that ground biochar exhibits the fastest early-stage water release among the three. This finding is critical when considering the practical application of ICAs: while such agents initially reduce the effective water-to-binder ratio by absorbing part of the mixing water, timely re-release is essential to support early hydration.

2.3.2.3 Thermogravimetric analysis

In addition to their absorption and release properties, the thermal stability of biochar and MgO is of particular relevance. Investigating the DTG curve presented in Figure 2.22(b), a distinct peak emerges between 230 °C and 400 °C, which is attributed to the dehydration of brucite ($Mg(OH)_2$). This feature provides valuable insight into the degree of hydration of MgO and its associated thermal stability. By combining the mass loss curve in Figure 2.22(b) with Equations (2.8) and (2.9), the brucite content in the MgO sample is quantified as approximately 3.27%.

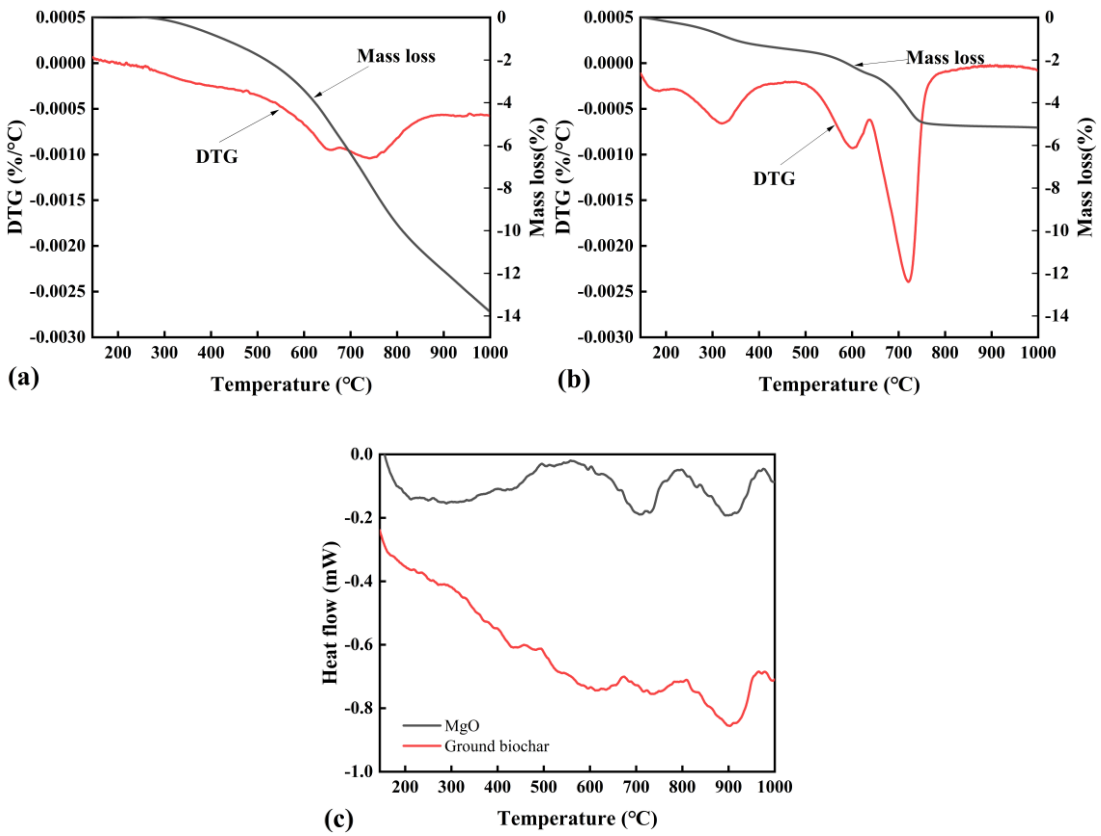


Figure. 2.22 TGA results of biochar and MgO: DTG and mass loss of biochar (a) DTG and mass loss of MgO (b) Heat flow (c)

Biochar exhibits two decomposition peaks between 550 °C and 850 °C. These peaks are associated with the breakdown of residual inorganic compounds or mineral impurities formed during pyrolysis [81]. In contrast, MgO within the same temperature range also presents a double-peak behavior, which can be explained by the stepwise decomposition of different carbonate-containing phases, such as calcite, magnesium calcite, and magnesium carbonate [83]. The overlapping yet distinct decomposition processes of these phases contribute to the emergence of two separate thermal events.

In summary, both biochar and MgO display multiple thermal transitions: (i) for MgO, the decomposition of brucite occurs between 230 °C and 400 °C, followed by the decomposition of carbonate-containing phases between 550 °C and 850 °C; (ii) for biochar, two distinct decomposition peaks are observed within 550 °C to 850 °C, arising from residual mineral phases.

2.4 Summary

This chapter provided a comparative characterization of three ICAs—LWA, RCA, biochar (both original and ground)—focusing on their water absorption, porosity, density and desorption behavior. To facilitate interpretation of the subsequent analyses in Chapters 4 and 5, Table 2.11 summarizes the key physical properties of the ICAs used for mortar production. The most relevant results are summarized below :

- LWA: Four types of LWA were tested (LT: 0–2 mm, LM: 0.63–1.25 mm, LC: 1.25–2.5 mm, LL: 2–5 mm). All exhibited high absorption capacity and rapid water uptake (full saturation within 24 h). Water release kinetics were size-dependent: larger particles range (LT and LL) showed faster early-stage desorption at 97% RH, while smaller particles range (LM and LC) exhibited slower and more prolonged release. Among them, LM was selected for mortar application due to its balanced absorption capacity and sustained release profile under high RH, whereas LT was used only for comparison in mixes where aggregates of similar size replaced sand.
- RCA: RCA was classified into three fractions—RF (0.315–0.63 mm), RM (0.63–1.25 mm), and RC (1.25–2.5 mm). Unlike LWA, RCA showed lower water absorption (typically under 10%) and slower desorption under identical RH conditions. Particle size influenced both density and absorption: finer RCA absorbed more water but had lower density due to higher paste content and porosity. Among the tested fractions, RC was retained for mortar application due to its relatively balanced density and water release profile, while RF and RM were used only for comparative purposes to assess the influence of particle size.
- Biochar: Both original (O.B.) and ground (G.B.) biochar reached saturation within 24 h. Grinding reduced total absorption but enhanced physical stability.

Water release tests revealed that both types had the highest desorption rates among all materials tested, especially at 97% RH (slope ≈ –4.4%/day). At lower RH (86% and 75%), original biochar exhibited slightly faster release, likely due to preserved macropore structure. These results highlight biochar—especially the ground form—as a highly efficient internal curing candidate with robust water transport behavior. G.B. was retained for mortar application owing to its superior mechanical stability, consistent release profile, and lower risk of premature pore collapse during mixing.

Table 2.11 The main properties of ICAs used for mortar production

Name	Size (mm)	Water absorption coefficient (%)	Specific surface area (m^2/g)	skeletal density (g/cm^3)
NS	0-4	0.05	-	2.001
LM	0.63-1.25	24.5	0.56	0.93
LT	0-2	31.6	1.66	0.873
RF	0.315-0.63	7.2	2.76	2.001
RM	0.63-1.25	5.8	3.94	2.048
RC	1.25-2.5	6.4	0.64	2.113
G.B.	-	103.1	363.14	1.141

In conclusion, this chapter provides a material-level comparison of various internal curing agents. LWA and ground biochar emerged as the most promising candidates based on their water release behavior at relevant RH levels for cement hydration. RCA exhibited moderate potential, while SAP and SIL require further dosage and timing control due to their slower release profiles. These findings inform the subsequent mortar design and performance analyses detailed in Chapters 3 to 6.

Chapter 3 Mortar Design, Preparation, and Characterization Methods

This chapter presents the design principles, mixture preparation, and characterization methods for the mortar systems developed in this study. Three ICAs—LWA, RCA, and biochar—were incorporated into different formulations to evaluate their effects on fresh and hardened properties, with detailed compositions, proportions, and testing procedures provided in the following sections.

3.1 Mortars designed with LWA and RCA

This study focuses on the engineering benefits of fine LWA and RCA in partial replacing of mortar' sand for particles ranges including in the range from 0 to 2.5 mm. Since ICAs carry a certain amount of water, the concept of the total water-to-binder ratio and effective water-to-binder ratio are introduced. The total water-to-binder ratio (W_{tot}/C) refers to the ratio calculated using the sum of the mixing water and the water carried by the ICAs, while the effective water-to-binder ratio (We_{ff}/C) is the water available for the cement hydration and for the concrete workability at the fresh state. Part of the mixing water was added to account for the 0.8% water absorption of sand, thereby minimizing the influence of sand water absorption on the mixture properties. This portion of water was not included in the calculation of either the total or effective water-to-binder ratio. The reference mortar, named REF, is characterized by W_{tot}/C and Aggregates/Cement (A/C) ratios equal to 0.45 and 2 respectively. The term'Aggregates' includes sand and curing agent, such as LWA and RCA. To determine the effect of LWA and RCA content and distribution, W_{eff}/C and A/C ratios are kept constant. The paste volume is similar for all the studied mixtures without taking into account the paste from RCA, and the ICAs are pre-saturated before being incorporated into the mixtures using the method presented in §2.3.

To balance the trade-off between minimizing the adverse impact of RCA and LWA on mechanical strength and enhancing their internal curing effectiveness, two contents of RCA and LWA—10% and 15%—were selected for investigation (Table 3.1). These percents were chosen based on previous studies [58, 63, 71], which reported that internal curing effects become noticeable at replacement rates above 10%, while strength reduction remains within an acceptable range below 20%. Accordingly, replacing sand with RCA or LWA at these levels allows us to examine performance under practical and efficient internal curing conditions. Mortar compositions are designated based on the particle size range of the internal curing agent, as specified in the tables in the chapter 2, and its replacement percentage. For example, for LWA with a particle size range of 0–2 mm (referred to as LT in Chapter 2), two sand replacement levels are studied: 10% and 15%. These mortars are labeled 'LT10' and 'LT15', as shown in the Table 3.1.

Table 3.1 LWA and RCA size and content in mortar

Name	Size of LWA (mm)	Content (%)
LM10	0.63-1.25	10
LM15	0.63-1.25	15
LT10	0-2	10
LT15	0-2	15
RF10	0.315-0.63	10
RF15	0.315-0.63	15
RM10	0.63-1.25	10
RM15	0.63-1.25	15
RC10	1.25-2.5	10
RC15	1.25-2.5	15

Two LWA particle size ranges are studied: 0–2 mm (LT10, LT15), chosen to match the particle size range of natural sand, and 0.63–1.25 mm (LM10, LM15), selected to allow comparison between LWA and RCA for the same particle size range. Each range is tested with 10% and 15% sand replacement. In the granular curve, 0.63–1.25 mm particles represent 31.7% of the LWA fraction, while 1.25–2 mm particles account for 65.4%. In this study, the ICAs (LWA and RCA) were introduced by replacing a fixed volume percentage of natural sand within the same particle size range; specifically, each

type of LWA or RCA substituted the corresponding granular fraction of sand rather than a global percentage from the entire sand matrix. The mix proportions with LWA are given in Table 3.2.

Table 3.2 Proportions of mortars with added LWA

Name	W_{eff}/C	W_{tot}/C	LWA content (%)	Cement (kg/m^3)	Sand (kg/m^3)	Added Water (kg/m^3)	LWA* (kg/m^3)	Internal curing water (kg/m^3)	Paste volume (m^3)
REF	0.45	0.45	-	649.49	1298.99	290.91	-	-	0.509
LM10		0.47	10	649.49	1169.09	290.91	58.59	14.35	0.509
LM15		0.48	15	649.49	1104.14	290.91	87.89	21.53	0.509
LT10		0.48	10	649.49	1169.09	290.91	58.19	18.39	0.509
LT15		0.49	15	649.49	1104.14	290.91	87.28	27.58	0.509

(*) LWA are saturated state

Based on the results from Chapter 2, batch No. 1 of RCA, which exhibited a higher water absorption capacity, was selected for investigation. To explore the detailed impact of size variation on internal curing effect, the selected RCA's ranges are: 0.315-0.63mm (mortars named 'RFxx' where 'xx' is the percentage of ICA), 0.63-1.25mm (mortars named 'RMxx'), and 1.25-2.5mm (mortars named 'RCxx'). This selection aims to provide a granular understanding of how different sizes contribute to the internal curing process. The RCA size and content for each type of mortar are listed in Table 3.1, while the detailed mix proportions are provided in Table 3.3.

Subsequently, acknowledging the practical considerations of engineering applications, particularly the ease of material screening, we expanded our investigation to include three RCA types with broader particle size ranges. These are: 0.315-1.25mm (mortars named 'RFMxx'), 0.315-2.5mm (mortars named 'RFMCxx'), and 0.63-2.5mm (mortars named 'RMCxx'). This phase of the study is designed to assess the feasibility

and effectiveness of using RCA with larger, more varied particle sizes in real-world construction scenarios, thereby bridging the gap between laboratory findings and engineering practice. The RCA size and content for each type of mortar are listed in Table 3.4, while the detailed mix proportions are provided in Table 3.5.

Table 3.3 Mixture proportion of mortar with RCA for size-effect analysis

Name	W_{eff}/C	W_{tot}/C	RCA content (%)	Cement (kg/m^3)	Sand (kg/m^3)	Added Water (kg/m^3)	RCA* (kg/m^3)	Internal curing water (kg/m^3)	Paste volume (m^3)
REF	0.45	0.45	-	649.49	1298.99	290.91	-	-	0.509
RF10		0.46	10	649.49	1169.09	290.91	111.31	7.35	0.509
RF15		0.46	15	649.49	1104.14	290.91	166.97	11.02	0.509
RM10		0.46	10	649.49	1169.09	290.91	112.28	6.85	0.509
RM15		0.46	15	649.49	1104.14	290.91	168.41	10.27	0.509
RC10		0.46	10	649.49	1169.09	290.91	114.1	6.73	0.509
RC15		0.46	15	649.49	1104.14	290.91	171.15	10.10	0.509

(*) RCA are saturated state

Table 3.4 RCA size and content in mortar for practical applications

Name	Size of LWA (mm)	Content of LWA (%)
RFM10	0.315-1.25	10
RFM15	0.315-1.25	15
RFMC10	0.63-2.5	10
RFMC15	0.63-2.5	15
RMC10	0.315-2.5	10
RMC15	0.315-2.5	15

Table 3.5 Mixture proportion of mortar with RCA of broader size ranges for practical applications

Name	W_{eff}/C	W_{tot}/C	RCA content (%)	Cement (kg/m^3)	Sand (kg/m^3)	Added Water (kg/m^3)	RCA (kg/m^3)	Internal curing water (kg/m^3)	Paste volume (m^3)
REF	0.45	0.45	-	649.49	1298.99	290.91	-	-	0.509
RFM10		0.46	10	649.49	1169.09	290.91	111.82	7.04	0.509
RFM15		0.46	15	649.49	1104.14	290.91	167.73	10.57	0.509
RFMC10		0.46	10	649.49	1169.09	290.91	112.93	6.89	0.509
RFMC15		0.46	15	649.49	1104.14	290.91	169.4	10.33	0.509
RMC10		0.46	10	649.49	1169.09	290.91	113.64	6.81	0.509
RMC15		0.46	15	649.49	1104.14	290.91	170.47	10.23	0.509

3.2 Mortars with biochar

This section explores innovative internal curing strategies, focusing on biochar and its interaction with another shrinkage reducer, MgO, in enhancing the curing efficiency of cement-based materials and their shrinkage mitigating capacity. The study evaluates the effectiveness of these materials both individually and in combination at different W/B ratios (Table 3.6). In this study, mortars incorporate 5% biochar and 6% MgO (by cement weight). The mortars are named B5-yy (5% biochar with 'yy' the water ratio), M6-yy (6% MgO), and B5M6-yy (5% biochar + 6% MgO). The 5% biochar content was chosen for its demonstrated ability to enhance water retention [80-83], while 6% MgO was selected for its moderate expansion properties, helping to reduce shrinkage [91-93]. The effectiveness of MgO as an expansive agent is largely determined by the W/B ratio, specifically by the availability of free capillary water and the characteristics of the porous network [93]. Thus, the effect of three water-to-binder (W_{tot}/B) ratios are

investigated: 0.45, 0.41, and 0.37. The mixtures' proportions are given in the Table 3.6. For each W/B, a mortar reference without biochar and MgO was also characterized.

A W/B ratio of 0.45, previously tested with LWA and RCA, serves as a control mixture since the available water is sufficient for binder hydration [32], promoting the MgO hydration and the brucite formation [92]. At lower W/B ratios (0.37 and 0.41), internal curing becomes increasingly crucial in sustaining hydration [38]. Additionally, the reduced porosity limits the space available for new product formation, such as brucite, while enhancing its confinement and contributing to matrix swelling [92]. This systematic investigation will provide valuable insights into the effectiveness of combining ICAs with shrinkage-reducing materials like MgO.

To further evaluate internal curing efficiency, the study compares biochar with traditional ICAs: superabsorbent polymers (SAP) and silica (SIL). Two selected contents of SAP (2% and 5.5% by MgO weight) and silica (6% and 15.5% by MgO weight) are chosen. The lower contents (2% SAP and 6% SIL) correspond to the recommended dosages for these internal curing agents and serve as a reference for comparison. The higher contents—5.5% SAP and 15.5% SIL—were specifically chosen to provide a water retention capacity equivalent to that of 5% biochar. This enables a direct and meaningful comparison of their performance in terms of hydration maintenance and shrinkage mitigation. Similarly, specimens incorporating SAP and silica are named based on their composition proportions: SAP2M6 (2% SAP + 6% MgO), SAP5.5M6 (5.5% SAP + 6% MgO), SIL6M6 (6% silica + 6% MgO), SIL15.5M6 (15.5% silica + 6% MgO). Their proportions are given in Table 3.7.

In this context, W_{tot} refers to the total amount of water added during mixing, and the binder B includes the combined mass of cement and MgO, excluding ICAs like SAP and biochar. Biochar, SAP and SIL are all pre-saturated, and the internal curing water means the water carried by them. Biochar, SAP, SIL and MgO are included in the paste volume.

Table 3.6 Mixture proportions of the mortar with biochar and MgO added

Name	W_{tot}/B	W_{eff}/B	W_{tot}/C	Cement (kg/m^3)	Sand (kg/m3)	Total water (kg/m^3)	Biochar (kg/m^3)	MgO (kg/m^3)	Internal curing water (kg/m^3)	Paste volume (m^3)
REF-45	0.45	0.45	0.45	649.49	1298.99	290.91	0	0	0	0.498
M6-45		0.45	0.47	613.29	1298.99	290.91	0	36.80	0	0.510
B5-45		0.40	0.45	631.01	1262.02	283.95	32.47	0	33.44	0.523
B5M6-45		0.40	0.48	595.84	1262.02	283.95	32.47	35.75	33.44	0.522
REF-41	0.41	0.41	0.41	685.86	1298.99	281.20	0.00	0.00	0	0.499
M6-41		0.41	0.43	647.05	1298.99	281.20	0	38.82	0	0.511
B5-41		0.36	0.41	665.25	1259.95	272.75	34.29	0.00	35.32	0.524
B5M6-41		0.36	0.43	627.64	1259.95	272.75	34.29	37.66	35.32	0.524
REF-37	0.37	0.37	0.37	725.77	1298.99	268.54	0	0	0	0.499
M6-37		0.37	0.39	684.74	1298.99	268.54	0	41.08	0	0.512
B5-37		0.32	0.37	703.49	1258.81	260.26	36.29	0	37.38	0.525
B5M6-37		0.32	0.39	663.63	1258.81	260.26	36.29	39.81	37.38	0.525

(*) Biochar is saturated state

Table 3.7 Mix proportions of the mortar with SAP, silica and MgO added

Name	W_{tot}/B	W_{eff}/B	W_{tot}/C	Cement (kg/m^3)	Sand (kg/m3)	Total Water (kg/m^3)	MgO (kg/m^3)	Internal curing water (kg/m^3)	Paste volume (m^3)
SAP2M6	0.45	0.43	0.47	613.29	1298.99	290.91	36.8	12.46	0.509
SAP5.5M6		0.40		613.29	1298.99	290.91	36.8	33.44	0.510
SIL6M6		0.43		613.29	1298.99	290.91	36.8	12.94	0.510
SIL15.5M6		0.40		613.29	1298.99	290.91	36.8	33.44	0.512

(*) SAP and SIL are saturated state

3.3 Mortars mixing process

The preparation of mortars involving saturated RCA and LWA necessitates a specific protocol. It begins by saturating the LWA and RCA during 24 hours before mixing as proposed in §2.3.1.1. Just before mortar fabrication, they are exposed to warm airflow until they reach a saturated surface-dry (SSD) state. The preparation of biochar differs due to its strong affinity for water, which makes conventional saturation methods less effective. To address this, the required amounts of biochar and water are pre-measured

and mixed 24 hours before batching as indicated in §2.3.2.1. The mixture is then sealed and left undisturbed to ensure uniform water absorption and optimal integration into the mortar.

The precise mixing procedure is as follows:

- Dry Mixing: Sand is added to the mixer, followed by cement and MgO. They are mixed at low speed for 30 seconds.
- Gradual Water Addition: A quarter of the total water content is introduced, followed by 30 seconds of low-speed mixing. This step is repeated three times for thorough incorporation. For the mixtures containing ICAs, as the ICAs (LWA, RCA, Biochar, Sil, SAP) are pre-saturated in water, they are added simultaneously with the water during this step of mixing.
- Scraping: The mixer is stopped, and any mortar adhering to the walls and bottom is scraped toward the center using a plastic spatula.
- Final Mixing: The mixture is then blended at high speed for 120 seconds to ensure a homogeneous mortar.

3.4 Techniques for Mortar Characterization

To comprehensively assess mortar properties, both microscopic and macroscopic analysis techniques are employed. Microscopic analysis focuses on hydration products and porosity using thermogravimetric analysis and water porosity respectively, providing insight into the material's internal structure and curing process. Macroscopic analysis evaluates mechanical properties, shrinkage behavior from early age to long term, and self-healing capacity.

The following chapter details the methodologies used to characterize mortar at these two scales, ensuring a thorough understanding of its behavior and durability.

3.4.1 Microstructure

3.4.1.1. Hydration products

To evaluate the hydration products and rates of the mortars, ThermoGravimetric Analysis (TGA) is performed once for each mixture at 7 and 28 days, stored in water at 20°C. After this period, the specimens undergo additional curing in water. Prior to TGA, the specimens (40cm×40cm×40cm) are dried at 105°C for 24 hours to remove free water. Then, the specimens are crushed, and samples are collected specifically from the inner core region to minimize the influence of external carbonation on analytical results. The collected material is then ground into a fine powder (passing through a 80 µm sieve) for analysis. Around 70 to 90 mg of the powdered sample is placed in a controlled nitrogen environment, where the temperature is gradually increased from 20 to 1000°C at a rate of 10°C per minute.

The degree of hydration is quantified by Equation (3.1):

$$\propto (t) = \frac{m_{el}(t)}{W_{el}(\infty) m_c} \times 100 \tag{3.1}$$

Where $m_{el}(t) = |\Delta m_{145℃\rightarrow1000℃}(t)| - |\Delta m_{550℃\rightarrow850℃}(t)| + m_{d,145℃\rightarrow1100℃}(t) - m_c \times PaF - m_B \times PaF(B) - m_{MgO} \times PaF(M)$; $m_{el}(t)$ is the mass of water bound to the cement at time t, $\Delta m_{145℃\rightarrow1000℃}(t)$ is the mass loss between 145 and 1000°C, $\Delta m_{550℃\rightarrow850℃}(t)$ is the mass loss between 550 and 850°C, $m_{d,145℃\rightarrow1000℃}(t)$ is the drift of the device between 145 and 1000°C between 145 and 1000°C, $W_{el}(\infty)$ is the quantity of water necessary for the complete hydration of the cement, in this test, it is taken as 0.24.

Since the processes at [400-550]°C and [550-850]°C are related to $Ca(OH)_2$ dehydration and decarbonation, respectively, the contents of portlandite and calcite in the mixture can be calculated using the Equations 2.7 and 3.2.

$$m_{CaCO3}(t) = \frac{[|\Delta m_{550℃\rightarrow850℃}(t)| + m_{d,550℃\rightarrow850℃}(t)] - m_c \times PaF}{m_s} \cdot \frac{M_{CaCO3}}{M_{CO2}} \tag{3.2}$$

Where, $\Delta m_{550°C\rightarrow800°C}(t)$ is the mass loss between 550 and 850°C, $m_{d,550°C\rightarrow800°C}(t)$ is the drift of the device between 550 and 850°C, M_{CaCO3} is the molar mass of portlandite (100g/mol), M_{CO2} is the molar mass of water (44g/mol).

Since the mass loss observed at [320–400] °C in this study corresponds to the dehydration of $Mg(OH)_2$, the brucite content in the MgO-containing specimens can be quantified using Equations (3.3):

$$m_{Mg(OH)2} = \left[|\Delta m_{320°C\rightarrow400°C}(t)| + m_{d,320°C\rightarrow400°C}(t)\right] \cdot \frac{M_{(MgOH)2}}{M_{H2O}} \quad (3.3)$$

Where $\Delta m_{320°C\rightarrow400°C}(t)$ is the mass loss between 320 and 400°C, $m_{d,320°C\rightarrow400°C}(t)$ is the drift of the device between 320 and 400°C.

3.4.1.2. Total water porosity

The total water porosity of the material is determined according to the NF P18-459 [152]. Three cylindrical specimens (4×6 cm) are prepared for each mixture and cured in water at 20±2°C for 28 days, after which their upper and lower surfaces are polished. They are then placed in a vacuum desiccator for 4 hours, followed by water saturation under vacuum conditions for an additional 44 hours to ensure full absorption. After saturation, the specimens' mass is measured in water (M_{eau}), then dried on the surface and weighed in air (M_{air}). Subsequently, they are oven-dried at 105°C until a constant mass is reached, ensuring that the mass variation does not exceed 0.05% within a 24-hour period. Finally, the dry mass (M_{sec}) is recorded, and porosity is calculated using the equation 3.4.

$$\varepsilon\ (\%) = \frac{M_{air} - M_{sec}}{M_{air} - M_{eau}} \times 100 \quad (3.4)$$

3.4.1.3. Water desorption curve

To evaluate the water desorption behavior of mortar under drying conditions, a stepwise R.H. test was conducted at a constant temperature of 20 °C. Four R.H. levels were selected to construct the water desorption isotherm: 97%, 90%, 85%, 75%. The

specimen size was 4 cm × 4 cm × 0.5 cm, cut from prismatic saturated samples (originally 4 cm × 4 cm × 16 cm). For each mixture, six specimens were prepared, three of which were reserved for carbonation testing.

Saturation procedure:

Before the desorption test, all specimens were vacuum saturated following the same procedure as in the water porosity test (§3.4.1.2). This involved placing the specimens in a desiccator under vacuum for 4 hours, followed by immersion in water while maintaining the vacuum for 48 hours. After saturation, specimens were surface-dried and weighed to record their initial saturated mass $m_{initial}$. The oven-dried mass m_{dry} was later obtained after 24 hours at 105 °C.

Desorption testing steps:

1. Specimens were placed in desiccators with controlled R.H. levels (starting at 97%).
2. At each R.H. stage, mass was monitored until stability was achieved—defined as a mass change of less than 0.01% over 7 consecutive days. Weighing intervals were: 24 h, 2 days, 3 days, 6 days, and then weekly until stability.
3. Once equilibrium was reached, the specimen mass under that R.H. (m_{RH}) was recorded.
4. The test then proceeded to the next R.H. level, and one specimen was removed at each R.H. step for a carbonation test.
5. After completing all R.H. stages, remaining specimens were dried at 105 °C to determine m_{dry}.

Saturation degree calculation :

The saturation degree S_w at each R.H. level was calculated as:

$$S_w = \frac{m_{RH} - m_{dry}}{m_{initial} - m_{dry}} \quad (3.5)$$

Where m_{RH} is specimen mass at the given R.H. level (g), $m_{initial}$ initial saturated mass (after vacuum saturation and surface drying) (g), m_{dry} is oven-dried mass after 105 °C for 24 h (g).

3.4.1.4. Scanning electron microscope (SEM)

Scanning Electron Microscopy (SEM) observations were conducted on 3-month-old mortar samples for two mixtures (LM10 and RC10). The SEM analysis was performed on paste slices impregnated with epoxy resin and subsequently polished using progressively finer grades of diamond paste (1200 μm, 9 μm, 3 μm, and 1 μm) [108].

The SEM system was configured to capture at least three Backscatter Electron (BSE) images per mixture and to perform Energy Dispersive Spectroscopy (EDS) elemental analysis at multiple points within the images. An accelerating voltage of 20 kV and a working distance of approximately 10 mm were used for SEM/EDS imaging. For EDS analysis.

To enhance the clarity of anhydrous and hydrated phases on a 2D surface, high magnifications (×1000 or ×3000) were selected for at least three representative images per mixture.

To quantify how the microstructure changes from the aggregate surface into the paste (i.e., across the ITZ), we analyzed high-resolution SEM-BSE images with a distance-based profiling approach adapted from established methods in cement microscopy [153-156]. In simple terms, each pixel in the paste was assigned a distance to the nearest aggregate boundary, and we then asked: “within a thin ring at that distance, what fraction of pixels are pores?” Plotting this fraction against distance yields a porosity-versus-distance profile that describes the ITZ.

The raw BSE images were first enhanced using CLAHE (Contrast Limited Adaptive Histogram Equalization) to improve contrast between pores, paste, and aggregates (Figure 3.1(a)).

After contrast enhancement, the BSE image was subjected to K-means [164] clustering to partition the pixels into three distinct classes:

Aggregate (light gray)

Cement paste matrix (medium gray)

Pores/voids (dark gray)

The algorithm minimizes the within-cluster variance by iteratively assigning pixels to the nearest cluster centroid and updating the centroids:

$$J = \sum_{i=1}^{k} \sum_{x_j \in C_i} \left\| x_j - \mu_i \right\|^2 \tag{3.6}$$

Where:

- $k = 3$ = number of classes,
- x_j = grey value of pixel j,
- C_i = set of pixels assigned to cluster i,
- μ_i= centroid of cluster i.

Convergence is reached when centroid shifts fall below a defined tolerance. As shown in Figure 3.1(b), the aggregate, paste, and pores were clearly separated.

(a) CLAHE (b) K-means (k=3) (c) LWA region

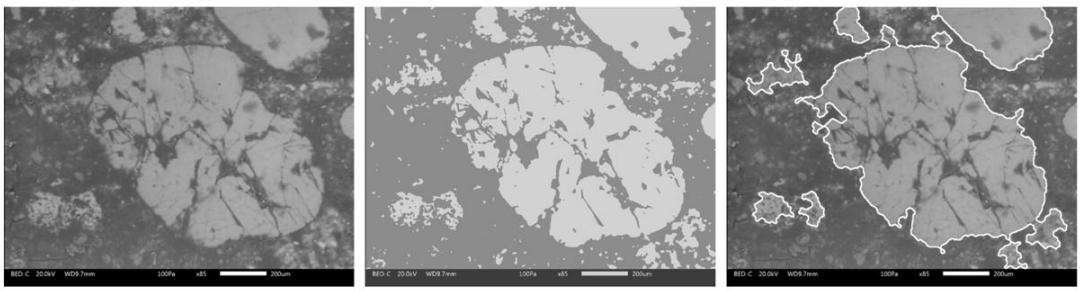


Figure 3.1. Tri-panel segmentation of LWA mortar BSE image : enhanced image (a); K-means segmentation (b); boundary overlay (c)

To define the paste domain, this mask was inverted, such that all non-aggregate pixels were considered part of the matrix region to define the LWA region boundary (Figure 3.1(c)).:

$$M_{paste}(x, y) = 1 - M_{agg}(x, y) \tag{3.7}$$

Where:

- $M_{agg}(x, y)$=1 if pixel (x,y) belongs to aggregate, 0 otherwise.
- $M_{paste}(x, y)$ thus identifies the cement paste domain.

All subsequent porosity analyses were constrained to this paste mask, excluding aggregates to avoid bias from their much brighter grayscale levels.

Two complementary approaches were applied to quantify porosity in the cement paste adjacent to the aggregate:

(a) Grayscale Histogram Analysis

Pores were identified as low-intensity pixels within the paste domain, based on thresholding of the grey-value histogram. The pore pixel set was defined as:

$$P = \{(x, y) \in M_{paste} \mid I(x, y) < T_{pore}\} \tag{3.8}$$

Where $I(x, y)$ is the pixel intensity and T_{pore} is the pore threshold obtained from the histogram valley.

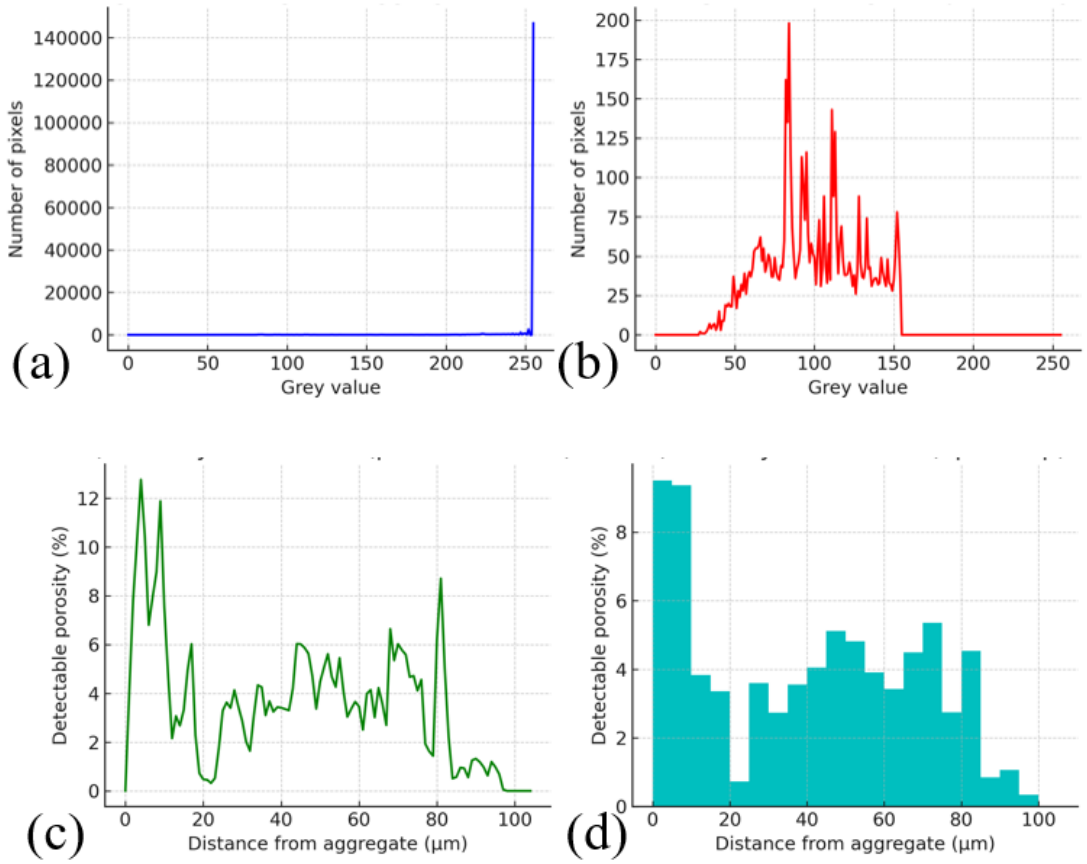


Figure 3.2. Brightness histogram (aggregate excluded) (a); Brightness histogram (pores only) (b); Porosity distribution (pixel resolution) (c); Porosity distribution (5 μm strip) (d) for LWA mortar

Figure 3.2(a) shows the full histogram of the paste region. Figure 3.2(b) isolates the pore-only histogram, describing the distribution of pore brightness.

The pore volume fraction (porosity) is then:

$$\emptyset = \frac{|P|}{|M_{paste}|} \times 100\% \tag{3.9}$$

(b) Distance-Based Porosity Analysis

To evaluate porosity distribution relative to the aggregate boundary, an Euclidean Distance Map (EDM) was computed from the aggregate surface outward into the paste:

$$D(x,y) = \min_{(u,v)\in\partial M_{agg}} \sqrt{(x-u)^2 + (y-v)^2} \tag{3.10}$$

Where ∂M_{agg} denotes the aggregate boundary.

Using this map, pores were grouped into concentric shells extending outward from the aggregate surface. Two levels of resolution were adopted:

Pixel resolution: porosity calculated per distance pixel (Figure 3.2(c)).

5 μm strips: porosity calculated in successive annuli of thickness 5 μm (Figure 3.2(d)).

The local porosity within a distance bin

$$\emptyset(d) = \frac{\left|\{(x,y) \in P \middle| d \le D(x,y) < d + \Delta d\}\right|}{\{(x,y) \in M_{paste} \middle| d \le D(x,y) < d + \Delta d\}} \times 100\% \tag{3.11}$$

This allows quantitative mapping of pore concentration as a function of distance from the aggregate.

3.4.1.5. Determination of Real Volume by Helium Pycnometry

The real volume of each mortar specimen was determined using a helium pycnometer (AccuPyc II 1340, Micromeritics), which calculates volume by helium gas displacement. This technique excludes inaccessible pores, thereby providing high measurement accuracy. For each mortar formulation, three replicate cylindrical specimens (maximum size Ø40 mm × 60 mm) were tested. All specimens had been prepared one year before testing and stored under sealed conditions in aluminum foil to

prevent moisture exchange. This ensured that the microstructural state at the time of measurement was representative of the long-term cured material, which is essential for evaluating the effect of ICAs on the intrinsic density of the hardened matrix. Prior to testing, the samples were dried at 105 °C for 48 h and cooled in a desiccator for 2 h. The measurement procedure (Figure 3.3) consisted of: (1) weighing the dried specimen using a precision balance; (2) placing it in the measurement chamber and sealing it; (3) initiating the test via the control software; (4) introducing helium gas at ~1.7 bar; (5) running 2–3 standard measurement cycles under the default settings (fill pressure 134.4 kPa; equilibration rate 0.0345 kPa/min); and (6) automatically recording the real volume and density. After the run, the specimen was removed and the helium supply was closed.



Figure 3.3 Measurement setup

3.4.1.6. Setting time

The setting process of the mortar is evaluated by continuously monitoring the compressive wave velocity through a cylindrical specimen (diameter: 8 cm, height: 4 cm), using two ultrasonic transducers operating at a central frequency of 54 kHz (Vikasonic device, Figure 3.4). The test is conducted with a pulse repetition rate of 1 s and a voltage of 2000 V. Measurements start immediately after mixing and continue for a duration of 4 days, while the specimens are maintained at a constant temperature of 20 ± 2 °C. In parallel, the internal temperature of the mortar is recorded using a

thermocouple embedded in the sample.

The ultrasonic velocity $V(t)$ is fitted using a multi-logistic fitting model (Equation (3.12)) [158, 162]. This model includes four fitted parameters: V_i the asymptotic velocity values (m/s), t_i the time corresponding to the inflection points (s), g_i the slope parameters controlling the rate of transition (s), C the initial baseline velocity (m/s). All parameters are calibrated using the Nonlinear Least Squares (NLS) fitting method.

$$V(t) = \sum_i \frac{V_i}{1+e^{\frac{t-t_i}{g_i}}} + C \tag{3.12}$$

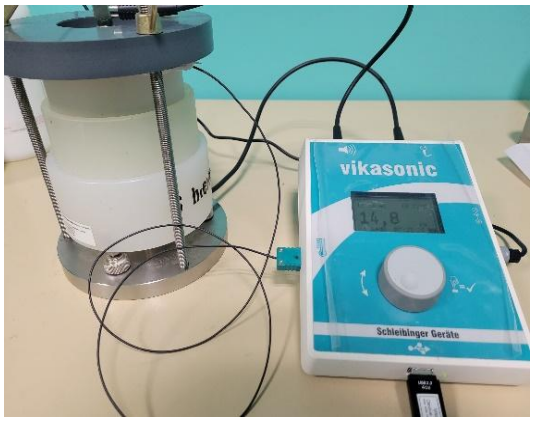


Figure 3.4 Vikasonic device

3.4.2 Mechanical performances

The preparation of specimens for mechanical strength tests follows the EN 196-1 standard [141]. After mixing, the mortar is cast into 4×4×16 cm molds, covered with plastic film, and cured in a moist air room for 24 hours. The specimens are then demolded. To evaluate the influence of ICAs on mechanical properties, two curing methods are employed: autogenous curing, where specimens are wrapped in two layers of aluminum film and stored at 20±2°C and 50%±5% R.H., and wet curing, conducted in a humidity-controlled room at 20°C and 95%±5% R.H. For each curing method, three specimens are tested at 7 and 28 days.

Flexural strength is first determined using a three-point bending test at a loading rate of (50 ± 10) N/s, in accordance with EN 196-1 [141] (Figure 3.5(a)). The fractured halves

resulting from the flexural test are then used to measure compressive strength, applying a loading rate of (2400 ± 200) N/s until failure (Figure 3.5(b)).

Additionally, the dynamic modulus is determined by measuring the velocity of ultrasonic compressive waves propagating through the mortar specimens (Figure 3.6). This test is conducted on the same specimens that are used for flexural test. Ultrasonic measurements are performed at 7 and 28 days using a transducer with a frequency of 50 MHz, with three specimens tested per mortar type.

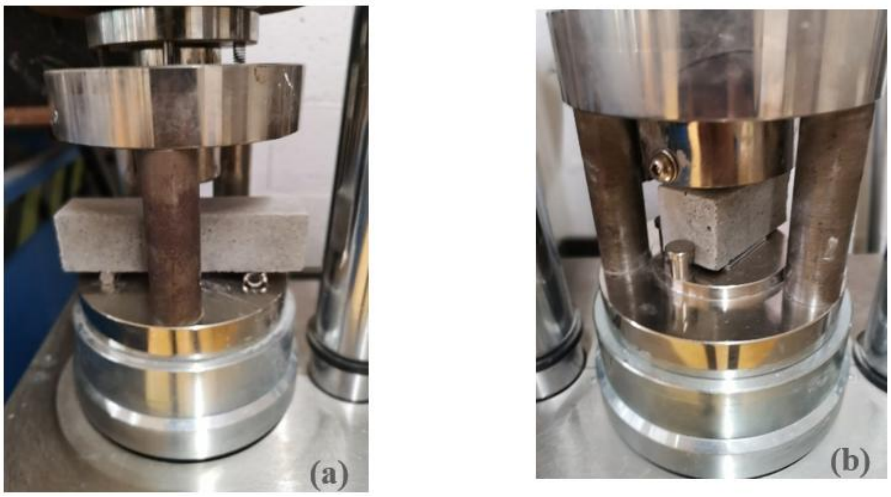


Figure. 3.5 Flextural (a) and compressive (b) strength test

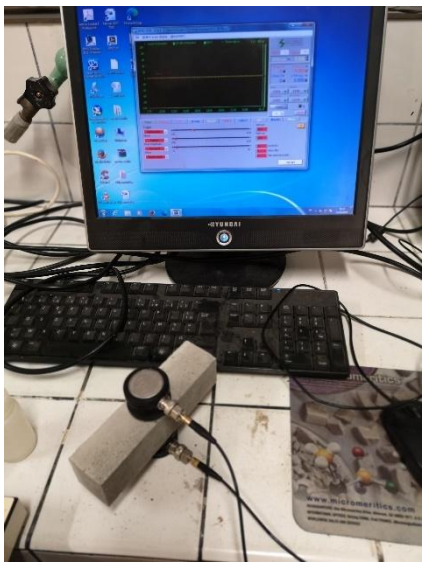


Figure. 3.6 Ultrasonic measurement

The dynamic modulus is calculated using the Equation 3.13.

$$E_d = \rho V^2 \frac{(1+\vartheta)(1-2\vartheta)}{(1-\vartheta)} \quad (3.13)$$

Where, E_d is the dynamic modulus of the material (GPa); $V=d/t$, the speed of longitudinal waves in the material (m/s); d the thickness of the material through which the wave passes (m); t the propagation duration of the wave during the test (s); ϑ is the Poisson's ratio of the material (-).

3.4.3 Shrinkages from early age to long term

Understanding shrinkage in cement-based materials is key to assessing long-term dimensional stability. This section outlines the methods used to measure autogenous shrinkage at very early age and both autogenous and drying shrinkage at long term. The tests used in this study are described below.

Two techniques are used to monitor the autogenous deformation since the setting time: shrinkage cone test and corrugated tube test.

3.4.3.1 Shrinkage Cone Test

The early-age shrinkage behavior of the mortars is assessed using the shrinkage cone method, a technique specifically designed to capture volumetric changes that occur during the very early stages of cement hydration. This test is particularly valuable because it allows for continuous monitoring of deformation from the moment of casting until the end of the setting period, thereby capturing shrinkage phenomena that conventional tests often overlook. Before setting, the shrinkage cone method provides insights into plastic shrinkage under drying condition and chemical shrinkage under autogenous condition. In the present work, we focus on the behavior after the setting for this last condition.

The test is conducted under controlled environmental conditions with shrinkage cone (Figure.3.7), typically at a temperature of 20 ± 1 °C and a relative humidity of 65 ± 5%. The test is performed in accordance with the procedure described by Eppers [159].

The shrinkage cone test is performed once for each mixture as follows (Figure.3.8):

1. First, put a layer of tapered plastic film on the surface of the shrinking cone to separate the mortar and shrinking cone.
2. Pour the mortar into the shrink cone and use the tool to compact (Figure.3.8 (4,5)).
3. To measure the autogenous shrinkage, it is required to prevent evaporation from the surface. A thin and transparent plastic film was used to cover the surface (Figure.3.8 (6)).
4. Sealing the surface sometimes led to the formation of bubbles under the plastic film during the test, notably altering the position of the reflector pad when this was put on top of the film. To avoid this effect, the reflector pad was directly placed into the concrete. Prior to that, the film and the pad were tightly connected to each other by double-faced adhesive tape (Figure.3.8 (6)).
5. Use brush to smoothen film, and the film was additionally fixed to the cone's outside by double-faced adhesive tape (Figure.3.8 (8)).

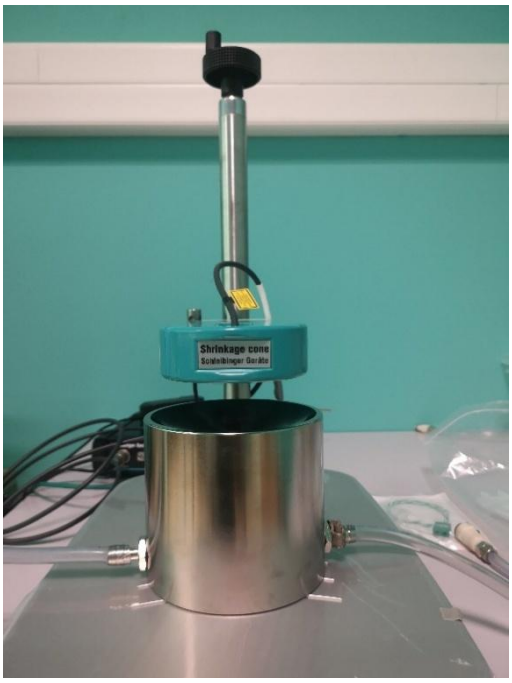


Figure 3.7 Shrinkage cone

The shrinkage is calculated by Eq (3.14):

$$\varepsilon(t) = \frac{\Delta L_i(t)}{L_0} \tag{3.14}$$

Where L_0 denotes the initial length (in mm) of the specimen. It is calculated as $L_0 = L_1 + \Delta L$ with L_1 the length (in mm) measured at the end of the test and ΔL the final shrinkage value (mm) recorded at the end of the test. $\Delta Li(t)$ represents the deformation (in mm) of specimen measured at time t, relative to the corrected initial length L_0. It reflects the cumulative length change (either shrinkage or expansion) that has occurred after the first day.

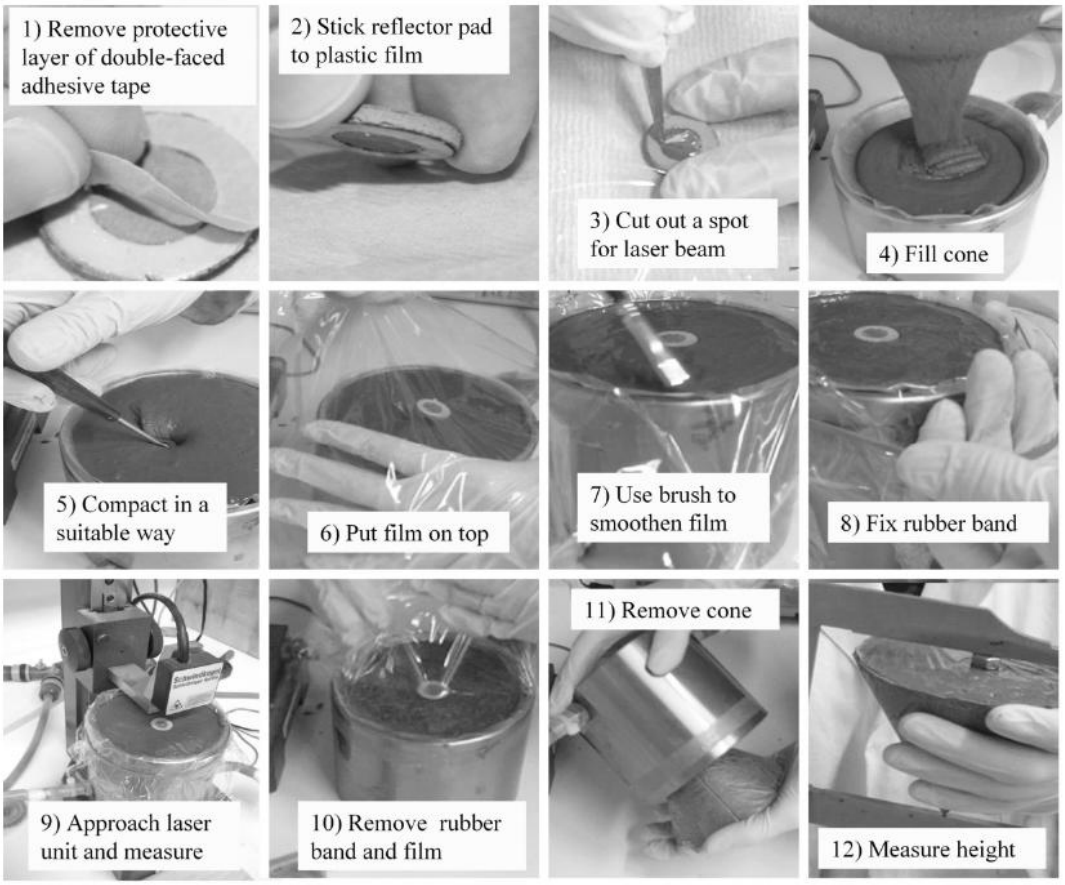


Figure 3.8 Measurement of autogenous shrinkage by the shrinkage cone method [159]

3.4.3.2 Corrugated Tube Test

The corrugated tube method offers a distinct advantage in measuring early-age shrinkage, particularly autogenous shrinkage, by enabling deformation monitoring starting from the setting time. Unlike traditional shrinkage tests that begin measurements after demoulding (typically at 24 hours), the corrugated tube setup

allows continuous shrinkage measurement of sealed specimens without external drying effects. This method effectively isolates the self-desiccation-induced deformation, providing a more accurate representation of autogenous shrinkage development from the moment the material transitions from plastic to solid state.

One time is performed for each mixture. The procedure commences by filling the corrugated tube with mortar, followed by securing the corrugated tube onto the vibrating table. The mortar is vibrated until dense, after which the top of the corrugated pipe is sealed. Subsequently, the specimen is placed in a controlled environment with constant temperature and humidity (20±2°C and 50% ±10% RH), for a duration equal to the setting time.

Upon completing this curing period, the digital meter is calibrated to zero using a control bar (Figure 3.9). Following the calibration, the control bar is removed, and the actual specimen is then positioned on the digital meter to initiate the testing process (Figure 3.10). This systematic approach ensures the accurate and controlled testing of the specimens.



Figure 3.9 Reference bar setting



Figure 3.10 Corrugated tube setting

3.4.3.3 Autogenous and Drying Shrinkage at Long Term

Long-term shrinkage behavior is analyzed to understand the combined effects of autogenous and drying shrinkage on mortar specimens. These tests help evaluate the effectiveness of ICAs in mitigating shrinkage over prolonged durations

The prism method, following the guidelines of EN 12617-4:2002 [160], is employed to evaluate both autogenous and total shrinkage of the mortar specimens. Mortar is cast into prismatic molds ($40 \times 40 \times 160$ mm), with three specimens prepared for each shrinkage condition per mortar type. After casting, the specimens are stored in a moist-air room for 24 hours. Upon demoulding, specimens designated for autogenous shrinkage are fully sealed with aluminum foil to prevent moisture exchange (Figure 3.11(a)), while those for drying shrinkage are sealed on the top and bottom surfaces only, allowing lateral drying (Figure 3.11(b)). All specimens are then stored in a controlled environment at 20 ± 2 °C and 50 ± 10% relative humidity. Length change is measured periodically using a retractometer with 1 μm resolution, and shrinkage is calculated according to Equation (3.14). The mass loss of the specimens is also monitored.

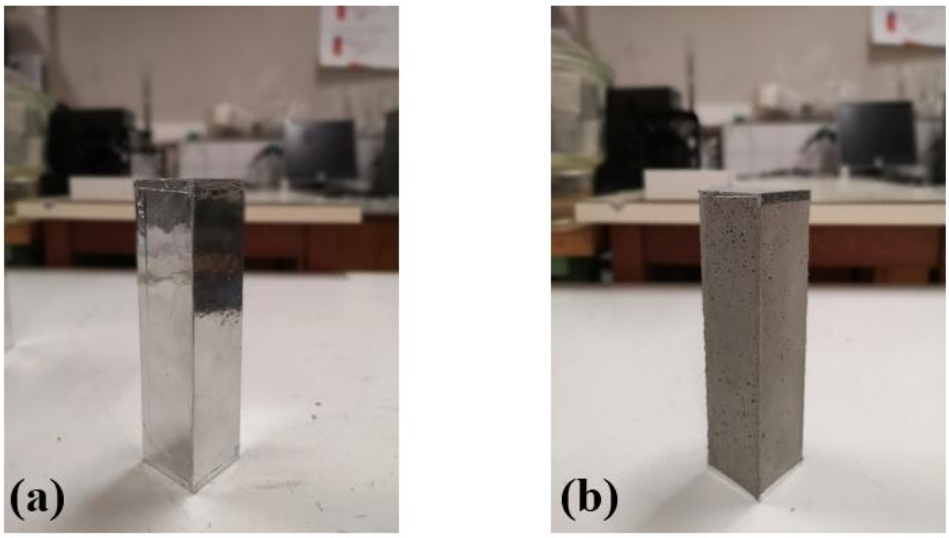


Figure. 3.11 Autogenous shrinkage specimen (a) Drying shrinkage specimen (b)

3.4.3.4 Measurement of the internal relative humidity

To investigate the evolution of IRH within mortar during the early stages of hydration and curing, high-precision Rotronic sensors with a measurement accuracy of ±0.8% RH are employed. IRH is an indicator of moisture (Equation (1.1)) transport and self-desiccation, particularly in mixtures incorporating ICAs.

Freshly mixed mortar - one test for each mixture - is placed into a sealed humidity measurement chamber, which is partially filled to approximately 50% of its volume. This setup ensures sufficient air space for vapor equilibrium and accurate humidity detection while minimizing moisture exchange with the external environment. The chamber is then sealed to maintain internal conditions.



Figure 3.12 RH measurement

Continuous monitoring is conducted over a 28-day period at 20°C. During the first 7 days—when hydration reactions are most active and moisture gradients evolve rapidly— IRH readings are recorded hourly to capture transient fluctuations. After this initial phase, the measurement frequency is reduced to once every 7 days to reflect the slower changes that characterize the later stages of curing. This extended observation period allows for a comprehensive assessment of the mortar's IRH behavior, from the fresh state to a mature microstructure.

3.4.4 Healing process

To comprehensively evaluate the self-healing capacity of the mixtures, WF test is conducted, providing a three-dimensional assessment of crack healing. The methodology follows the procedure validated in the European Round Robin Test (RRT) under the SARCOS COST action (https://www.sarcos.eng.cam.ac.uk), which aimed to standardize self-healing evaluation techniques in cementitious materials. This approach has been successfully implemented to monitor the healing process in various studies [6, 17]. Two cylindrical specimens (Φ11×H20 cm) are prepared for each composition. After demolding, they are stored in a controlled humid chamber at 95±5% RH and 20°C until reaching a cracking age of 28 days.

For mixtures incorporating MgO-coated ICAs, the coating was prepared by mixing MgO powder with water at a 1:1 mass ratio. The resulting paste was applied to the ICA surface using a mechanical mixer to ensure uniform coverage, after which the coated aggregates were stored at 20 ± 2 °C and 50 ± 10% RH for 24 h to allow complete setting of the coating layer.

Three days before testing (at 25 days), each specimen is sectioned into three disks (Φ11×H5 cm). At 28 days, pre-cracking is induced using a splitting test, ensuring a CW of 0.2 ± 0.05 mm at a controlled loading rate of 0.05 mm/min, with visual monitoring (Figure 3.13(a,b)). The CW is then measured on both disk surfaces using a reflective microscope at multiple points immediately after cracking (0D), and after 7 days (7D), 28 days (28D), and 90 days (90D) of curing (Figure 3.13(c)). The HR of CW can be calculated as:

$$HR(t) = \frac{CW_0 - CW_t}{CW_0} \times 100\% \quad (3.15)$$

Where W_0 (μm) denotes the initial CW (0D), and W_t (μm) represents the average CW at curing age t (d).

After crack measurement, the specimens undergo a specific curing procedure. They are stored at 20°C and 50% RH for 24 hours to ensure proper adhesion of PVC tubes (Φ_{inner} = 100 mm, H = 200 mm) to their upper face. Once adhesion is secured, they are further

dried at 20°C and 60% RH for 24 hours before the WF test.

For testing, the PVC tubes are filled with 1.55 liters of tap water. To monitor WF through the cracks, specimens are positioned on a support above a precision balance (100 mg accuracy) (Figure 3.14). The WF rate is recorded at 5, 10, 15, 20, 25, and 30 minutes, calculated in liters per minute (l/m), using three disks per composition. Additionally, the water level is monitored for 3 hours.

WF tests are conducted at key curing stages: 0D, 7D, 28D, and 90D. After WF testing, all disks are stored vertically in designated containers according to their mixture. Two different curing methods were employed. In the first method, the samples were placed in the humidity chamber (95±5% RH and 20°C) for standard curing. In the second method, the samples were first sealed in a plastic bag in the humidity chamber (95±5% RH and 20°C), as illustrated in Figure 3.15.

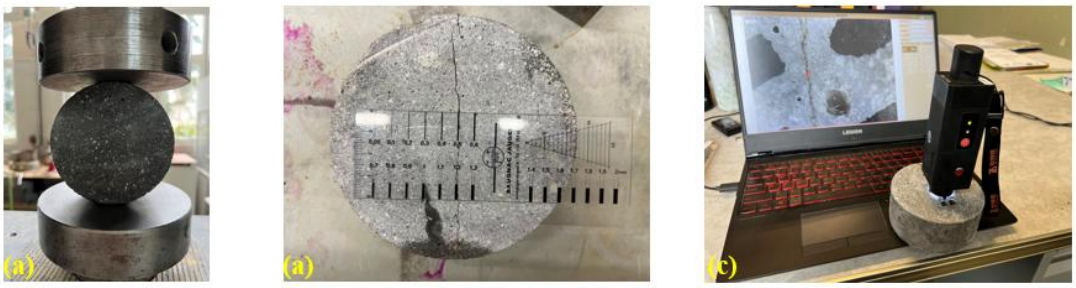


Figure. 3.13 Crack Induction (a) CW control (b) and measurement (c)



Figure. 3.14 Water Permeability test



Figure. 3.15 The second curing method

The HR is a key metric in this analysis and is calculated as per Equation 3.16.

$$HR(t) = \frac{W_{unhealed}(0D) - W_{healing}(t)}{W_{unhealed}(0D)} \times 100 \quad (3.16)$$

Where *HR(t)* represents the HR at time t in percentage (%),$W_{unhealed}$ *(0D)* the initial WF immediately after cracking at 0D in liters per minute (l/min), $W_{healing}$*(t)* the WF after a specific healing period denoted as 't' in liters per minute (l/min).

Before conducting the water permeability test, the specimens were pre-cracked to obtain a target CW of less than 0.3 mm. However, the specimens used in this study tended to exhibit brittle failure during the splitting test, making it challenging to achieve the desired CW. To address this issue, polypropylene (PP) fibers with an aspect ratio of 300–600 were incorporated into the mixture (Figure 3.16) to enhance the ductility of the specimens, thereby slowing the propagation of cracks and facilitating the control of CW within the target range. A fiber dosage of 0.12% by volume was adopted in this study.



Figure. 3.16 Polypropylene fiber

3.5 Summary

In this chapter, a comprehensive and innovative methodology was developed for the design, preparation, and evaluation of mortar mixtures incorporating various ICAs. The formulation strategies ensured consistency across different mixtures by controlling both effective and total water-to-binder ratios, thereby enabling meaningful comparisons. All experimental procedures—including mixing, curing, mechanical testing, microstructural analysis, and shrinkage measurement—were carried out under standardized and tightly controlled conditions to ensure data reliability and reproducibility.

A distinctive feature of this work is the integration of macro- and meso-scale analyses within a single experimental framework. TGA was used for detailed hydration analysis, while shrinkage behavior was monitored through an original combination of early-age and long-term methods: the shrinkage cone and corrugated tube tests (for mixtures related to biochar) enabled high-resolution tracking of autogenous deformation from the earliest hours, whereas the prism method, conducted in accordance with EN 12617-4, quantified long-term shrinkage.

The self-healing capacity was evaluated using the WF test, a method adapted from the SARCOS COST Round Robin Test and, in this study, applied to mixtures containing MgO-coated ICAs. This enabled a quantitative, time-resolved assessment of crack-sealing effectiveness by tracking the reduction in WF rate through through-thickness cracks across different curing regimes. The coordinated application of these complementary methods—ranging from microstructural characterization to macroscopic performance testing—constitutes a novel, multi-scale, and multi-parameter approach to understanding how internal curing strategies influence shrinkage mitigation, hydration development, and mechanical performance.

Chapter 4. Size and content effect of LWA and RCA as internal curing agent

Although LWA has been extensively studied and widely accepted as an effective ICA, the combined influence of its particle size and dosage on hydration kinetics, shrinkage behavior, and self-healing performance remains an area of active investigation. RCA, while also capable of providing internal curing due to its residual porosity and pre-saturated nature as shown in the chapter 2, is less studied in this regard [140] and often treated as a by-product rather than a functional curing material [139]. Existing studies often treat LWA and RCA separately, and few comparative analyses [109] consider both materials under a unified testing framework with controlled particle size ranges and replacement levels.

The primary objective of this chapter is to evaluate how variations in particle size and content of LWA and RCA affect their internal curing performance and self-healing capacity in cement-based materials – this last property will be analyzed in the chapter 6. This work aims to bridge the gap in the literature by systematically comparing these two types of porous aggregates under equivalent experimental conditions. Particular attention is paid to their influence on IRH, autogenous shrinkage, and recovery of mechanical and transport properties after cracking.

This chapter is organized into five main sections:

- Section 4.1 introduces the concept of Protected Paste Volume (PPV) and examines how varying the size and content of LWA and RCA affects the spatial distribution of internal curing agents and their capacity to protect the surrounding paste.
- Section 4.2 presents hydration and microstructural analyses, including hydration products, porosity, and ITZ characteristics, to clarify how particle size and content of ICA influence microstructure.

- Section 4.3 reports the mechanical properties—compressive strength, flexural strength, and dynamic modulus—of mortars with different LWA and RCA gradations and content, linking these properties to the observed microstructural changes.
- Section 4.4 details the shrinkage behavior from early-age autogenous deformation to autogenous, total, and drying shrinkages at long term, highlighting the role of internal curing in mitigating these deformations.
- Section 4.5 summarizes the key findings and compares the performance of LWA and RCA, identifying optimal particle size and dosage combinations for effective internal curing.

By exploring both materials under consistent test protocols, this chapter contributes to a deeper understanding of aggregate-based internal curing and provides practical guidance for material design in shrinkage-sensitive applications.

4.1 Protected paste volume ratio

To investigate how ICAs influence the spatial distribution of curing water in mortar, a numerical simulation was conducted to estimate the Protected Paste Volume (PPV)—defined as the volume of cement paste located within a specified distance from saturated internal curing particles. The simulation was carried out using the modeling tool provided by the Internal Curing Homepage of the National Institute of Standards and Technology (NIST) [151]. The model is based on the following key assumptions:

(1) Spherical particles: Aggregates (both normal-weight and ICAs) are modeled as spherical inclusions randomly packed in a two-dimensional cross-section ;

(2) Uniform distribution: Internal curing particles are assumed to be homogeneously dispersed within the mortar matrix ;

(3) Effective curing radius: Water from each saturated LWA or RCA particle is assumed to migrate radially outward and be fully effective within a fixed curing

radius (typically between 0.05 mm and 2.0 mm). In these numerical simulations, this curing distance is an input parameter. Calculations were performed for a range of assumed water migration distance of 0.05–2.0 mm to assess their effect on protected paste volume, with 1 mm highlighted as a reference value. This reference distance corresponds to the maximum effective range before capillary pores in the paste become discontinuous due to hydration, as suggested by the Powers model [99] and Bentz's protected paste approach [3]. While this study did not directly measure migration distance, the 1 mm assumption reflects literature consensus that water transfer from saturated LWA or RCA to paste is driven by capillary tension gradients—where smaller pores in the cement matrix exert stronger suction than the larger pores in ICAs—until equilibrium or pore discontinuity occurs.

(4) No overlap correction: Regions influenced by multiple particles are counted in total PPV without deduction for overlap.

For each assumed migration distance, the simulation generates a spatial map of curing influence and computes the corresponding PPV. The simulation results are visualized in Figures 4.1 and 4.2. In these figures, red particles represent normal-weight aggregates (sand), yellow particles indicate ICAs (LWA or RCA), and the surrounding paste is shaded from dark to light blue to represent distance from the curing particle surface (0.05 mm to 2.0 mm), which corresponds to the extent of the protected paste zone.".

Based on these assumptions, the protected volume of cement paste located within the defined curing distance of all internal curing particles is calculated. This section compares the internal curing efficiency of several particle size groups of LWA (LM (0.63–1.25 mm) and LT (0–2 mm)) and RCA (RF (0.315–0.63 mm), RM (0.63–1.25 mm) and RC (1.25–2.5 mm)), as well as two replacement levels (10% and 15%).

For each water migration distance, the protected volume ratio of cured cement paste is calculated as the ratio between the volume of protected paste V_p (m^3) and the total

volume of the cement paste V_t (m^3). The protected paste volume ratio, φ, is determined by summing all paste regions located within the assumed migration distance from any internal curing particle, based on a geometric analysis of their spatial distribution. The protected paste volume ratio φ (%) is then given by Equation 4.1 [151]:

$$\varphi = \frac{V_p}{V_t} \tag{4.1}$$

Tables 4.1 and 4.2, along with Figure 4.3, present the protected paste volume (PPV) ratio of mortars incorporating various sizes and contents of LWA and RCA under different assumed water migration distances.

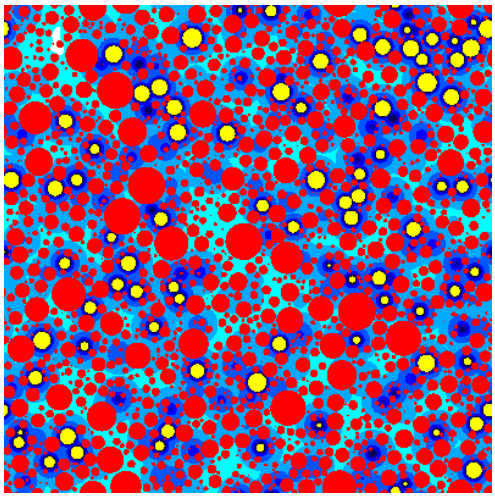
Table 4.1 Protected paste volume ratio: effect of LWA content and particle size

Migration distance of internal curing water (mm) – input data	Protected paste volume ratio (%)			
	LM10	LM15	LT10	LT15
0.05	3.32	4.96	2.17	4.13
0.10	7.02	10.45	4.49	8.54
0.20	14.84	21.80	9.23	17.41
0.50	38.73	53.10	23.64	42.06
1.00	78.31	90.63	53.68	79.64
2.00	99.91	100.00	96.18	99.85

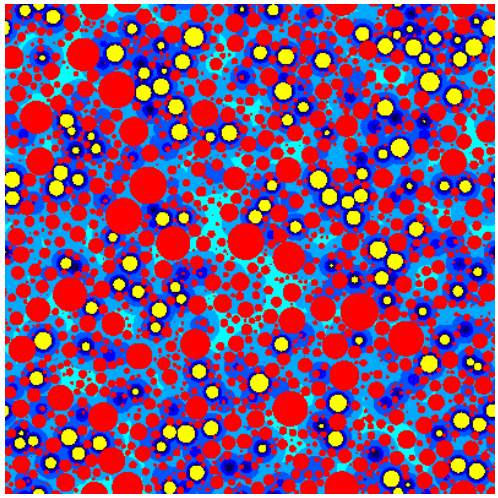
Table 4.2 Protected paste volume ratio: effect of RCA content and particle size

Migration distance of internal curing water (mm) – input data	Protected paste volume ratio (%)					
	RF10	RF15	RM10	RM15	RC10	RC15
0.05	6.99	10.40	3.32	4.96	1.49	2.26
0.10	15.59	22.91	7.02	10.45	3.03	4.61
0.20	34.58	48.44	14.84	21.80	6.06	9.17
0.50	81.15	92.84	38.73	53.10	14.83	22.10
1.00	99.91	99.99	78.31	90.63	33.70	47.78
2.00	100.00	100.00	99.91	100.00	77.93	90.46

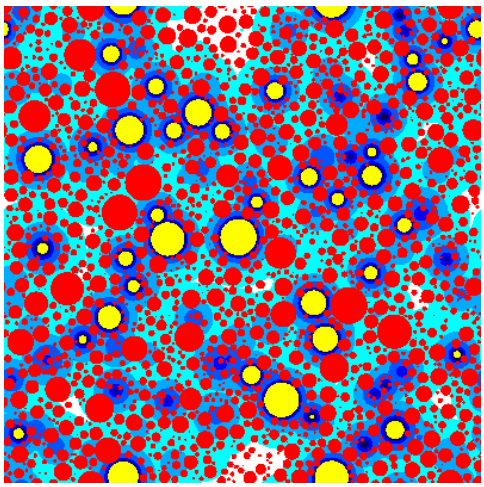
At a migration distance of 1 mm, increasing the internal curing agent (ICA) content from 10% to 15% consistently leads to higher PPV, with finer particles providing more extensive coverage due to their more uniform distribution.



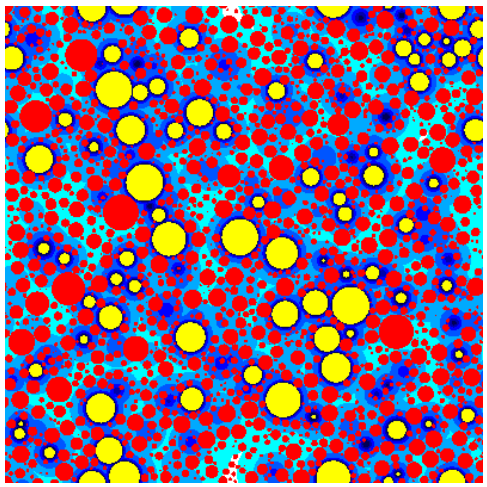
(a) LM (10% content)



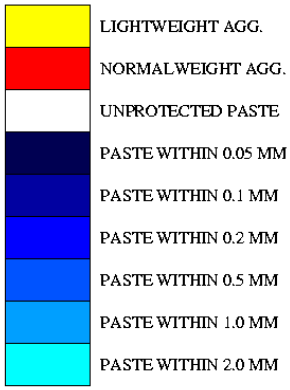
(b) LM (15% content)



(c) LT (10% content)

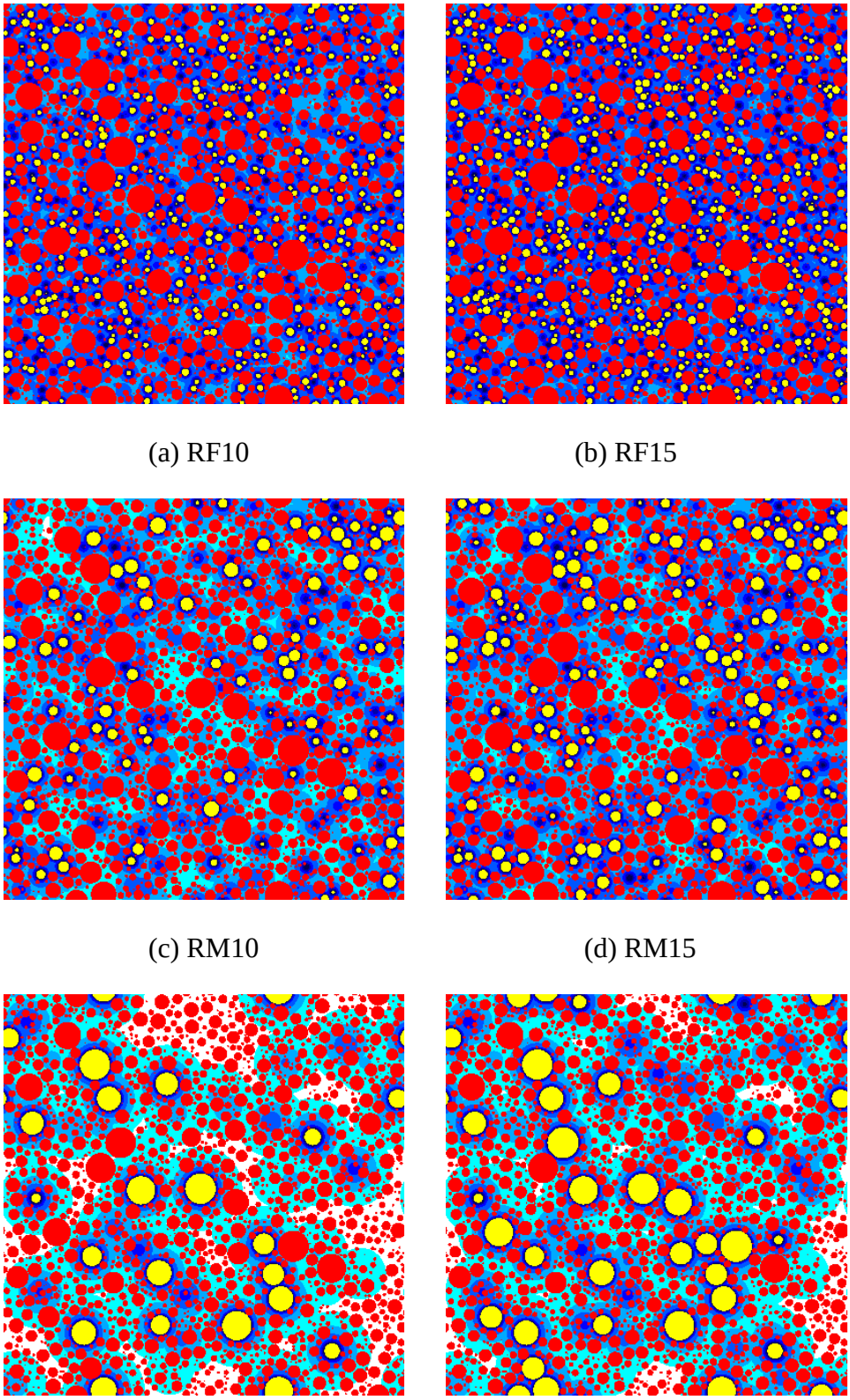


(d) LT (15% content)



(e) Color legend of aggregates and protected paste zones

Figure. 4.1 The distribution of sand, LWA and free water



(a) RF10 (b) RF15

(c) RM10 (d) RM15

(e) RC10 (f) RC15

Figure.4.2 The distribution of sand, RCA (in yellow) and free water— Color legend is similar to that given in Figure 4.1(e)

For LWA, the LM series shows higher PPV ratio than LT at equivalent content and migration distance (Figure 4.3) This is primarily because LT contains a higher proportion (~65%) of coarse particles (>1.25 mm), while LM contains more particles in the 0.63–1.25 mm range, resulting in a more homogeneous spatial distribution. The impact of increasing content is more significant for LT than for LM: at 1 mm, LT15 achieves approximately 48% higher PPV ratio than LT10, whereas LM shows an improvement of around 16% (Table 4.1).

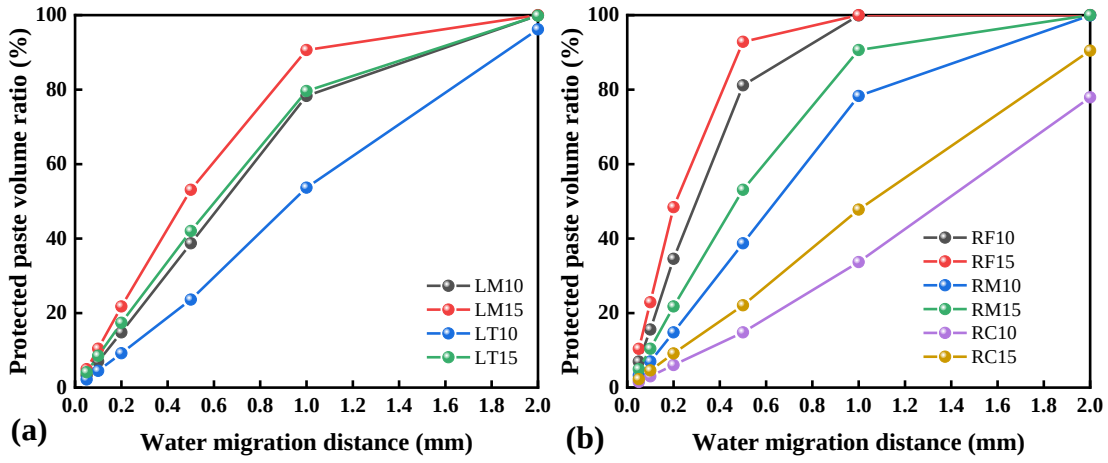


Figure. 4.3 Protected paste volume ratio as function of the water migration distance for LWA (a) and RCA (b)

For RCA, the trend RF > RM > RC remains consistent across all migration distances (Figure 4.3). The finest RCA (RF) can nearly fully protect the paste even at short migration distances, while the coarsest type (RC) covers only a limited volume. Increasing RCA content has a more pronounced effect for coarser particles (Table 4.2), which initially have lower coverage efficiency.

Under comparable geometric conditions, LWA generally provides slightly higher PPV ratio than RCA, owing to its more regular particle shape, higher porosity, and greater internal water content. These characteristics allow LWA to sustain water transport over longer distances, effectively giving it a larger curing radius compared to RCA. For an assumed migration distance of 2 mm, the majority of the cement paste can be cured by internal water alone.

4.2 Hydration and microstructure of mortars with LWA and RCA

This section is primarily dedicated to the analysis of the impact of LWA and RCA on cement hydration and its influence on the pore structure of the mixture.

4.2.1 Hydration products

To evaluate the hydration behavior of the mixtures, we conducted TGA analysis, resulting in the determination of DTG curves. Figures 4.4 and 4.5 shows the curves for the mixtures with LWA and RCA respectively over a period of 7 days and 28 days. . In each mixture, regardless of the effective water-to-binder ratio, an initial peak appears within the temperature range of 105 °C to 250 °C mainly related to the onset of C-S-H bond dissociation. A second peak associated with the dehydration of $Ca(OH)_2$ is located between 400°C and 550°C. A third peak emerges between 550°C and 850°C. This particular peak aligns with the process of decarbonation.

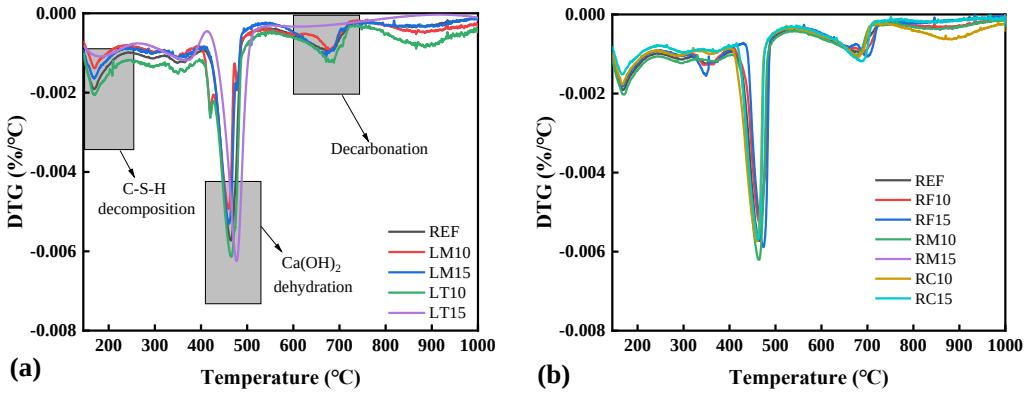


Figure. 4.4 DTG curves of mixtures with LWA (a) and RCA (b) at 7 days

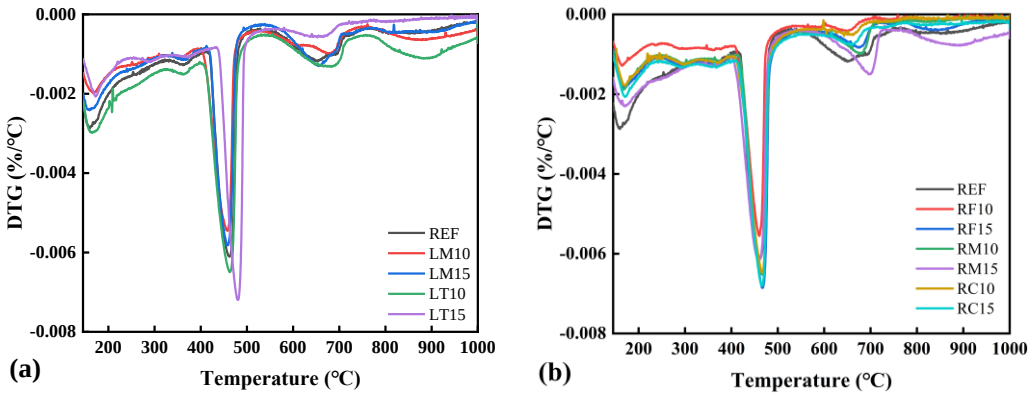


Figure. 4.5 DTG curves of mixtures with LWA (a) and RCA (b) at 28 days

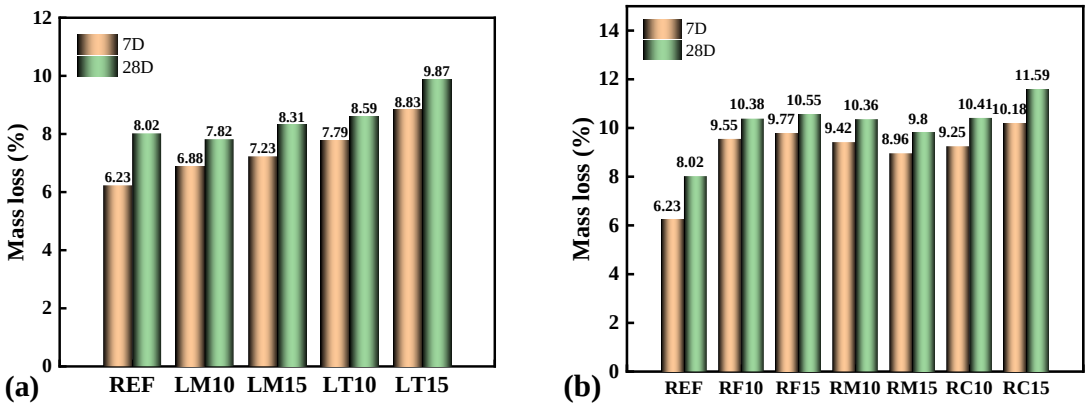


Figure. 4.6 Mass loss from 105 to 550°C at 7 days and 28 days for t mortars with LWA (a) and RCA (b)

Figure 4.6 presents the mass loss between 105 °C and 550 °C, which corresponds primarily to the dehydration of bound water in hydration products and the dehydroxylation of portlandite. For LWA mortars (Figure 4.6(a)), most mixtures exhibit a higher mass loss than REF at both 7 and 28 days, indicating a higher amount of hydration products formed as a result of internal curing. This interpretation is consistent with the higher portlandite contents measured in these mixtures at both ages (Figures 4.7(a) and 4.8(a)), which confirm that water stored in LWA was effectively released to sustain hydration.

For RCA mortars (Figure 4.6(b)), mass loss values are also consistently higher than in REF, with the largest differences observed at 28 days. This can be attributed to two synergistic effects: (i) the internal curing provided by RCA, which supports continued

hydration, and (ii) the residual hydrated cement paste within RCA particles, which contributes additional bound water upon heating. The higher portlandite contents in all RCA mixtures at 7 and 28 days (Figures 4.7(b) and 4.8(b)) further corroborate this interpretation. Overall, the mass loss data, when considered alongside phase composition results, clearly demonstrate that both LWA and RCA promote hydration beyond the level achieved in REF, with RCA mixtures showing a more pronounced increase at later ages due to the combined influence of internal curing and pre-existing hydrated phases.

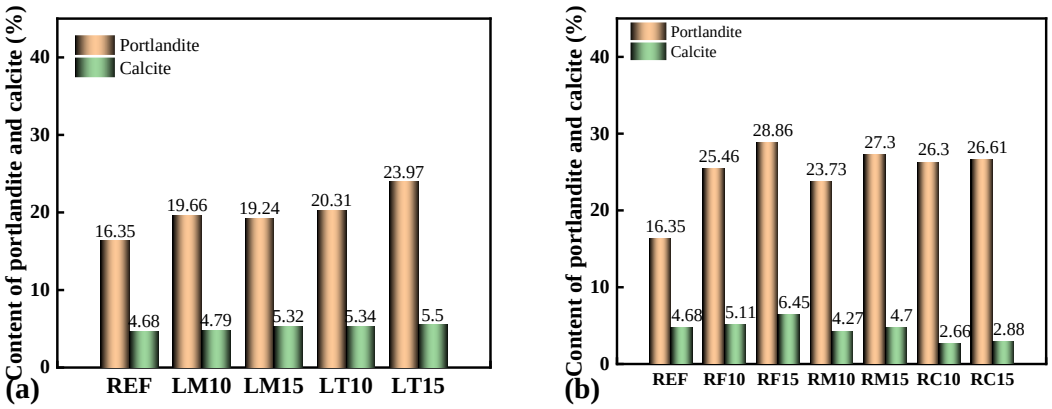


Figure. 4.7 Portlandite and calcite content at 7 days for the reference mortar, mortars with LWA (a) and mortar with RCA (b)

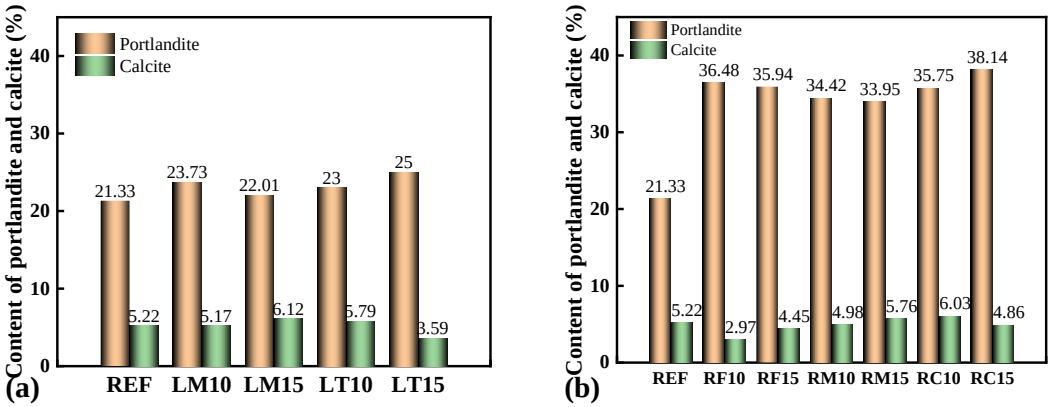


Figure. 4.8 Portlandite and calcite content at 28 days for the reference mortar, mortars with LWA (a) and mortar with RCA (b)

Figure 4.7(a) shows that incorporating LWA enhances early-age hydration. At 7 days, all LWA-modified mortars (LM10, LM15, LT10, LT15) exhibit higher portlandite

content than the reference (REF), indicating effective internal curing. LT15 has the highest portlandite content (23.97%), followed by LT10, LM15, and LM10. This suggests that both increasing LWA dosage and adjusting particle size promote early hydration, with LM particles in the smaller size range benefiting from better spatial distribution, and LT particles in the larger size range providing greater water retention.

From 7 to 28 days (Figure 4.8(a)), trends diverge: LM10 shows continued portlandite increase, while LM15 plateaus, implying either early hydration completion or that excess fine LWA may disrupt paste continuity. LT15 maintains its advantage, likely due to higher water storage capacity and slower water release, consistent with previous studies [34]. Calcite content remains quite similar across LWA mixtures, except for LT15, which exhibits a slight decrease. This reduction cannot be simply attributed to delayed carbonation, since LM15 does not exhibit the same trend. At present, the exact reason for this reduction is uncertain and may be related to combined effects of internal curing and microstructural development, which requires further investigation.

RCA also significantly promotes hydration as evidenced by the greater increase in portlandite content between 3 and 28 days, compared to the reference mix (REF) (Figures 4.7(b) and 4.8(b)). The extent of this improvement depends on the particle size distribution and the proportion of each fraction in the blend. Fine RCA (RF) contributes to a higher residual portlandite content (Figure 2.14) due to its greater reactivity and available surface for nucleation, whereas coarse RCA (RC) provides lower portlandite accumulation but improves internal water storage, thereby sustaining hydration over longer periods. Consequently, mixtures enriched with RF exhibit greater early-age portlandite gains, while those with larger fractions of RC may differ in long-term water release and hydration behavior. Calcite content slightly increases in mixtures with coarse RCA (e.g., RC10 and RC15), likely due to pre-existing carbonation in RCA.

4.2.2 Porosity

4.2.2.1 Total porosity

LWA and RCA affect the porosity of cement-based mixtures through two main mechanisms: their inherent internal porosity and the interfacial transition zones (ITZ) formed between aggregates and surrounding mortar. Figures 4.9 show the impact of different aggregate types and contents on water porosity at 28 days.

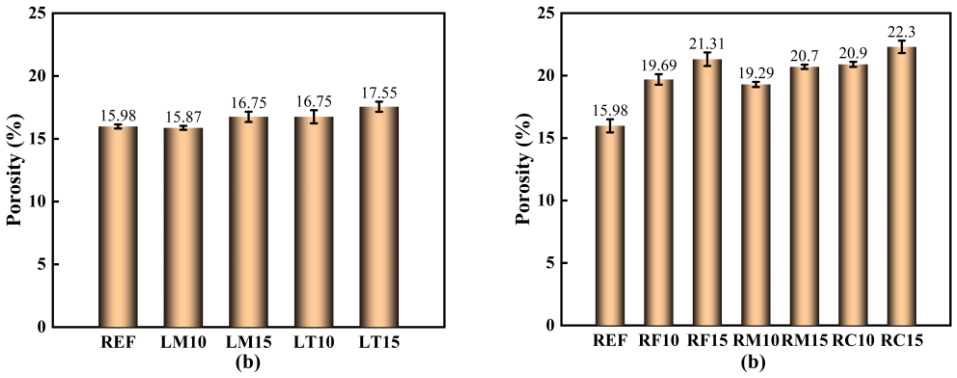


Figure. 4.9 Effect of LWA (a) and RCA (b) on the porosity of mortars at 28 days

Compared to the reference (REF) with a total water porosity of 15.98%, mixtures containing RCA exhibit significantly higher porosity. Specifically, RF15, RM15 and RC15 reach porosities of 21.31%, 20.70% and 22.30%, respectively. In contrast, LM15—containing LWA particles similar in size to RM—displays lower porosities of 16.93%. These results indicate that RCA contributes more substantially to increased porosity than LWA at comparable particle sizes and replacement levels. The elevated porosity in RCA mixtures is mainly due to adhered residual cement paste on RCA surfaces, which promotes interconnected pores between RCA and fresh mortar. This effect intensifies in RC mixtures, where larger particle sizes increase interface area and heterogeneity, further raising porosity. Conversely, LWA particles tend to have more stable, less permeable surfaces, resulting in weaker pore connectivity [35]. Mortars with larger particles (LT and RC) show higher porosity as well as the mortars with 15% of ICAs. Overall, aggregate type and content, especially RCA, have a more pronounced

effect on porosity than particle size alone.

4.2.2.2 ITZ

Figures 4.10 and 4.11 illustrate the interfacial microstructure of LWA mortar. The brightness histograms reveal a relatively broad distribution of pore grey values, reflecting a heterogeneous yet finely dispersed pore system. The porosity profile extends over a wider region, up to ~100 μm from the aggregate boundary, with detectable porosity fluctuating between 2–12%. Although pores appear near the aggregate surface, their concentration gradually attenuates with distance, suggesting the presence of a more gradual and uniform ITZ around LWA. This dispersed distribution pattern is indicative of a more stable microstructure that may enhance durability and promote effective internal curing.

By contrast, Figures 4.12 and 4.13 show the results for RCA mortar. The brightness histograms display a much narrower range of pore grey values, concentrated in low-intensity regions, which reflects the dominance of larger and more evident voids. The porosity distribution is confined to a thin interfacial zone of ~25 μm, where porosity levels can reach 20–25% at the aggregate boundary before decreasing sharply. Such a localized concentration of pores indicates the presence of a weaker and more porous ITZ, which is consistent with the fractured and heterogeneous nature of RCA.

(a) CLAHE (b) K-means (k=3) (c) LWA region

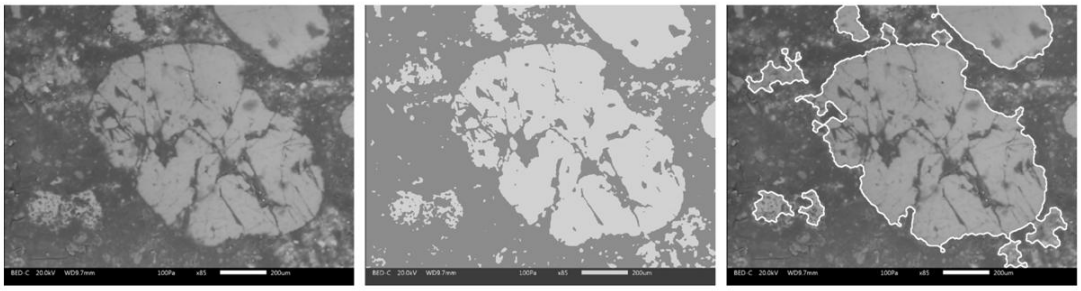


Figure. 4.10. Tri-panel segmentation of LWA mortar BSE image : enhanced image (a); K-means segmentation (b); boundary overlay (c)

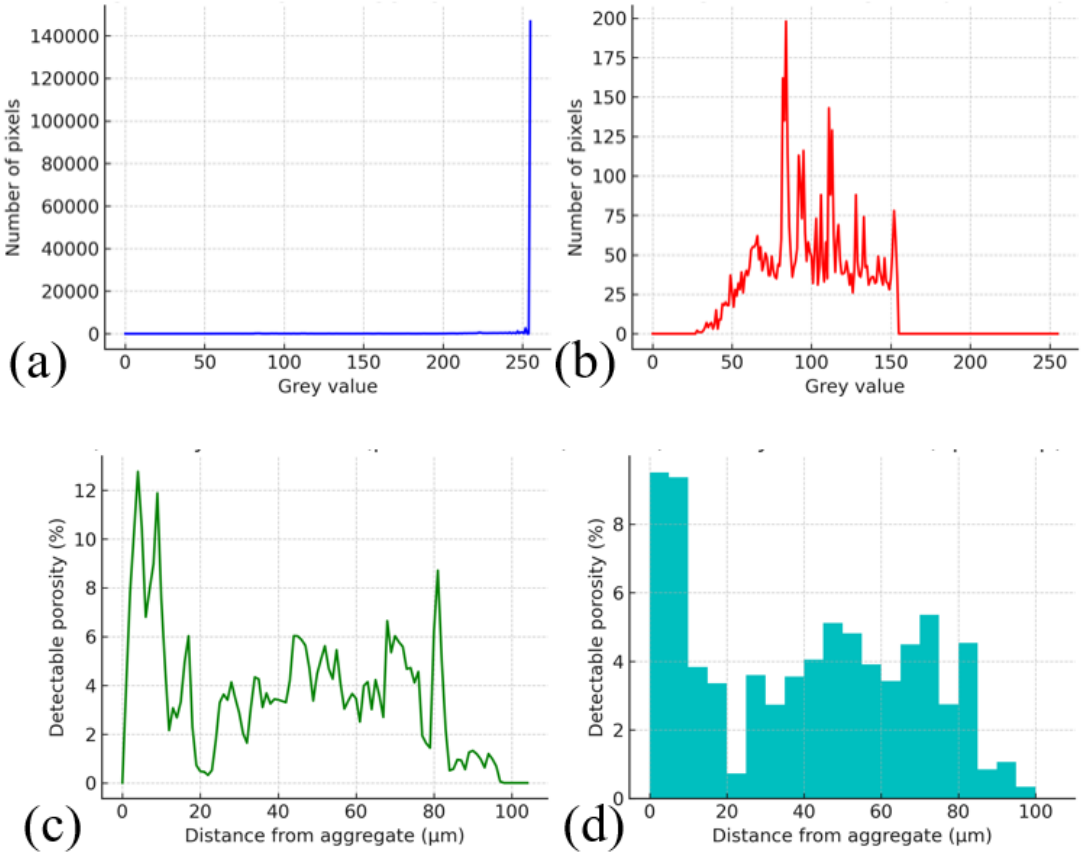


Figure. 4.11. Brightness histogram (aggregate excluded) (a); Brightness histogram (pores only) (b); Porosity distribution (pixel resolution) (c); Porosity distribution (5 μm strip) (d) for LWA mortar

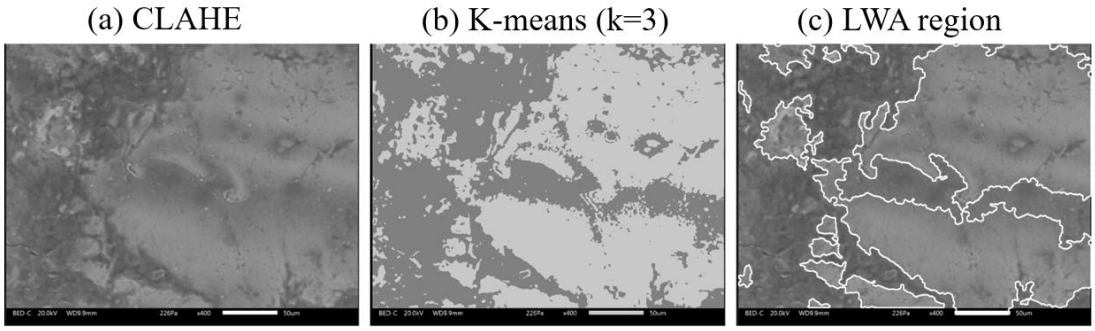


Figure. 4.12. Tri-panel segmentation of RCA mortar BSE image : enhanced image (a); K-means segmentation (b); boundary overlay (c)

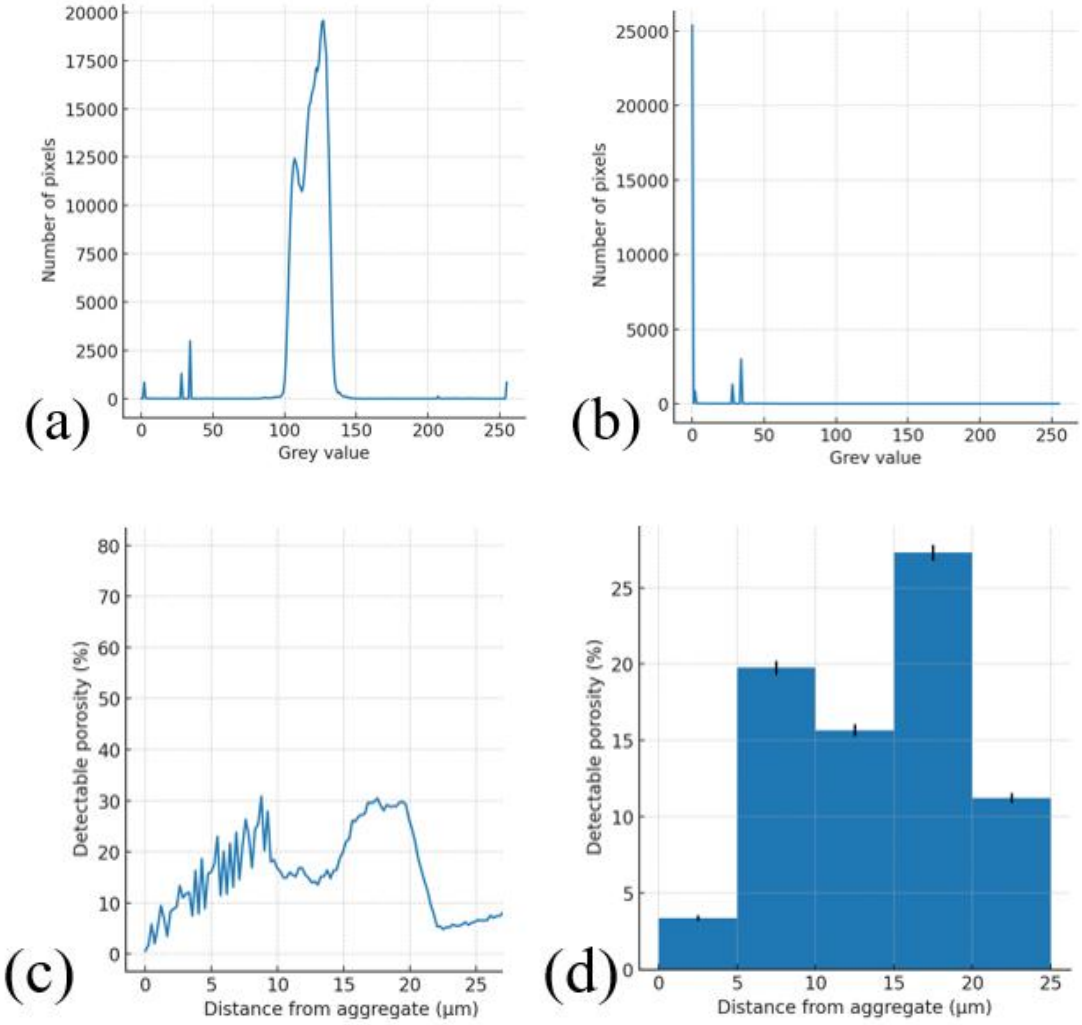


Figure. 4.13. Brightness histogram (aggregate excluded) (a); Brightness histogram (pores only) (b); Porosity distribution (pixel resolution) (c); Porosity distribution (5 μm strip) (d) for RCA mortar

Overall, comparison between LWA and RCA mortars highlights distinct differences in pore structure at the ITZ. LWA mortars exhibit a more gradual and dispersed porosity

gradient, whereas RCA mortars are characterized by highly porous interfacial regions. These microstructural features help explain the superior durability and internal curing capacity of LWA systems, in contrast to the compromised mechanical integrity and long-term performance often associated with RCA.

4.2.2.3 Water Desorption Curves

Figure 4.14 displays the saturation degree (S_w) as function of the relative humidity (R.H.) for all the studied mixtures (see Appendix A for the variations of S_w with R.H. and time). The degree of saturation remains higher for the Reference for all relative humidities. LM10 exhibits a similar saturation trend to the reference (Figure 4.14(a)). RM15 also follows this pattern up to a saturation degree of approximately 85%, after which its behavior diverges (Figure 4.14(b)). Mortars with coarser ICAs (LT, RC) undergo more significant desaturation, whereas finer RCA types (RF10, RM10) retain moisture more effectively, likely due to their shorter water migration paths and higher spatial coverage (Figure 4.3(b)). This highlights the critical influence of type of ICA and their particle size and porosity on drying behavior.

The desorption behavior shown in Figure 4.14(c) highlights the kinetic differences between LWA and RCA mortars. LWA mixtures (LM10 and LM15) exhibit a more pronounced and rapid reduction in saturation degree when RH decreases, indicating faster short-term water release. In contrast, RCA mixtures (RM10 and RM15) display a slower decline, reflecting more sustained moisture retention and a delayed response to external drying. This direct comparison confirms that LWA favors immediate release, while RCA provides a more gradual supply of internal water, which is beneficial for long-term humidity stabilization within the matrix.

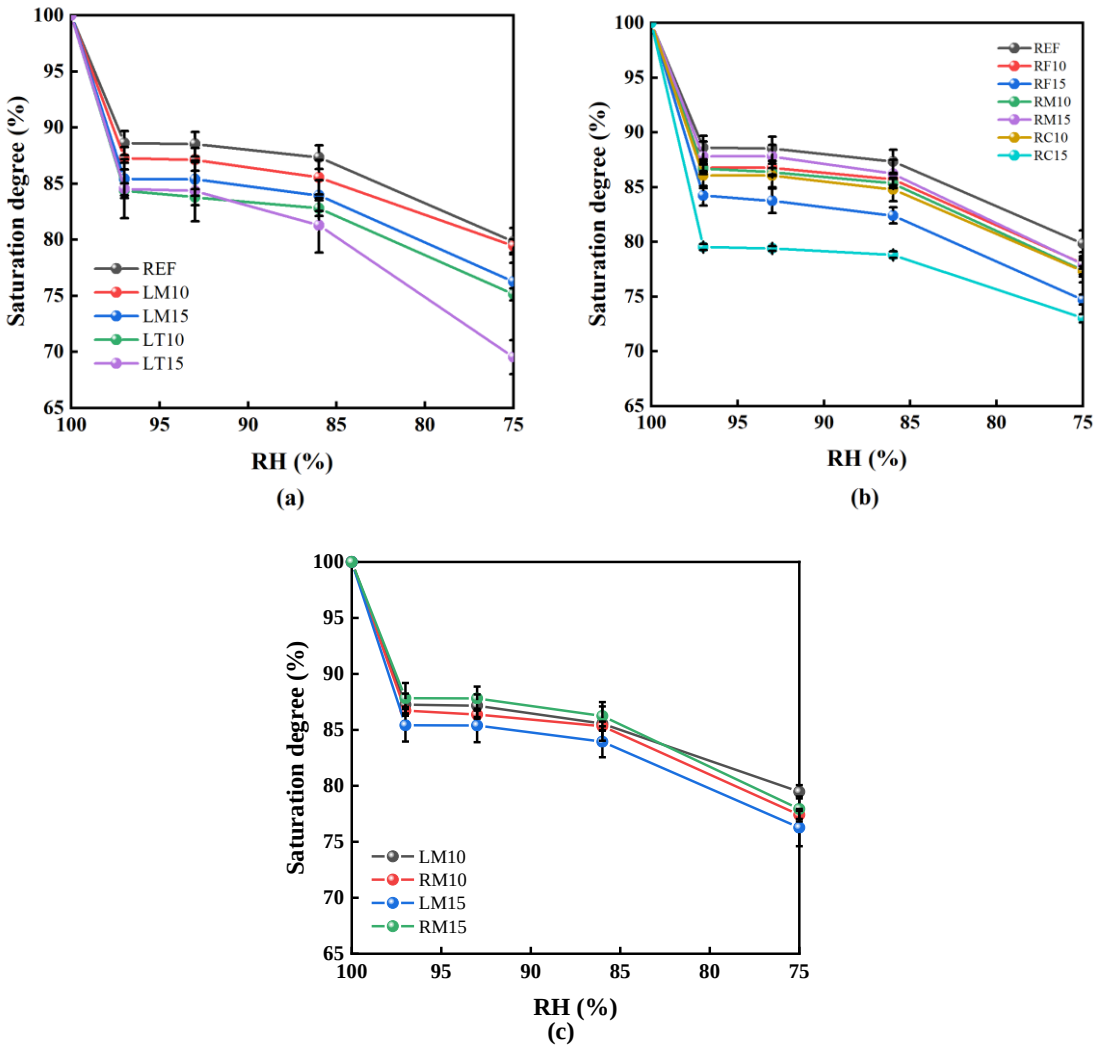


Figure. 4.14 Evolution of the Saturation degree with R.H. for the mortars with LWA (a); RCA (b); and the comparison of LM10, RM10,LM15 and RM15 (c)

4.3 Mechanical properties of mortars with LWA and RCA

One of the key objectives of this study is to identify the optimal content of ICAs—LWA and RCA—that can effectively mitigate shrinkage **without compromising mechanical performance**. This balance is crucial for practical applications, where dimensional stability and mechanical integrity must be achieved simultaneously.

Although LWA and RCA are known to promote internal curing by gradually releasing absorbed water and enhancing cement hydration, their inherent characteristics—such as high porosity and low elastic modulus—may adversely affect the strength of the

mixture [63]. Therefore, it is essential to evaluate how variations in **aggregate type, content, and particle size** influence the mechanical behavior of mortar, and to determine the point at which the benefits of internal curing outweigh the potential mechanical drawbacks.

This section investigates the compressive and flexural strength of mortars incorporating different sizes and dosages of LWA and RCA as well as their dynamic Young modulus. The results are analyzed in conjunction with porosity and hydration indicators to understand how internal curing efficiency relates to mechanical performance, and to guide the selection of optimal ICA configurations.

4.3.1 Compressive strength

Figures 4.15 and 4.16 present the compressive strength of mortars with LWA and RCA under both water and autogenous curing at 7 and 28 days. Under water curing, the presence of sufficient external moisture reduces the influence of internal curing; thus, strength losses mainly reflect the lower mechanical properties and higher porosity of the aggregates (Figure 4.9).

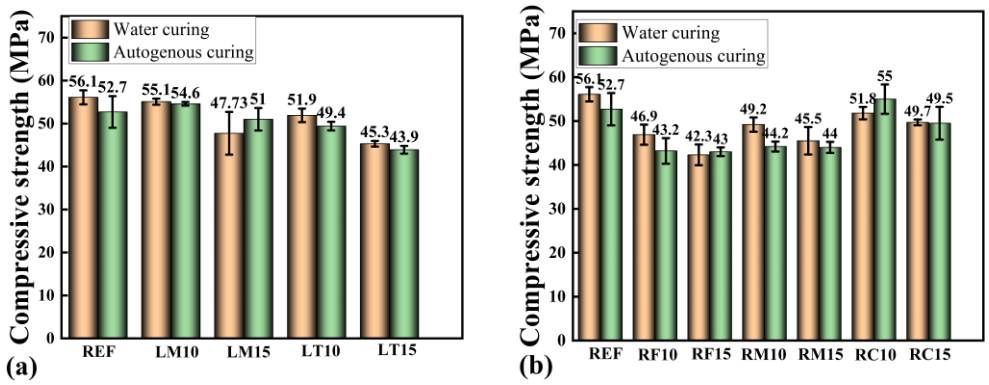


Figure. 4.15. Compressive strength of mortars at-7-day for LWA (a) and for RCA (b)

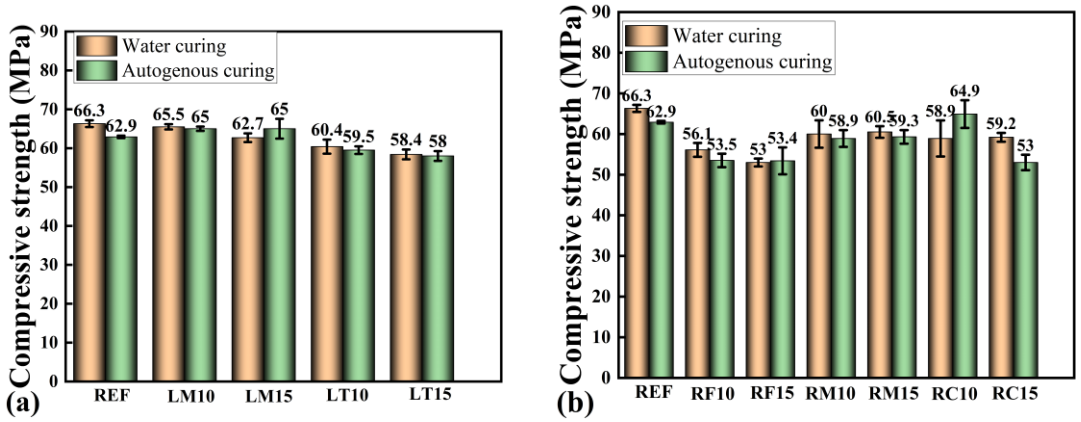


Figure. 4.16. Compressive strength of mortars at 28-day for LWA (a) and for RCA (b)

Under water curing, REF achieves 56.1 MPa at 7 days, while LM10 and LM15 show only slight reductions (55.1 MPa and 54.6 MPa, −1.8% and −2.7%). In contrast, mixtures with coarser LWA (LT10 and LT15) and finer RCA (RF10, RF15) display more pronounced strength decreases, up to −23%, reflecting the impact of particle size and porosity. This trend continues at 28 days: LM10 and LM15 nearly match REF (65.5 MPa and 65.0 MPa vs. 66.3 MPa), while LT and RCA mixtures show larger reductions, particularly fine RCA (RF15 at 53.4 MPa, −19.5%). It appears that smaller LWA sizes tend to better preserve compressive strength, while very fine particles of RCA reduce strength. The compressive strength also decreases with the content of ICAs.

Under sealed curing, the reference presents a reduction of its compressive strength for both studied ages. This reduction is more limited for mortars with LWA and RCA, except for RF10 and RM10 at 7 days, and for RF10 and RC15 at 28 days—In comparison (Figure 4.14(c)), LWA mixtures (LM10, LM15) exhibit a slightly quicker drop in saturation degree, reflecting their faster water release kinetics, whereas RCA mixtures (RM10, RM15) sustain higher saturation for longer, indicating steadier internal moisture retention. It supports the internal curing effectiveness of both LWA and RCA. Moreover, LM10 and LM15 present a superior compressive strength at 28 days than that of the reference as well as RC10.

In conclusion, while LWA and RCA reduce strength under water curing due to aggregate properties, their internal curing benefits are evident under sealed conditions. The particle size ranges 0.63-1.25 (LM and RM) as well as RC for 10% of RCA appear to be the most favorable, as they help minimize the negative effects of the intrinsic porosity of the internal curing agents while still maintaining a beneficial impact on hydration.

4.3.2 Flexural strength

The flexural strength results (Figure 4.17) closely correspond with the previously reported compressive strength data. Under water curing, both sets of results show that incorporating LWA and RCA generally reduces mechanical performance compared to the reference. This reduction is mainly attributed to the lower intrinsic strength of these aggregates—typical crushing strengths for LWA range from 4 to 12 MPa, and for RCA between 5 and 20 MPa depending on residual cement paste content, whereas natural sand usually exceeds 50 MPa [108]—as well as their higher porosity. In both compressive and flexural tests, mixtures containing finer RCA particles (RF series) and higher aggregate contents experience the greatest strength losses, while those with mid-sized particles (LM10, RM10) demonstrate smaller reductions. This underscores the advantageous role of the 0.63–1.25 mm particle size range in optimizing internal curing benefits while limiting the negative effects of aggregate porosity.

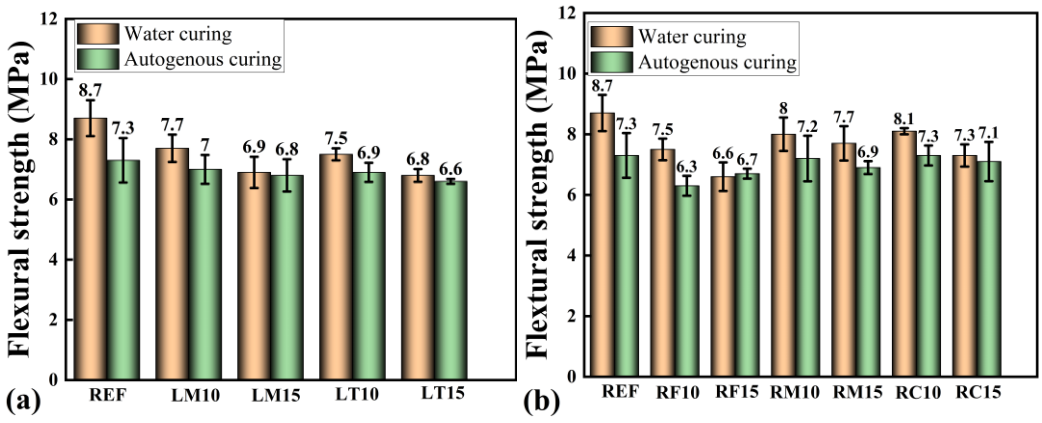


Figure. 4.17. Flexural strength at 7-days for LWA (a) and RCA (b) mortars

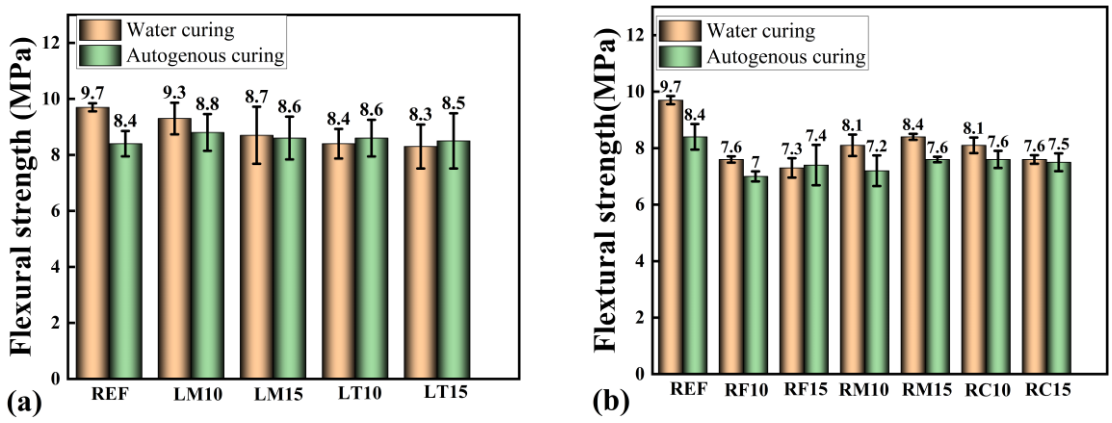


Figure. 4.18. Flexural strength at 28 days for LWA (a) and RCA (b) mortars

However, differences emerge in the degree of strength recovery under autogenous curing. No RCA mixture exceeds the strength of the reference. At 7 days, similar values are observed for the following compositions: RM10, RC10 and RC15. A different behavior characterizes LWA mortars. At 28 days, all the LWA mortars present a similar or superior value of flexural strength than the reference under the same curing. This difference of behavior between LWA and RCA mortars is directly related to the ITZ and its presence in RCA affecting directly the tensile and bending strength of the mortars. This reflects the higher sensitivity of flexural performance to ITZ quality and microstructural defects, compared to compressive strength, which relies more on bulk matrix densification and hydration.

Overall, both strength assessments confirm that internal curing enhances hydration and mitigates strength losses in the absence of external moisture, with the particle size range of 0.63–1.25 mm (LM and RM) as well as RC for 10% of RCA, emerging as optimal for limiting the negative impact of aggregate porosity while maintaining effective internal curing. The results underscore the need to consider aggregate type, size, and content carefully, especially when targeting improved flexural performance in low-moisture curing conditions.

4.3.3 Dynamic modulus

Figure 4.19 shows the dynamic modulus of mortars with LWA and RCA under water and autogenous curing at 7 and 28 days. The trends are consistent with those observed for compressive and flexural strengths, reflecting the combined effects of aggregate stiffness, porosity, and hydration.

Under water curing, dynamic modulus reductions relative to REF are mainly due to the high porosity of the ICAs, as observed in compressive and flexural strength results. At 7 days, LM10, LT10, and RM10 retain around 89–98% of REF, while higher ICA contents or finer RCA (RF10, RF15) drop to 84–89%. These trends match the early-age mechanical strength losses previously reported, where finer RCA and higher ICA content were the most penalizing. By 28 days, continued hydration narrows the gap, with LM10, LT10, and RM10 reaching 94–97% of REF, confirming that hydration progression partially offsets the porosity penalty.

A similar trend is observed under autogenous curing when comparing the results with the reference for the same curing condition. However, the dynamic modulus values are always lower under autogenous curing compared to those obtained under water curing. This can be explained by the measurement method, as compression waves travel more slowly in air than in water. In fact, water content in the porosity is reduced due to its consumption during hydration, leading to a larger gaseous phase. Nevertheless, this gap between the two curing conditions is smaller for mortars with RC, which can be attributed to the lower porosity of these aggregates and their lower residual cement paste content (resulting in fewer interfacial zones).

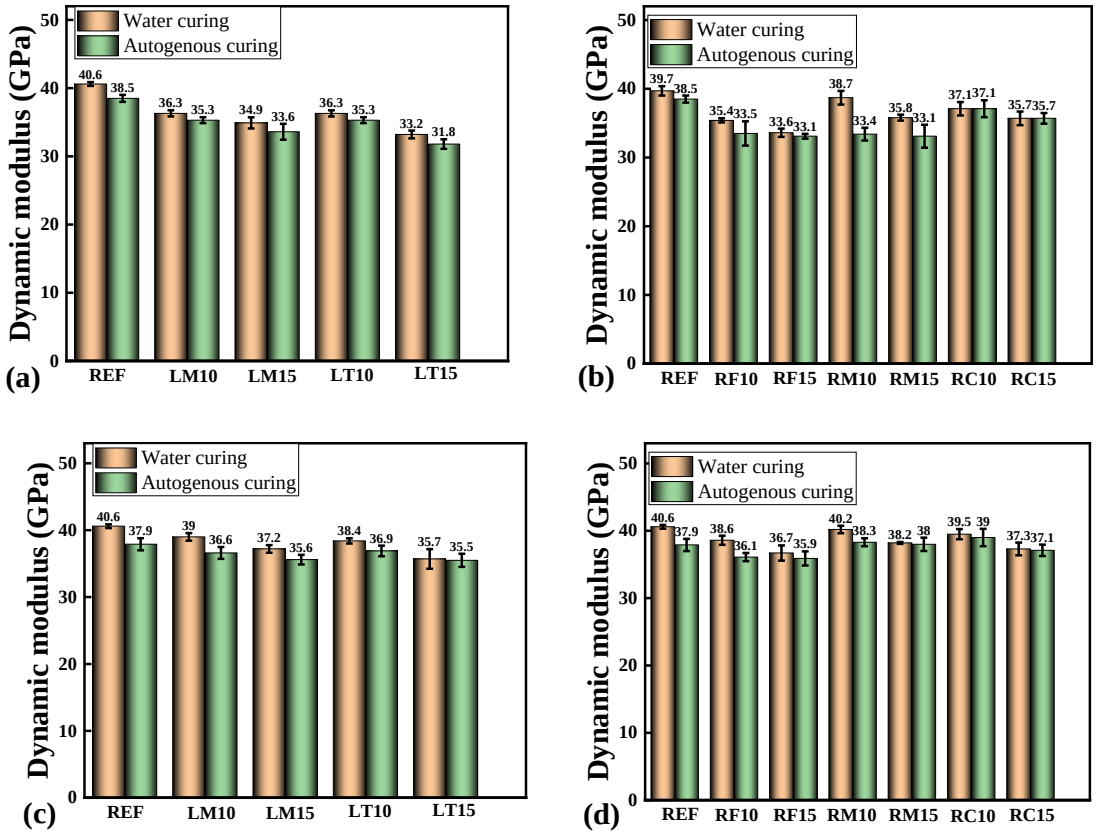


Figure. 4.19. Dynamic modulus at 7 days of LWA (a) and RCA (b) mortars, and at 28 days for LWA (c) and RCA (d) mortars

4.3.4 Summary

Across compressive, flexural, and dynamic modulus results, both LWA and RCA reduce performance under water curing due to their lower intrinsic strength and higher porosity, with finer RCA (RF) and higher ICA contents causing the largest losses. Mid-sized particles (0.63–1.25 mm, LM and RM) as well as RC for 10% of RCA consistently offer the best balance between limiting porosity effects and maintaining internal curing benefits. But RCA leads to a larger reduction in mechanical strength than LWA, due to its higher porosity [8] and the presence of adhered old cement paste Under autogenous curing, internal curing from both aggregate types mitigates these losses, with LWA often matching or exceeding reference strengths at 28 days, while RCA never surpasses it. Dynamic modulus values remain lower under autogenous

curing than under water curing, partly due to the measurement method and reduced pore water.

4.4 Autogenous Shrinkage of mortars with LWA and RCA

This section aims to evaluate how the incorporation of LWA and RCA influences the autogenous shrinkage of mortar, with the ultimate goal of identifying particle size ranges and replacement levels that can effectively mitigate self-induced volume deformation without compromising mechanical performance. Autogenous shrinkage is monitored using prism specimens under sealed curing conditions, and particular attention is given to the roles of aggregate type (LWA vs. RCA), particle size (e.g., LM, LT, RF, RM, RC), and content (10% vs. 15%). The correlation between autogenous shrinkage behavior and internal RH, porosity, and the spatial distribution of protected paste volume is also examined. By systematically comparing the effects of LWA and RCA under equivalent conditions, this section provides key insights into the efficiency of different porous aggregates in controlling self-desiccation-driven shrinkage.

4.4.1 Autogenous deformation before 1 day

Figure 4.20 illustrates the evolution of autogenous deformation in mortars incorporating various ICAs over the first 24 hours. The deformation is initialized at the initial setting (Table 4.3).

As shown in Figure 4.20(a), mortars with LWA exhibit larger measured autogenous deformation within the first 20 h than REF. Among the LWA series, LT15 reaches the highest value at 20 h (≈135.0 μm/m; Table 4.4), whereas LM10 shows the lowest (114.6 μm/m). The higher deformation recorded for LWA mixtures is instead attributed mainly to the lower effective modulus of the composite introduced by LWA; for a comparable pore-pressure history, a more compliant skeleton produces a larger strain ($\varepsilon \approx P / K_{eff}$). This relation follows directly from linear elastic theory, where the pore-pressure P is considered as the internal stress acting on the skeleton and K_eff is the effective bulk

modulus of the composite mortar [153]. In addition, the high porosity of LWA and the early ITZ development locally delay stiffness gain, further increasing the measured strain during the first hours after initial setting ("Day 0").

Table. 4.3. Setting time

Name	Initial setting time (h)	Final setting time (h)
REF	3.63	5.59
LM10	3.83	5.41
LM15	3.95	5.52
LT10	3.75	5.31
LT15	3.95	5.40
RF10	3.65	5.45
RF15	3.70	5.40
RM10	3.60	5.51
RM15	3.65	5.55
RC10	3.62	5.61
RC15	3.65	5.65

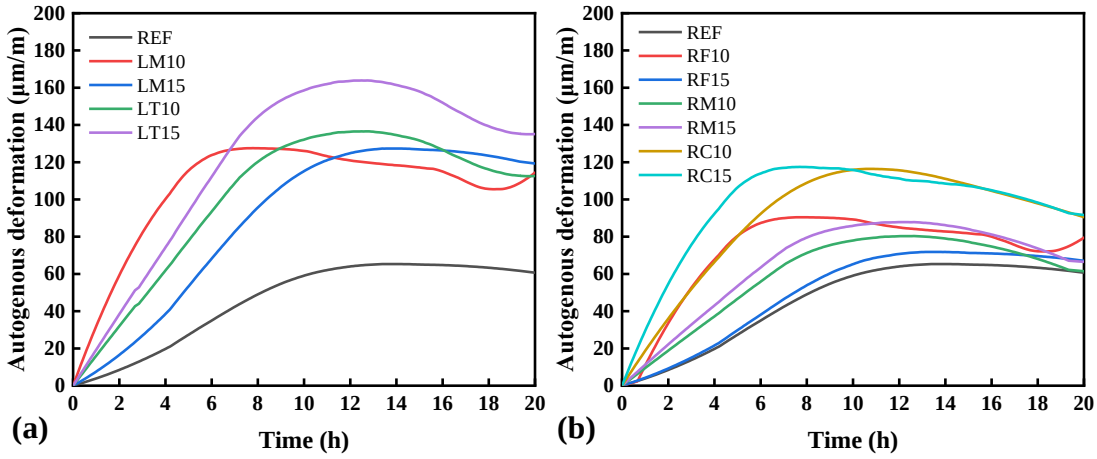


Figure. 4.20. Autogenous shrinkage before 1 day for mortar with LWA (a) and RCA (b) - "Day 0" refers to the initial setting

Figure 4.20(b) shows the RCA-modified mortars. Their deformations are generally lower than those of the LWA series (e.g., RM10 ≈ 61.5 μm/m and RC15 ≈ 91.7 μm/m at 20 h). Although the W_{total}/C of the RCA mixtures is lower than that of the LWA mixtures (implying less internal water available to reduce suction), RCA particles are stiffer and less compliant than LWA. The higher composite stiffness offsets the pore-

pressure effect and yields a smaller macroscopic strain over the same time window. Consequently, increasing RCA content from 10% to 15% does not lead to a proportional increase in deformation, because changes in moisture transport (slower in RCA) are counterbalanced by the concurrent increase in composite stiffness.

Table. 4.4. Autogenous shrinkage at 12h and 20h after initial setting time

Name	12h after initial setting time (μm/m)	20h after initial setting time (μm/m)
REF	64.10	60.69
LM10	120.84	114.62
LM15	124.99	119.28
LT10	136.51	112.61
LT15	163.81	135.02
RF10	84.88	79.70
RF15	70.81	67.06
RM10	80.30	61.47
RM15	87.85	66.50
RC10	115.56	90.39
RC15	111.13	91.65

In summary, the autogenous deformation within 20 h depends on the competition between (i) pore-pressure mitigation governed by internal water supply (IRH control) and (ii) the effective stiffness of the mortar governed by the ICA type and volume. LWA provides stronger internal curing but also lowers K_{eff}, resulting in larger measured strain than RCA in this very-early-age regime; RCA provides weaker internal curing yet maintains a higher K_{eff}, resulting in smaller strain. Therefore, W_total/C alone does not predict the early-age autogenous deformation; the governing balance is between the suction history and the composite mechanical compliance.

While Figure 4.20 illustrates the overall deformation within 1 day referenced to the initial setting, part of the measured strain still contains plastic deformation before the final setting. To isolate the true autogenous shrinkage, the curves were reinitialized at the final setting time, as shown in Figure 4.21.

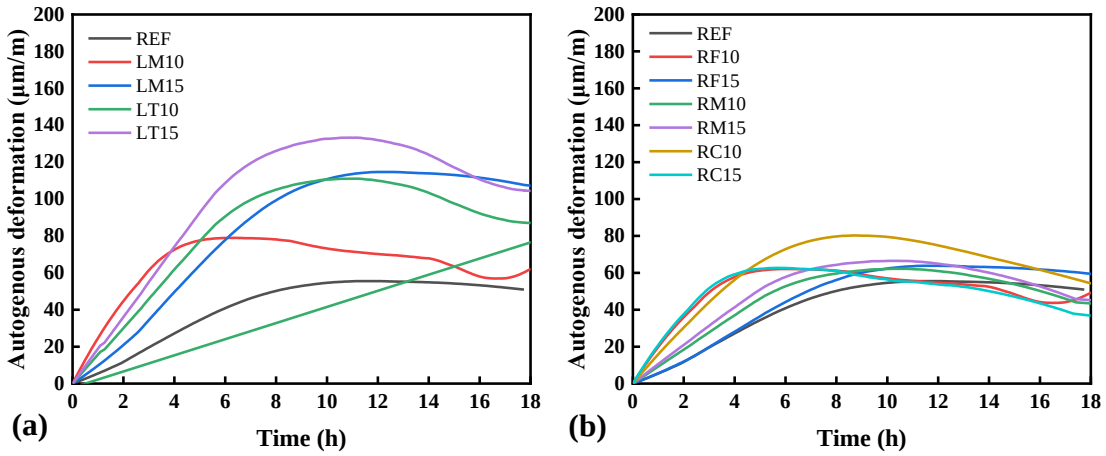


Figure. 4.21. Autogenous shrinkage before 1 day for mortar with LWA (a) and RCA (b) - "Day 0" refers to the final setting

Figure 4.21(a) shows that LWA mortars develop greater autogenous shrinkage than REF within the first 24 h, and the magnitude increases with both dosage and particle size. Among the LWA series, LT15 exhibits the largest shrinkage, whereas LM10 remains the lowest. The higher deformation in mixtures with larger or more abundant LWA can be attributed to the accelerated hydration occurring at very early ages. The additional internal water promotes faster reaction kinetics, and as the solid skeleton rapidly gains stiffness, a greater fraction of chemical shrinkage may be converted into measurable autogenous deformation.

Figure 4.21(b) indicates that RCA mortars exhibit more moderate shrinkage, with smaller differences between replacement levels. RC15 records slightly higher shrinkage than RC10 or RM10, yet the overall values remain well below those of LWA mixtures. This behavior is consistent with the lower absorption and slower release kinetics of RCA, which reduce the intensity of early-age self-desiccation.

Taken together, the comparison underscores that resetting to the final setting time does not change the overall trend but clarifies that the higher shrinkage associated with LWA primarily stems from its water release and pore structure, whereas RCA shows a less pronounced influence due to its lower porosity and more gradual water transport.

4.4.2 Effect of LWA from 1 day to long term

This section presents the evolution of autogenous shrinkage of mortars incorporating LWA. Figure 4.22(a) illustrates the evolution of autogenous shrinkage over the first 28 days. After one day of curing in a humidity chamber, specimens were demolded and stored under sealed conditions. All mixtures display a continuous increase in autogenous shrinkage, with the highest deformation rate occurring during the first 7 days. Thereafter, shrinkage progresses more slowly, particularly for REF and the LT series.

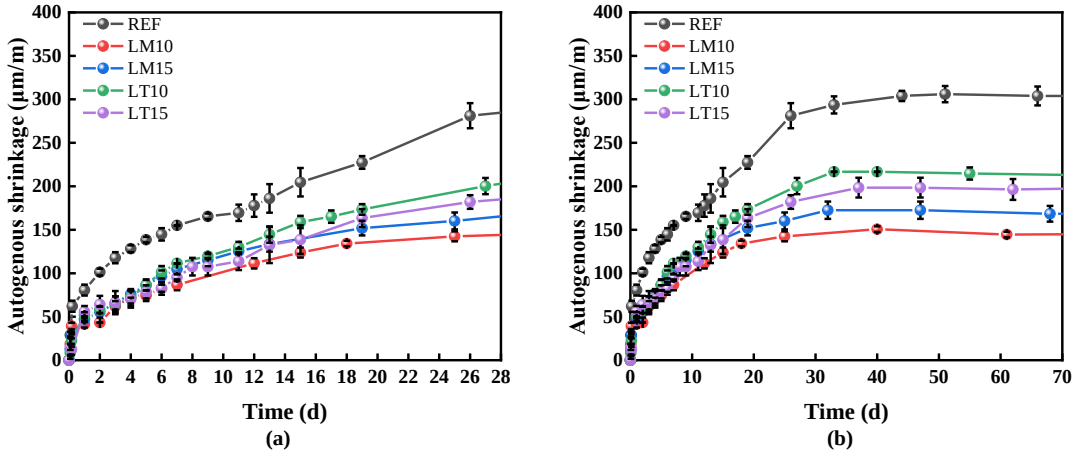


Figure. 4.22. Autogenous shrinkage of mortar with LWA during the first month (a) and at long-term (b) - "Day 0" refers to 1 day

At 7 days, LM10, LM15, LT10, and LT15 record shrinkage values of 86.7, 104.7, 111.5, and 95.1 μm/m—representing 55.9%, 67.6%, 71.9%, and 61.4% of REF, respectively. Their corresponding IRH (Figure 4.22) is higher than that of REF (84.4%), reaching 91.3% (LM10), 89.4% (LM15), 88.1% (LT10), and 89.1% (LT15). At 28 days, shrinkage increases to 144.1, 170.3, 201.2, and 182.3 μm/m (50.2%, 56.5%, 70.7%, and 64.3% of REF), while IRH decreases but remains above REF's value of 79.0%—namely 82.2% (LM10), 81.1% (LM15), 80.3% (LT10), and 80.8% (LT15). These results confirm that pre-saturated LWA effectively mitigates autogenous shrinkage, with the LM series showing the greatest reduction.

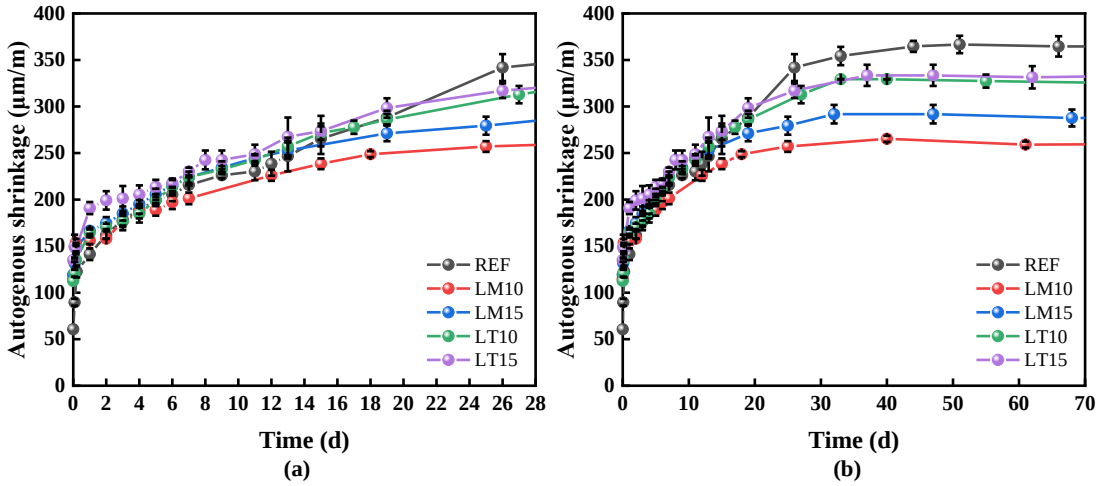


Figure. 4.23. Total autogenous shrinkage of mortar with LWA during the first month (a) and long-term (b), obtained by combining autogenous deformation (cone test, Day 0–1) with autogenous shrinkage after 1 day - "Day 0" refers to 1 day

Compared with the conventional curves in Figure 4.22, Figure 4.23 presents the total autogenous shrinkage, obtained by combining the autogenous deformation before setting measured during Day 0–1 using the shrinkage cone test with the autogenous shrinkage recorded after Day 1. In the short term—i.e., during Day 0–1 and the first few days thereafter—the reduction provided by LWA is not obvious in the total curves: the values of different mixtures remain close and the variations largely fall within the experimental scatter. This behavior suggests that the early deformation before setting, likely governed by paste consolidation and settlement under sealed conditions, plays a dominant role in the magnitude of total deformation and may temporarily mask the influence of internal curing.

Once the system enters the autogenous stage and capillary suction becomes the primary driving force (≈3–7 d onward), the curves begin to diverge: LWA mixtures exhibit a lower growth rate and maintain smaller cumulative values than REF. The relative ranking established at this stage persists in the long term (Figure 4.23(b)), with LM10 consistently showing the lowest total shrinkage, followed by LM15, LT10, and LT15. Therefore, including the pre-setting stage increases the absolute shrinkage values but compresses the contrast in the very-early-age regime; the beneficial effect of LWA—

particularly LM10—becomes evident after setting, as hydration progresses and internal curing helps sustain a higher IRH.

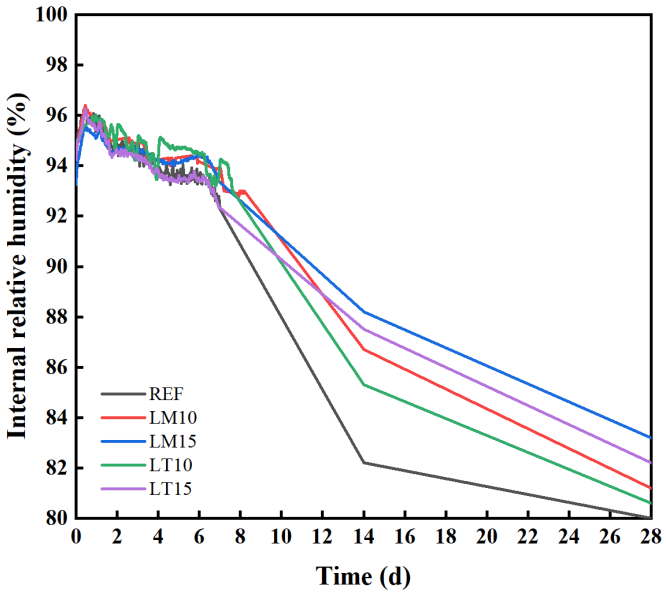
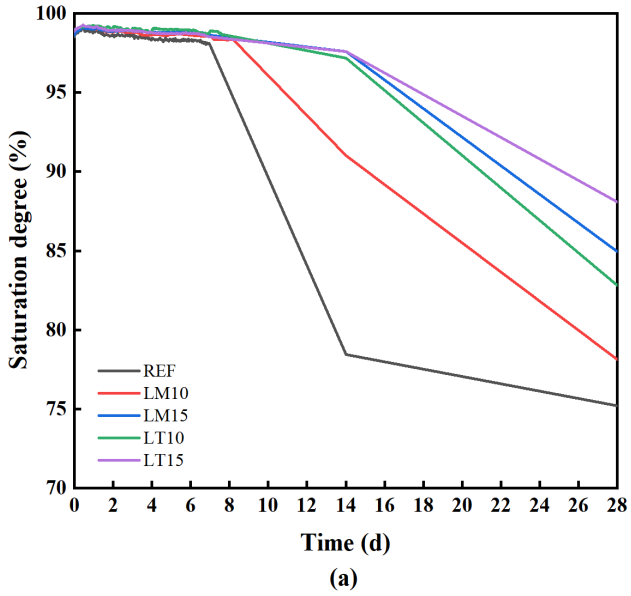


Figure. 4.24. IRH of mortar with LWA under autogenous condition



(a)

Figure. 4.25. Evolution of saturation degree in mortars with LWA under autogenous conditions

Mass loss at 70 days also supports the validity of the sealed curing conditions: REF loses 0.012% of mass, LM10 0.014%, LM15 0.007%, LT10 0.016%, and LT15 0.015%.

These small values confirm that autogenous conditions were effectively maintained throughout the test.

Figure 4.25 presents the evolution of saturation degree, obtained by using the data from Figure 4.24 and Figure 4.14(a). This transformation illustrates how variations in I.R.H during hydration influence pore saturation in cementitious matrices under sealed conditions. For the reference mixture, the curve reveals three distinct stages: (1) an initial stability (0–7 days) with a minimal change in saturation degree, (2) a rapid drop (7–13 days) and (3) a gradual reduction (13–28 days) due to ongoing water consumption. In contrast, mortars containing LWA display only the two first stages and their duration are more important. This reflects the continuous water release from LWA, which buffers self-desiccation and maintains higher saturation degrees.

The rate of saturation decrease follows the order: REF (fastest) > LM10 > LT10 ≈ LM15 > LT15 (slowest). This trend is directly related to the amount of water supplied by the internal curing agent, which is highest for LT15 and lowest for LM10 (Table 2.2 and 3.1). Accordingly, LT15 sustains saturation for the longest period, while REF, lacking any internal water supply, desaturates most rapidly.

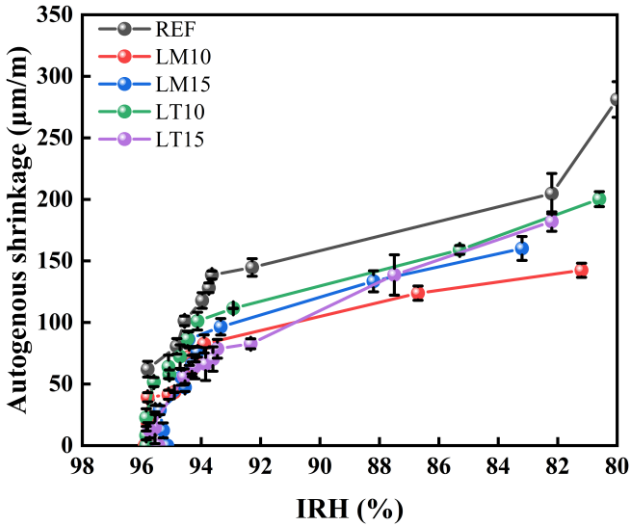


Figure. 4.26. Autogenous shrinkage as function of IRH

Figure 4.26 shows autogenous shrinkage versus IRH, revealing three distinct phases for REF but only two for LWA mortars. The initial phase (96–94% IRH) features a steep shrinkage increase, indicating high capillary stress sensitivity early in self-desiccation. Its slope is the steepest slope for REF (Table 4.5), and the lowest for LM10. Between 94% and 82%, shrinkage growth slows and the slope is lower (Table 4.5). Below 82% I.R.H, only REF shows an accelerated shrinkage rate, suggesting that additional mechanisms [106] beyond autogenous effects may be active in this low-humidity range. For the same change in IRH (Figure 4.24), REF exhibits the greatest shrinkage, followed by LT10, while LM10 shows the least shrinkage despite a faster desaturation kinetics (Figure 4.25).

Interestingly, LM15 shrinks more than LM10 despite higher LWA and water content brought by ICA. This is due to diminishing returns from increased LWA, as overlapping curing zones reduce effective water distribution, consistent with Bentz's findings on geometric saturation (Table 4.1, Figure 4.3). Previous studies (e.g., Bentz [151]) have similarly reported that beyond a certain threshold, increasing the amount of ICA yields only marginal benefits due to geometric saturation. Overall, the spatial distribution and size of LWA particles matter more than total water content. LM10 achieves an optimal balance, reducing 28-day shrinkage by nearly 50% compared to REF. These results align with previous studies demonstrating finer LWA's superior internal curing efficiency [145, 151].

In conclusion, autogenous shrinkage reduction is governed not only by preserving IRH through protected paste volume but also by the efficiency of water release and the mechanical response of the composite. As shown in Table 4.1, higher LWA contents (e.g., LM15 and LT15) provide superior protected paste volume ratios at short migration distances (LM15: 53.10% at 0.5 mm and 90.63% at 1.0 mm), which suggests a stronger capacity to maintain internal water coverage compared with LM10 (38.73% and 78.31%, respectively). However, despite its lower PPV, LM10 achieves the most effective shrinkage mitigation in practice. This superiority is attributed to its more

uniform particle distribution and balanced release kinetics, which enhance water availability in critical zones without excessively reducing the matrix stiffness. Therefore, while higher LWA contents enlarge the protected paste volume, an optimized dosage such as LM10 can deliver the best overall reduction in autogenous shrinkage by balancing spatial coverage, release dynamics, and mechanical integrity.

Table. 4.5 Slopes of Autogenous Shrinkage vs. IRH

Name	Slope 96-94% (μm/m·d⁻¹)	Slope 94-82% (μm/m·d⁻¹)
REF	-54.27	-6.56
LM10	-32.86	-5.73
LM15	-45.92	-6.28
LT10	-50.68	-6.23
LT15	-40.56	-9.89

4.4.3 Effect of RCA from 1 day to long term

Figure 4.27 show that all RCA particle sizes reduce autogenous shrinkage compared to REF. During the first week, RF10 exhibits shrinkage close to REF, while RM10 and RC10 register much lower values (130 μm/m and 95 μm/m at 7 days—83.8% and 61.2% of REF, respectively). These differences stem from variations in RCA pore structure [42].

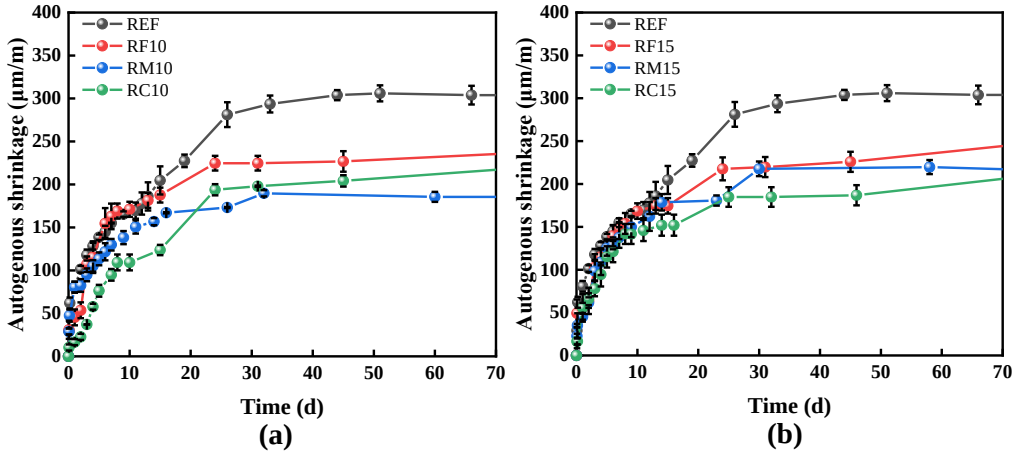


Figure. 4.27. The effect of RCA particle size on autogenous shrinkage with 10% RCA (a) and 15% RCA (b) - "Day 0" refers to 1 day

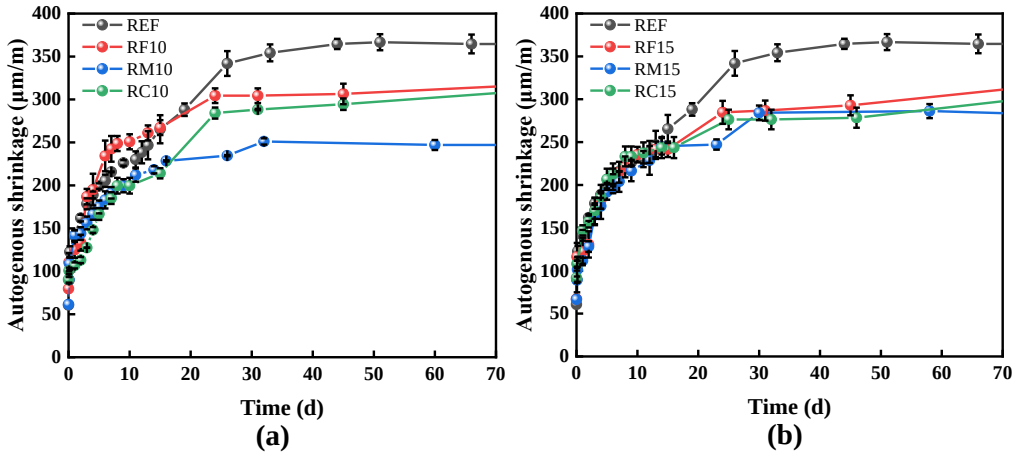


Figure. 4.28. The effect of RCA particle size on total autogenous shrinkage with 10% RCA (a) and 15% RCA (b), obtained by combining autogenous deformation (cone test, Day 0–1) with autogenous shrinkage after 1 day - "Day 0" refers to 1 day

Figure 4.28 presents the total autogenous shrinkage of mortars with different RCA particle sizes, obtained by combining the early deformation during Day 0–1 with the autogenous shrinkage measured after Day 1. Compared with the conventional results in Figure 4.27, the absolute shrinkage values are higher in the very early stage because the pre-setting deformation is included. However, the relative influence of RCA particle size remains similar. At 7 days, RC10 still exhibits the lowest shrinkage, followed by RM10 and RF10, while REF shows the highest value. The differences between mixtures become more distinct after 3–7 days, when capillary suction governs the deformation. In the long term (Figure 4.28(b)), the ranking established in the early autogenous stage is preserved: RC10 maintains the most effective reduction, RM10 provides a moderate effect, and RF10 remains closest to REF.

The evolution of IRH in mortars incorporating RCA is illustrated in Figure 4.30. All RCA mortars demonstrate a slower IRH reduction compared to REF as well as a higher saturation degree (Figure 4.31), indicating some internal curing effect. The evolution of IRH (Figure 4.30) reveals that, unlike LWA mortars—which display only two phases—RCA mixtures exhibit the same three distinct phases as REF. This behavior is directly linked to the lower additional water content supplied by RCA compared to LWA (Table 2.2, 2.3 and 3.1). As a result, RCA mortars cannot maintain a prolonged

high saturation degree (Figure 4.31), leading to an early onset of the second and third phases, similar to REF. Notice that the saturation degree decreases faster for the mortars with a higher content of RCA : RF15, RM15, RC15) (Figure 4.31).

It appears that shrinkage trends do not directly follow IRH preservation. As shown in Figures 4.29, RM and RC achieve greater shrinkage reduction than RF despite only moderate IRH retention. This behavior contrasts sharply with LWA systems, where finer gradations (e.g., LM10) achieved a greater shrinkage mitigation. One explanation lies in the reduced tortuosity and more favorable pore connectivity of larger RCA particles, which enables more timely water release to support early hydration. It is in agreement with the results presented at the Figure 2.17 showing a faster water release at 97% R.H. for RC. As shown by Figure 4.31, the saturation degree of RC10 still drops steadily, and the long-term IRH is not notably higher than RM or RF (Figure 4.30).

For the same change in IRH, RC mortars exhibit lower shrinkage (Figure 4.32), It is worth noting, however, that its behavior is quite similar to that of RM mortars, whereas RF mortars behave more like REF (Figure 4.32). It appears that the benefit of RC lies in early-stage water availability rather than sustained curing (Figure 4.32). For RCA, performance is driven more by pore structure and timing of water release than by IRH level alone.

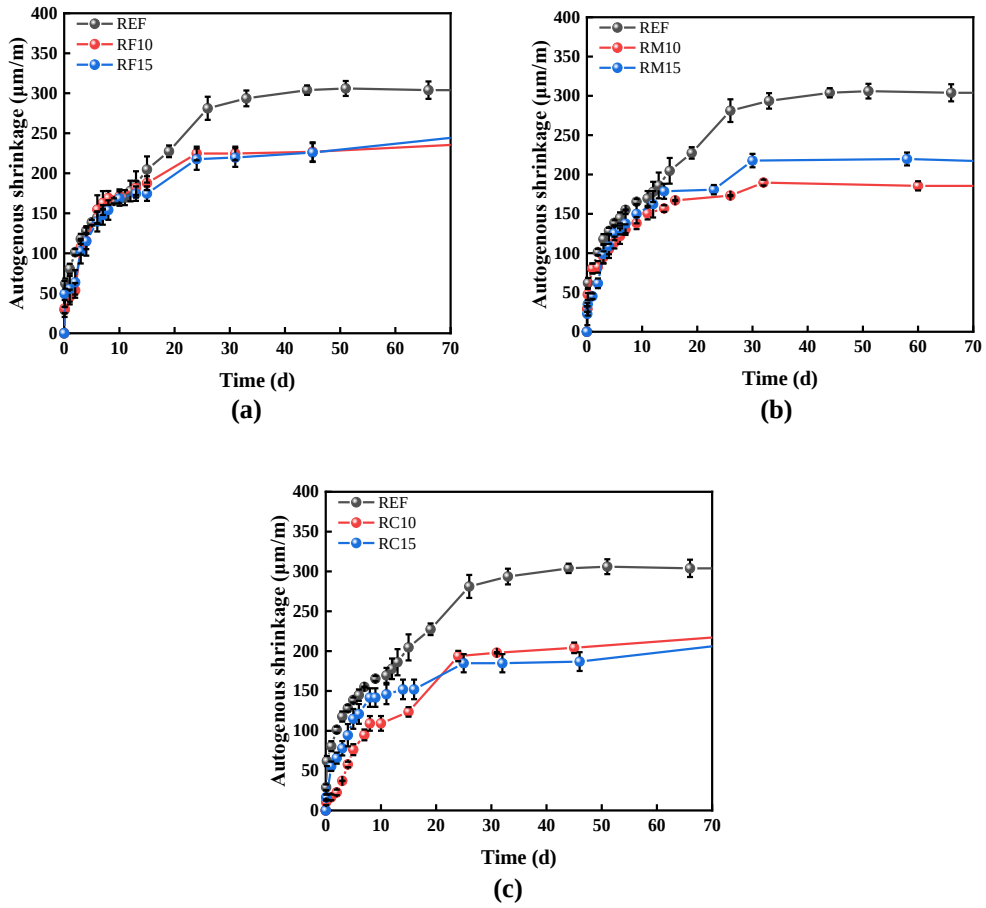


Figure. 4.29. The effect of RCA content on autogenous shrinkage for the Size of RCA: 0.315-0.63mm (a) 0.63-1.25mm (b) and 1.25-2.5mm (c) - "Day 0" refers to 1 day

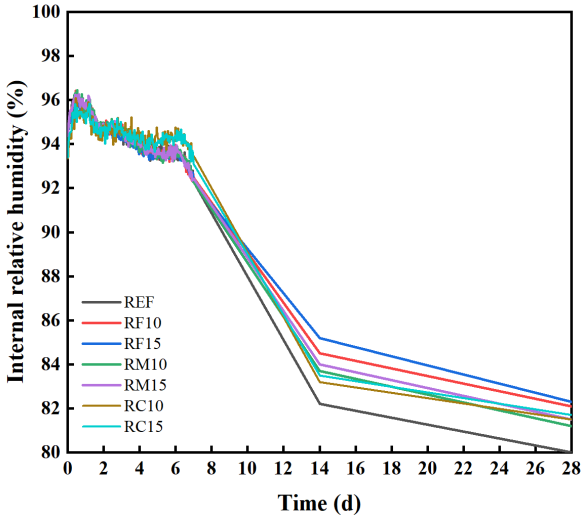


Figure. 4.30. IRH of mortar with RCA under autogenous condition

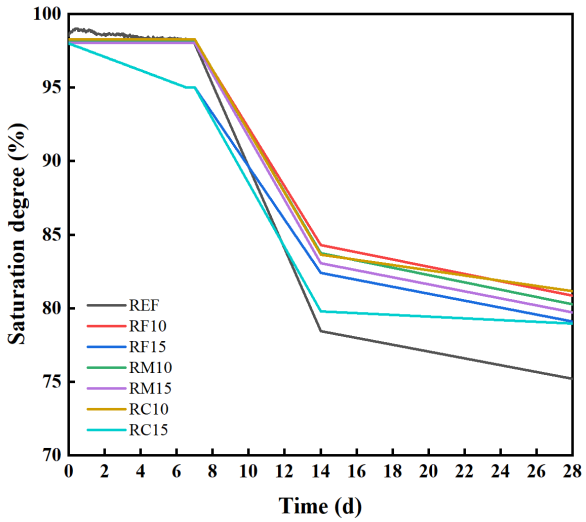


Figure. 4.31. Evolution of saturation degree in mortars with RCA under autogenous condition

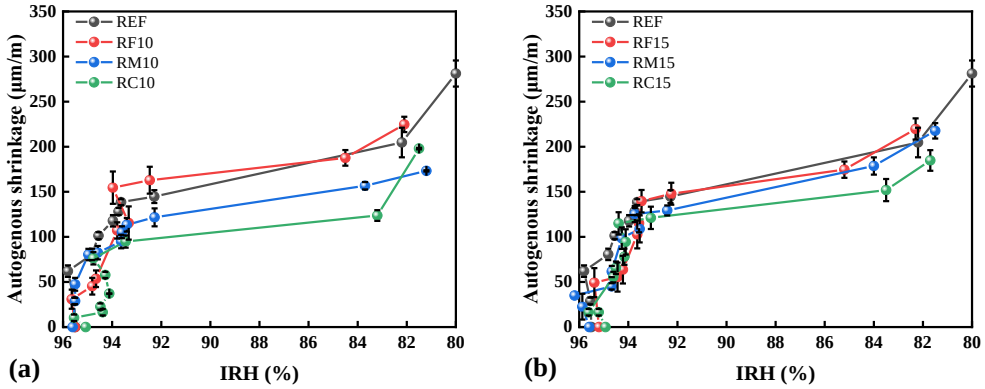


Figure. 4.32. Autogenous shrinkage as function of IRH for 10% RCA (a) and for 15% RCA (b)

Table. 4.6 Slopes of Autogenous Shrinkage vs. IRH

Name	Slope 96-94% (μm/m·d⁻¹)	Slope 94-82% (μm/m·d⁻¹)
REF	-54.27	-6.56
RF10	-37.14	-7.33
RF15	-30.81	-7.92
RM10	-59.60	-5.20
RM15	-48.98	-6.26
RC10	-42.73	-2.82
RC15	-54.03	-3.22

Globally, these results show that the RCA performance as an internal curing agent depends strongly on particle size and slightly on its content as summarized hereafter:

• Coarse RCA (RC) provides low shrinkage through rapid early water release but offers limited long-term curing. Increasing RC content slightly enhances shrinkage reduction by improving early release and spatial coverage (as supported by protected paste simulations);

• Fine RCA (RF) releases water too late, giving the highest shrinkage. Increasing its content from 10% to 15% has negligible effect because fine pores trap water [42], preventing timely curing;

• Medium RCA (RM) achieves the best balance—steady early release, reduced capillary tension, and uniform particle dispersion—leading to consistently low shrinkage. However, higher RM content slightly increases shrinkage due to hydration of residual old paste, which promotes self-desiccation.

For RCA, shrinkage mitigation is governed by the interplay between pore structure, water-release kinetics, and particle distribution, rather than by IRH retention or dosage alone. RCA mortars therefore benefit most from a medium gradation that optimizes both retention and release. This particle size range corresponds to that which provides the greatest autogenous shrinkage reduction with LWA, LM10.

4.4.4 Effect of broader particles size ranges for RCA

To improve the applicability of internal curing with RCA in real-world practice, this section investigates RCA types derived directly from sieve-based classification rather than narrowly controlled single-size particles. The aim is to examine whether these more representative particle groups—RFM, RFMC, and RMC—can still deliver effective shrinkage mitigation without additional processing or artificial blending.

Figure 4.33(a) illustrates the autogenous shrinkage behavior of mortars containing these RCA blends at 10% replacement. During the early hydration stage (first 7 days),

shrinkage values across all RCA mixtures closely track that of REF, with differences generally within 30 μm/m. This similarity indicates a minimal contribution from internal curing at early ages, which aligns with the relatively low water absorption capacity of RCA (5–6%, Table 2.3)—significantly less than that of lightweight aggregates (LWA). This limited water uptake delays the onset of effective internal curing due to slower water release. These results are quite similar that observed in the Figure 4.32, except for RC10.

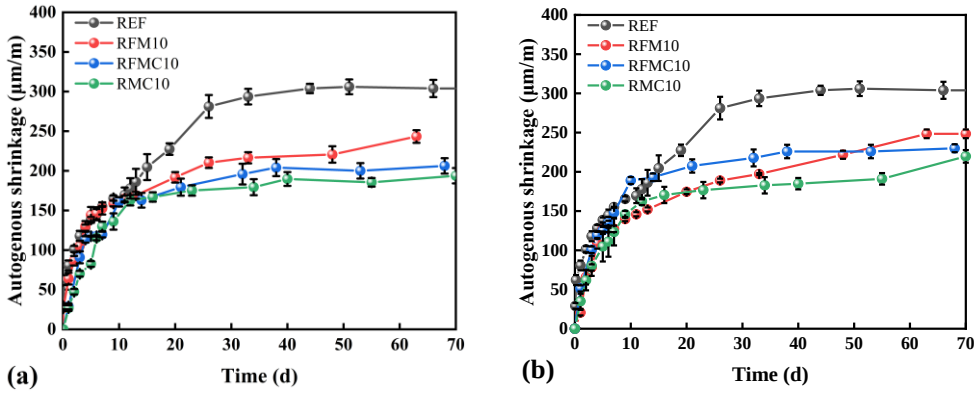


Figure. 4.33. The effect of RCA particle size on autogenous shrinkage: 10% RCA (a) 15% RCA (b) - "Day 0" refers to 1 day

Beyond 7 days, shrinkage in RCA mortars progressively diverges from REF. Between 7 and 28 days, mortars containing coarser RCA ratios (RMC) exhibit markedly slower shrinkage development than REF and the RF-rich mortars (RFM and RFMC). This trend reflects the initiation of internal water release from larger pores, supporting ongoing hydration and shrinkage mitigation.

Beyond 28 days, the differences among RCA blends become more pronounced: RMC10 (179.36 μm/m) achieves the greatest shrinkage reduction, followed by RFMC10 (195.89 μm/m), and then RFM10 (210.32 μm/m). This ranking correlates strongly with the content of fine RCA (RF, 0.315–0.63 mm) within each blend—RFM contains the highest RF proportion, while RMC excludes it altogether. When integrated with previous findings (Figure 4.29), these results reaffirm that fine RCA particles contribute least to internal curing, whereas medium (RM, 0.63–1.25 mm) and coarse

ratios (RC, 1.25–2.5 mm) perform comparably well, owing to their larger pore structures that facilitate more efficient and sustained water release.

Figure 4.33(b) extends this analysis to 15% RCA content, confirming the same pattern: REF > RFM15 > RFMC15 > RMC15 in terms of shrinkage magnitude. Although differences remain subtle, this consistency underscores the detrimental effect of increasing fine RCA content on curing efficiency, while the exclusion of fine particles (as in RMC) yields modest performance gains.

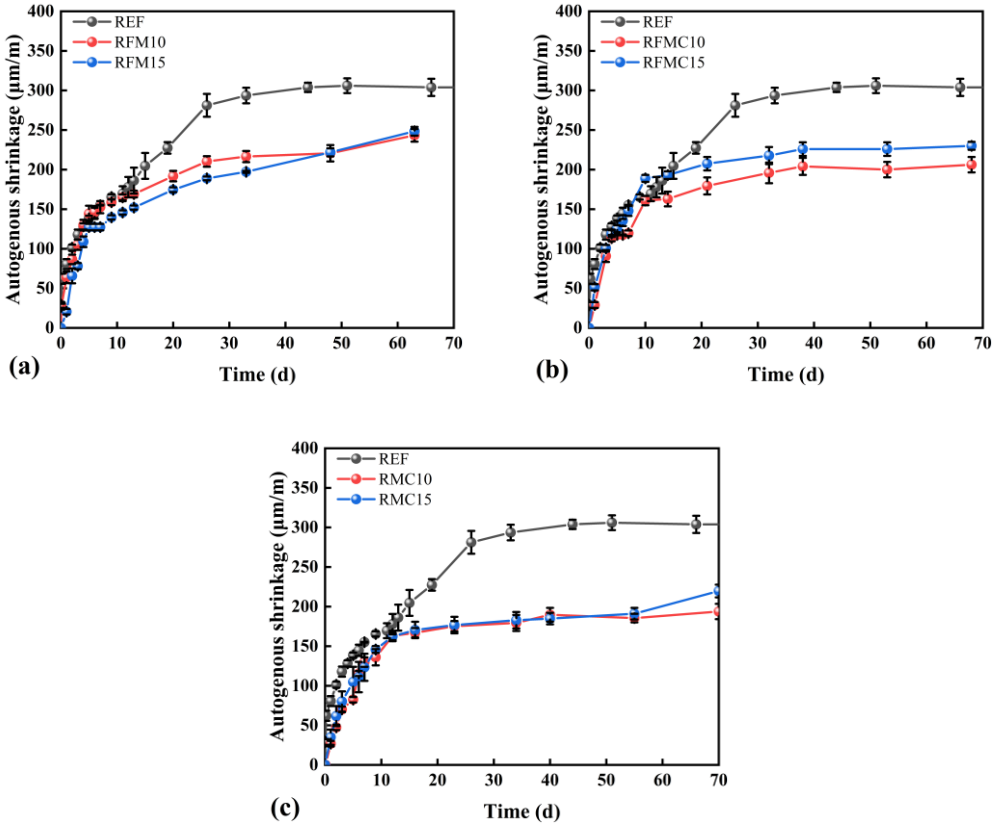


Figure. 4.34. The effect of RCA content on autogenous shrinkage - Size of RCA : 0.315-0.63mm (a) Size of RCA : 0.63-1.25mm (b) Size of RCA : 1.25-2.5mm (c) - "Day 0" refers to 1 day

Further exploring RCA dosage effects, Figure 4.34 shows that increasing RFM content from 10% to 15% marginally reduces autogenous shrinkage, suggesting that higher water availability partially compensates for RF's limited release capacity. In contrast, RFMC and RMC show negligible shrinkage changes with increased content,

highlighting that particle size distribution and pore connectivity dominate over aggregate dosage in determining curing effectiveness.

To ensure the validity of the shrinkage results, the mass loss at 70 days was also monitored. All mixtures exhibited extremely low values (ranging from 0.001% to 0.017%), confirming that water exchange with the environment was negligible throughout the test. Therefore, the observed differences in autogenous shrinkage can be attributed to internal curing efficiency rather than differences in external drying. Compared with previous studies relying on narrowly graded single-size RCA ratios, this simplified sieve-based classification approach produces consistent shrinkage trends and clearly differentiates the effects of fine, medium, and coarse ratios. These results indicate that the method is sufficiently robust for practical application without additional particle size control.

4.5 Total and Drying Shrinkages of mortars with LWA and RCA

In this section, the drying begins at 1 day and the drying shrinkage is calculated as the difference between total shrinkage and autogenous shrinkage presented in §4.4

4.5.1 The effect of LWA

To comprehensively evaluate the shrinkage behavior of LWA-modified mortars, both total shrinkage and drying shrinkage were examined. As shown in Figure 4.35(a), during the first two weeks all LWA mixtures displayed total shrinkage values similar to REF, despite previously showing much lower autogenous shrinkage (Figure 4.22(a)). This indicates that the reduction in autogenous shrinkage provided by internal curing was offset by a simultaneous increase in drying shrinkage (Figure 4.35(c)). Clearer differences emerged after 14 days. At 56 days, total shrinkage ranked: LT15 > LT10 > REF ≈ LM15 > LM10. LT mixtures, particularly LT15, reached the highest

shrinkage (~1150 μm/m), while LM10 had the lowest (~900 μm/m). The results highlight the influence of both LWA type and content: higher water absorption and faster release (LT) increased long-term total and drying shrinkage, while controlled release (LM10) limited it.

However, drying shrinkage for LWA is always higher, even for LM10 and LT10 (Figure 4.35(c)), which show a mass loss similar to REF (Figure 4.35(b)). It increases with both LWA content and particle size. At 56 days, drying shrinkage exceeded REF by +36.4% (LT15), +19.5% (LT10), +17.3% (LM15), and +12.6% (LM10). Note that this ranking is directly related to the w_{tot}, which is highest for LT15 and lowest for REF (Table 3.2) - consistent with prior studies [145] indicating that a higher W/C ratio leads to a higher drying shrinkage.

Mass loss data (Figure 4.35(b)) revealed that higher LWA content accelerated early evaporation. Within one day of demolding, LT15 lost nearly twice as much mass as REF, while LM15 lost +22.2%. This rapid loss matches the desorption kinetics in Figure 4.14(a).

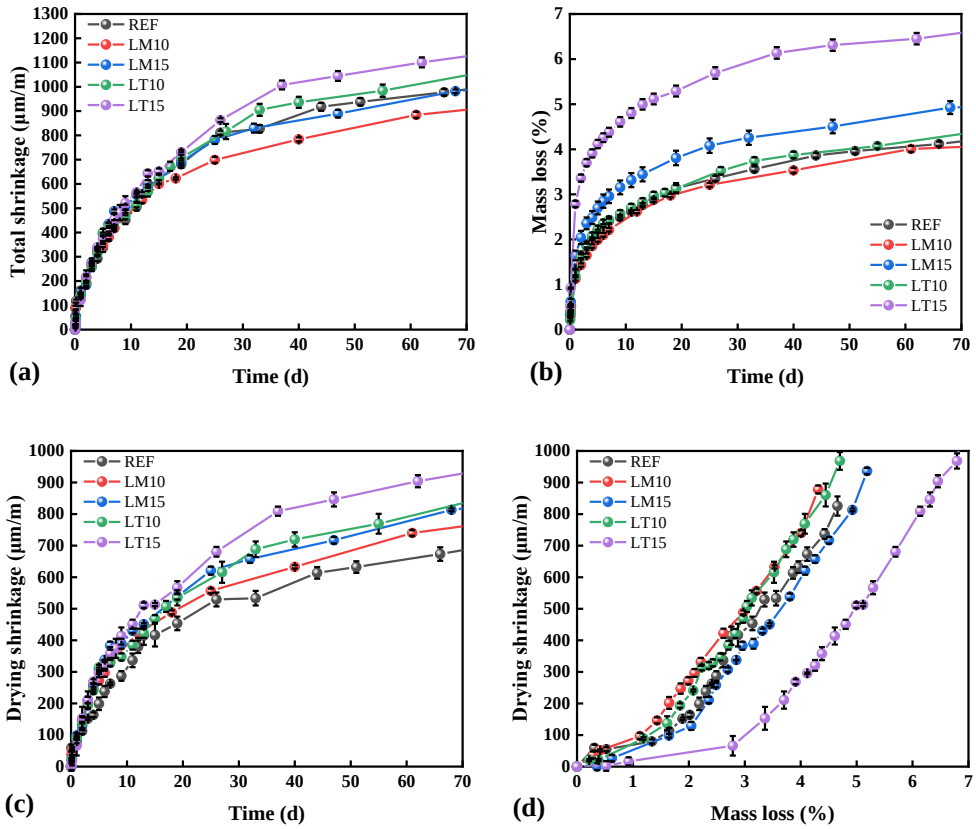


Figure. 4.35. The effect of LWA content and particle size under drying : Total shrinkage (a); Mass loss (b); Drying shrinkage (c) Drying shrinkage as function of the mass loss (d)

Figure 4.35(d) plots mass loss and drying shrinkage together, revealing two distinct stages :

- In Stage 1 (0–~2 days – Table 4.7), specimens undergo rapid mass loss with minimal shrinkage (< 100 μm/m) - up to about 2.8% in LT15, with progressively lower values for LM15, LT10, LM10, and REF. This phase corresponds to the initial evaporation of free water while internal humidity remains high. The mass loss of this step increases with the content of LWA and the content of internal water curing (Table 3.2).

- Stage 2 (>1-2 days) shows an approximately linear relationship between mass loss and drying shrinkage. While the slopes for all LWA mixtures are close (Table 4.7), a slight difference is observed, decreasing in the order: LT10 >

LT15 > LM10 > LM15 > REF. This means that the slope is reduced when the LWA volume increases and when the particle size range is narrowed. Since a nearly identical ranking is observed for the autogenous shrinkage of LWA mortars (Figure 4.18), it can indicate that late-age drying shrinkage is governed partially gouverned by the gradual migration of pre-absorbed water from the LWA into the surrounding paste, where it eventually evaporates through interconnected pores. This internal water release, while beneficial for mitigating autogenous shrinkage, can sustain drying shrinkage over time, as function of the ICAs distribution in the paste matrix and the internal water curing. In this context, LM10—with its better particle distribution and balanced pore structure demonstrated in § 4.1 and 2.3—achieves a favorable balance between preserving IRH, mitigating autogenous shrinkage, and limiting the slope of drying shrinkage.

Table. 4.7 The slope of the second stage of the drying shrinkage versus mass loss curve

Type	The transition point to the second step (d)	The mass loss at the transition point (%)	Slope (μm/m·%$^{-1}$)
REF	2	1.7	238.55
LM10	2	1.5	242.05
LM15	2	2.1	239.12
LT10	2	1.7	247.19
LT15	1	2.8	244.62

While internal curing mitigates autogenous shrinkage by maintaining internal RH and reducing early capillary tension, mixtures with high internal water curing content intensifying early drying shrinkage. This is particularly evident in LT15 and LM15. But the distribution of LWA and the protected paste volume affect also the drying shrinkage evolution as shown by LT10.

Despite higher drying shrinkage, the overall benefit remains significant—especially for LM10, which achieved a 56-day total shrinkage 6.6% lower than REF (900 μm/m vs. 963 μm/m). LM10's moderate absorption and controlled desorption limit drying

shrinkage while delivering substantial autogenous shrinkage reduction, making it the optimal balance among tested LWAs.

4.5.2 The effect of RCA

Figures 4.36(a)(c) present the total and drying shrinkage behavior of mortars containing different RCA types and contents. In the first 14 days, all mixtures—including REF and RCA mortars—show quite similar drying and total shrinkage, suggesting that RCA exerts little influence on early-age deformation. This early similarity mirrors the behavior observed in LWA mortars (Figure 4.36(a-c)), where total shrinkage also matched REF despite much lower autogenous shrinkage. But the addition of RCA is also not beneficial in reducing autogenous shrinkage during this period, except for RC10 (Figure 4.27) —a behavior that diverges from that of mortars with LWA.

Figures 4.36(a)(c) show that both total and drying shrinkage increase with finer RCA particles (RF)—a behavior similar to that observed for autogenous shrinkage (Figure 4.29)—and with increasing RCA content. This latter trend is directly related to the higher water content of RCA, which contributes to internal curing (Table 2.3). The fine RCA group (RF), characterized by high porosity and substantial attached old paste (Figure 2.14, 2.15), contributes to greater internal water release and faster drying.

Comparison of the mixtures ranked by drying shrinkage, total shrinkage, and the amount of water available for internal curing, as shown in the relationships hereafer :

- Ranking of the mixtures by total shrinkage at long term (Figure 4.36(a)) – similar for the mass loss (Figure 4.36(b)):

  RC10 < RM10 < RC15 < REF≈RM15<RF10 <RF15

- Ranking of the mixtures by drying shrinkage at long term (Figure 4.36(c)):

  RC10 < REF < RM10≈RC15 < RM15 <RF10 < RF15

- Ranking of the mixtures by internal water content of RCA:

RC10 < RM10 <RF10 < RC15 < RM15 < RF15

indicates that particle size has a greater influence on both total and drying shrinkage than the water content located into internal curing agents. This underscores the critical role of particle distribution within the mortar matrix.

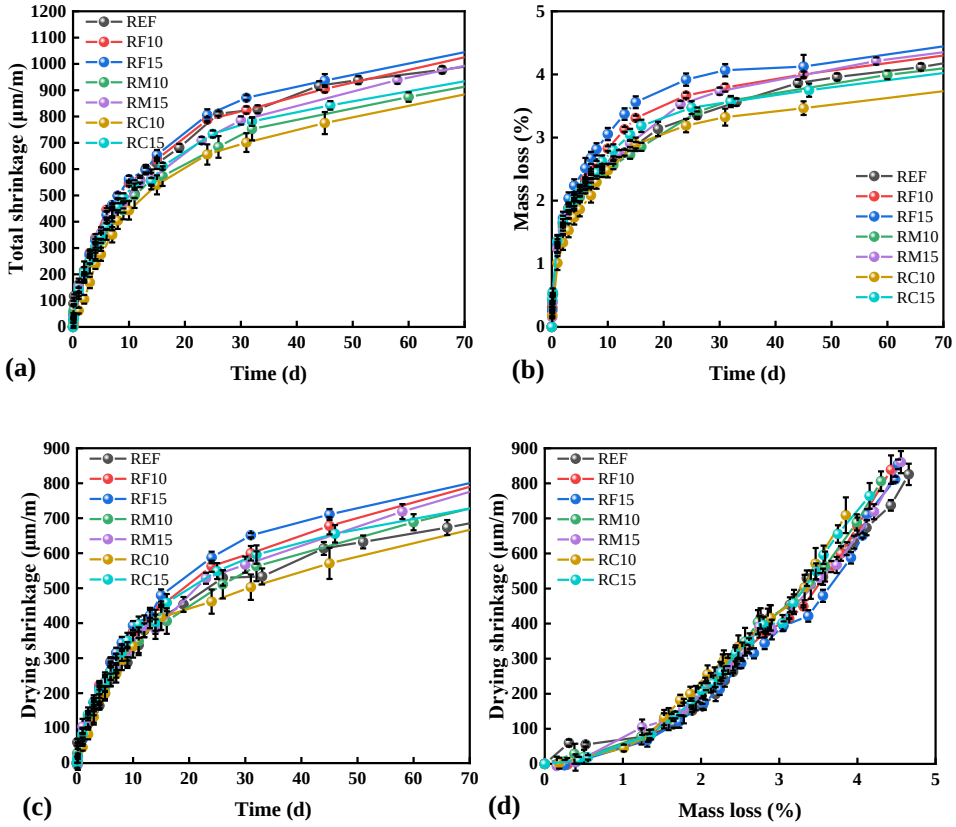


Figure. 4.36. The effect of RCA content and particle size under drying : Total shrinkage (a); Mass loss (b); Drying shrinkage (c); Drying shrinkage as function of the mass loss (d)

Table. 4.8 The slope of the second stage of the drying shrinkage versus mass loss curve

Type	The transition point to the second step (d)	The mass loss at the transition point (%)	Slope (μm/m·%$^{-1}$)
REF	2	1.7	238.55
RF10	2	1.6	235.53
RF15	2	1.7	251.98
RM10	2	1.2	242.16
RM15	2	1.2	237.42
RC10	2	1.3	232.10
RC15	2	1.4	241.75

LWA has a more important effect on increasing drying shrinkage than RCA. By 56 days, LM10 exhibits a drying shrinkage of +12.6%, higher than RM10 at +4.7%, while LM15 reaches +17.3%, compared to +10.4% for RM15. This comparison shows that, although both RCA and LWA mortars experience increased drying shrinkage with higher ICA content, the effect is substantially more pronounced for LWA, highlighting their higher water absorption and faster desorption as shown by the evolution of their mass loss (Figures 35(b) and 36(b)).

The slope of the Stage-2 shrinkage–mass loss curve (Figure 4.36(d)) reflects the sensitivity of volume change to moisture loss at later ages. For RCA mortars, REF shows a slope of 238.55 μm/m per % mass loss (Table 4.8). RF15 has the highest slope (251.98), indicating finer RCA induces more shrinkage per unit water lost. RC10 has the lowest (232.10), even slightly below REF. Increasing coarse RCA content from 10% to 15% produces only a modest slope increase, showing limited sensitivity.

4.5.3 Effect of broader particles size ranges for RCA

Figure 4.37 (c) shows that incorporating RCA from the second category increases long-term drying shrinkage. At 56 days, all RCA mixtures exhibit greater shrinkage than REF. In particular, RMC15 shows the highest increase (24.9%), followed by RMC10 (16.3%), RFM15 (14.4%), RFMC15 (12.1%), RFMC10 (10.1%), and RFM10 (6.7%).

Total shrinkage results in Figure 4.37(a) confirm these trends. Most RCA mixtures display similar total shrinkage over the 56-day period, with variations generally within 30 μm/m. This indicates that the increase in drying shrinkage is often compensated by reductions in autogenous shrinkage, especially in mixtures with coarser RCA (e.g., RMC). Thus, while broader particle gradations intensify drying deformation, they may not translate to proportionally higher total shrinkage.

Figure 4.37(b) supports these observations through mass loss data. RMC15 exhibits the highest early-stage mass loss, reaching 16.4% more than REF at 3 days, consistent with its large particle size and high RCA content, which promote faster moisture release under drying conditions. In contrast, RFM10 and REF have nearly identical mass loss, while other RCA mixtures lose less moisture overall.

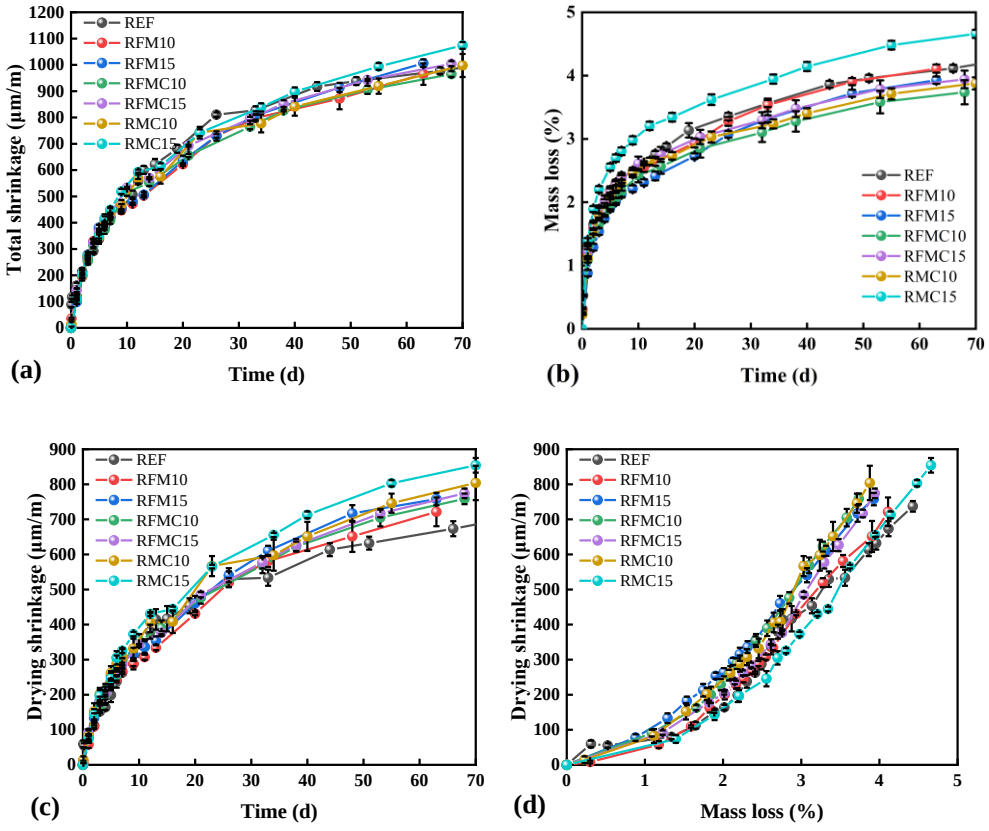


Figure. 4.37 The effect of RCA content and particle size under drying: Total shrinkage (a); Mass loss (b); Drying shrinkage (c); Drying shrinkage as function of the mass loss (d); These results highlight two main trends:

1. Drying shrinkage increases with RCA content when the particles range is larger;

2. Wider particle size distributions (e.g., RMC and RFMC) lead to greater drying shrinkage, suggesting less favorable performance in terms of deformation control.

Interestingly, Figure 4.37(d) and Table 4.9 reveal that the slope of the second stage shrinkage–mass loss curve is significantly higher for RFMC10, RFMC15, RMC10, and RMC15—all increasing by approximately 21–23% compared to REF. This means that, despite lower or similar mass loss, these mortars undergo more shrinkage per unit of water lost, reflecting a higher sensitivity to drying.

Table. 4.9 The slope of the second stage of the drying shrinkage versus mass loss curve

Type	The transition point to the second step (d)	The mass loss at the transition point (%)	Slope (μm/m·%$^{-1}$)
REF	2	1.7	238.55
RFM10	2	1.6	247.07
RFM15	2	1.3	246.59
RFMC10	2	1.5	292.89
RFMC15	2	1.8	290.57
RMC10	2	1.5	288.86
RMC15	2	2.2	290.57

Broader RCA gradations (e.g., RFMC) produce a more deformable composite due to lower stiffness, higher porosity, and weak ITZ in the adhered mortar. Their non-uniform particle packing generates heterogeneous pore networks and uneven moisture release, which cause localized shrinkage gradients and stress concentrations, ultimately exacerbating long-term drying deformation. Consequently, RCA mixtures with broader particle size ranges—particularly RMC—exhibit more severe drying shrinkage and higher shrinkage-to-mass-loss sensitivity, whereas fine, well-graded RCA (e.g., RFM10) provides better dimensional stability

4.6 Summary

This study systematically evaluated the influence of LWA and RCA particle size and

content on mechanical performance, shrinkage behavior, and internal curing efficiency in mortar. The results confirm that both materials can enhance hydration and mitigate autogenous shrinkage through internal water release, but their effects strongly depend on gradation and dosage.

Among LWA mixtures, LM10 (0.63–1.25 mm, 10%) delivered the best balance of properties—maintaining strength close to or above REF while effectively reducing autogenous shrinkage and avoiding significant increases in drying shrinkage. For RCA, RC10 (1.25–2.5 mm, 10%) achieved similar total shrinkage to REF while retaining competitive strength, outperforming finer RCA ratios that tended to increase drying deformation.

A key insight is that coarser RCA, despite lower absorption, can outperform finer particles in shrinkage control, while moderate amounts of fine LWA can provide efficient internal curing without compromising dimensional stability. These findings identify LM10 and RC10 as optimal internal curing strategies and provide a quantitative framework for selecting aggregate gradation–content combinations to achieve durable, shrinkage-resistant cement-based materials. These mixtures will therefore be selected to investigate the self-healing capacity of mortars incorporating internal curing agents, in order to assess the effect of these materials on crack healing.

Chapter 5 Effect of biochar on internal curing of cement-based materials

Given the low water absorption of lightweight aggregates (LWA) and recycled concrete aggregates (RCA), biochar presents an intriguing alternative for internal curing. Biochar, for instance, can absorb water up to 7-8 times its own mass. The performances of this product are compared to more traditional ICA, such as SAP and silica. Indeed, SAP has been shown to absorb more than 70 times its own mass of water and silica can absorb up to 30–40% of its own mass of water [148, 163]. Given their high water absorption capacities, these materials offer the possibility of reducing shrinkage when used for internal curing [50, 163].

This chapter provides a comprehensive exploration of the influence of biochar on internal curing in cement-based systems. The synergistic effects when biochar is combined with MgO, another shrinkage reducer, is also investigated with 5% biochar and 6% MgO by weight of cement, examining their performance across three water-to-binder ratios (0.45, 0.41, and 0.37) to evaluate the impact of water content and porosity on hydration and the expansive capacity of MgO. Mixture proportions are detailed in Table 3.6.

To benchmark biochar's effectiveness, traditional curing agents (SAP and silica) in combination with MgO are also investigated under two scenarios: SAP at 2% and 5.5% by weight of MgO, and silica at 6% and 15.5% by weight of MgO. Notably, 5% biochar, 5.5% SAP, and 15.5% silica provide equivalent amounts of internal curing water. These key mixture proportions are summarized in Table 3.7.

5.1 Hydration and pore structure of mortars with biochar

This section is primarily dedicates to the analysis of the impact of biochar on cement hydration and its influence on the pore structure of the mixture.

5.1.1 Hydration products

To investigate the hydration products, TGA analysis is performed to obtain DTG curves, presented in Figures 5.1 (3 days) and 5.2 (28 days). Regardless of the water-to-binder ratio, all mixtures display an initial peak between 105 °C and 250 °C, corresponding to the onset of C–S–H bond dissociation. In MgO-containing mixtures, a second peak appears between 320 °C and 400 °C, consistent with the dehydration of brucite ($Mg(OH)_2$) to MgO [91]. A third peak, observed between 400 °C and 550 °C, is attributed to the dehydration of $Ca(OH)_2$. At higher temperatures, a fourth peak between 650 °C and 710 °C corresponds to decarbonation, while a fifth, unique to biochar-added mixtures, appears between 710 °C and 850 °C, reflecting the decarbonation of biochar-derived phases (Figure 2.22(a)) [82].

At 3 days (Figure 5.1), both B5M6 and B5 exhibit two distinct peaks within the 650–850 °C range, whereas M6 shows only a single peak. The appearance of two peaks indicates overlapping decomposition processes in mixtures containing biochar. This observation is consistent with the thermal behavior of raw biochar shown in Figure 2.22(a, c), where biochar displays a broad and significant mass loss in this temperature region. Thus, the presence of biochar introduces additional decomposition signals, resulting in stronger and more complex thermal responses compared with the reference or MgO-only mixtures.

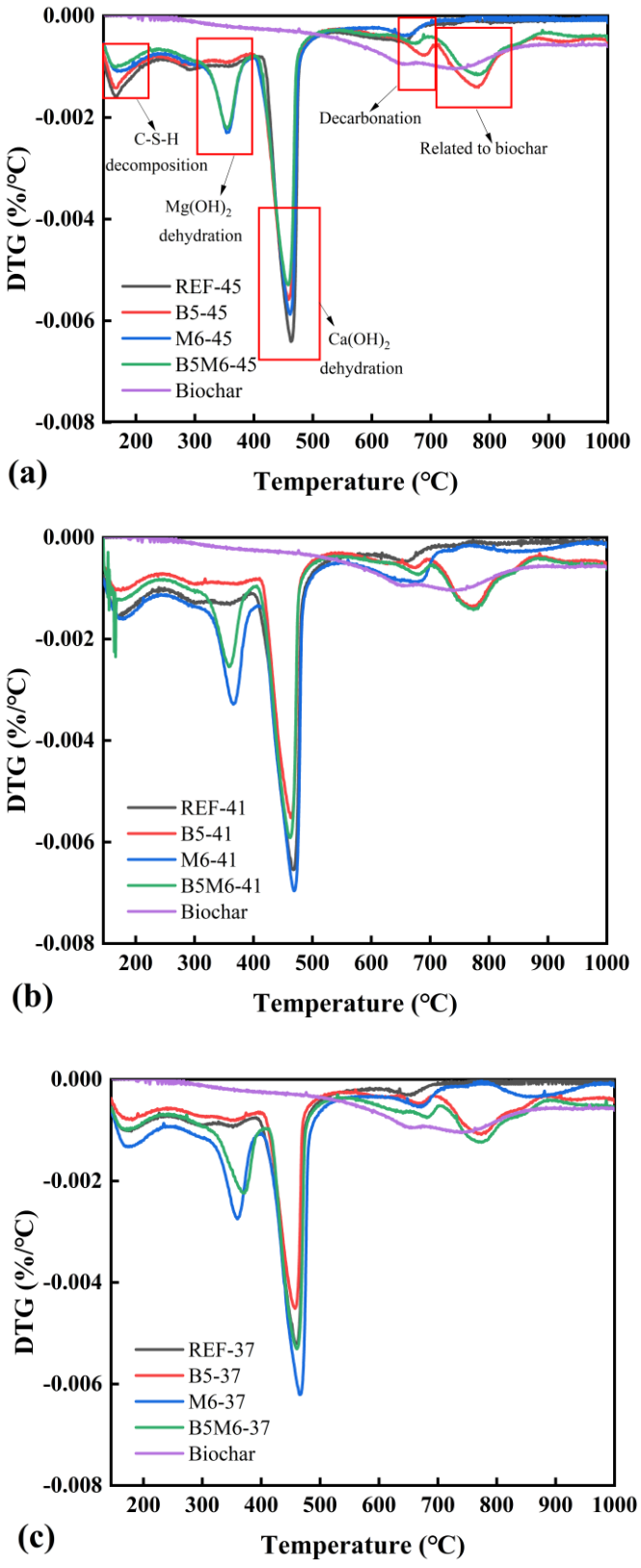


Figure. 5.1 DTG curves for different water-to-binder ratios at 3 days: W_{tot}/B=0.45(a), W_{tot}/B =0.41(b), W_{tot}/B =0.37 (c)

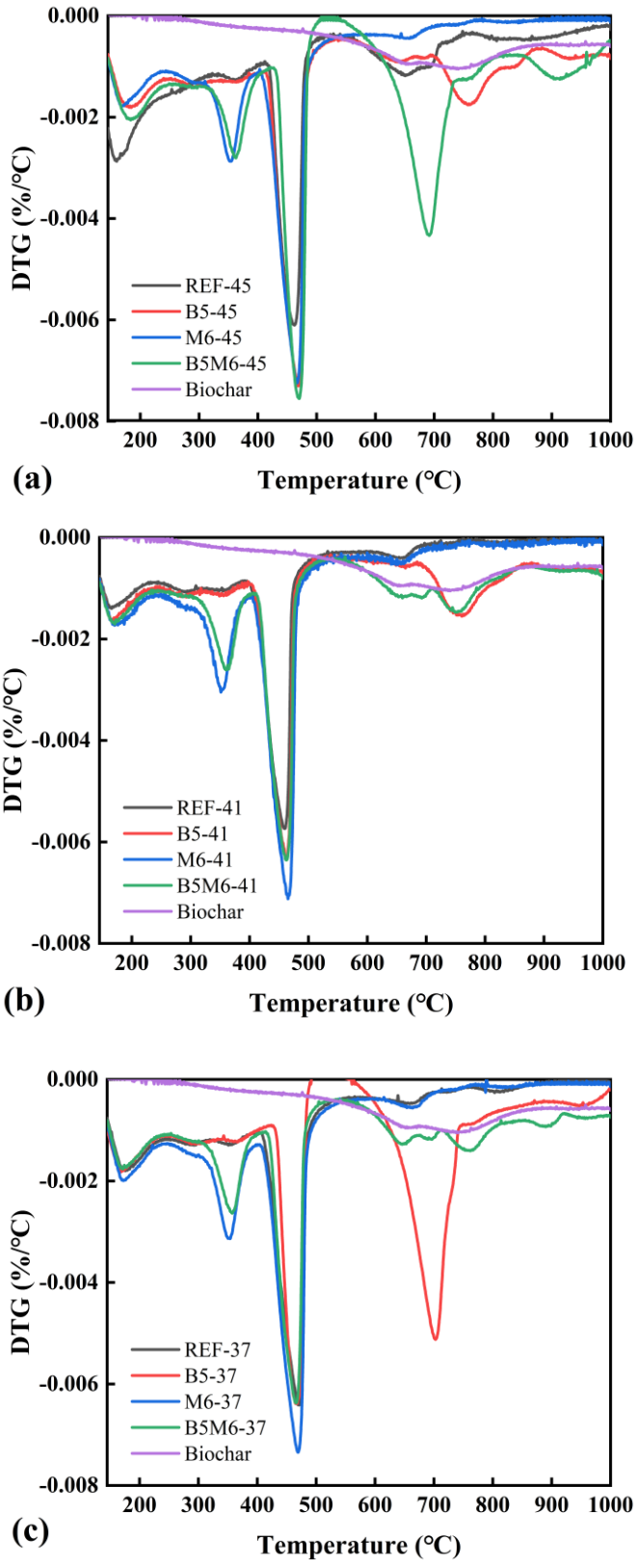


Figure. 5.2 DTG curves for different water-to-binder ratios at 28 days:

W_{tot}/B=0.45(a), W_{tot}/B =0.41(b), W_{tot}/B =0.37(c)

At 28 days (Figure 5.2), the distinction becomes more evident. For B5M6 (Figure 5.2(a)), a particularly strong peak near 700 °C is observed, reflecting the combined influence of biochar-related decomposition (as also seen in Figure 2.22) and the decomposition of secondary magnesium carbonate phases formed in the MgO-containing system. In contrast, B5 (Figure 5.2(c)) also exhibits a pronounced peak around 700 °C, which aligns closely with the dominant decomposition of biochar residues itself, as identified in its standalone TGA/DTG results (Figure 2.22).

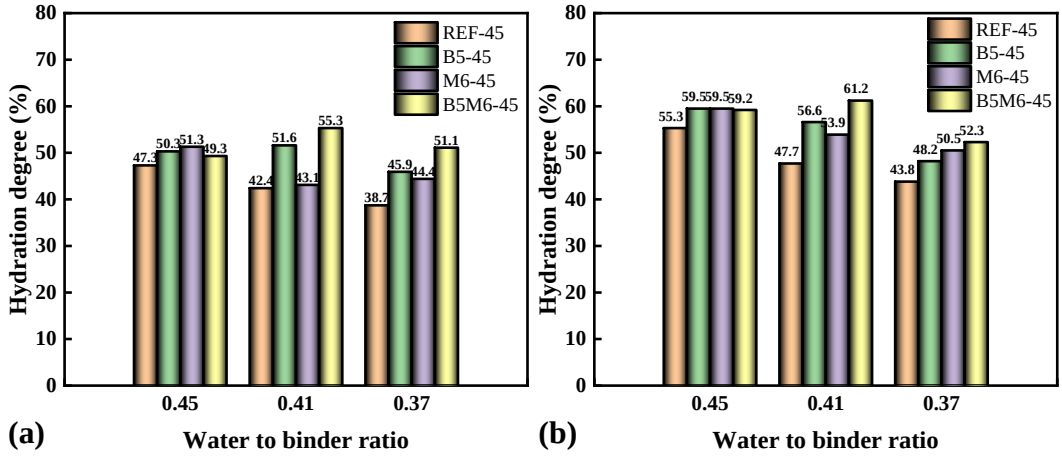


Figure. 5.3 Degree of hydration at 3-day (a) and 28-day (b)

Figure 5.3 illustrates the degree of hydration of the mixtures at 3 and 28 days, calculated from the TGA results using Equation 3.5. At 3 days (Figure 5.3(a)), B5-45 shows a higher hydration degree (51.3%) compared to REF-45 (47.2%). This behavior is amplified with the reduction of the W_{total}/B ratio, confirming that the incorporation of biochar promotes early hydration by providing additional nucleation sites. The same behavior is observed for B5M6, suggesting that the combination of biochar and MgO leads to a synergistic effect in the early age hydration process.

At 28 days (Figure 5.3(b)), the hydration degree of all mixtures increases, yet the relative differences among them become less pronounced for mixtures with a W/B ratio of 0.45. REF-45, B5-45, M6-45, and B5M6-45 display values of 55.3%, 59.5%, 59.5%, and 59.2%. The behavior changes as the E/L ratio decreases, reflecting an increased degree of hydration induced by the incorporation of biochar, MgO, and their combined

effect. Specimens B5M6-41 and B5M6-37 exhibit a higher degree of hydration compared to the reference mortars, highlighting the synergistic advantage of this combination in promoting long-term hydration. For completeness, Appendix B (Figure B.1) presents the mass loss within the 105–550 °C range, which further supports the evaluation of hydration products considered in this section.

Figure 5.4 shows the mass loss between 320 °C and 400 °C for both 3-day and 28-day specimens. The content of brucite is referenced from Appendix B (Figure B.2). As expected, this mass loss is greater in M6 and B5M6 for all water-to-binder ratios and curing ages. This increase is attributed to brucite formation resulting from MgO hydration. To isolate the specific contribution of MgO on this temperature interval, a simple subtraction method was applied: the mass loss of REF was subtracted from that of M6, and the mass loss of B5 was subtracted from that of B5M6. This procedure provides an estimate of the mass loss in M6 and B5M6 directly associated with MgO hydration products, while also revealing the influence of internal curing agent on their formation. The results are shown in Figure 5.5.

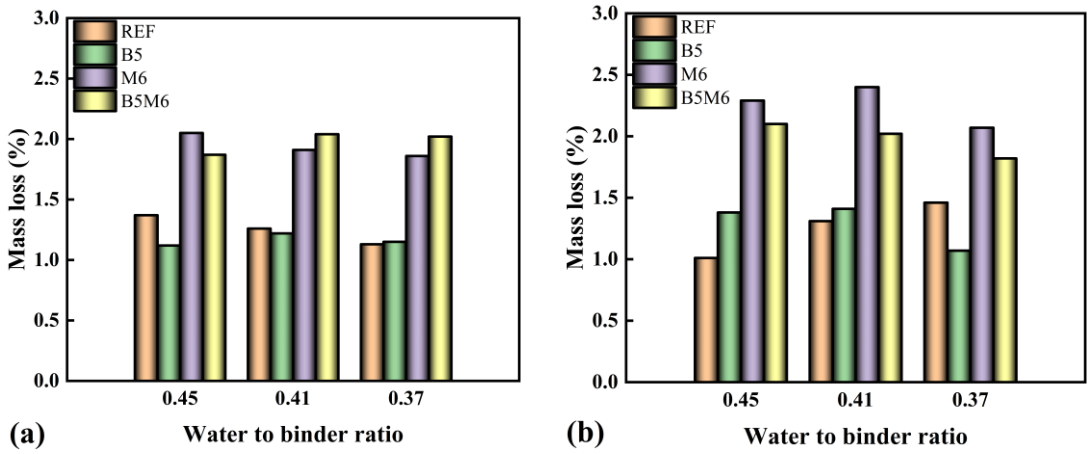


Figure. 5.4 Mass loss in [320 °C - 400°C] at 3-day (a) and 28-day (b)

At 3 days, B5M6 shows slightly higher mass loss than M6, with increases of 10.4%, 24.5%, and 18.7% for total water-to-binder ratios of 0.45, 0.41, and 0.37, respectively (Figure 5.5(a)). This is explained by the internal curing effect of biochar, which releases stored water, enhancing both MgO and cement hydration. At W_{total}/B = 0.45, water

availability is sufficient in both mixtures, resulting in a closer MgO hydration levels and nearly identical mass losses.

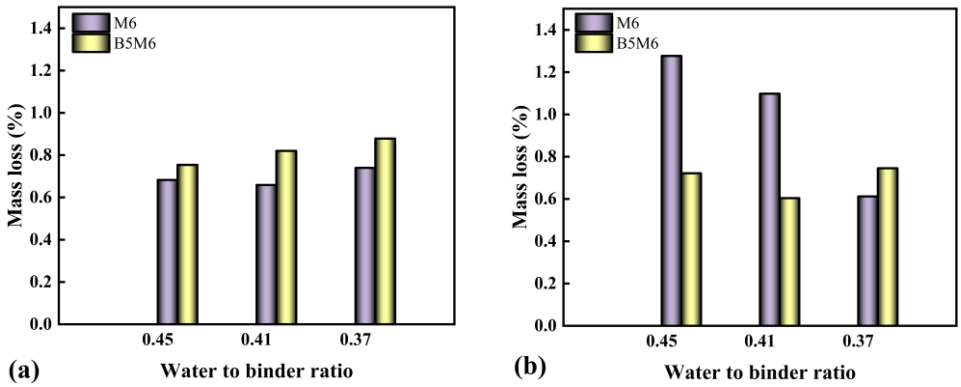


Figure. 5.5 Mass loss associated with MgO hydration products at 3-day (a) and 28-day (b)

In contrast, at 28 days, the trend reverses, with M6 exhibiting greater mass loss than B5M6 (Figure 5.5(b)). This difference reflects the hydration behavior of the moderately reactive MgO as the product used in the present study, which continues to hydrate as function of time when water remains available as for $W_{total}/B = 0.45$. For B5M6, the brucite content in B5M6 is lower at 28 days compared to 3 days. This decrease can be partially explained by several factors:

- With the advancement of the hydration process, a part of the $Mg(OH)_2$ may carbonate to form $MgCO_3$ or react with silicates to produce more stable phases such as M–S–H, which decompose at higher temperatures and therefore do not contribute to the 320–400 °C mass loss [97].
- The brucite formed at early ages is generally poorly crystalline and decomposes more readily, whereas after 28 days it tends to become more crystalline and thermally stable, reducing the measured mass loss in this range [143].
- The lower water-to-binder ratio (e.g., 0.37) in these mixtures limits pore connectivity and the availability of free water, thereby restricting further MgO hydration and the late-age formation of $Mg(OH)_2$.

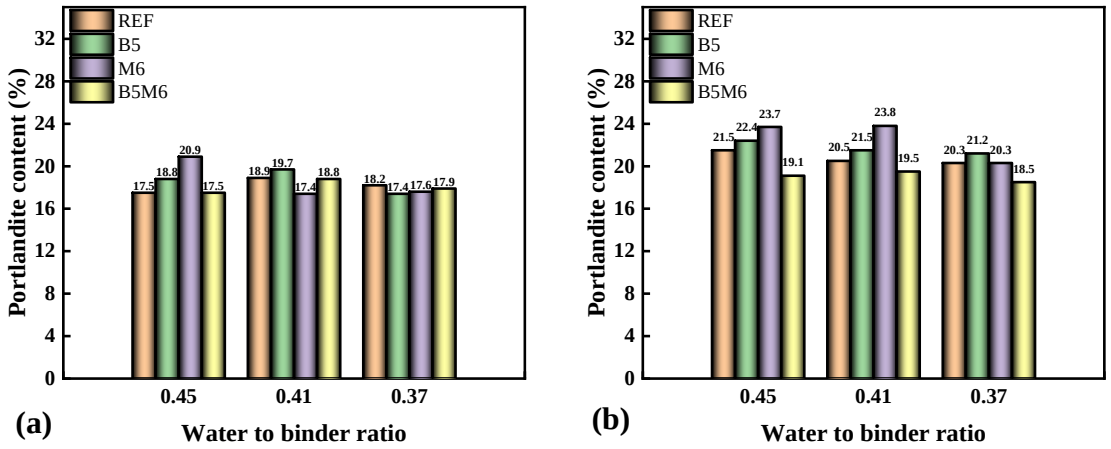


Figure. 5.6 Portlandite content at 3-day (a) and 28-day (b)

Figure 5.6 presents the Portlandite content of the mixtures at 3 and 28 days. The mass losses within the temperature range [400-550]°C, linked to the decomposition of portlandite are presented in the Appendix B (Figure B.2). At W_{total}/C = 0.45, B5 consistently shows higher Portlandite levels than REF, with 18.8% vs. 17.5% at 3 days and 22.4% vs. 21.5% at 28 days, highlighting the positive effect of biochar on cement hydration. A similar trend is observed at W/C = 0.41, where B5 exceeds REF by 4.2% at 3 days and 4.4% at 28 days. At a lower W/C of 0.37, B5 initially shows slightly lower Portlandite than REF at 3 days (17.4% vs. 18.2%). This difference may be attributed to the water retention effect of biochar, which could delay early hydration to some extent. However, as biochar gradually releases water, Portlandite content rises to 21.2% at 28 days, surpassing REF's 20.3%.

For B5M6, Portlandite content at 3 days is comparable to REF (Figure 5.6 (a)). At 28 days, it is slightly lower. It can be partially explained by the reduction of the cement content in these mixtures (Table 3.6) and by a carbonation of the portlandite as shown in the Figure 5.6(b).

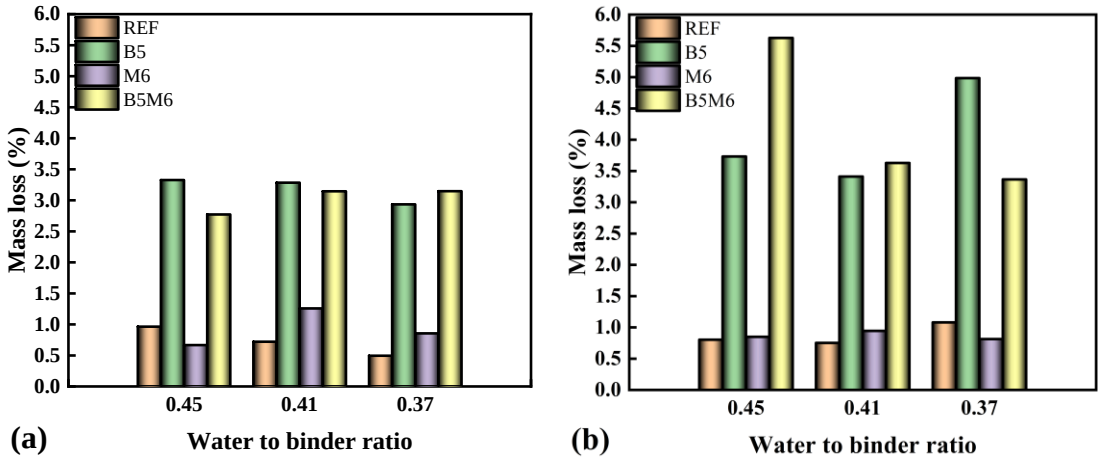


Figure. 5.7 Mass loss in [600℃ - 850℃] at 3-day (a) and 28-day (b)

Figure 5.7 presents a detailed analysis of mass loss in the temperature range of 600–850 °C. The analysis focuses on the evolution of this parameter because multiple types of carbonates, such as calcium and magnesium carbonate, may decompose here. Despite this complexity, a calculation was carried out to estimate the calcite content, based on the hypothesis that it is the only carbonation product present. The results of this calculation are presented in Figure 5.8.

For both studied ages, B5 and B5M6 exhibit higher mass loss on this temperature interval. It can partially be explained by the presence of the biochar (Figure 2.22(a)), but this difference stays for the calcite where the effect of biochar is taken into account with its PaF (Equation 3.2).

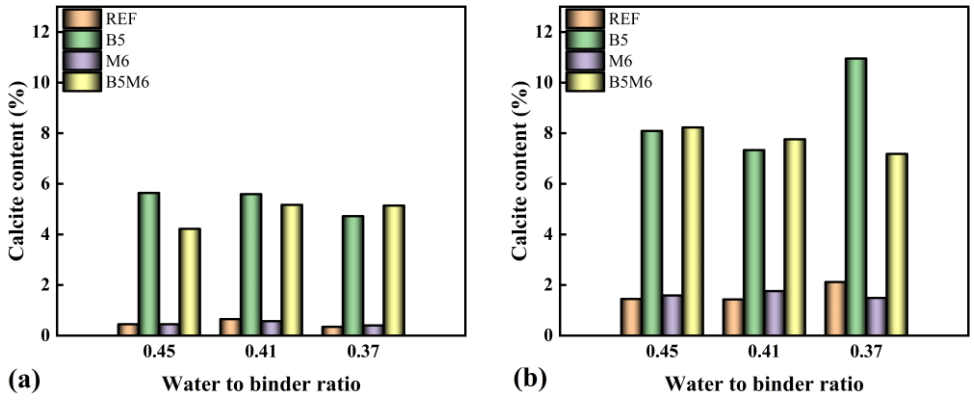


Figure. 5.8 Calcite content: at 3-day (a) and 28-day (b)

5.1.2 Total water porosity and real density

Figure 5.9 illustrates the effect of biochar and MgO additions on the total water porosity of the studied mortars. Overall, the inclusion of biochar or MgO has a limited impact on total porosity.

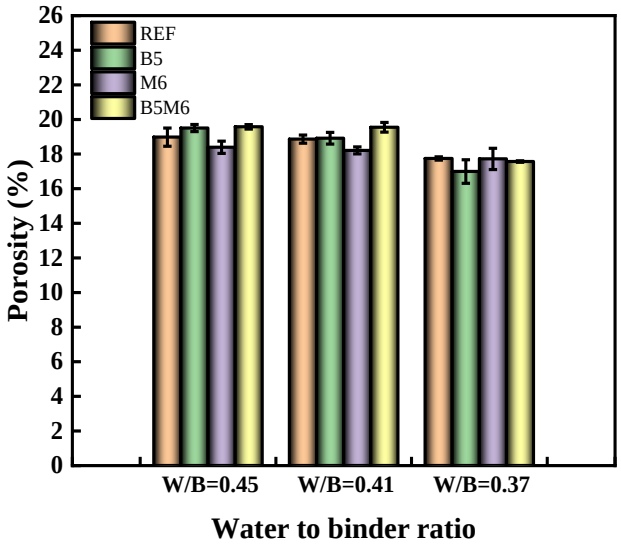


Figure. 5.9 Water porosity for all the studied mortars at 28 days

At a total water-to-binder ratio of 0.45, adding biochar (B5, B5M6) slightly increases porosity by 2.8%, reflecting the inherently porous nature of biochar. A quite similar observation is made for the total water-to-binder ratio of 0.41. In contrast, MgO shows minimal influence, except at a W/B ratio of 0.41, where it causes a modest reduction in porosity. At a lower W/B ratio of 0.37, all mixtures exhibit reduced porosity due to the denser matrix and lower initial water content.

Figure 5.10 provides further insight by comparing the real volume of the mixtures, measured using a helium pycnometer, with the apparent volume calculated from specimen dimensions. The observed difference between apparent and real density reflects the inherent porosity of each mixture, since the apparent density is calculated based on the bulk volume including pores, whereas the real density corresponds to the

solid phase alone. Consequently, a larger discrepancy between the two densities implies a higher pore content within the mixture (Figure 5.10).

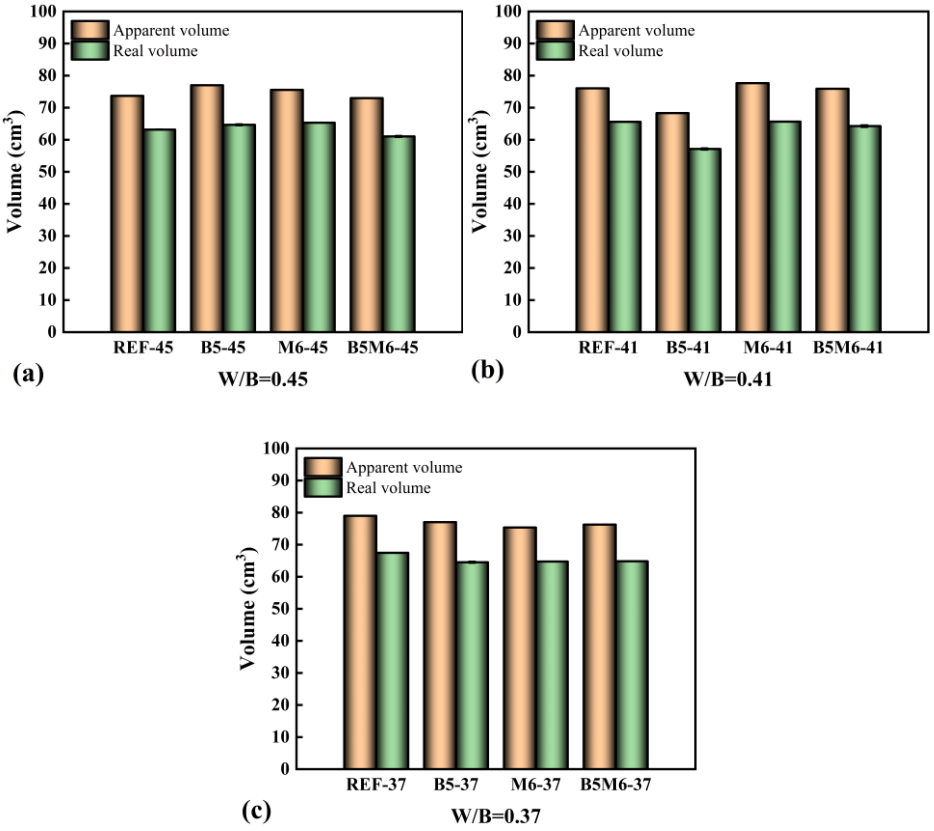


Figure. 5.10 Real volume at W_{tot}/B=0.45 (a), W_{tot}/B =0.41 (b), W_{tot}/B =0.37 (c)

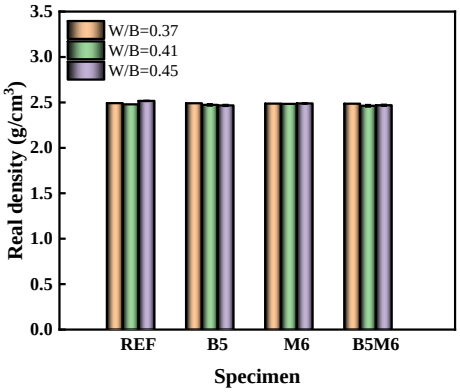


Figure. 5.11 Real density of all the studied mixtures

Finally, Figure 5.11 highlights the effect of biochar and MgO on real density. Consistent with the porosity results, the addition of either material has minimal impact on true density, indicating that these additions do not significantly alter the compactness

of the matrix. This finding has practical implications for the design and application of biochar- or MgO-modified mixtures.

5.2 Mechanical properties of mortars with biochar

This section systematically examines the influence of biochar on the mechanical properties of cement-based materials, focusing on two key aspects: its effect on compressive strength and the internal solidification phenomena [91] it induces. In this context, the term internal solidification refers simply to the transformation of pore solution into solid hydration products within the pore system of the matrix, especially inside biochar pores and in the adjacent ITZ. The analysis clarifies the mechanisms through which biochar contributes to strength development and provides a comprehensive understanding of its role in internal curing.

5.2.1 Compressive strength

Figure 5.12(a) shows the compressive strength of the mixtures at 3 days. At this early stage, the addition of biochar alone has little effect on strength, whereas the inclusion of MgO—either alone or combined with biochar—causes a measurable reduction. This decrease is mainly due to two factors: (1) early MgO hydration consumes part of the available water, limiting cement hydration, and (2) MgO partially replaces cement, reducing the binder content (Table 3.6), and this effect is slightly amplified with the addition of biochar (B5M6). In all cases, compressive strength increases as the total water-to-binder ratio decreases.

At 28 days (Figure 5.12(b)), the same trend with respect to the water-to-binder ratio is observed in agreement with the water porosity results (Figure 5.9). Biochar and MgO alone have negligible influence on strength, but their combined use results in notable reductions of 7.2%, 11.3%, and 6.6% for W_{total}/B ratios of 0.45, 0.41, and 0.37, respectively. This combined effect is attributed to the reduction of cement replacement by MgO and biochar (Table 3.6), the reduction of the effective water-to-binder ratio

due to water retained by biochar (Table 3.6) and thus the water available for the hydration, as well as further water consumption during MgO hydration.

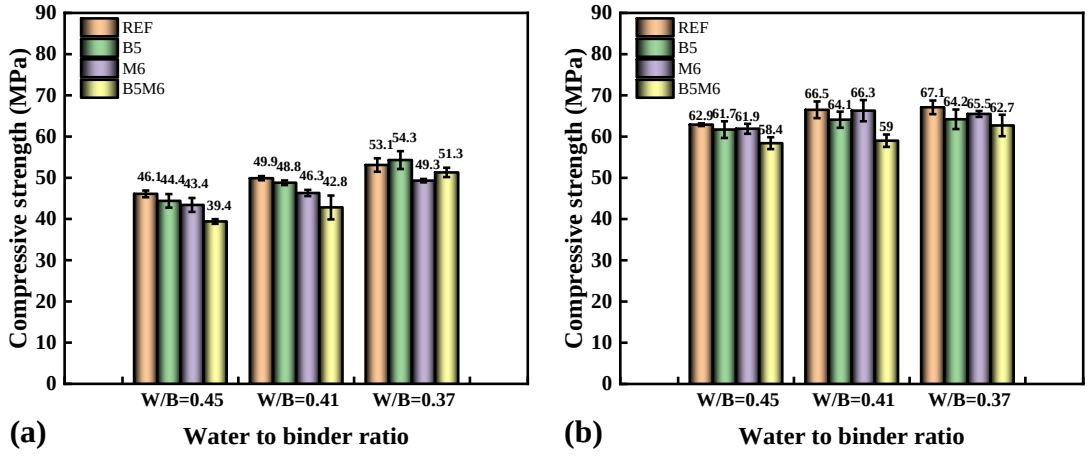


Figure. 5.12 Compressive strength for all the studied mortars at 3-day (a) and 28-day (b)

5.2.2 Flexural strength

Figure 5.13(a) presents the 3-day flexural strength for all studied mortars. The flexural strength for REF increases for a total water-to-binder ratios of 0.37, but decreases for a total water-to-binder ratios of 0.41, which may be related to the additional mixing water increasing early-age capillary porosity that was not fully compensated by hydration products. For 0.45 and 0.37, neither biochar nor MgO shows a significant effect on strength in comparison to REF. The reduction observed for B5M6 is aligned with compressive strength results: reduction of cement content and consumption of water for the MgO hydration, reducing the amount accessible for cement hydration. At a ratio of 0.41, the addition of biochar leads to a slight increase of the flexural strength.

Figure 5.13(b) illustrates the 28-day flexural strength. At total water-to-binder ratios of 0.41 and 0.37, biochar and MgO again show minimal influence. At 0.45, however, M6 exhibits a slightly higher flexural strength than REF. This improvement results from the adequate water supply at a higher W/B ratio, which ensures sufficient cement

hydration while allowing MgO to hydrate gradually without significantly competing for water.

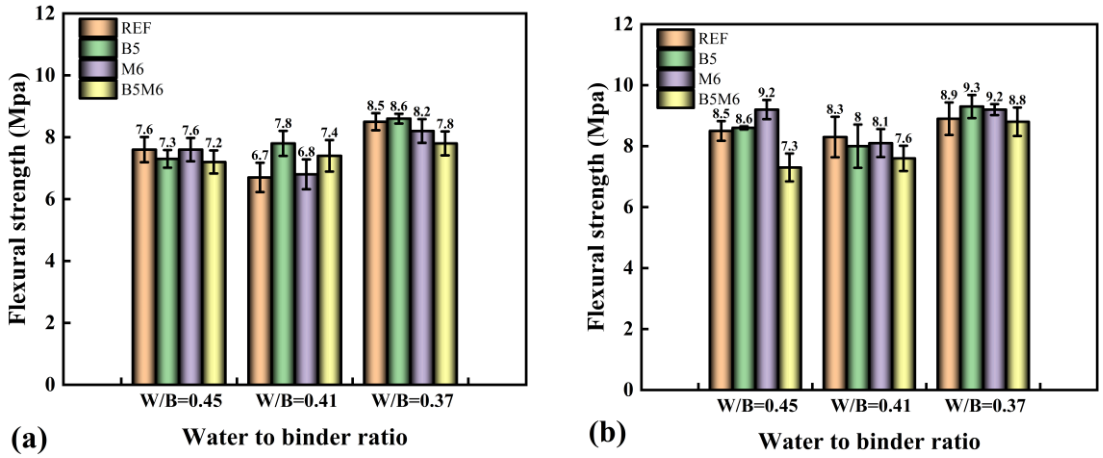


Figure. 5.13 Flexural strength for all the studied mortars at 3-day (a) and 28-day (b)

Finally, for ratios of 0.45 and 0.41, B5M6 shows slightly lower strength than REF. But a lower ratio (0.37) seems to be benefit for the coupling of MgO and biochar as the flexural strength of B5M6 is similar to that of REF. It could be related to the role of ICA played by biochar as internal water supply could improve the hydration of MgO and cement at long term.

5.2.3 Dynamic modulus

Figure 5.14(a) presents the 3-day dynamic modulus for all studied mortars. At a total water-to-binder ratio of 0.45, the incorporation of biochar results in a marked reduction: B5 and B5M6 show decreases of 8.4% and 12.4%, respectively, compared to REF. This reduction is attributed to the inherently high porosity of biochar, which slows down the compressive wave's propagation. Smaller decreases are also observed at total water-to-binder ratios of 0.41 and 0.37, indicating that biochar consistently induces a slight reduction in dynamic modulus regardless of the mix proportion. The effect of MgO (M6) is negligeable.

Figure 5.14(b) shows the 28-day dynamic modulus. At this age, the water-to-binder ratio exerts no substantial effect on the dynamic modulus except for 0.37. This last

observation is directly related to the mortar porosity (Figure 5.9). The trend observed at 3 days persists: for mixtures with a total water-to-binder ratio of 0.45, biochar continues to cause a modest decrease in dynamic modulus, while this effect decreases with the W_{total}/B ratios and is negligible for a total water-to-binder ratio of 0.37. This confirms a densification of the matrix with the reduction of the W_{total}/B ratio, as observed in the Figure 5.11.

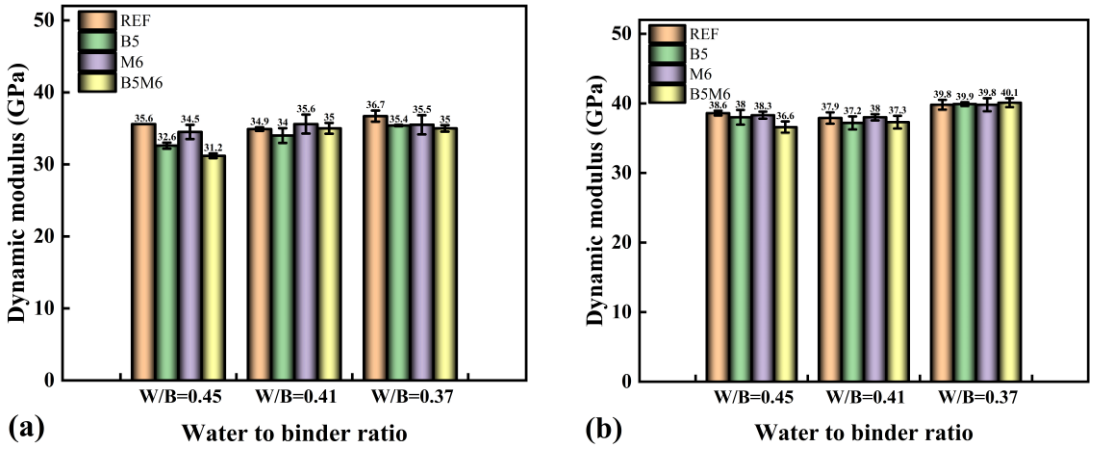


Figure. 5.14 Dynamic modulus for all the studied mortars at 3-day (a) and 28-day (b)

5.2.4 Summary

Overall, the mechanical performance of the mixtures is strongly influenced by the total water-to-binder ratio, with compressive and flexural strengths generally increasing as W_{total}/B decreases. Biochar alone has little impact on compressive or flexural strength, while MgO—particularly when combined with biochar—tends to cause slight reductions, especially at early ages. These reductions are linked to cement replacement, water retention by biochar, and additional water consumption during MgO hydration, which together lower the water available for cement hydration. Nevertheless, at lower W_{total}/B ratios (0.37), the combined use of MgO and biochar can partially mitigate strength losses, possibly due to the internal curing effect of biochar enhancing long-term hydration.

Regarding the dynamic modulus, biochar consistently induces a modest decrease, more pronounced at higher W_{total}/B ratios, due to its high intrinsic porosity. MgO has negligible influence. At 28 days, the effect of biochar on dynamic modulus becomes minimal for low W_{total}/B ratios, reflecting matrix densification in agreement with porosity and density measurements.

5.3 Autogenous Shrinkages of mortars with biochar

In this section, the effect of the ICAs, specifically biochar, SAP, and silica, on the autogenous shrinkage is investigated from early age to the long term.

5.3.1 Deformation at early age

The conventional prism method, while useful, can solely assess autogenous deformation in specimens after demolding, overlooking the deformations that occur prior to demolding—an important aspect of evaluation. To address this, the corrugated tube method was used in our study to assess autogenous deformation before demolding.

5.3.1.1 Validation of the methodology

Figure 5.15 compares the autogenous shrinkage results measured during the first week by two different methods, namely the corrugated tube method and the prismatic specimen method. Overall, both approaches exhibit a consistent trend, indicating that the autogenous shrinkage develops rapidly within the first few days and then slows down afterwards. For REF-45 (Figure 5.15(a)) and B5-45 (Figure 5.15(b)), the magnitude of shrinkage obtained from the corrugated tube method is slightly higher than that from the prismatic specimens (14μm for REF-45 and 40μm for B5-45 at 7 days), but the two remain comparable within the experimental scatter. For M6-45 (Figure 5.15(c)) and B5M6-45 (Figure 5.15(d)), both methods produce closely matched values across the entire measuring period (22μm difference for M6-45 and 3μm

difference for B5M6-45). These results confirm that the corrugated tube method can effectively capture the evolution of autogenous shrinkage and provides results in good agreement with those obtained from prismatic specimens. Consequently, the methodology applied in this study is validated for further investigation of autogenous shrinkage.

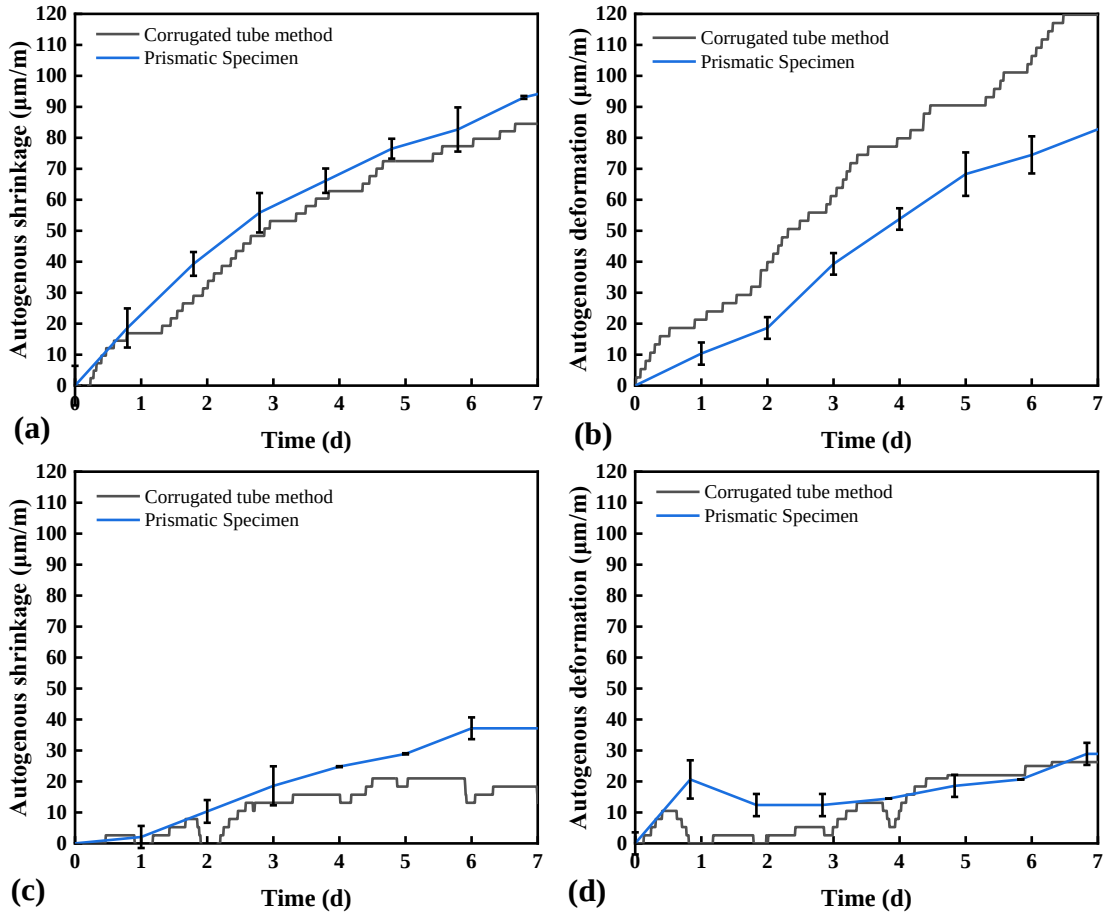


Figure. 5.15 Comparison of autogenous shrinkage results obtained by two methods in the first week after 1 day of curing: REF-45 (a); B5-45 (b); M6-45 (c); B5M6-45 (d) – at the time '0', the specimens are 1 day old.

5.3.1.2 Deformations at early age

It is important to note that conducting the corrugated tube test after the final setting time of the mixture ensures more reliable results. Consequently, determining the setting time of the specimen before employing the corrugated tube method becomes essential.

In our investigation, the initial and final setting times were measured using the

ultrasonic method, as illustrated in Table 5.1 for all mixtures. The addition of MgO notably delays setting, due to the moderately reactive nature of MgO used in this study. Specifically, the REF mixture showed initial and final setting times of 3.63 hours and 5.59 hours, respectively. The incorporation of biochar (B5) slightly extended these times to 4.13 hours and 6.36 hours, which can be attributed to its water absorption and delayed release behavior and the reduction of the cement content. When only MgO was added (M6), the setting times increased further to 4.78 hours and 7.36 hours. Most notably, the B5M6 mixture exhibited the longest setting times—5.50 hours for initial setting and 8.47 hours for final setting—reflecting the combined effects of biochar-induced internal curing and the delayed hydration kinetics of MgO.

To investigate autogenous deformation before demolding, the corrugated tube test was conducted starting two hours after the final setting time to ensure structural stability. The results for mixtures with a water-to-binder ratio of 0.45 are shown in Figure 5.16.

The REF mixture exhibited minimal deformation, with a brief period of slight expansion followed by stabilization. The B5 mixture showed a slightly greater expansion, likely due to internal curing effects from biochar and gradual water release.

Table. 5.1 Setting time

Name	Initial setting time (h)	Final setting time (h)
REF	3.63	5.59
B5-45	4.13	6.36
M6-45	4.78	7.36
B5M6-45	5.5	8.47

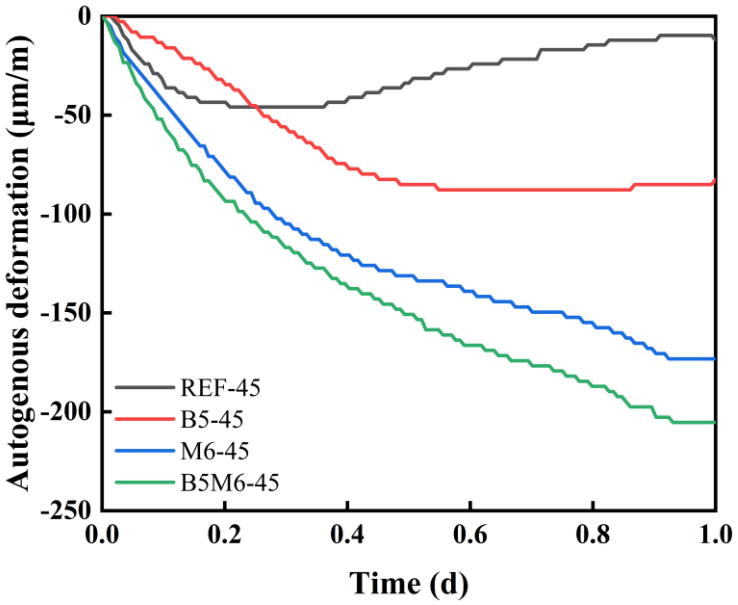


Figure. 5.16 Autogenous shrinkage during the 1st day

In contrast, the M6 mixture displayed significant expansion, reaching over +200 μm/m by the end of the first day. This expansion is attributed to the early-age hydration of MgO and the formation of brucite, which is known to produce volume increase.

Notably, the B5M6 mixture exhibited the highest degree of expansion, approaching +250 μm/m. This suggests that the combination of MgO and biochar creates a synergistic effect: biochar provides additional internal water, which enhances the extent of MgO hydration and magnifies the expansion behavior prior to demolding.

5.3.2 Autogenous deformation beyond 1 days

5.3.2.1 Effect of biochar, MgO and their coupling

Figure 5.17 illustrates the evolution of autogenous shrinkage from day 1 to 28 days as a function of the water-to-binder (W_{tot}/B) ratio and the incorporation of biochar, MgO, and their combination. At a W_{tot}/B ratio of 0.45 (Figure 5.17(a)), the reference specimen (REF) exhibits rapid shrinkage during the first month, reaching 155 μm/m at 7 days and 285 μm/m at 28 days. Specimen B5, containing 5 wt% biochar, shows a marked

reduction, with shrinkage limited to 116 μm/m and 207 μm/m, corresponding to decreases of 25.3% and 26.4% compared to REF. Specimen M6, incorporating 6 wt% MgO, displays an even greater reduction of 46.8% at 7 days and 53.8% at 28 days. The most significant effect is observed in specimen B5M6, where shrinkage decreases by 86.7% and 83.8% at 7 and 28 days, respectively, highlighting the strong water-retention capacity of biochar and the additional compensation effect provided by MgO.

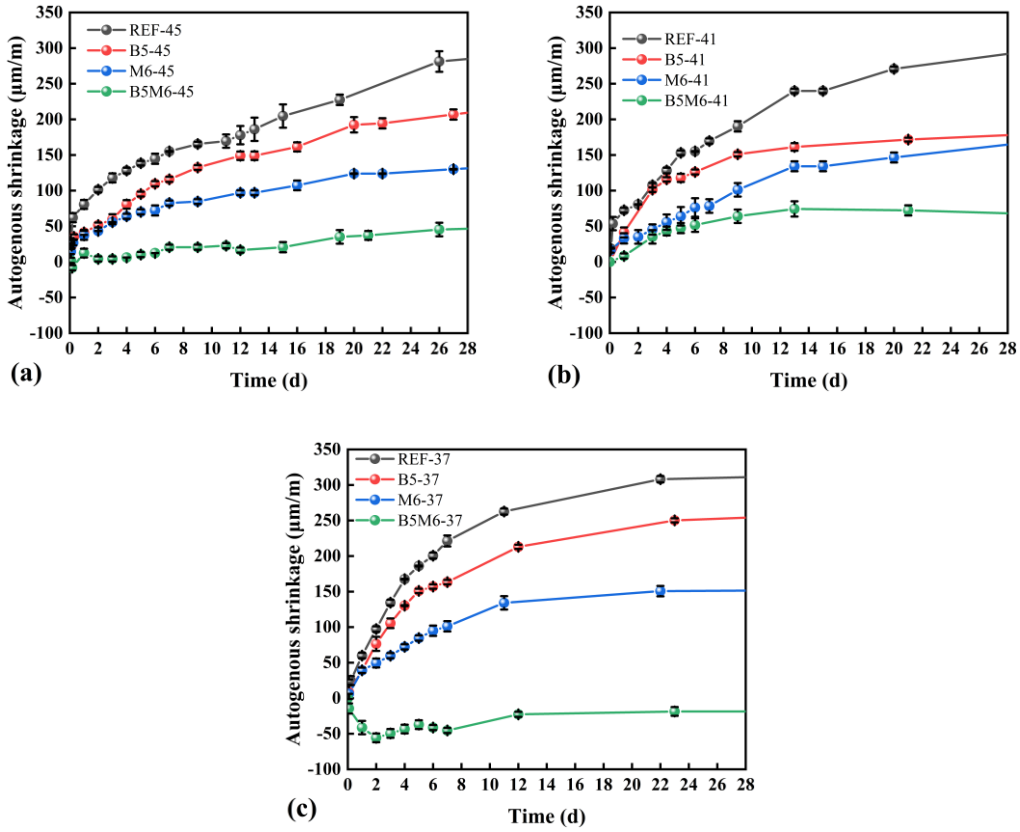


Figure. 5.17 Effects of biochar, MgO and their combinations on autogenous shrinkage at different water-to-binder ratios in the first month: W_{tot}/B=0.45 (a), W_{tot}/B=0.41 (b), W_{tot}/B=0.37 (c) - at the time '0', the specimens are 1 day old.

When the W_{tot}/B ratio is lowered to 0.41 (Figure 5.17(b)), REF exhibits shrinkage of 170 μm/m and 295 μm/m at 7 and 28 days, respectively. Specimen B5 shows reductions of 21% and 40.6%, whereas specimen M6 exhibits decreases of 53.7% and 46.6%. Specimen B5M6 maintains substantial shrinkage control, with reductions of 68.1% and 77.6% at 7 and 28 days, respectively. At this lower W_{tot}/B ratio, the internal curing

effect of biochar becomes more pronounced, while the synergistic contribution of MgO appears less significant than at 0.45.

At a further reduced W_{tot}/B ratio of 0.37 (Figure 5.17(c)), specimen B5 shows autogenous shrinkage of 163 μm/m and 260 μm/m at 7 and 28 days, corresponding to reductions of 26.2% and 14.6% compared to REF. Specimen M6 displays more pronounced decreases of 54.3% and 52.3% over the same periods. Remarkably, specimen B5M6 shows no shrinkage and instead exhibits slight expansion, with deformations of –45 μm/m at 7 days and –18 μm/m at 28 days.

Beyond the first month, Figure 5.18 shows that autogenous shrinkage evolves differently, with minimal or no deformation during the second month. At a W_{tot}/B ratio of 0.45 (Figure 5.18(a)), shrinkage at 56 days measures 304, 237, 132, and 35 μm/m for REF, B5, M6, and B5M6, respectively. Compared with 28-day values, REF and B5 show increases of 8.2% and 14.6%, respectively, whereas M6 remains almost constant and B5M6 decreases by 22.2%. These findings suggest that the incorporation of biochar and MgO helps limit late-stage shrinkage through improved water retention and sustained MgO hydration, consistent with the hydration results shown in Figure 5.3 and 5.5. At a W_{tot}/B ratio of 0.41 ((Figure 5.18(b)), 56-day shrinkage values are 318 μm/m for REF, 192 μm/m for B5, 150 μm/m for M6, and 62 μm/m for B5M6. Relative to 28-day measurements, REF and B5 exhibit small increases of 6% and 4.3%, respectively, while M6 decreases by 12.3% and B5M6 remains stable. At the lowest W_{tot}/B ratio of 0.37 (Figure 5.18(c)), REF and B5 show slight increases of 5.2% and 9.7% from 28 to 56 days, whereas M6 and B5M6 display no further deformation, indicating shrinkage stabilization. Collectively, these findings highlight the importance of W_{tot}/B ratio, biochar, and MgO in mitigating both early-age and long-term autogenous shrinkage.

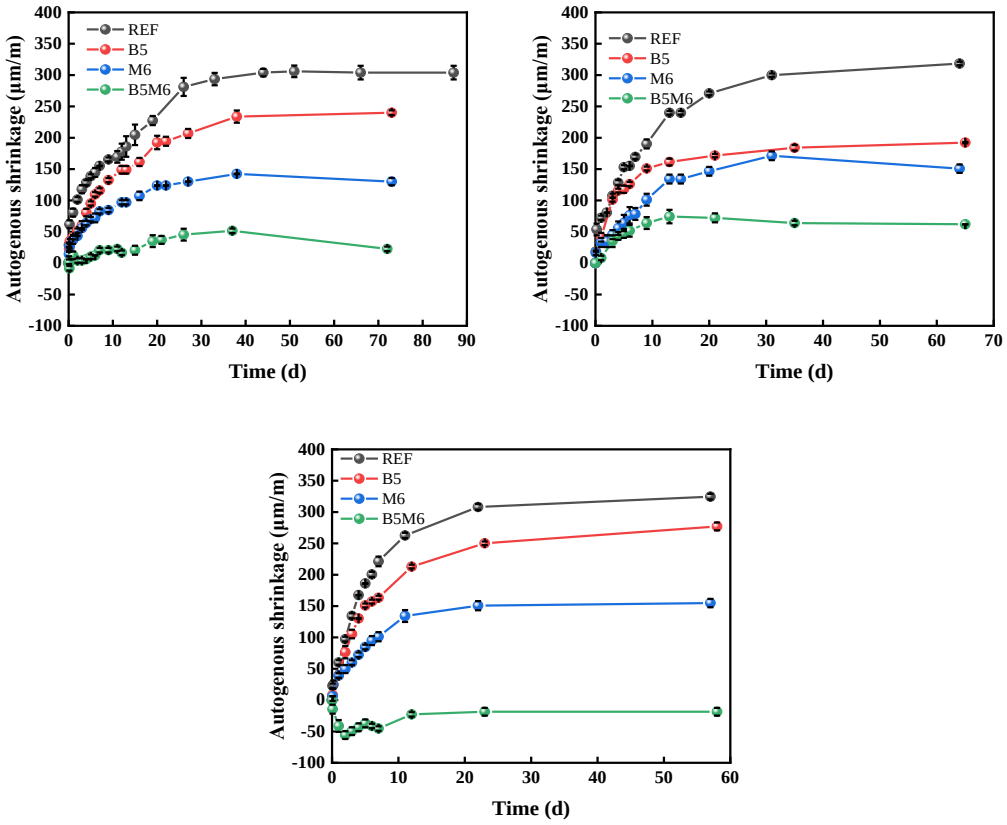


Figure. 5.18 Effects of biochar, MgO and their combinations on autogenous shrinkage at different water-to-binder ratios in the first two months

5.3.2.2 Effect of W/B ratio

Figure 5.19 highlights the influence of the W_{tot}/B ratio on autogenous shrinkage kinetics and the role of pore size–brucite coupling in promoting swelling at the macroscale and mitigating shrinkage. For REF, increasing W_{tot}/B reduces the initial slope of the shrinkage curve, indicating that specimens with lower W_{tot}/B ratios are more prone to early-age shrinkage; however, all curves stabilize after the first month (Figure 5.19(a)).

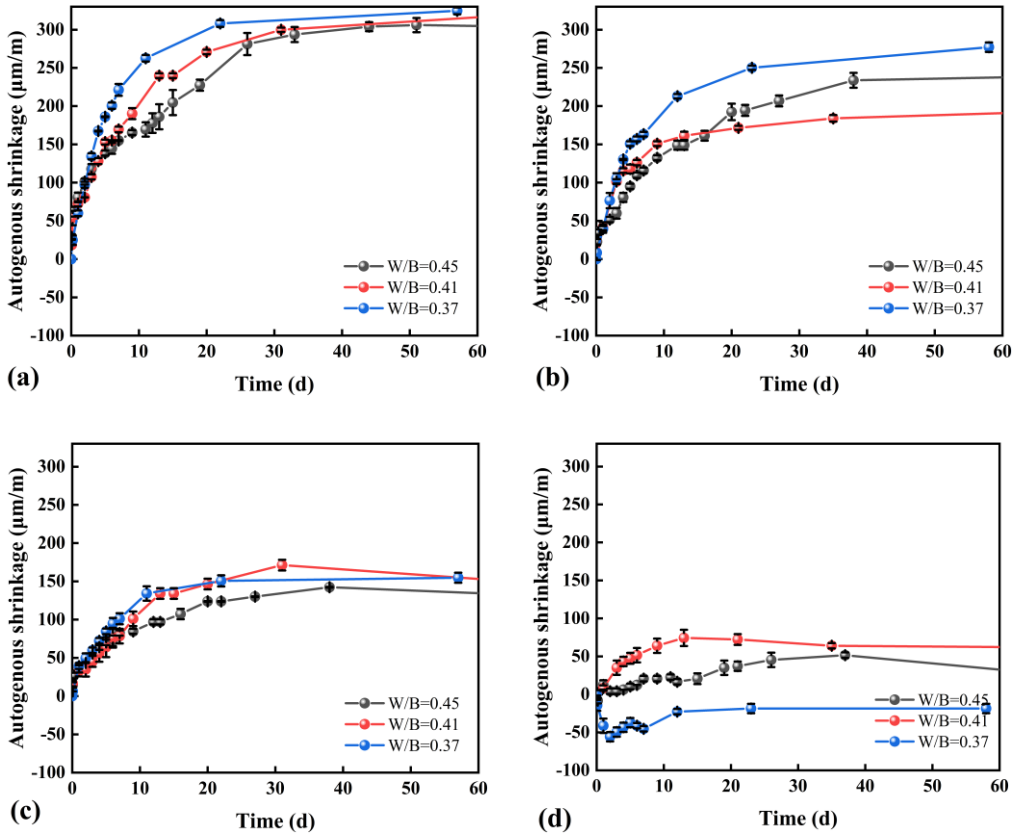


Figure. 5.19 Influence of water-binder ratio on autogenous shrinkage of different specimens: REF (a), B5 (b), M6 (c), B5M6 (d)

Specimens B5 follow a similar trend during the first week, regardless of W_{tot}/B, but the curve for W_{tot}/B = 0.41 stabilizes earlier, reflecting the enhanced shrinkage mitigation of biochar as an internal curing agent (ICA) at this ratio (Figure 5.19(b)). For M6, early autogenous shrinkage also decreases with increasing W_{tot}/B due to the higher free water content, which lowers capillary pressure as for REF (Figures 5.19(a–c)). At long term, deformations are slightly higher for W_{tot}/B = 0.41 and 0.37 but remain comparable, indicating effective coupling between brucite formation and pore refinement, which provides sufficient swelling to reduce shrinkage. For B5M6, deformation remains minimal across all W_{tot}/B ratios, with W_{tot}/B = 0.37 even showing slight expansion, attributed to the enhanced internal curing provided by biochar, which facilitates hydration of both cement and MgO, a phenomenon amplified at lower W_{tot}/B ratios due to reduced pore size.

5.3.2.3 Internal relative humidity

Figure 5.21 illustrates the evolution of autogenous shrinkage as a function of IRH (Figure 5.20 shows the development of IRH), highlighting the beneficial effect of coupling MgO with biochar. For a given IRH. gradient, the B5M6 mortars exhibit a lower autogenous shrinkage gradient across all W_{tot}/B ratios, confirming the synergistic action of the two additives. A similar trend is observed for the M6 mortar at a W_{tot}/B ratio of 0.37, indicating the positive contribution of brucite formation in a confined environment, which promotes matrix expansion and effectively limits shrinkage.

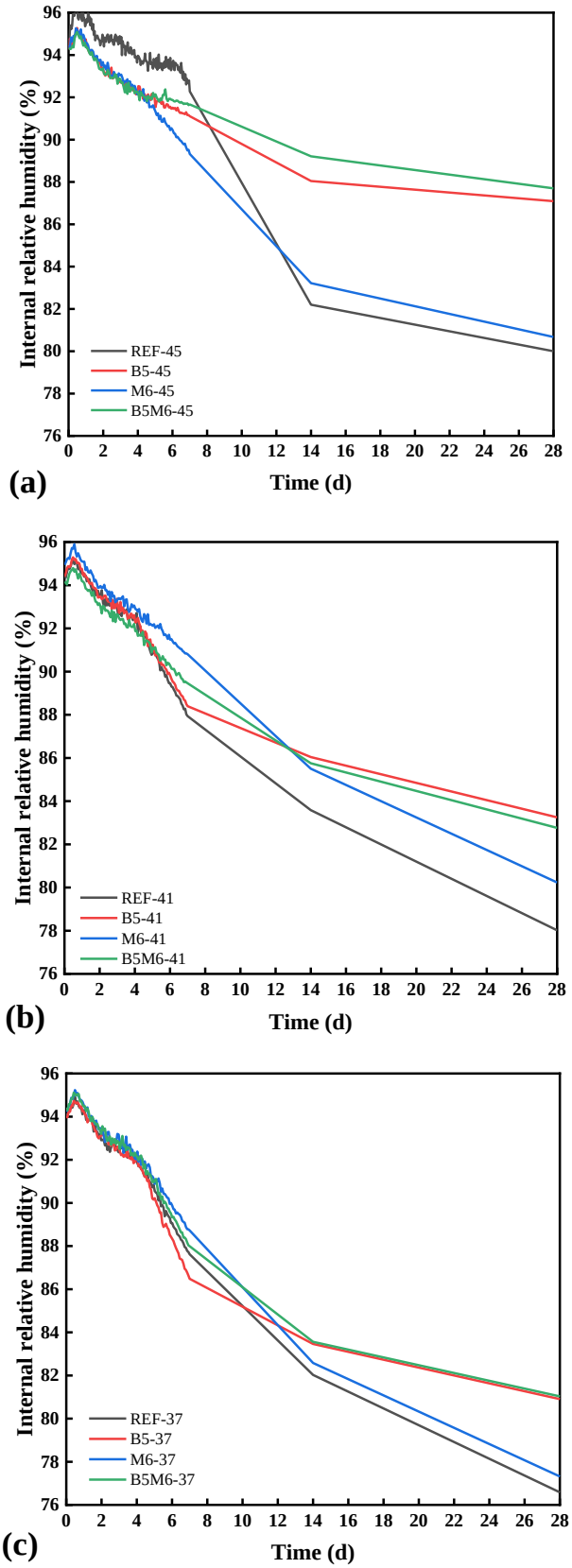


Figure 5.20. Effects of biochar, MgO and their combinations on IRH at different water-to-binder ratios – 0.45 (a), 0.41 (b), 0.37 (c)

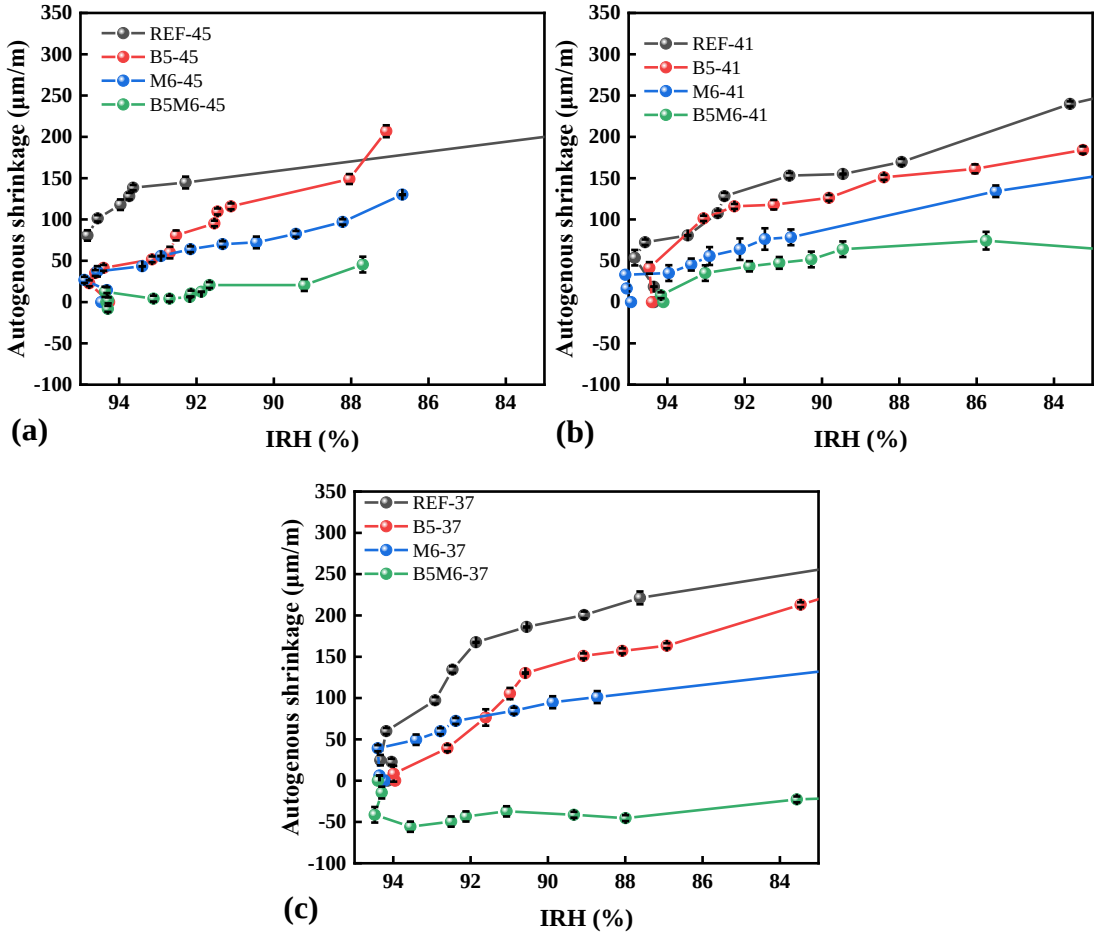


Figure. 5.21 Autogenous shrinkage that develops with IRH at different water-to-binder ratios: W_{tot}/B =0.45 (a), W_{tot}/B =0.41 (b), W_{tot}/B =0.37 (c)

5.3.2.4 Comparison with SAP and SIL

Figure 5.22 compares the efficiency of three internal curing agents—biochar, SAP, and silica—in providing water to sustain MgO hydration and mitigate autogenous shrinkage. At early ages, B5M6 shows the lowest shrinkage (21 μm/m at 7 days) due to biochar's rapid water release, whereas SAP2M6 and SIL6M6 exhibit higher values (85 and 93 μm/m). Long-term performance reveals silica's potential, with SIL15.4M6 achieving 53.3% and 37.1% lower shrinkage than B5M6 at 28 and 56 days, respectively. SAP, however, shows mixed results, with pre-saturation increasing porosity.

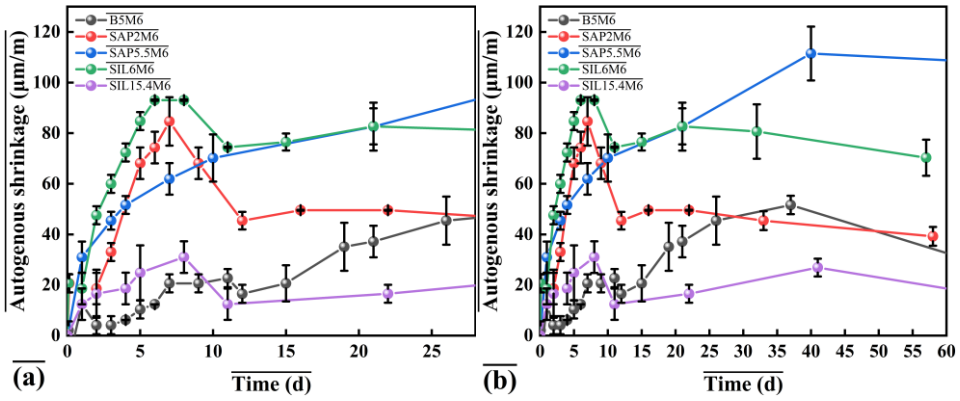


Figure. 5.22 The combined effect of other ICAs and MgO on autogenous shrinkage: The first month (a) The first two month (b)

5.3.3 Autogenous deformation from setting time

Figure 5.23 presents the autogenous shrinkage evolution for mortars with a water-to-binder ratio of 0.45, obtained by combining early measurements from the corrugated tube method with post-demolding data from prismatic specimens to ensure a continuous curve. Because the deformation occurring during the first day is included, the long-term autogenous shrinkage values appear lower than those obtained when only post-demolding data are considered. The reference mortar (REF-45) exhibits the highest shrinkage, exceeding 200 μm/m at 28 days. Incorporation of biochar (B5-45) significantly mitigates shrinkage through internal curing, while MgO alone (M6-45) further reduces deformation and induces slight early-age expansion due to its expansive hydration. The combined system (B5M6-45) achieves the greatest mitigation, with minimal shrinkage and even stable expansion, demonstrating a strong synergistic effect between biochar and MgO.

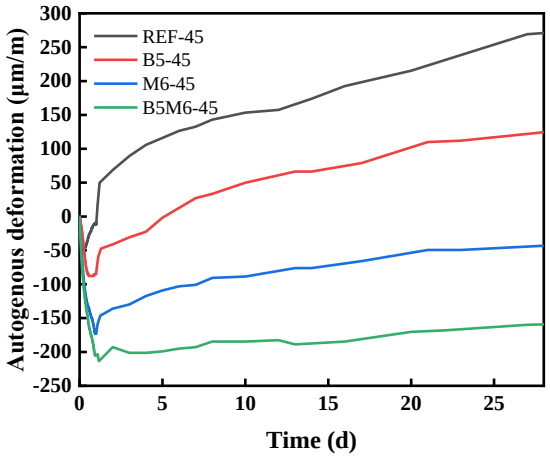


Figure. 5.23 Autogenous shrinkage from final setting time

5.4 Total and drying shrinkages of mortars with biochar

In this section, the total and drying shrinkage of mortars incorporating biochar, with or without MgO, are evaluated under drying conditions and compared to reference mixtures. The objective is to assess the benefits of biochar as an internal curing agent and its interactions with MgO in mitigating total shrinkage under more complex conditions characterized by the coupled effects of hydration and drying in the mortar matrix.

5.4.1 Total shrinkage

Figure 5.24 presents the total shrinkage of mortars containing biochar and MgO under drying condition for the three studied water-to-binder ratios (W_{total}/B = 0.45, 0.41, and 0.37). At W_{total}/B = 0.45, mixtures M6 and B5M6 show a clear reduction in total shrinkage compared to REF (810 μm/m at 28 days), reaching 665 and 634 μm/m at 28 days, corresponding to decreases of 17.3% and 22.6%, respectively. This beneficial effect persists at 56 days, with reductions of 13.2% and 16.9% relative to REF, mainly reflecting the pronounced decrease in autogenous shrinkage achieved by MgO and the MgO–biochar combination (Figure 5.17).

At $W_{total}/B = 0.41$, only M6 continues to provide meaningful shrinkage mitigation, with reductions of 10.8% and 11.4% at 28 and 56 days, respectively. Biochar-containing mixtures (B5, B5M6), however, do not reduce total shrinkage and for B5 even slightly exceed REF. At the lowest W_{total}/B ratio of 0.37, neither MgO nor biochar offers discernible benefits; biochar alone may even have a marginally adverse effect.

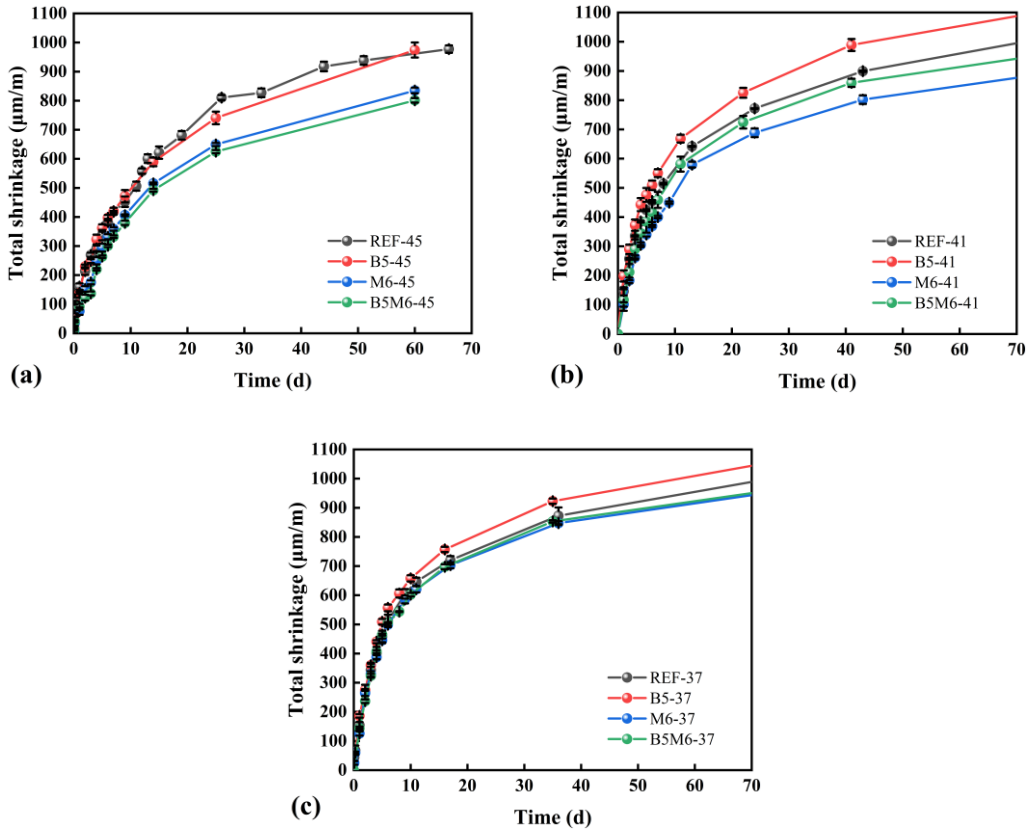


Figure. 5.24 Total shrinkage in the first two months: $W_{total}/B=0.45$ (a), $W_{total}/B=0.41$ (b), $W_{total}/B=0.37$ (c)

5.4.2 Drying shrinkage

Figure 5.25 presents drying shrinkage and mass loss for the four specimens at the different water-to-binder ratios.

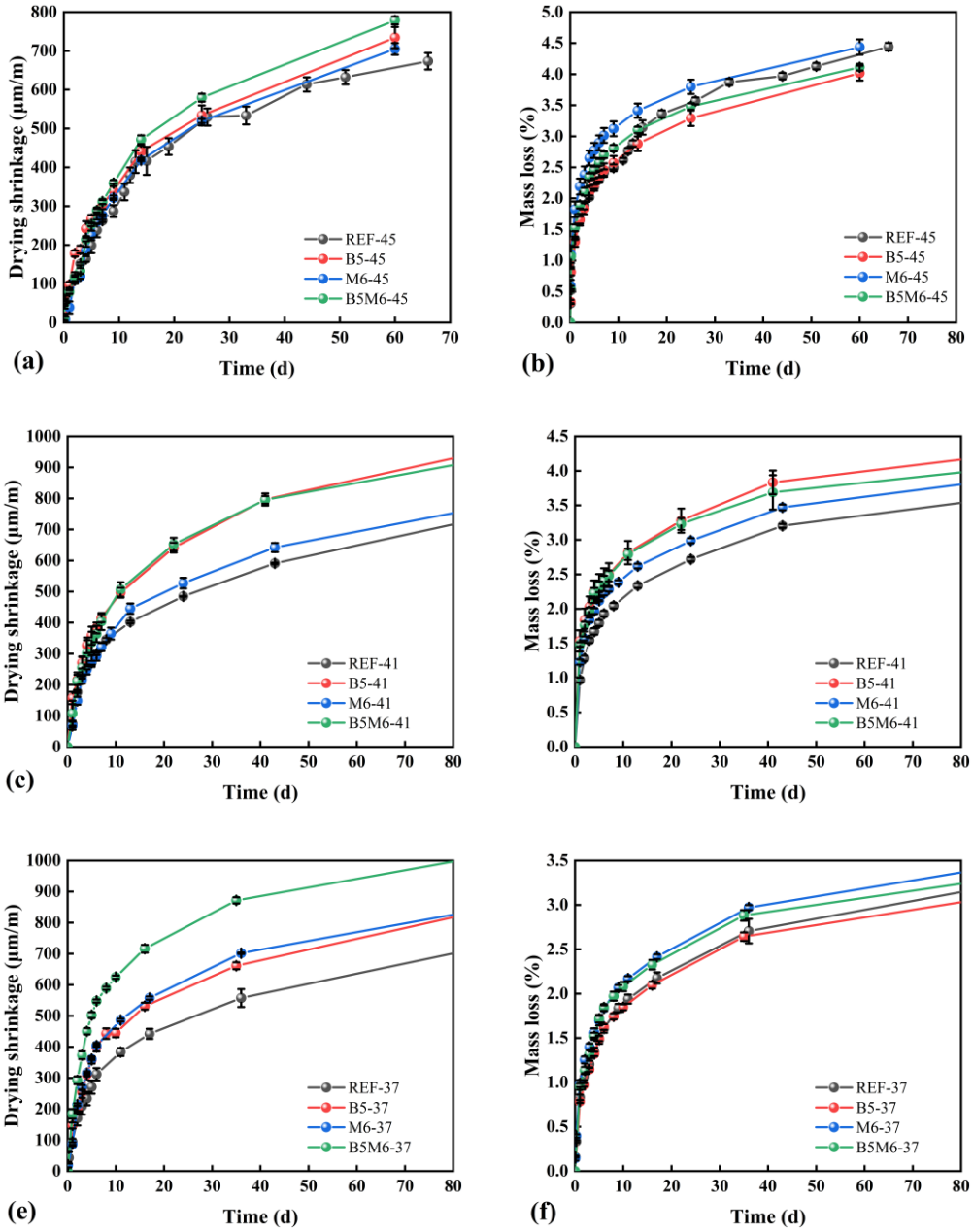


Figure. 5.25 Drying shrinkage and corresponding mass loss at different water-to-binder ratios in the first two months: Drying shrinkage for W_{total}/B=0.45 (a); Mass loss for W_{total}/B=0.45 (b); Drying shrinkage for W_{total}/B=0.45 (c); Mass loss for W_{total}/B=0.45 (d); Drying shrinkage for W_{total}/B=0.45 (e); Mass loss for W_{total}/B =0.45 (f);

At a W_{total}/B ratio of 0.45 (Figure 5.25(a–b)), drying shrinkage in B5, M6, and B5M6 shows a slight increase compared to the reference (REF) at long term. Mass loss of M6 is slightly higher than that of REF. For W_{total}/B = 0.41 (Figure 5.25(c–d)), the inclusion

of biochar (B5 and B5M6) leads to greater drying shrinkage. Mass loss in B5, M6, and B5M6 is also higher than in REF, further contributing to increased drying shrinkage. At the lowest W_{total}/B ratio of 0.37 (Figure 5.25(e–f)), B5, M6, and B5M6 continue to exhibit higher drying shrinkage than REF, with B5M6 showing the most pronounced effect—surpassing REF by 60.1% at 28 days and 49.3% at 56 days. In summary, biochar and MgO do not reduce drying shrinkage, and a negative effect is even observed as the W/B ratio decreases, particularly for mortars with biochar. It could be partially explained by their fast water release with the relative humidity reduction (Figure 2.20) and to the effect of the coupling between drying and hydration, reducing the MgO hydration and the swelling capacity of the matrix.

Figure 5.26 presents the drying shrinkage curve alongside mass loss data, offering valuable insights into the specimen's behavior. This curve can be effectively divided into two distinct stages, each with its characteristics:

- The initial stage occurs as the specimen transitions from the curing room to the drying environment. At the beginning of this stage, the intial IRH is relatively high, resulting in significant water loss due to evaporation with a limited drying shrinkage. This initial stage spans approximately two days, corresponding to mass losses falling within the range of 0-2.1 (W/B=0.45), 0-1.2 (W/B=0.41), and 0-1.1 (W/B=0.37) on the Figure 5.26.
- The second stage present a linear evolution for the drying shrinkage as function of the mass loss. The slope of this evolution is given in Table 5.2 for all the studied mixtures.

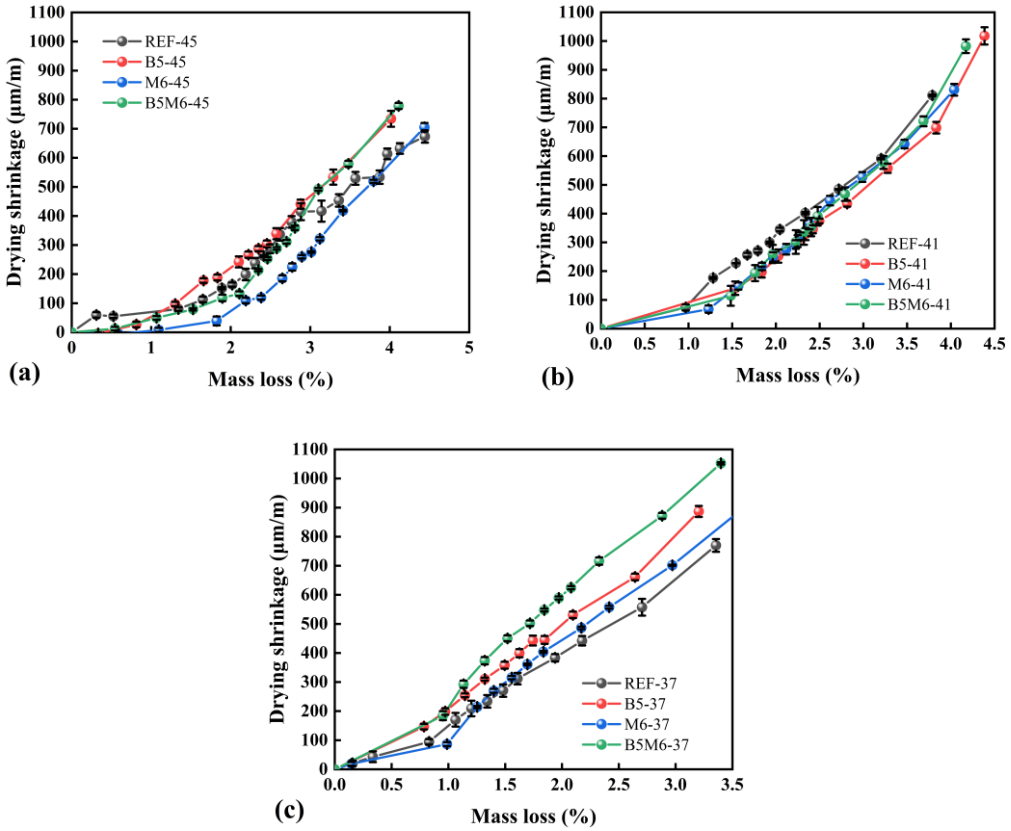


Figure. 5.26 Drying shrinkage that develops with mass loss: W/B=0.45 (a) W/B=0.41 (b) W/B=0.37 (c)

Upon reviewing Table 5.2, it becomes evident that, regardless of the water-to-binder ratio, the slopes of the curves follow the sequence REF < B5 < M6 < B5M6. When the water-to-binder ratio is 0.45, the slopes of B5 and REF are similar. However, this gap widens as the water-to-binder ratio decreases.

These results show that the boundary conditions of the experiments affect the effectiveness of ICAs as observed by [150]. Under drying conditions, external drying accelerates water loss through evaporation, generating negative capillary pressure that drives the rapid release of stored curing water from the biochar pores. Although this process can help reduce plastic cracking at very early ages, it simultaneously weakens the sustained internal curing effect that would otherwise mitigate autogenous shrinkage. Consequently, the expected benefits of biochar addition diminish as the severity of drying increases, particularly at lower W/B ratios where the pore structure is denser and

water transport is more restricted.

Table. 5.2 The slope of the second stage of the drying shrinkage versus mass loss curve

Specimen	The transition point to the second step (d)	The mass loss at the transition point (%)	Slope (μm/m·d⁻¹)
REF-45	2	1.7	223.21
B5-45	3	1.8	226.15
M6-45	2	2.2	248.52
B5M6-45	3	2.1	323.47
REF-41	2	1.3	222.39
B5-41	1	1.5	241.41
M6-41	1	1.2	274.37
B5M6-41	1	1.5	264.34
REF-37	2	1.1	243.71
B5-37	3	1.1	286.43
M6-37	1	1	289.43
B5M6-37	2	1.1	333.57

Taken together, these findings highlight the nuanced role of boundary conditions in determining ICA performance. While MgO and MgO–biochar combinations can effectively reduce total shrinkage under moderate W/B ratios (e.g., 0.45), their efficacy decreases substantially when external drying dominates. This underscores the need to tailor internal curing strategies not only to mixture composition but also to environmental exposure, ensuring that shrinkage mitigation remains effective under practical service conditions.

5.4.3 Comparison with SAP and SIL

Figure 5.27 shows that, under drying conditions, SIL6M6, SIL15.4M6, and B5M6 develop a quite similar total shrinkage, indicating that silica–MgO systems and the biochar–MgO composite provide a comparable effectiveness. By contrast, SAP2M6 records total shrinkage of 774 μm/m at 28 days and 938 μm/m at 56 days, closely tracking the REF mixture at both ages (Figure 5.24). The trend is more pronounced for SAP5.5M6, which exhibits the largest total shrinkage among the ICA–MgO systems.

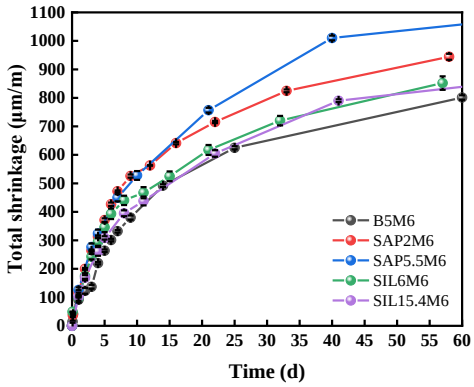


Figure. 5.27 The combined effect of other ICAs and MgO on total shrinkage

Figure 5.28 provides valuable insights into the collective impact of various ICAs in conjunction with MgO on drying shrinkage and mass loss within the studied specimens. Figure 5.28(a) highlights the markedly higher drying shrinkage of SAP2M6 and SAP5.5M6, exceeding B5M6 by 16.8% and 25.1% at 28 days, respectively. This increase stems from the intrinsic behavior of SAP. Upon absorbing water, SAP swells significantly; however, under drying conditions, the sharp drop in IRH accelerates water release, causing rapid polymer contraction. This contraction elevates capillary pressure, thereby intensifying drying shrinkage [63]. The high slopes in Table 5.3 (317.03 for SAP2M6 and 305.93 for SAP5.5M6) confirm that SAP-containing mixtures undergo faster shrinkage rates during the second stage, reflecting the unstable water retention and desorption kinetics of SAP.

In contrast, B5M6 exhibits a slope of 323.47, which, although high, is accompanied by a lower shrinkage magnitude at 28 days, indicating that biochar provides more gradual and buffered water release. Conversely, SIL6M6 and SIL15.4M6 show shrinkage trends similar to B5M6. This similarity is attributed to the higher volume stability of silica and biochar, which experience minimal deformation during water release, thus limiting capillary pressure build-up. Correspondingly, the lower slopes of SIL6M6 (255.82) and SIL15.4M6 (298.88) in Table 5.3 demonstrate that silica-containing mixtures maintain more stable shrinkage rates during the second stage, corroborating their enhanced dimensional stability.

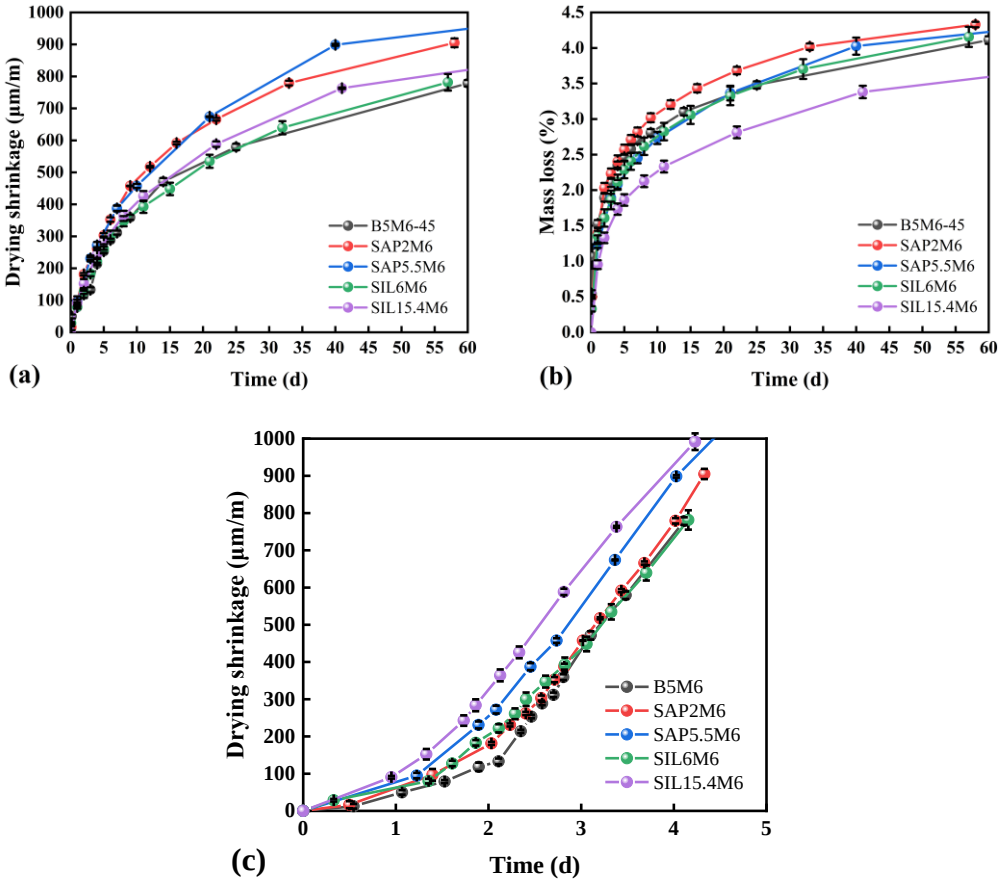


Figure. 5.28 The combined effect of other ICAs and MgO on drying shrinkage in the first two months: Drying shrinkage (a), Mass loss (b), Drying shrinkage that develops with mass loss (c)

Table. 5.3 The slope of the second stage of the drying shrinkage versus mass loss curve

Specimen	The transition point to the second step (d)	The mass loss at the transition point (%)	Slope (μm/m·d^{-1})
B5M6-45	3	2.1	323.47
SAP2M6	2	2	317.03
SAP5.5M6	3	1.9	305.93
SIL6M6	2	1.6	255.82
SIL15.4M6	2	1.3	298.88

5.4.4 Effect of the curing

To mitigate early mass loss due to sudden drying (Figure 5.24), an alternative curing

method (ACM) was explored and compared with normal curing (NC) whose the results were presented previously. All the specimens were demoulded after one day. For NC, specimens were dried immediately at 50% RH and 20 °C. For ACM, they were stored in sealed plastic bags for two days at 20 °C before drying began on the third day (ACM). The study focused on M6 and B5M6 mortars with W_{total}/B ratios of 0.45 and 0.37 to assess how curing conditions influence shrinkage and mass loss.

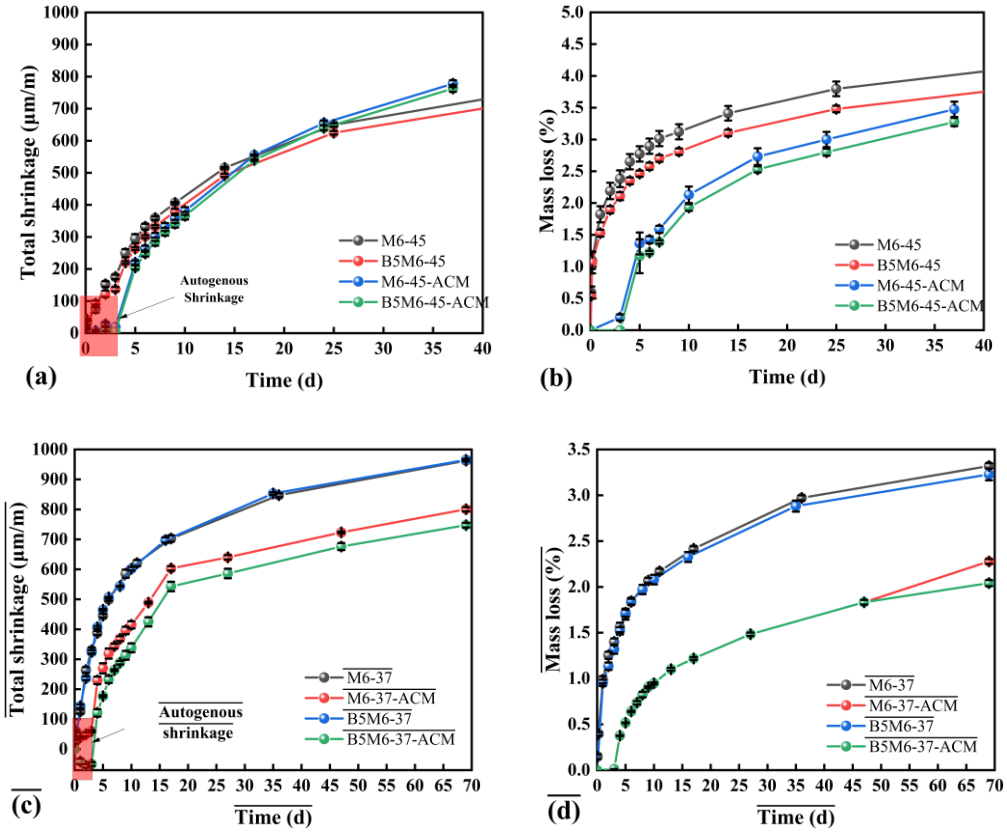


Figure 5.29 Comparison of total shrinkage and mass loss for two curing methods measurements starting from demolding: Total shrinkage (a) and Mass loss (b) forW_{total} /B=0.45, Total shrinkage (c) and Mass loss (d) for W_{total} /B=0.37

Results in Figure 5.29 show that ACM did not reduce the total shrinkage for mixtures with $W_{total}/B = 0.45$, as the high water content still allowed substantial evaporation once drying commenced. In contrast, for $W_{total}/B = 0.37$, ACM effectively reduced early-age shrinkage and slowed its progression, yielding reductions of 21.9% for M6 and 16.2% for B5M6 at 56 days. Mass loss data confirm these trends: ACM specimens with

W_{total}/B = 0.45 displayed faster long-term mass loss after Day 10, while those with W/B = 0.37 exhibited lower mass loss rates during the first two weeks.

These findings show that ACM is ineffective at high W_{total}/B but beneficial at low W_{total}/B, where it better preserves internal water and mitigates drying-induced deformation.

5.5 Summary

This study assessed mainly the influence of biochar and its synergy with MgO on the shrinkage behavior of cement mixtures across different water-to-binder ratios (W_{total}/B). These results show :

- *Autogenous Shrinkage Reduction*: Biochar, MgO, and especially their combination (B5M6) effectively reduce autogenous shrinkage, achieving up to 83.8% reduction at W_{total}/B = 0.45 and even expansion at W_{total}/B = 0.37.
- *Role of W/B Ratio*: Optimal mitigation is achieved by B5 at W_{total}/B = 0.41 and B5M6 at W_{total}/B = 0.37.
- *Swelling Behavior of MgO*: M6 exhibits continuous swelling, reaching 250 µm/m after 1 day, with swelling starting before demolding.
- *Water Release Dynamics*: Faster water release from biochar leads to lower early-age shrinkage compared to SAP and silica for a same water content.
- *Total and Drying Shrinkage*: At W_{total}/B = 0.45, M6 and B5M6 slightly reduce total shrinkage; at lower W_{total}/B, no benefit is observed. SAP increases total shrinkage, while silica has minimal effect. Drying shrinkage trends mirror total shrinkage.
- *Curing Method Influence*: The alternative curing method is ineffective at W_{total}/B = 0.45 but significantly reduces shrinkage and mass loss at W_{total}/B = 0.37.

Overall, shrinkage behavior depends strongly on ICA type, W/B ratio, and curing method, with biochar–MgO combinations offering the most promising results under optimized conditions.

Chapter 6. The effect of LWA and RCA on self-healing capacity

The ability of cementitious materials to autonomously repair microcracks—known as self-healing—is crucial for enhancing durability and reducing long-term maintenance in concrete structures. By limiting manual intervention, self-healing contributes to lower labor costs and extended service life.

This chapter examines the impact of LWA and RCA on the self-healing performance of mortar, with particular attention to the type of ICA and its coating, as well as the influence of curing conditions. These ICAs, by releasing stored water, may promote continued hydration and crack healing under sealed conditions.

The evaluation is conducted through 2D and 3D crack monitoring, tracking changes in CW and WF through the cracks, respectively, to determine the HR as a function of time. The objective is to identify optimal mixtures that promote efficient self-healing, thereby enhancing the sustainability and durability of cement-based materials. Based on the results in Chapter 4, LM10 and RC10 were selected as they exhibited optimal combinations of a good strength retention and shrinkage mitigation.

Six mortar compositions were prepared for self-healing evaluation, as summarized in Table 6.1. LM10 and RC10 contained 10% LWA and RCA, respectively, without encapsulation. LMC10 and RCC10 had the same aggregate content but were fully coated with hydrated MgO, while LM10C5 and RC10C5 combined 10% uncoated aggregate with an additional 5% encapsulated in MgO. The MgO coating was intended to promote healing by releasing expansive hydration products upon contact with water, aiding crack closure.

Two curing methods were applied: standard water curing and sealed plastic bag curing. Water-cured specimens (LM10, RC10, LMC10, RCC10, LM10C5, RC10C5) assessed the effect of aggregate type, content, and MgO encapsulation under saturated conditions. Sealed specimens (REF, LMC10, RCC10) allowed evaluation of healing driven solely

by internal curing, eliminating the influence of external water.

Table 6.1 Characteristics of the studied mortars for crack healing

Mixture	LWA content (%)	RCA content (%)	Coating
REF	0	0	-
LM10	10	0	-
RC10	0	10	-
LMC10	10	0	10% LWA with coating
RCC10	0	10	10% RCA with coating
LM10C5	15	0	5% LWA with coating
RC10C5	0	15	5% RCA with coating

6.1 Healing process under water curing

6.1.1 Crack width evolution : 2D approach

All specimens were continuously water-cured, both before and after WF tests. The average residual CW and the average HR, calculated from CW relative to the initial CW at 0 days (0D), are key indicators of self-healing capacity (Equation 3.15). For the mixtures tested, initial average CW values ranged from 201 μm to 230 μm (Table 6.2). CW evolution was assessed after 7, 28, and 90 days of water curing.

Figure 6.1 illustrates the relative change in CW as function of time, providing a clear overview of the self-healing dynamics of each mixture. This evolution is further illustrated by images of cracks on the specimen surface (Figure 6.2). Healing kinetics were strongly influenced by both mixture composition and initial CW. Initial cracks measuring 100–200 μm healed significantly faster than larger cracks, particularly in specimens with MgO-coated aggregates, where encapsulated water enhanced healing efficiency.

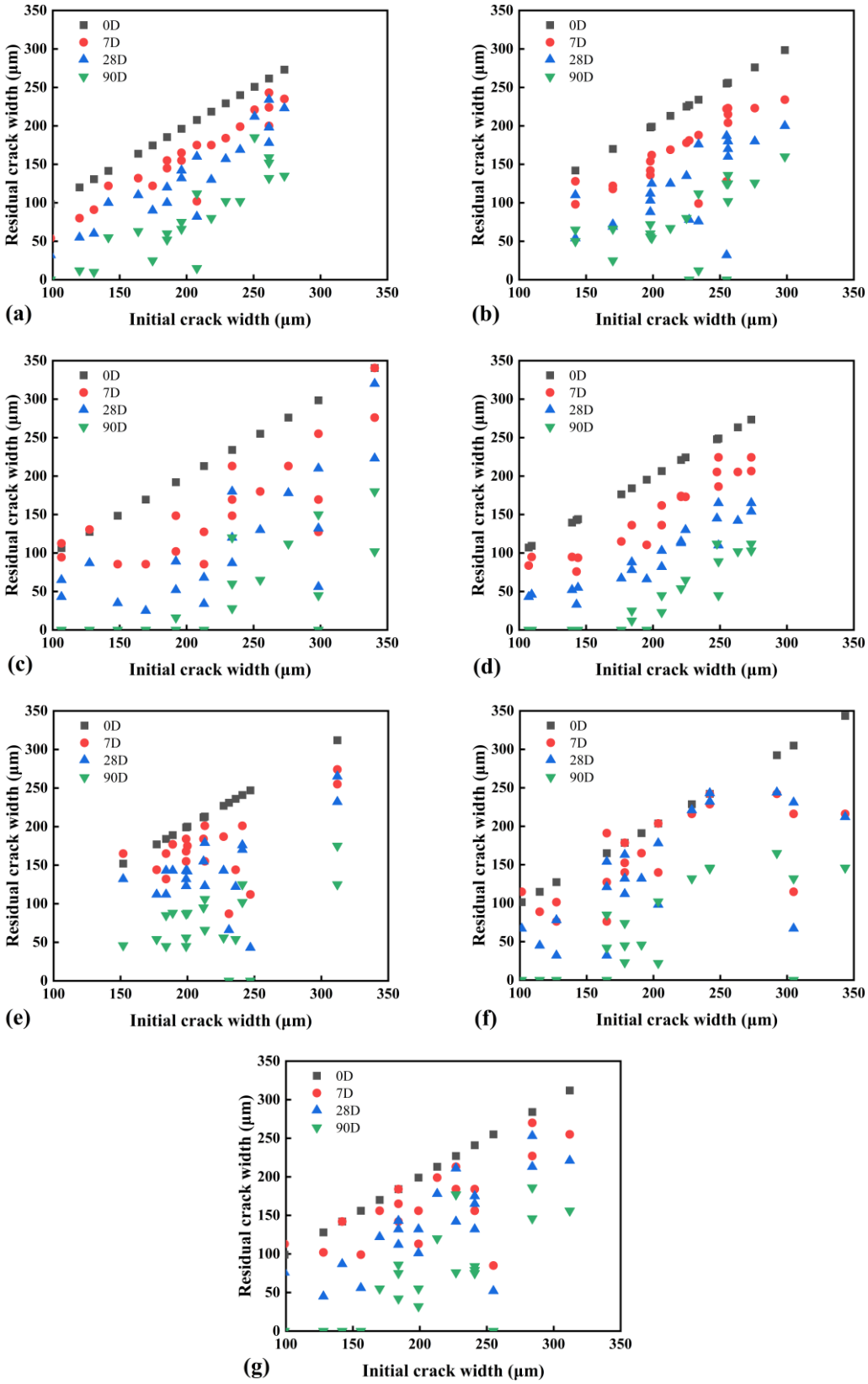


Figure. 6.1 CW evolution for REF (a) LM10 (b) LMC10 (c) LM10C5 (d) RC10 (e) RCC10 (f) RC10C5 (g)

After 90 days of water (90D), nearly all the initial cracks in the 100–150 μm range were completely closed. In MgO-coated mixtures (LMC10, LM10C5, RCC10, RC10C5), a substantial proportion of cracks 150–200 μm also healed, confirming both faster and more complete closure in these systems. Moreover, some initial cracks superior to 250 μm are also completely healed for all mixtures with a MgO-coating after 90 days of water curing. This long-term effect is linked to internal curing from encapsulated water, protected by the MgO coating within LWA and RCA, which sustains hydration and accelerates self-healing.

Table 6.2 Average initial and residual CW under water curing for all the studied mortars

Mixture	CW at 0D (μm)	CW at 7D (μm)	CW at 28D (μm)	CW at 90D (μm)
REF	201±51	169±57	134±57	80±54
LM10	230±46	168±44	121±50	75±46
LMC10	216±73	149±70	121±87	51±62
LM10C5	226±58	169±55	98±42	42±42
RC10	218±40	173±43	142±49	75±42
RCC10	228±76	182±63	140±73	65±61
RC10C5	209±55	166±51	137±59	72±6

Table 6.3 HR at 90D for cracks with different CW rate

Mixture	HR of all CW (%)	HR for the initial CW = [100-200] μm (%)	HR for the initial CW = [200-350] μm (%)
REF	60.2	73.2	52.3
LM10	67.4	80.6	58.6
LMC10	76.4	93.5	62.3
LM10C5	81.4	97.8	70.3
RC10	65.6	83.4	55.3
RCC10	71.5	91.3	58.9
RC10C5	65.6	82.6	60.2

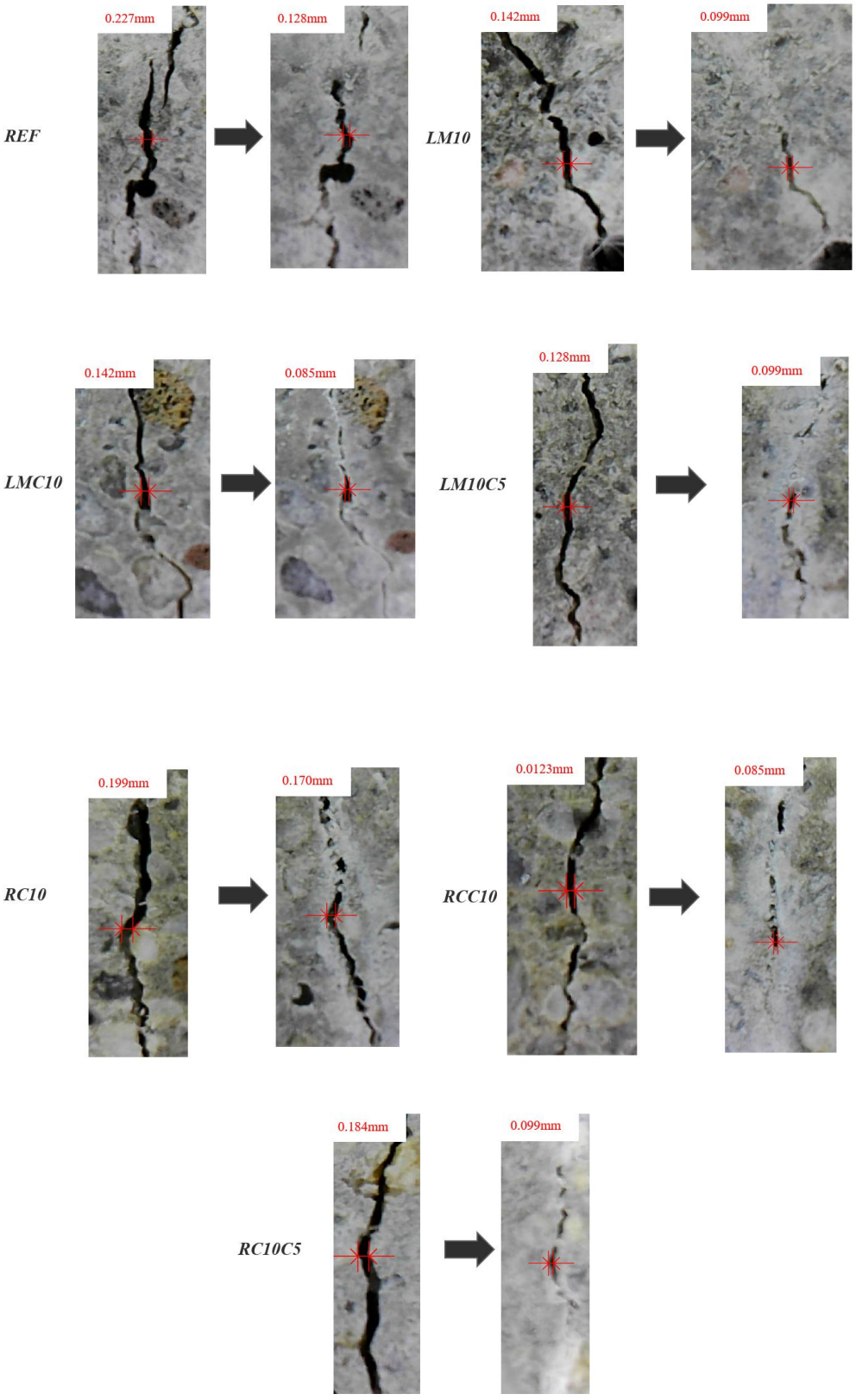


Figure. 6.2 Crack evolution on the specimen surface from 0D to 90D for all the studied mixture

Table 6.3 presents both the average HR and HR values categorized by CW. Two ranges were considered: 100–200 μm, favorable for closure through autogenous healing, and >200 μm, which typically requires additional autonomous healing.

The REF mixture exhibited the lowest average HR (60.2%), whereas the incorporation of ICAs enhanced healing performance. LWA-based systems outperformed RCA, with LM10 achieving 67.4% and further increasing to 76.4% with MgO coating (LMC10) and 81.4% when a combination of coated and uncoated ICAs was used (LM10C5). RCA-based systems also showed improvements, though to a lesser extent (RC10: 65.6%; RCC10: 71.5%).

When analyzed by CW, ICAs markedly improved healing of cracks smaller than 200 μm, reaching near-complete closure (e.g., LM10C5: 97.8%). Healing of larger cracks (>200 μm) was also enhanced, particularly when ICAs were partially coated to retain the healing solution, achieving up to 70.3% HR (LM10C5).

In summary, ICAs significantly enhance crack-healing efficiency, with LWA systems outperforming RCA. MgO coating provides additional benefits, though complete closure is mainly achieved in smaller cracks. These observations, however, are based on surface crack closure and may not represent the full extent of microstructural recovery—further analysis is needed to assess internal healing.

A recurring phenomenon, illustrated in Figure 6.2, was the formation of white precipitates along the cracks for all mixtures. This visual evidence further supports the role of the MgO coating combined with ICAs in improving self-healing performance, highlighting its potential for developing more durable and sustainable cement-based materials.

6.1.2 Water Flow : 3D approach

In this section, the HR was determined from the WF through cracks under an initially fixed water head. The evolution of WF is provided in Appendix C, while the

corresponding HR, calculated using Equation (3.16), is shown in Figure 6.3. Here, HR is analyzed as a function of the initial CW. To this end, two initial WF ranges, [10–15] g/min and [15–35] g/min, were selected, with the corresponding CW values summarized in Table 6.4. For each CW range, Figure 6.3 compares the HR evolution of all studied mixtures.

Table 6.4 Initial WF for specimens having a similar CW at 0D

Initial WF (g/min)	[10–15]	[15–35]
Initial CW (μm)	[100-200]	[200-350]

After 7 days of water curing (7D), mixtures with 10% and 15% LWA (LM10, LMC10, LM10C5) showed the highest HR values—34%, 35%, and 34%, respectively—compared to ~30% for RCA-based mixtures and the reference (REF). This improvement is attributed to LWA's higher water retention capacity (Tabel 2.2). After 28 days of water curing (28D), REF reached an HR of 50%, while LM10, LMC10, and LM10C5 rose to 57%, 60%, and 64%. RCA-based mixtures also exceeded slightly REF, reaching 53% (RC10), 55% (RCC10), and 53% (RC10C5). The benefit of MgO coating became more evident, with LM10C5 outperforming its uncoated counterpart. After 90 days of water curing (90D), complete healing (HR = 100%) was achieved by mixtures with a MgO-coating, while REF, LM10, and RC10 recorded 94%, 97%, and 96%, respectively. These results confirm that MgO coating effectively preserves internal water in LWA and RCA, enabling sustained hydration and long-term healing.

For specimens with initial CWs of [100–200 μm] (Figure 6.3(b)), HR values are higher compared to Figure 6.3(a). At 7D, REF exhibited 39%, while LM10, LMC10, and LM10C5 reached 42%, 44%, and 41%, respectively; RCA-based mixtures remained slightly lower at 37–39%. At 28D, LWA-based mixtures again outperformed REF (61%) and RCA-based mixtures (~64–65%), with LM10C5 achieving the highest recovery of 72%. By 90D, all mixtures reached complete recovery (HR = 100%),

suggesting that moderate CWs can be fully healed when sufficient internal water is available, particularly with the aid of MgO coating.

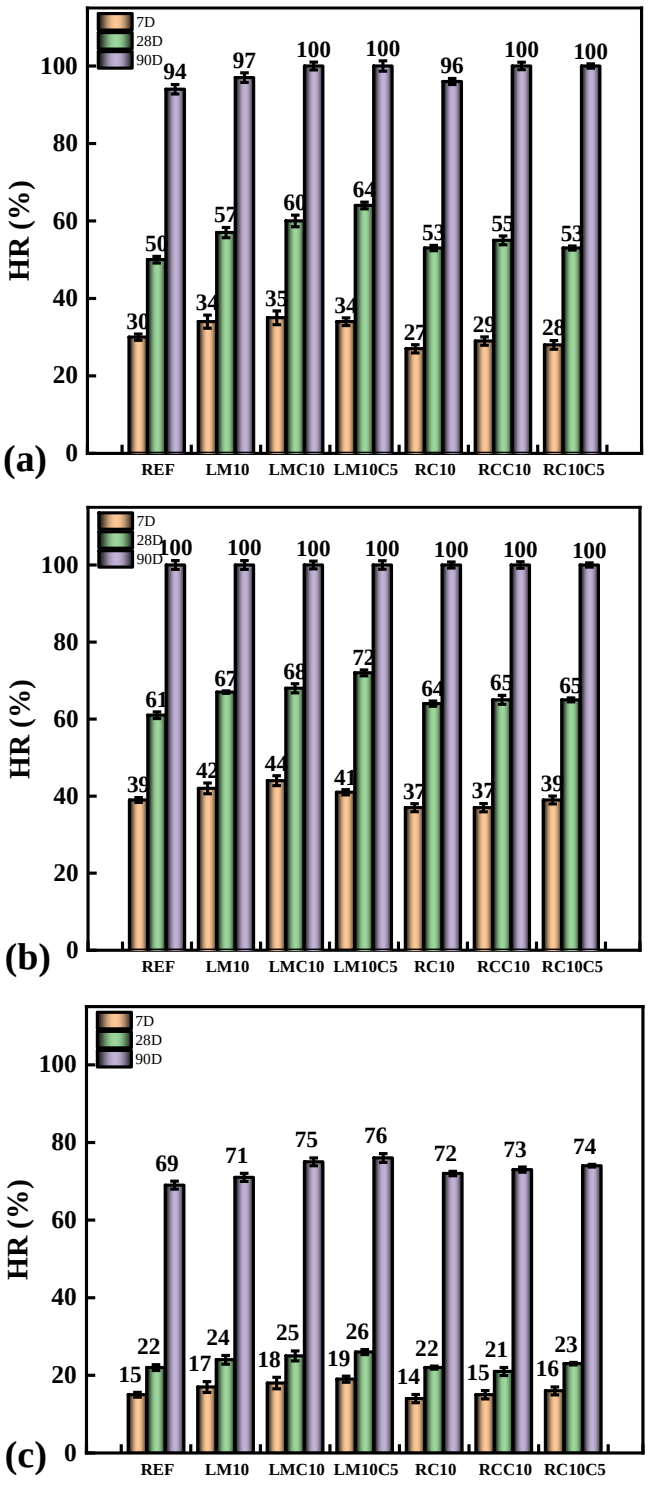


Figure. 6.3 Evolution of HR from the WF measurement for all the CW (a), the initial CW = [100-200] μm (b), the initial CW = [200-350] μm (c)

When the initial CW is further enlarged to [200–350 μm] (Figure 6.3(c)), the overall recovery become more limited. At 7D, HR values for all mixtures are below 25%, with

LM10, LMC10, and LM10C5 (17–19%) slightly outperforming REF (15%) and RCA-based systems (14–16%). At 28D, LM10C5 showed the highest recovery (26%), compared with REF (22%) and RCA-based mixtures (~21–23%). At 90D, the differences narrowed, but LM10C5 still reached 76%, while REF and RCA-based systems recorded ~69–74%. These results indicate that although wider cracks reduce the healing potential, the presence of LWA and MgO coating improves both the extent and rate of recovery, demonstrating their robustness in enhancing self-healing across different crack scales.

6.2 Healing process under sealed condition

To better replicate real-world curing conditions—where continuous access to external water is uncommon—additional tests were conducted under strictly sealed conditions. This approach aimed to assess self-healing performance in environments more representative of practical applications. By isolating the specimens from external moisture, the study focused on the contribution of ICAs to crack healing through internal curing.

After the initial WF tests, the specimens were sealed in plastic bags and stored in a controlled-humidity environment. This setup eliminated external water supply, enabling evaluation of the healing effect of water released from the aggregates. The tested specimens included the reference mix (REF), mortar with 10% coated LWA (LMC10), and mortar with 10% coated RCA (RCC10), all demolded after 28 days of standard curing. CW and WF were monitored from 0D to 90D, providing insights into long-term self-healing behavior under more realistic curing conditions.

6.2.1 Crack width evolution: 2D approach

Table 6.5 and Figure 6.4 illustrate the evolution of CW from initial cracking (0 days) to 90 days under sealed curing conditions. The reference specimens (REF) show a modest reduction of ~37.9% after 90 days of curing (Table 6.5). It reflects the limited

capacity of autogenous healing based on mechanism linked to residual hydration and carbonation.

Table 6.5 The evolution in CW and HR calculated with Equation (3.15) from 0D to 90D under sealed condition

Mixture	Average initial CW (μm)	7D		28D		90D	
		CW (μm)	HR (%)	CW (μm)	HR (%)	CW (μm)	HR (%)
REF	206±66	198±72	3.9	164±68	20.4	128±42	37.9
LMC10	239±66	224±65	2.1	152±64	36.4	72±56	69.9
RCC10	218±60	213±61	2.3	148±61	32.1	87±63	60.1

In contrast, LMC10 exhibited significantly enhanced healing, with average CWs decreasing from ~239 μm by 36.4% after 28 days and 69.9% after 90 days of curing. This accelerated performance is attributed to internal water supplied by LWA, which sustains hydration and promotes efficient crack closure. RCC10 also showed substantial healing (~60.1% CW reduction); although slightly slower than LMC10, these results confirm the effectiveness of recycled coarse aggregate in supporting internal curing and self-healing without external water. For LMC10 and RCC10, cracks closed more rapidly, allowing complete healing on surface for some cracks up to 220 μm and 150 μm, respectively (Figure 6.4). These results underscore the clear benefit of internal curing in enhancing self-healing.

Table 6.6 HR at 90D for cracks with different CW

Mixture	HR of all CW (%)	HR for the initial CW = [100-200] μm (%)	HR for the initial CW = [200-350] μm (%)
REF	37.9	48.3	25.6
LMC10	69.9	78.9	60.3
RCC10	60.0	69.2	51.4

Table 6.6 highlights the dependence of healing performance on the initial CW. For narrower cracks [100–200 μm], both LMC10 (78.9%) and RCC10 (69.2%) exhibited much higher HR than REF (48.3%), confirming the effectiveness of ICAs in promoting nearly complete healing under favorable conditions. However, when the CW increased to [200–350 μm], the recovery ratios declined significantly for all mixtures, with REF

reduced to only 25.6%. Nevertheless, LMC10 and RCC10 still maintained relatively high values of 60.3% and 51.4%, respectively, demonstrating that the beneficial effect of MgO-coated aggregates remains evident even under more severe crack scenarios.

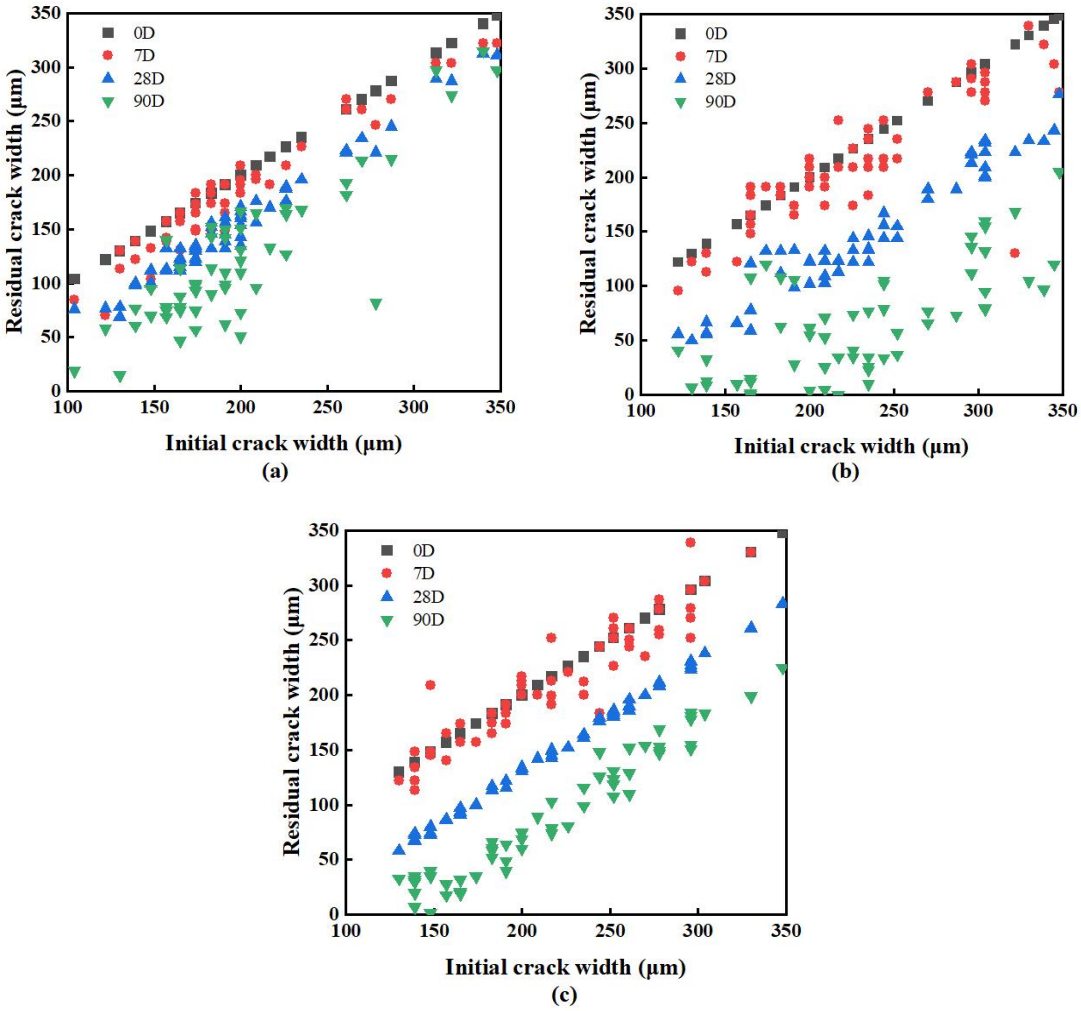


Figure 6.4. CW evolution for specimen REF (a), LMC10 (b) and RCC10 (c).\

6.2.2 Water flow: 3D approach

The previous results obtained from 2D observations are further validated using WF measurements, which provide a three-dimensional assessment of crack closure and healing efficiency.

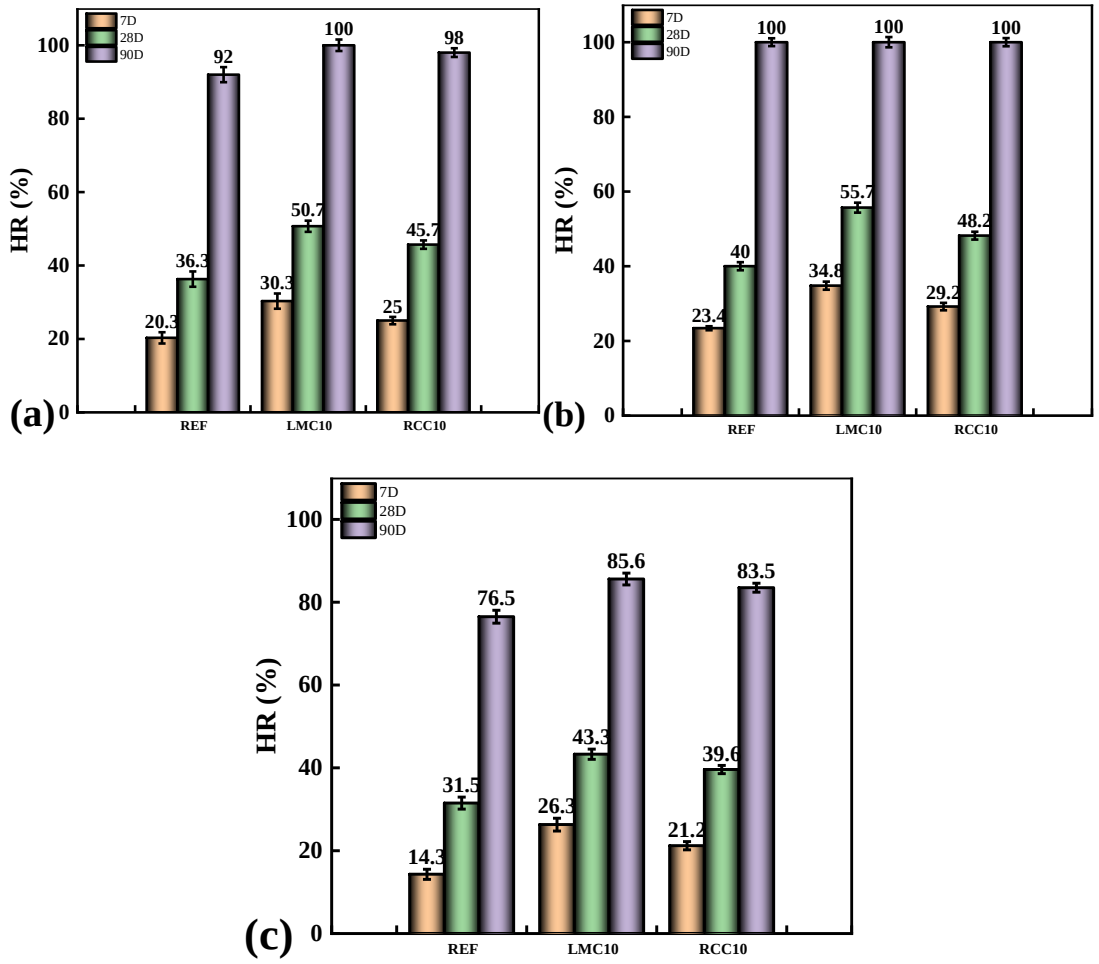


Figure 6.5. Evolution of HR for RCA, LMC10, and RCC10 under sealed curing for all the CW (a), the initial CW = [100-200] μm (b), the initial CW = [200-350] μm (c)

Under sealed curing, ICA significantly enhances HR, as shown in Figure 6.5(a). At 7 days, HR values reached 20.3% for REF, 30.3% for LMC10, and 25.0% for RCC10, indicating faster initiation of self-healing when ICAs were used. Between 7 and 28 days, HR increased by 16.0 % for REF, 20.4 % for LMC10, and 20.7 % for RCC10, confirming accelerated early-to-midterm kinetics due to ICA. From 28 to 90 days, REF exhibited the largest increase of HR (+55.7 %), nearly matching ICA mixtures (92% for REF vs. 100% and 98% for LMC10 and RCC10), likely due to additional water ingress coming from WF testing that promoted late hydration.

For narrow cracks (100–200 μm), shown in Figure 6.5(b), HR values were higher overall. At 7 days, REF, LMC10, and RCC10 reached 23.4%, 34.8%, and 29.2%, respectively, and by 28 days, LMC10 (55.7%) and RCC10 (48.2%) outperformed REF

(40.0%). All mixtures reached full healing (HR = 100%) at 90 days, confirming the ease of closure for smaller cracks.

For wider cracks (200–350 μm), Figure 6.5(c) shows modest HR growth up to 28 days but substantial long-term improvement, with RCC10 achieving 83.5% at 90 days, compared to 85.6% for LMC10 and 76.5% for REF. Although RCA-based mixtures generally displayed lower HR than those incorporating LWA, they still contributed to healing through mechanisms such as rougher interfacial surfaces and gradual accumulation of hydration products. The reduced efficiency of RCA is mainly linked to its less effective water release, which limits sustained internal curing compared to LWA. Nevertheless, the use of RCA can still enhance crack closure relative to the reference mortar. Overall, ICA improves HR across all CWs, with LMC10 providing rapid early-stage healing, while RCC10 demonstrates a moderate but measurable improvement in long-term recovery.

6.3 Summary

This chapter investigated the self-healing behavior of cementitious mortars containing LWA and RCA under water and sealed curing over 90 days, using CW and WF measurements. Under water curing, LWA-based (LM10) and RCA-based (RC10) mixtures showed improved healing due to internal water release, while MgO-coated aggregates (LMC10 and RCC10) achieved even higher HRs. Under sealed conditions, REF exhibited limited healing, whereas LMC10 and RCC10 maintained high HR, confirming that internal water alone can drive long-term self-healing.

LWA provided superior internal curing compared to RCA due to its higher porosity, while MgO coating enhanced water retention and facilitated sustained healing. Uncoated RC10 and LM10 were effective under water curing, but MgO-coated LMC10 and RCC10 delivered the most significant healing, even for larger cracks. These results demonstrate the synergistic effect of internal curing and MgO encapsulation, offering a practical strategy to enhance autonomous self-healing and improve the durability of

cementitious materials under moisture-limited conditions.

Chapter 7 General Conclusion

This thesis addressed the challenge of early-age cracking in cementitious materials by evaluating the effectiveness of internal curing strategies in enhancing both shrinkage control and self-healing capacity. In response to the growing demand for durable and sustainable concrete, the research focused on LWA, RCA, and biochar as ICAs. These materials were investigated for their ability to store and gradually release internal water, thereby sustaining cement hydration, mitigating autogenous and drying shrinkage, and enabling autonomous crack closure without external intervention.

A comprehensive experimental program was designed to:

(i) characterize the water absorption and release behavior of various ICAs;

(ii) evaluate their influence on hydration kinetics, mechanical performance, and shrinkage of mortar mixtures; and

(iii) assess self-healing under different curing regimes, including continuous water exposure and sealed conditions.

Effect of Pre-saturation of LWA and RCA

Pre-saturation ensured that aggregate pores were filled with water before mixing, enabling effective internal water reservoirs. The gradual release of this water during hydration reduced autogenous shrinkage and supported long-term hydration. Optimal results were obtained when pre-saturation was combined with suitable aggregate size and content. For coarse, high-porosity aggregates, vacuum-assisted pre-saturation maximized water uptake and improved internal curing efficiency. Conversely, incomplete saturation or poorly proportioned aggregate blends reduced these benefits.

Effect of LWA Particle Size and Content

LWA size and dosage significantly influenced mechanical properties. Finer particles (0.63–1.25 mm) enhanced compressive strength, flexural strength, and dynamic modulus by improving water distribution and internal curing efficiency. Larger particles tended to lower strength due to weaker matrix–aggregate interfaces and higher porosity. Increasing LWA content generally increased available curing water but could reduce

strength if excessive, as the porosity effect outweighed hydration benefits.

Effect of LWA on Autogenous Shrinkage

Finer LWA particles reduced autogenous shrinkage by improving spatial distribution of internal water. Higher contents, especially with larger particles, also mitigated shrinkage through greater water storage. Among tested mixtures, LM10 provided the most balanced performance, improving shrinkage resistance, mechanical strength, and self-healing simultaneously.

Effect of RCA Particle Size and Content

RCA incorporation generally reduced compressive strength due to its weaker intrinsic properties. Increasing RCA content rarely compensated for this loss through internal curing alone, although sealed curing conditions improved hydration from stored internal water and partially restored strength. Autogenous shrinkage mitigation was observed, especially in early stages, but finer RCA delayed water release, limiting early-age benefits. Over time, this delayed release supported later hydration. Drying shrinkage was more sensitive to RCA particle size and content, with higher porosity and smaller particles accelerating moisture loss and increasing shrinkage under drying conditions. Among the tested mixtures, RC10 (particle size 1.25–2.5 mm) under sealed curing achieved the most balanced performance, offering effective autogenous shrinkage mitigation and acceptable mechanical strength, while avoiding the excessive drying shrinkage observed in finer-particle RCA mixtures.

Effect of Biochar Pre-treatment

Biochar absorbed and released water rapidly, with near-maximum absorption achieved after 24 hours, making prolonged soaking unnecessary. Saturated biochar effectively contributed curing water, reducing shrinkage. Fine grinding slightly reduced total absorption but improved dispersion and matrix integration, enhancing performance under high relative humidity conditions.

Effect of Biochar, MgO, and Their Combination on Mechanical Properties

Biochar alone had limited impact on compressive and flexural strength but reduced dynamic modulus due to its porosity. MgO, whether alone or combined with biochar,

slightly reduced strength because of its expansive nature and delayed hydration. Combined use required careful proportioning to avoid excessive strength loss, especially at higher water-to-binder ratios where the effects of porosity and expansion were amplified.

Effect of Biochar, MgO, and Their Combination on Shrinkage

All three approaches—biochar, MgO, and their combination—reduced autogenous shrinkage, with the most significant reductions observed at lower water-to-binder ratios. MgO was particularly effective in mixtures with w/b of 0.41 and 0.37. However, drying shrinkage tended to increase slightly with ICA addition.

Crack Healing and HR Analysis

Self-healing performance was governed by ICA characteristics, particularly aggregate coating and particle content. Narrower cracks healed more rapidly. MgO coatings acted as moisture-retaining barriers, sustaining hydration and improving long-term HR. LWA mixtures achieved high HR values, with MgO-coated variants performing best due to extended water availability. These findings confirm the importance of both internal water storage and surface modification in promoting crack healing and enhancing durability.

Overall Conclusions

This study demonstrates that the performance of ICAs depends on their pre-saturation state, particle size, content, and interaction with other additives such as MgO. Well-designed ICA systems can significantly enhance hydration, control shrinkage, and improve autonomous crack healing, contributing to the development of durable and sustainable cementitious materials. The findings provide practical guidance for mixture optimization in both laboratory research and field applications, supporting the broader goal of eco-efficient, resilient concrete structures.

Reference

[1] Suzuki M, Meddah M S, Sato R. Use of porous ceramic waste aggregates for internal curing of high-performance concrete[J]. Cement and concrete research, 2009, 39(5): 373-381.

[2] Henkensiefken R, Briatka P, Bentz D, et al. Plastic shrinkage cracking in internally cured mixtures made with pre-wetted lightweight aggregate[J]. Concrete international, 2010, 32(2): 49-54.

[3] Bentz D P, Geiker M R, Hansen K K. Shrinkage-reducing admixtures and early-age desiccation in cement pastes and mortars[J]. Cement and concrete research, 2001, 31(7): 1075-1085.

[4] Darquennes, A., Rozière, E., Khokhar, M.I. , Turcry, Ph. , Loukili, A. , Grondin, F., 2012, "Long-term deformations and cracking risk of concrete with high content of mineral additions", Materials and Structures, 45, pp.1705-1716.

[5] Atsbha, T.G., Zhutovsky, S., The effect of external curing methods on the development of mechanical and durability-related properties of normal-strength concrete, Construction and Building Materials, 2022, 342: 127973.

[6] Ammar, L., 2022. Self-healing capacity of cementitious materials: Enhancement with expansive agents and mineral additions. Ph.D. Thesis, INSA Rennes, France.

[7] P. Mounanga, Etude expérimentale du comportement de pâtes de ciment au très jeune âge: hydratation, retraits, propriétés thermophysiques. PhD thesis, Nantes, 2003.

[8] Yang, G., Rao, Z., Wang, Z., & Yang, C. (2022). Internal curing using pre-wetted recycled coarse aggregate in recycled aggregate concrete: Effects on mechanical properties and durability. Materials, 15(15), 5383.

[9] Kushwah, S., Ranjan, A., Kumar, S., Kumar, S., & Bansal, P. P. (2024). Mixture of biochar as a green additive in cement-based materials: Pre-soaked biochar as an internal curing agent. Journal of Materials Science and Technology, 180, 88–101.

[10] Benboudjema, F., Darquennes, A., 2015, "Fissuration par retrait gêné dans les ouvrages en béton armé", Techniques de l'Ingénieur, c2255, 21p.

[11] Darquennes, A., Staquet, S., Delplancke-Ogletree, M.-P., Espion, B., 2011, "Effect of autogenous deformation on the cracking risk of slag cement concretes", Cement and Concrete Composites, 33, pp.368-379.

[12] Lura P. Autogenous deformation and internal curing of concrete[J]. 2003.

[13] Jensen O M , Hansen P F .Autogenous deformation and RH-change in perspective[J].Cement & Concrete Research, 2001, 31(12):1859-1865.

[14] Buffo Lacarriere, L., Baron, S., Barre, F., Chauvel, D., Darquennes, A., Dubois, J.-P., Gayete, J.-J., Grondin, F., Kolani, B., Lançon, H., Loukili, A., Moreau, G., Rospars, C., Sellier, A., Torrenti, J.-M. (2016). "Restrained shrinkage of massive reinforced concrete structures: Results of the project CEOS.fr." European Journal of Environmental and Civil Engineering, 20(7), 785–808.

[15] Aıtcin P C. The durability characteristics of high performance concrete: a review[J].

Cement and concrete composites, 2003, 25(4-5): 409-420.
[16] Darquennes, A., Khokhar, I., Rozière, E., Loukili, A., Grondin, F., Staquet, S., 2011, "Early age deformations of concrete with high content of mineral additions", Construction & Building Materials, 25, pp.1836-1847.
[17] Wang Y, Li X, Liu R. The capture and transformation of carbon dioxide in concrete: A review[J]. Symmetry, 2022, 14(12): 2615.
[18] Ammar, L., Hannawi, K., Darquennes, A., 2021. Effect of crystalline admixtures on deformation and self-healing. In: 2nd International Conference on Construction Materials for Sustainable Future (CoMS-2020/21), Slovenia, April 20–21.
[19] Lura P, Pease B, Mazzotta G B, et al. Influence of shrinkage-reducing admixtures on development of plastic shrinkage cracks[J]. ACI materials journal, 2007, 104(2): 187.
[20] Henkensiefken R, Nantung T E, Weiss W J. Reducing restrained shrinkage cracking in concrete: examining the behavior of self-curing concrete made using different volumes of saturated lightweight aggregate[C]//2008 Concrete Bridge ConferenceFederal Highway AdministrationNational Concrete Bridge CouncilMissouri Department of TransportationAmerican Concrete Institute (ACI). 2008.
[21] Henkensiefken R, Nantung T, Weiss J. Saturated lightweight Aggregate for internal curing in low w/c mixtures: monitoring water movement using X-ray absorption[J]. Strain, 2011, 47: e432-e441.
[22] Castro J, Keiser L, Golias M, et al. Absorption and desorption properties of fine lightweight aggregate for application to internally cured concrete mixtures[J]. Cement and Concrete composites, 2011, 33(10): 1001-1008.
[23] Bentz D P. A review of early-age properties of cement-based materials[J]. Cement and Concrete Research, 2008, 38(2): 196-204.
[24] Chang-Wen M, Qian T, Wei S, et al. Water consumption of the early-age paste and the determination of "time-zero" of self-desiccation shrinkage[J]. Cement and concrete research, 2007, 37(11): 1496-1501.
[25] Application of super absorbent polymers (SAP) in concrete construction: state-of-the-art report prepared by Technical Committee 225-SAP[M]. Springer Science & Business Media, 2012.
[26] Hiller K H. Strength reduction and length changes in porous glass caused by water vapor adsorption[J]. Journal of Applied Physics, 1964, 35(5): 1622-1628.
[27] Tazawa E, Miyazawa S. Influence of cement and admixture on autogenous shrinkage of cement paste[J]. Cement and concrete research, 1995, 25(2): 281-287.
[28] Almusallam A A. Effect of environmental conditions on the properties of fresh and hardened concrete[J]. Cement and Concrete composites, 2001, 23(4-5): 353-361.
[29] Gong, J., Mao, Z., Cao, Z., Huang, X., & Deng, M. (2023). Effect of different fineness of cement on the autogenous shrinkage of mass concrete under variable temperature conditions. Materials, 16(6), 2367.
[30] Hajibabaee A, Moradllo M K, Behravan A, et al. Quantitative measurements of curing methods for concrete bridge decks[J]. Construction and Building Materials,

2018, 162: 306-313.
[31] Farid Benboudjema, François Soleilhet, Xavier Jourdain, Fabrice Gatuingt. Effect of drying on the mechanical performances of concrete. Computational Modelling of Concrete Structures, Euro-C 2018, 2018, Bad Hofgastein, Austria. hal-02153183
[32] Liu J, Shi C, Ma X, et al. An overview on the effect of internal curing on shrinkage of high performance cement-based materials[J]. Construction and Building Materials, 2017, 146: 702-712.
[33] ASTM C989-10. Standard Specification for Slag Cement for Use in Concrete and Mortars. ASTM International, West Conshohocken, PA, 2010.
[34] Jensen O M, Hansen P F. Water-entrained cement-based materials: II. Experimental observations[J]. Cement and concrete research, 2002, 32(6): 973-978.
[35] Bentur A, Igarashi S, Kovler K. Prevention of autogenous shrinkage in high-strength concrete by internal curing using wet lightweight aggregates[J]. Cement and concrete research, 2001, 31(11): 1587-1591.
[36] Ghourchian S, Wyrzykowski M, Lura P, et al. An investigation on the use of zeolite aggregates for internal curing of concrete[J]. Construction and Building Materials, 2013, 40: 135-144.
[37] Weber S, Reinhardt H W. A new generation of high performance concrete: concrete with autogenous curing[J]. Advanced cement based materials, 1997, 6(2): 59-68.
[38] Lura P, Bentz D P, Lange D A, et al. Pumice aggregates for internal water curing[C]//Proceedings of International RILEM Symposium on Concrete Science and Engineering: A Tribute to Arnon Bentur. RILEM Publications SARL Evanston, 2004: 22-24.
[39] Zhutovsky S, Kovler K, Bentur A. Efficiency of lightweight aggregates for internal curing of high strength concrete to eliminate autogenous shrinkage[J]. Materials and Structures, 2002, 35(2): 97-101.
[40] Darquennes, A., Vasylchenko, M., Benboudjema, F., 2016. Size effect on the drying shrinkage of cement-based materials: Experimental investigations and poromechanical modeling. Cement and Concrete Research, 88, pp.30–41.
[41] Malbois, M., Darquennes, A., De Sa, C., Benboudjema, F., 2015, “Experimental study on effects of aggregates restraint on delayed behavior of cementitious materials”, CONCREEP-10, Vienne, 21-23 Septembre.
[42] El-Hawary M, Al-Sulily A. Internal curing of recycled aggregates concrete[J]. Journal of Cleaner Production, 2020, 275: 122911.
[43] Cusson D, Hoogeveen T. Internal curing of high-performance concrete with pre-soaked fine lightweight aggregate for prevention of autogenous shrinkage cracking[J]. Cement and Concrete Research, 2008, 38(6): 757-765.
[44] Lyu Y, Huang H, Ye G, et al. Autogenous shrinkage of zeolite cement pastes with low water-binder ratio[C]//14th International Congress on the Chemistry of Cement (ICCC 2015). 2015: 1-8.
[45] Lura P, Wyrzykowski M, Tang C, et al. Internal curing with lightweight aggregate

produced from biomass-derived waste[J]. Cement and concrete research, 2014, 59: 24-33.

[46] Rößler C, Bui D D, Ludwig H M. Rice husk ash as both pozzolanic admixture and internal curing agent in ultra-high performance concrete[J]. Cement and Concrete Composites, 2014, 53: 270-278.

[47] de Sensale G R, Ribeiro A B, Gonçalves A. Effects of RHA on autogenous shrinkage of Portland cement pastes[J]. Cement and concrete composites, 2008, 30(10): 892-897.

[48] Huang Z Y, Zhang C B. Effect of porous superfine powder on the performance of ultra-high performance concrete[J]. Bull. Chin. Ceram. Soc, 2015, 7: 22-27.

[49] Wyrzykowski M, Ghourchian S, Sinthupinyo S, et al. Internal curing of high performance mortars with bottom ash[J]. Cement and Concrete Composites, 2016, 71: 1-9.

[50] Wang P, Chen H, Chen P, et al. Effect of internal curing by super absorbent polymer on the autogenous shrinkage of alkali-activated slag mortars[J]. Materials, 2020, 13(19): 4318

[51] Li Z, Wyrzykowski M, Dong H, et al. Internal curing by superabsorbent polymers in alkali-activated slag[J]. Cement and Concrete Research, 2020, 135: 106123.

[52] Yang J, Sun Z, De Belie N, et al. Self-healing ability of cracks in alkali-activated slag systems incorporating superabsorbent polymers[J]. Cement and Concrete Research, 2023, 170: 107183.

[53] De Grave L, Tenório Filho J R, Snoeck D, et al. Poly (aspartic acid) superabsorbent polymers as biobased and biodegradable additives for self-sealing of cementitious mortar[J]. Journal of Sustainable Cement-Based Materials, 2023, 12(8): 925-940.

[54] Mihaljevic S N, Chidiac S E. Effective free water diffusion coefficient of cement paste internally cured with superabsorbent polymers[J]. Journal of Building Engineering, 2022, 45: 103600.

[55] Liu J, Farzadnia N, Khayat K H, et al. Effects of SAP characteristics on internal curing of UHPC matrix[J]. Construction and Building Materials, 2021, 280: 122530.

[56] Chidiac S E, Mihaljevic S N, Krachkovskiy S A, et al. Efficiency measure of SAP as internal curing for cement using NMR & MRI[J]. Construction and Building Materials, 2021, 278: 122365.

[57] Snoeck D, Goethals W, Hovind J, et al. Internal curing of cement pastes by means of superabsorbent polymers visualized by neutron tomography[J]. Cement and Concrete Research, 2021, 147: 106528.

[58] Jiang D, Li X, Lv Y, et al. Autogenous shrinkage and hydration property of alkali activated slag pastes containing superabsorbent polymer[J]. Cement and Concrete Research, 2021, 149: 106581.

[59] S.-i. Igarashi, A. Watanabe, Experimental study on prevention of autogenous deformation by internal curing using super-absorbent polymer particles, in: Volume changes of hardening concrete: testing and mitigation Proceedings of the international RILEM conference, 2006, pp. 77–86.

[60] Jindal A, Mehra D. Effects of Inclusion of SAP as an Internal Curing Agent in Concrete–A Review[J]. Civil Engineering Infrastructures Journal, 2024.
[61] Hong G, Kim J, Song C, et al. Effect of internal curing by superabsorbent polymers on the densification and microstructural development of cementitious materials exposed to different environmental conditions[J]. Construction and Building Materials, 2024, 411: 134778.
[62] Zheng S, Chen H, Xiao Y, et al. Water distribution characteristics of capillary absorption in internally cured concrete with superabsorbent polymers[J]. Construction and Building Materials, 2024, 418: 135446.
[63] Tutkun B, Barlay E S, Yalçınkaya Ç, et al. Effect of internal curing on shrinkage and cracking potential under autogenous and drying conditions[J]. Construction and Building Materials, 2023, 409: 134078.
[64] Chen F, Bai S, Guan X, et al. Influence of type and particle size of superabsorbent polymer on early water distribution and internal curing zone properties of cement paste[J]. Cement and Concrete Composites, 2024, 150: 105526.
[65] Jin Z, Xie F, Cai D, et al. Experimental study on fracture and acoustic emission properties of internally cured concrete with super absorbent polymer subjected to high temperature[J]. Journal of Building Engineering, 2023, 77: 107471.
[66] Jensen O M, Lura P. Techniques and materials for internal water curing of concrete[J]. Materials and Structures, 2006, 39(9): 817-825.
[67] Henkensiefken R, Bentz D, Nantung T, et al. Volume change and cracking in internally cured mixtures made with saturated lightweight aggregate under sealed and unsealed conditions[J]. Cement and Concrete Composites, 2009, 31(7): 427-437.
[68] Wang D, Shi C, Wu Z, et al. A review on ultra high performance concrete: Part II. Hydration, microstructure and properties[J]. Construction and Building Materials, 2015, 96: 368-377.
[69] Babcock A E, Taylor P. Impacts of internal curing on concrete properties[J]. 2015
[70] Zhang J, Wang Q, Zhang J. Shrinkage of internal cured high strength engineered cementitious composite with pre-wetted sand-like zeolite[J]. Construction and Building Materials, 2017, 134: 664-672.
[71] Hwang S D, Khayat K H, Youssef D. Effect of moist curing and use of lightweight sand on characteristics of high-performance concrete[J]. Materials and structures, 2013, 46(1): 35-46.
[72] Akcay B, Tasdemir M A. Effects of distribution of lightweight aggregates on internal curing of concrete[J]. Cement and Concrete Composites, 2010, 32(8): 611-616.
[73] RecyBeton (2018). Recyclage du béton dans le béton : tout savoir sur les granulats recyclés. Éditions Le Moniteur, Paris.
[74] Whwah, M. S.; Mahmmod, L. M. R.; Abdoulhaleem, H. H.; Dulaimi, A. (2024). Internal Curing Utilising Recycled Concrete Aggregate: A Sustainable Approach for Improving High-Strength Concrete's Performance.
[75] Corinaldesi V, Moriconi G. Influence of mineral additions on the performance of

100% recycled aggregate concrete. Constr Build Mater 2009;23:2869–76.
[76] Gómez-Soberón JMV. Porosity of recycled concrete with substitution of recycled concrete aggregate: an experimental study. Cem Concr Res 2002;32:1301–11.
[77] Katz A. Properties of concrete made with recycled aggregate from partially hydrated old concrete. Cem Concr Res 2003;33:703–11.
[78] Rao A. Experimental investigation on use of recycled aggregates in mortar and concrete [thesis]. Kanpur (India): Indian Institute of Technology, Kanpur; 2005.
[79] Zhang Y, Maierdan Y, Guo T, et al. Biochar as carbon sequestration material combines with sewage sludge incineration ash to prepare lightweight concrete[J]. Construction and Building Materials, 2022, 343: 128116.
[80] Cuthbertson D, Berardi U, Briens C, et al. Biochar from residual biomass as a concrete filler for improved thermal and acoustic properties[J]. Biomass and bioenergy, 2019, 120: 77-83.
[81] Wang D, Jantwal A, Kaynak E, Sas G, Das O. Promoting internal curing in concrete by replacing sand with sustainable biochar. Case Studies in Construction Materials, 2025, 22: e04542.
[82] Du J, Wang Y, Bao Y, Sarkar D, Meng W. Valorization of waste-derived biochar in ultra-high-performance concrete (UHPC): pretreatment, characterization, and environmental benefits. Construction and Building Materials, 2023, 409: 133839.
[83] Sirico A, Bernardi P, Sciancalepore C, et al. Biochar from wood waste as additive for structural concrete[J]. Construction and Building Materials, 2021, 303: 124500.
[84] Van Tuan N, Ye G, van Breugel K. Internal curing of ultra high performance concrete by using rice husk ash[C]//International RILEM Conference on Material Science. RILEM Publications SARL, 2010: 265-274.
[85] Mechtcherine V, Dudziak L, Hempel S. Mitigating early age shrinkage of ultra-high performance concrete by using super absorbent polymers (SAP)[J]. Proceedings of the Creep, Shrinkage, and Durability Mechanics of Concrete and Concrete Structures, 2009: 847-853.
[86] Zhutovsky S, Kovler K, Bentur A. Influence of cement paste matrix properties on the autogenous curing of high-performance concrete[J]. Cement and Concrete Composites, 2004, 26(5): 499-507.
[87] Lura P, Jensen O M, Van Breugel K. Autogenous shrinkage in high-performance cement paste: An evaluation of basic mechanisms[J]. Cement and concrete research, 2003, 33(2): 223-232.
[88] Ye G. Mitigation of autogenous shrinkage of ultra-high performance concrete by rice husk ash[J]. Journal of the Chinese Ceramic Society, 2012, 40(2): 212-216.
[89] Van Tuan N, Ye G, Van Breugel K, et al. Hydration and microstructure of ultra high performance concrete incorporating rice husk ash[J]. Cement and Concrete Research, 2011, 41(11): 1104-1111.
[90] Bui D D. Rice husk ash a mineral admixture for high performance concrete[J]. 2001.
[91] Zhang J, Lv T, Hou D, et al. Synergistic effects of fly ash and MgO expansive additive on cement paste: Microstructure and performance[J]. Construction and

Building Materials, 2023, 371: 130740.
[92] Cui Y, Wang H, Liu K, et al. Rheological, deformation behaviors and mechanical changes of MgO-containing concretes with different strength[J]. Journal of Building Engineering, 2023, 64: 105593.
[93] Oppong F, Yao N, Zhang W, et al. Tentative application of expansive cementitious materials in grouting–A systematic review[J]. Case Studies in Construction Materials, 2023, 18: e02113.
[94] El-Hawary M, Internal curing of concrete using recycled concrete aggregates as a medium for water supplementation, Journal of Cleaner Production, 2020, 159: 286–296.
[95] Sanjeewa H V A N, Asamoto S. A review of mechanical properties of deteriorated concrete due to delayed ettringite formation and its influence on the structural behavior of reinforced concrete members[J]. Construction and Building Materials, 2024, 422: 135795.
[96] Aghaee K, Sposito R, Thienel K C, et al. Effect of additional water or superplasticizer on key characteristics of cement paste made with superabsorbent polymer and other shrinkage mitigating materials[J]. Cement and Concrete Composites, 2023, 136: 104893.
[97] Zhao X, Mao Z, Huang X, et al. Effect of Curing Conditions on the Hydration of MgO in Cement Paste Mixed with MgO Expansive Agent[J]. Materials, 2023, 16(11): 4032.
[98] Li M, Liu J, Tian Q, et al. Efficacy of internal curing combined with expansive agent in mitigating shrinkage deformation of concrete under variable temperature condition[J]. Construction and Building Materials, 2017, 145: 354-360.
[99] T.C. Powers, T.L. Brownyard, Studies of the physical properties of hardened Portland cement paste//Journal Proceedings, 43(9) (1946) 101-132.
[100] Hansen T C. Physical structure of hardened cement paste. A classical approach[J]. Materials and Structures, 1986, 19(6): 423-436.
[101] Hasholt M T, Jensen O M, Kovler K, et al. Can superabsorent polymers mitigate autogenous shrinkage of internally cured concrete without compromising the strength?[J]. Construction and Building Materials, 2012, 31: 226-230.
[102] Lura P, Jensen O M, Igarashi S I. Experimental observation of internal water curing of concrete[J]. Materials and structures, 2007, 40(2): 211-220.
[103] Yang L, Shi C, Liu J, et al. Factors affecting the effectiveness of internal curing: A review[J]. Construction and Building Materials, 2020: 121017.
[104] Castro J, Henkensiefken R, Nantung T, et al. LWA absorption and desorption: the influence on the microstructure and transport properties of internally cured mortars[J]. CONSEC10, 2010.
[105] Tazawa E, Miyazawa S. Effect of constituent and curing conditions on autogenous shrinkage of concrete[C]. Proceedings of International Workshop on Autogenous Shrinkage of Concrete, Japan, 1998: 269–280.
[106] Zhutovsky S, Kovler K, Bentur A. Assessment of distance of water migration in internal curing of high-strength concrete[J]. ACI SP-220 ‘Autogenous

deformation of concrete'. Farmington Hills, Michigan, 2004: 181-197.
[107] Bentz D P, Snyder K A. Protected paste volume in concrete: Extension to internal curing using saturated lightweight fine aggregate[J]. Cement and concrete research, 1999, 29(11): 1863-1867.
[108] Akcay B, Tasdemir M A. Optimisation of using lightweight aggregates in mitigating autogenous deformation of concrete[J]. Construction and Building Materials, 2009, 23(1): 353-363.
[109] Lu B, Shi C, Zheng J, et al. Carbon dioxide sequestration on recycled aggregates[M]//Carbon dioxide sequestration in cementitious construction materials. Woodhead Publishing, 2018: 247-277.
[110] Yang Saili. Experimental study on the physical and mechanical properties and substance transfer law of internally cured self-compacting concrete[D]. Dalian University of Technology, 2017.
[111] Elsharief A, Cohen M D, Olek J. Influence of lightweight aggregate on the microstructure and durability of mortar[J]. Cement and Concrete research, 2005, 35(7): 1368-1376.
[112] Sarkar S L, Satish C, Leif B. Interdependence of microstructure and strength of structural lightweight aggregate concrete[J]. Cement and Concrete Composites, 1992, 14(4): 239-248.
[113] Bentz D P. Influence of internal curing using lightweight aggregates on interfacial transition zone percolation and chloride ingress in mortars[J]. Cement and concrete composites, 2009, 31(5): 285-289.
[114] Chia K S, Zhang M H. Water permeability and chloride penetrability of high-strength lightweight aggregate concrete[J]. Cement and concrete research, 2002, 32(4): 639-645.
[115] Issa C A, Debs P. Experimental study of epoxy repairing of cracks in concrete[J]. Construction and Building Materials, 2007, 21(1): 157-163.
[116] QY Zuo, HQ Chu, XP Yang, et al. Research on the effect of cationic surfactants on the healing effect of concrete cracks repaired by electrodeposition method [J]. Concrete, 2020 (3): 33-38.
[117] De Belie, N., Gruyaert, E., Al-Tabbaa, A., Antonaci, P., Baera, C., Bajãre, D., Darquennes, A., Davies, R., Ferrara, L., Jefferson, T., Litina, C., Miljevic, B., Otlewska, A., Ranogajec, J., Roig, M., Paine, K., Pawel, L., Serna, P., Tulliani, J.-M., Vucetic, S., Wang, J., Jonkers, H. (2018). A review on self-healing concrete for damage management of structures. Advanced Materials Interfaces, 5(17), 1800074.
[118] Vijay K, Murmu M, Deo S V. Bacteria based self healing concrete–A review[J]. Construction and Building Materials, 2017, 152: 1008-1014.
[119] Feng J, Dong H, Wang R, et al. A novel capsule by poly (ethylene glycol) granulation for self-healing concrete[J]. Cement and Concrete Research, 2020, 133: 106053.
[120] Self-healing phenomena in cement-Based materials: state-of-the-art report of RILEM technical committee 221-SHC: self-Healing phenomena in cement-Based

materials[M]. Springer Science & Business Media, 2013.1-17.
[121] Sangadji S. Can self-healing mechanism helps concrete structures sustainable?[J]. Procedia engineering, 2017, 171: 238-249.
[122] Zhang W, Zheng Q, Ashour A, et al. Self-healing cement concrete composites for resilient infrastructures: A review[J]. Composites Part B: Engineering, 2020, 189: 107892.
[123] Snoeck D, De Belie N. Repeated autogenous healing in strain-hardening cementitious composites by using superabsorbent polymers[J]. Journal of Materials in Civil Engineering, 2016, 28(1): 1-11
[124] Kua H W, Gupta S, Aday A N, et al. Biochar-immobilized bacteria and superabsorbent polymers enable self-healing of fiber-reinforced concrete after multiple damage cycles[J]. Cement and Concrete Composites, 2019, 100: 35-52
[125] Liu H, Huang H, Wu X, et al. Effects of external multi-ions and wet-dry cycles in a marine environment on autogenous self-healing of cracks in cement paste[J]. Cement and Concrete Research, 2019, 120: 198-206
[126] Wang J , Dewanckele J , Cnudde V , et al. X-ray computed tomography proof of bacterial based self-healing in concrete[J]. Cement & Concrete Composites, 2014, 53:289-304
[127] Edvardsen C . Water Permeability and Autogenous Healing of Cracks in Concrete[J]. Aci Materials Journal, 1999, 96(4):448-454
[128] Han B, Zhang L, Ou J. Smart and Multifunctional Concrete Toward Sustainable Infrastructures[M]. Springer Singapore, 2017. 117-155
[129] Khaliq W, Ehsan M B. Crack healing in concrete using various bio influenced self-healing techniques[J]. Construction and building materials, 2016, 102: 349-357.
[130] Tziviloglou E, Wiktor V, Jonkers H M, et al. Bacteria-based self-healing concrete to increase liquid tightness of cracks[J]. Construction and Building Materials, 2016, 122: 118-125.
[131] Han S, Jang I, Choi E K, et al. Bacterial self-healing performance of coated expanded clay in concrete[J]. Journal of Environmental Engineering, 2020, 146(7): 04020072.
[132] Kanellopoulos A, Giannaros P, Al-Tabbaa A. The effect of varying volume fraction of microcapsules on fresh, mechanical and self-healing properties of mortars[J]. Construction and Building Materials, 2016, 122: 577-593.
[133] Jakubovskis R, Jankutė A, Guobužaitė S, et al. Prolonging bacterial viability in biological concrete: Coated expanded clay particles[J]. Materials, 2021, 14(11): 2719.
[134] Alghamri R, Kanellopoulos A, Al-Tabbaa A. Impregnation and encapsulation of lightweight aggregates for self-healing concrete[J]. Construction and Building Materials, 2016, 124: 910-921.
[135] Alghamri R, Kanellopoulos A, Litina C, et al. Preparation and polymeric encapsulation of powder mineral pellets for self-healing cement based materials[J]. Construction and building Materials, 2018, 186: 247-262.

[136] EN 1097-6. Tests for mechanical and physical properties of aggregates-Part 6: Determination of particle density and water absorption[J]. 2013.

[137] EN 933–1. Tests for geometrical properties of aggregates‐part 1: Determination of particle size distribution[J]. The Office for Standards Metrology and Testing, 2012.

[138] IFSTTAR. Test N° 78:2011. Tests on granulates in concrete: measurement of total water absorption of crushed sand.

[139] Tam V W Y, Gao X F, Tam C M, et al. New approach in measuring water absorption of recycled aggregates[J]. Construction and building materials, 2008, 22(3): 364-369.

[140] Tegguer A D. Determining the water absorption of recycled aggregates utilizing hydrostatic weighing approach[J]. Construction and Building Materials, 2012, 27(1): 112-116.

[141] EN 196-1. European committee for standardization[J]. Methods of testing cement–Part 1: Determination of strength, 1995.

[142] Khaliq W, Javaid W. Efficiency Comparison of Conventional and Unconventional Curing Methods in Concrete[J]. ACI Materials Journal, 2017, 114(2).

[143] Zhang Z, Li S, Chen P, et al. Mitigating shrinkage in ultra-high performance concrete using MgO expansion agents with different activity levels[J]. Frontiers in Materials, 2022, 9: 1033467.

[144]He T, Xiang W, Zhang J, et al. Influence of Water-Binder Ratio on the Mechanical Strength and Microstructure of Arch Shell Interface Transition Zone[J]. Buildings, 2022, 12(4): 491.

[145] Akcay B, Tasdemir M A. Optimisation of using lightweight aggregates in mitigating autogenous deformation of concrete[J]. Construction and Building Materials, 2009, 23(1): 353-363.

[146] Bentz D P, Snyder K A. Protected paste volume in concrete: Extension to internal curing using saturated lightweight fine aggregate[J]. Cement and concrete research, 1999, 29(11): 1863-1867.

[147] Gupta S, Kua H W, Dai Pang S. Biochar-mortar composite: Manufacturing, evaluation of physical properties and economic viability[J]. Construction and Building Materials, 2018, 167: 874-889.

[148] Cannazza G, Cataldo A, De Benedetto E, et al. Experimental assessment of the use of a novel superabsorbent polymer (SAP) for the optimization of water consumption in agricultural irrigation process[J]. Water, 2014, 6(7): 2056-2069.

[149] M. Shand, A. Al-Tabbaa, J. Qian, L. Mo, and F. Jin, Magnesia Cements: From Formulation to Application. Newnes, 2020.

[150] Radlinska A, Rajabipour F, Bucher B, et al. Shrinkage mitigation strategies in cementitious systems: A closer look at differences in sealed and unsealed behavior[J]. Transportation Research Record: Journal of the Transportation Research Board, 2008, 2070: 59-67.

[151] Bentz D P, Garboczi E J, Snyder K A. A hard core/soft shell microstructural model

for studying percolation and transport in three-dimensional composite media[J]. 1999..

[152] NF P 18-459: Granulats – Détermination de l'absorption d'eau des granulats recyclés. Paris, France: AFNOR; 2010.

[153] Wong, H. S., & Buenfeld, N. R. (2006). Euclidean Distance Mapping for computing microstructural gradients at interfaces in composite materials. Cement and Concrete Research, 36(6), 1076–1089.

[154] Karen, C. (2004). Microstructure analysis of ITZ in high performance concretes. Cement and Concrete Research.

[155] Larbi, J. A. (2013). The Microstructure of the Interfacial Transition Zone. PhD Thesis, Delft University of Technology.

[156] Bajja, Z. (2016). Influence de la microstructure sur le transport diffusif dans les mortiers à base de CEMI + Fumée de silice. Université Paris-Saclay.

[157] Otsu, N. (1979). A threshold selection method from gray-level histograms. IEEE Transactions on Systems, Man, and Cybernetics, 9(1), 62–66.

[158] Robeyst, N., Gruyaert, E., Grosse, C. U.: Monitoring the setting of concrete containing blast-furnace slag by measuring the ultrasonic p-wave velocity. Cement and Concrete research, 38(10), 1169-1176 (2008).

[159] S. Eppers, C. Müller, The shrinkage cone method for measuring the autogenous shrinkage – an alternative to the corrugated tube method, in: O.M. Jensen, M.T. Hasholt, S. Laustsen (Eds.), International RILEM Conference on Use of Superabsorbent Polymers and Other New Additives in Concrete, RILEM Publications SARL, 2010, pp. 67–76. ISBN: 978-2-35158-104-9.

[160] EN 12617-4. Products and systems for the protection and repair of concrete structures – Test methods – Part 4: Determination of shrinkage [J]. 2002.

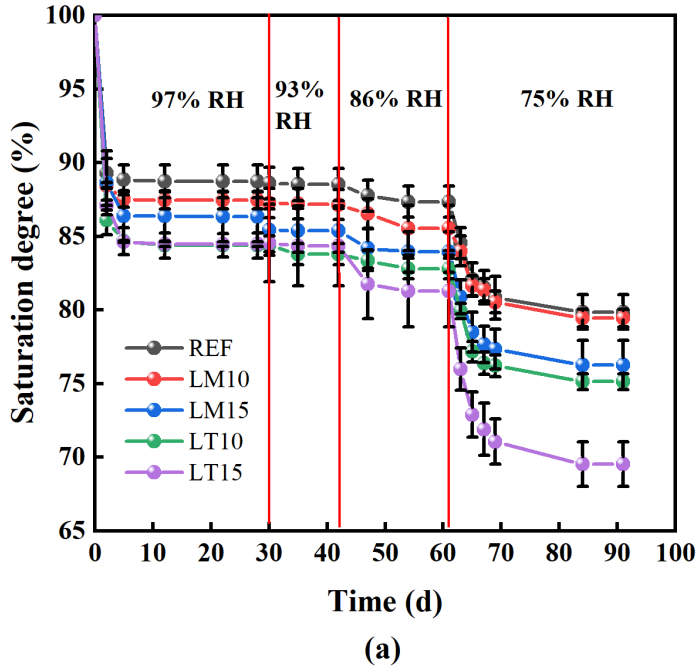
[161] Huang, H., Yuan, Y., Zhang, W., & Zhu, L. (2021). Property assessment of high-performance concrete containing three types of fibers. International Journal of Concrete Structures and Materials, 15, 39.

[162] Li, L., 2024. Delayed deformation of alkali sulphates activated materials under autogenous condition. Ph.D. Thesis, INSA Rennes, France

[163] Chua, H. T., Ng, K. C., Chakraborty, A., Oo, N. M., & Othman, M. A. (2002). Adsorption characteristics of silica gel + water systems. Journal of Chemical & Engineering Data, 47(5), 1177–1181

[164] Kocaba, V. Development and evaluation of methods to follow microstructural development of cementitious systems including slags, PhD theses. EPFL, 20-50 (2009).

Appendix A



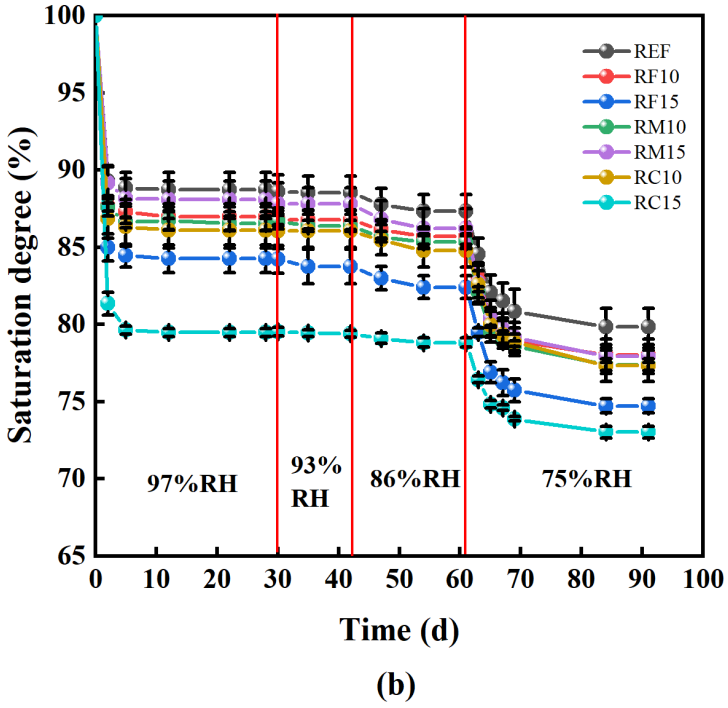


Figure. A.1 Evolution of the Saturation degree with R.H. and time for the mortars with LWA added (a) - mortars with RCA added (b)

Appendix B

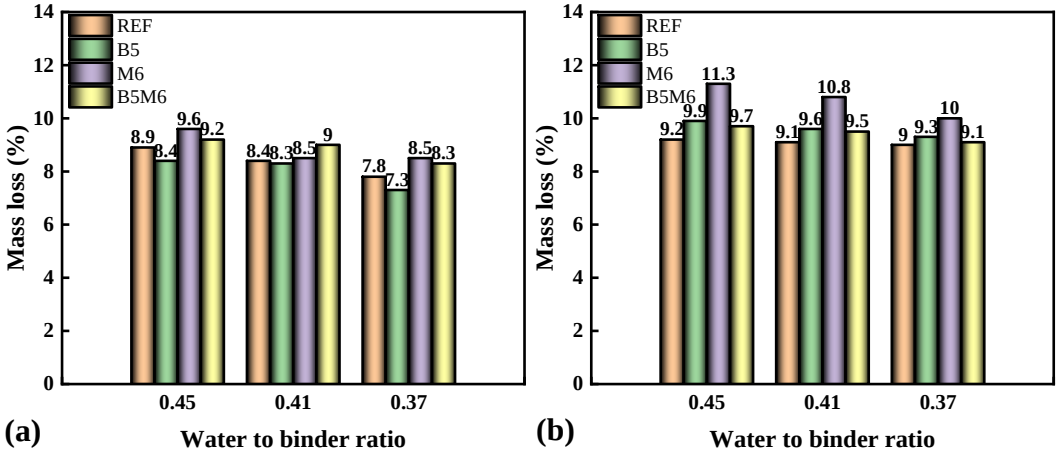


Figure. B.1. Mass loss in [105 ℃ - 550℃] at 3-day (a) and 28-day (b)

Figure B.1 illustrates the mass loss of different mixtures in the range of 105–550 ℃ at 3 and 28 days, which primarily corresponds to the dehydration of C–S–H and AFt/AFm phases as well as the dehydroxylation of $Ca(OH)_2$ and $Mg(OH)_2$. This mass loss is therefore indicative of the amount of hydration products formed.

At 3 days (Figure B.1 (a)), both M6 and B5M6 exhibit higher mass losses compared to REF (9.2% and 9.0% vs. 8.9% at W/B = 0.45), suggesting that the incorporation of MgO accelerates the formation of hydration products. The combined use of biochar and MgO (B5M6) also shows a slight enhancement relative to REF. In contrast, B5 consistently shows lower mass loss than REF across all W/B ratios, which confirms that biochar absorbs part of the mixing water and lowers the effective water-to-binder ratio, thereby retarding early hydration.

At 28 days (Figure B.1 (b)), all mixtures exhibit higher mass losses compared to 3 days, indicating the continuous development of hydration. M6 and B5M6 still record significantly higher values than REF (e.g., 11.3% and 10.8% vs. 9.4% at W/B = 0.45), reflecting the contribution of ongoing MgO hydration in producing additional chemically bound water. On the other hand, B5 shows values comparable to or slightly lower than REF, suggesting that biochar does not directly promote hydration at later

ages; instead, its main role is likely related to water distribution and internal curing rather than increasing chemically bound water.

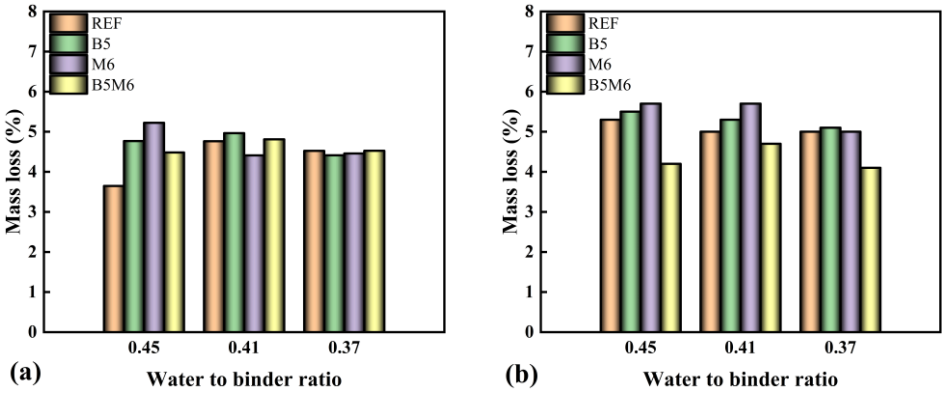


Figure. B.2 Mass loss in [400℃ - 550]℃ at 3-day (a) and 28-day (b)

Appendix C

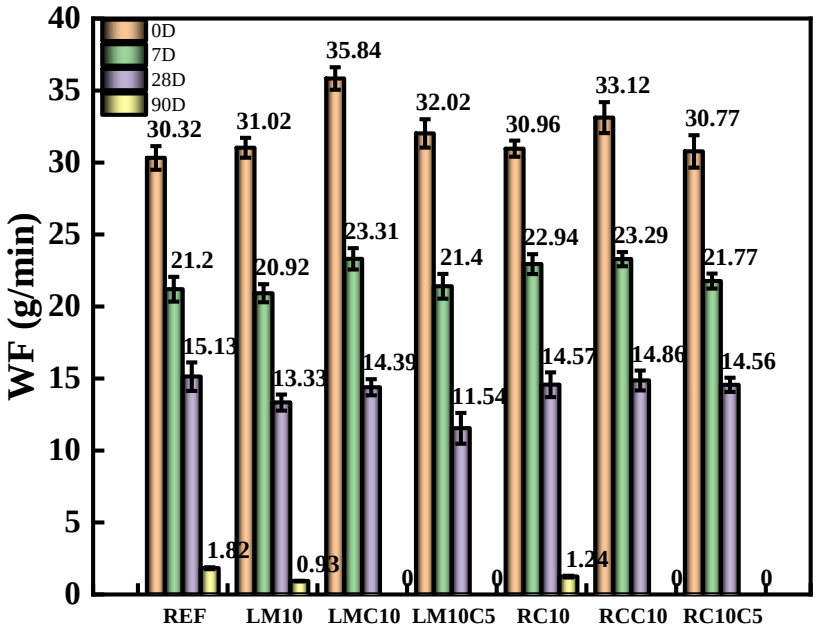


Figure. C.1 Evolution of WF evolution for REF, LM10, LMC10, LM10C5, RC10, RCC10 and RC10C5 under water curing

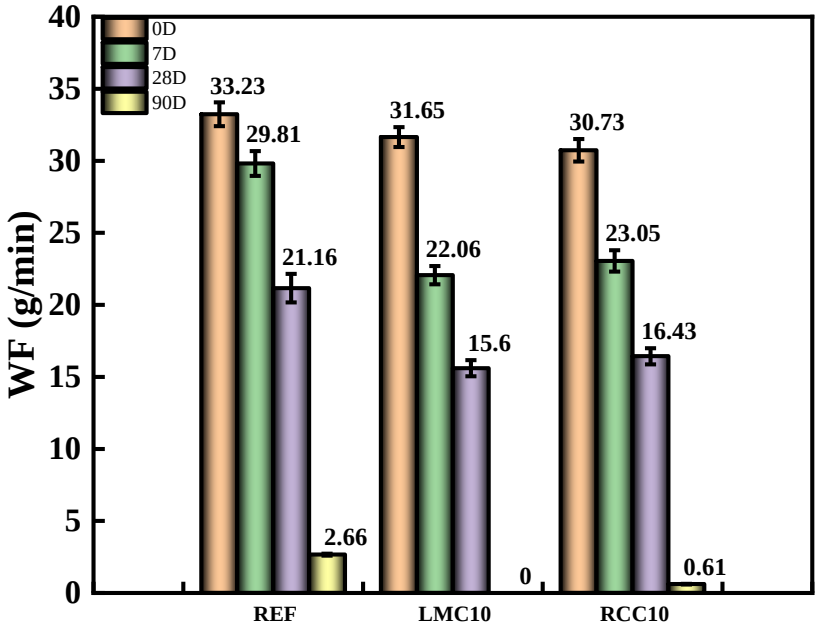


Figure. C.2 Evolution of WF for RCA, LMC10, and RCC10 under sealed curing

Titre : Effet de la cure interne sur le retrait et l'auto-cicatrisation des matériaux cimentaires

Mots clés : Cure interne; Retrait endogène; Retrait de dessiccation ; Auto-cicatrisation;

Granulats légers; Granulats recyclés; Biochar

Résumé : Cette recherche traite du problème de la fissuration prématurée du béton en étudiant le rôle des matériaux de cure interne dans la réduction du retrait endogène et du retrait de dessiccation, ainsi que dans l'amélioration des capacités d'auto-cicatrisation des matériaux à base de ciment. Plus précisément, les granulats légers (LWA), les granulats de béton recyclé (RCA) et le biochar ont été systématiquement étudiés afin d'évaluer leur comportement d'absorption et de libération d'eau, ainsi que leurs effets sur l'hydratation du ciment, la structure poreuse, les propriétés mécaniques et l'auto-cicatrisation.

Premièrement, des expériences ont été menées pour déterminer l'influence de différentes tailles et teneurs en LWA et RCA sur l'efficacité de la cure interne dans les mortiers. Les résultats ont montré que les granulats de petite taille réduisent plus efficacement le retrait endogène, améliorent la distribution de l'humidité relative interne et renforcent les performances mécaniques. En outre, les RCA présentent une excellente capacité de libération d'eau en raison de la pâte de ciment résiduelle à leur surface, ce qui améliore considérablement l'auto-cicatrisation du matériau.

Deuxièmement, l'incorporation de biochar dans le mortier a été étudiée en ce qui concerne son influence sur le processus d'hydratation et la structure des pores. Il a été démontré que le biochar réduit efficacement le retrait à jeune âge grâce à sa porosité élevée et à sa libération efficace d'eau. De plus, les effets de la combinaison du biochar avec de l'oxyde de magnésium (MgO) ont été examinés, montrant des améliorations notables des propriétés mécaniques et de la réduction du retrait.

Enfin, des méthodes 2D et 3D ont été mises en œuvre pour évaluer la capacité d'auto-cicatrisation apportées par les matériaux de cure interne. La combinaison de LWA et de RCA a considérablement accéléré la fermeture des fissures et amélioré la durabilité à long terme des matériaux à base de ciment.

Title : Effect of internal curing on shrinkage and self-healing of cementitious materials

Key words : Internal curing; Autogenous shrinkage; Drying shrinkage ; Self-healing; Lightweight aggregate; Recycled concrete aggregate; Biochar

Abstract : This research addresses the issue of early-age cracking in concrete by investigating the role of internal curing materials in mitigating autogenous and drying shrinkage, as well as enhancing self-healing capabilities of cement-based materials. Specifically, lightweight aggregates (LWA), recycled concrete aggregates (RCA), and biochar were systematically studied to assess their water absorption and release behaviors and their effects on cement hydration, pore structure, mechanical properties, and self-healing abilities.

Firstly, experiments were conducted to determine the influence of different particle sizes and contents of LWA and RCA on internal curing efficiency in mortar. Results indicated that smaller-sized aggregates more effectively reduced autogenous shrinkage, improved internal humidity distribution, and enhanced mechanical performance. Furthermore, RCA exhibited excellent water-release capabilities due to residual cement paste on their surfaces, significantly improving the self-healing capacity of the material.

Secondly, the incorporation of biochar into mortar was studied regarding its influence on hydration processes and pore structure. It was found that biochar effectively reduced early-age shrinkage due to its high porosity and effective water release. Additionally, the synergistic effects of combining biochar with magnesium oxide (MgO) were investigated, showing substantial improvements in mechanical properties and shrinkage reduction.

Lastly, two-dimensional and three-dimensional monitoring techniques were utilized to systematically evaluate the enhancements in self-healing performance provided by internal curing materials. The combination of LWA and RCA notably accelerated crack closure rates and significantly improved the long-term durability of cement-based materials.